The University of
Nottingham

# Experimental and simulation studies of iron oxides for geochemical fixation of $CO_2$-$SO_2$ gas mixtures

Susana García, MEng.

Thesis submitted to the University of Nottingham
for the degree of Doctor of Philosophy

July 2010

This Thesis is dedicated to Mamel

*"...There is still time to avoid the worst impacts of climate change if strong collective action starts now...*

*...The transition to a low-carbon economy will bring challenges for competitiveness but also opportunities for growth...* "

Nicholas Stern, 2006

# Abstract

Successful geological sequestration of carbon in deep saline aquifers as a technological strategy to reduce $CO_2$ emissions and combat climate change requires accurate predictive models of rock-brine-$CO_2$ interactions, which need to be validated and refined through comparisons with laboratory experiments.

The main objective of this Thesis is to study, experimentally and theoretically, whether iron oxides-containing subsurface formations would be potential reservoirs for sequestering $CO_2$-$SO_2$ gas mixtures derived from fossil fuel combustion processes. Benefits could be then derived of co-injecting sulfur with $CO_2$-dominated gas streams.

Experiments were conducted with two natural samples, hematite ($\alpha$-$Fe_2O_3$) and goethite ($\alpha$-FeOOH), using a high pressure-high temperature system designed to simulate conditions in geologic formations deeper than 800 m, where the supercritical state of $CO_2$ can be taken advantage of. Solid samples were allowed to react with a NaCl-NaOH brine and $SO_2$-bearing $CO_2$-dominated gas mixtures. Reacted solids were examined for mineralogical changes and collected fluids analysed to provide data on the fate of dissolved species.

Experimentally, brine composition and $SO_2$ content of the gas stream greatly influenced the pH of the system as well as mineralogical changes. Increasing reaction times, fine powders (< 38 μm), low values of solids concentration (10g/L) and reaction temperatures up to 100°C enhanced minerals dissolution and precipitation of secondary phases. Carbonates precipitates, siderite

($FeCO_3$) and dawsonite ($NaAl(OH)_2CO_3$), were observed as a result of the experiments along with some S-bearing phases and some residual salt. Reaction pressure was seen to have a major effect on availability of dissolved $SO_2$ and $CO_2$.

# Affirmation

The work reported in this thesis is solely the work of the author and has not been published elsewhere except for the following publications.

**Conference Proceedings**

Garcia S., Maroto-Valer M.M., Rosenbauer R.J. and Palandri J. *$CO_2$-$SO_2$ mixtures as feed to co-sequestration processes in geological formations.* CD rom International Symposium about Capture and Storage of $CO_2$, Seville, Spain, 2008.

Garcia S., Maroto-Valer M.M., Rosenbauer R.J.and Palandri J. *Ferric iron-bearing sediments as potential repositories for geological carbon dioxide storage.* Book of Abstracts of the 7th European Conference on Coal Research and its Applications, pg 58-59, Cardiff, UK, 2008.

Garcia S., Rosenbauer R.J., Palandri J. and Maroto-Valer M.M. *Sequestration of non-pure carbon dioxide streams in geological formations.* CD rom 7th Annual Conference on Carbon Capture & Sequestration, Pittsburgh, USA, 2008.

Garcia S. and Maroto-Valer M.M. *Understanding the chemical transformations in ferric iron containing sediments during carbon dioxide sequestration.* Book of Abstracts of the "Future energy: Chemical solutions" Conference, pg O10, Nottingham, UK, 2007.

Garcia S. and Maroto-Valer M.M. *Ferric iron-bearing sediments: Experimental assessment of their potential usage as a $CO_2$ mitigation option.* Proceedings of CHEMRAWN-XVII and ICCDU-IX Conference on Greenhouse Gases - Mitigation and Utilization, Kingston, Canada, 2007.

**Refereed Conference Proceedings**

Garcia S., Maroto-Valer M.M., Rosenbauer R. and Palandri J., *Injection of $CO_2$-$SO_2$ mixtures in geological formations as a potential approach for $CO_2$ storage*, Prep. Pap. – Am. Chem. Soc., Div. Fuel Chem. **2008**, 53(2), 735-736.

Garcia S. and Maroto-Valer M.M., *Carbon sequestration in sediments containing ferric iron*, International Conference on Coal Science and Technology (ICCS&T) **2007**, Nottingham, UK. ISBN 978-92-9029-438-2.

**Journal Publications**

Garcia S., Kaminska A. and Maroto-Valer M.M., *Underground carbon dioxide storage in saline formations*, Waste and Resource Management, 2010, accepted.

**Journal Publications in preparation**

Garcia S., Maroto-Valer M.M., Rosenbauer R.J. and Palandri J. *Sequestration of non-pure carbon dioxide streams in geological formations: $CO_2$-$SO_2$ reaction with goethite.* Applied Geochemistry.

Garcia S., Maroto-Valer M.M., Rosenbauer R.J. and Palandri J. *Evaluation of reaction variables in the geochemical trapping of* $CO_2$*-*$SO_2$ *gas mixtures with hematite.* Applied Geochemistry.

Garcia S., Maroto-Valer M.M., Rosenbauer R.J. and Palandri J. *Experimental and simulation studies of goethite-containing repositories as a novel concept for* $CO_2$ *sequestration.* International Journal of Greenhouse Gas Control.

# Acknowledgments

Firstly, I would like to acknowledge and thank my supervisor Professor Mercedes Maroto-Valer for her support, continuous guidance and excellent supervision throughout my PhD. Thank you for giving me the chance to be part of a fantastic research group and for having faith in me. I also would like to thank Bob Rosenbauer from the United States Geological Survey (USGS) and Dr. Jim Palandri from the University of Oregon. They welcomed me and made of my stay in the US a great experience. Thank you for all I learnt with you and for your continuous support ever since.

The financial support of the Centre for Innovation in Carbon Capture and Storage (CICCS) through the Engineering and Physical Sciences Research Council, EPSRC (EP/F012098/1), as well as the Department of Chemical and Environmental Engineering at the University of Nottingham are gratefully acknowledged. Also, thank you to the University of Nottingham Business-Engineering and Science Travel Scholarships (BESTS) Programme for financial support to carry out my work in US.

I would also like to thank Mick Fletcher, Jim Oswin and Phil Bennett for their great job in building up my experimental rig. I couldn't have done it without them. Thank you for your patience. Thank you also to Fred Anderton for his help with the electronical part of the rig and for his patience. Also, I would like to extend my gratitude to the rest of technicians who keep the place running and take care of the postgraduate labs, and to all the staff in the Department of Chemical and Environmental Engineering.

I would like to deeply acknowledge Dr. Ignacio Villar for his time, expertise and help with XPS analyses. But above all, thank you for been such a good friend. I would also like to extend a special thanks to: Dave Clift for his help with XRD analyses; Ron Perry for his help with ICP-AES analysis; Junfeng Qin, Larry Miller and Gil Ambats at USGS for their help and assistance in the lab, IC analyses and spectrophotometric analyses respectively.

I'm very grateful to all those postgraduates who I have shared office and labs with during my PhD. Thank you for a great office and lab atmosphere. Special thanks go to my dear friends and colleagues who supported me during this time: George, Silvy, Mari, Cova, Nacho, Ilich, Edu, Mark, Fabiola, Andy, Marian, Vale, Rob, John, Johnny, Trev, Will, Karl, Manu, Rich, Mara, Marta... Thank you for all the laughs, good moments, pub crawls and friendship. A special mention goes to George Alexander for his great help when I first started, Mark Kennedy for his support and help at all times and especially in my writing-up period, and Cova for her great support during the office hours we shared together in my writing-up period. Thank you also to the chemistry crew and those I met outside the University for contributing to this great experience.

I would love to thank my family, who I missed a lot and means everything to me in my life and I also missed Mery and our coffee times.

Of course, THANK YOU Mamel for just being you and being so incredibly special. Thank you for been always there for me.

# Abbreviations

| | |
|---|---|
| BE | Binding Energy |
| CCGT | Combined Cycle Gas Turbine |
| CCJ | Carbon Capture Journal |
| CCP | $CO_2$ capture project |
| CCS | Carbon Capture and Storage |
| CO2CRC | Cooperative Research Centre for Greenhouse Gas Technologies |
| EGR | Enhanced Gas Recovery |
| ELVs | Emission Limit Values |
| EOR | Enhanced oil recovery |
| EU | European Union |
| f | fugacity |
| IEA | International Energy Agency |
| IGCC | Integrated Gasification Combined Cycle |
| IPCC | Intergovernmental Panel on Climate Change |
| LCPD | Large Combustion Plants Directive |
| Ln | Litres under normal conditions |
| LNG | Liquefied Natural Gas |

| | |
|---|---|
| m | molality (mol/kg solvent) |
| M | Molarity (mol/L) |
| MFC | Mass Flow Controller |
| OJ | Official Journal (of the European Communities) |
| RCSPs | Regional Carbon Sequestration Partnerships |
| rpm | revolutions per minute |
| SCCS | Scottish Centre for Carbon Storage |
| TDS | Total Dissolved Solids |
| UN | United Nations |
| US-DOE | United States Department of Energy |
| WEO | World Energy Outlook |

# Table of contents

# CHAPTER 1

# INTRODUCTION

# 1. Introduction

Carbon dioxide capture and storage (CCS) is one of the climate change mitigation strategies considered for stabilization of carbon dioxide ($CO_2$) concentrations in the atmosphere. It involves capturing $CO_2$ arising from industrial and energy-related sources, transport to a storage site and isolation there from the atmosphere for a very long period of time (IPCC, 2005).

Amongst the different mechanisms by which $CO_2$ can be trapped underground, mineral trapping is believed to be comparatively slow (hundreds to thousands of years) but is also considered the safest and most permanent one because $CO_2$ is converted to stable carbonate minerals (Bergman and Winter, 1995, Reichle et al., 1999, IPCC, 2005). To date, studies have focused on Ca-, Mg- and $Fe^{II}$-bearing sediments to precipitate aqueous $CO_2$ as calcite ($CaCO_3$), magnesite ($MgCO_3$), siderite ($FeCO_3$) or ankerite ($CaFe(CO_3)_2$) (Pruess et al., 2001, Rosenbauer et al., 2005). Recent studies have considered the injection into $Fe^{III}$-bearing sediments, provided that a reducing agent is available for $Fe^{III}$ reduction to $Fe^{II}$, and therefore, precipitation of $CO_2$ as siderite ($FeCO_3$). Sulfur dioxide ($SO_2$) gas is a potential reductant since it is a component of the flue gas and could be co-injected with $CO_2$ instead of separated from the gas stream at great expense (Palandri and Kharaka, 2005, Palandri et al., 2005).

Most of existing coal-fired power plants remove $SO_x$ from exit gases but, in the future, plants may simultaneously treat $CO_2$ and other gas constituents derived from fossil fuel combustion ($SO_x$, $NO_x$...). Then, the novel concept of co-disposal of flue gas-derived $CO_2$-$SO_2$ gas streams could become of high interest for a full-scale CCS project.

## 1.1. Iron presence in geological formations

Iron, with an average concentration of 51 g/kg, is the third most abundant cationic element in the earth's crust after Si (269 g/kg) and Al (81 g/kg) (Brownlow, 1979, Cornell and Schwertmann, 2003). Therefore, there is hardly any rock completely free from iron. It occurs in nature in a variety of rocks and soil minerals in oxidation states II and III.

By convention, rocks are divided into three groups: magmatic, metamorphic and sedimentary rocks. Iron ores are also rocks and are common in all three groups, containing iron oxide minerals of varying nature and abundance. There are three different types of sedimentary rocks: mudrocks (65%), sandstones (20-25%) and carbonate rocks (10-15%) (Cornell and Schwertmann, 2003). The iron content of sediments varies greatly with the type of rock: total iron in red sandstone and mudstones averages 1.7 to 3.5%; an average range for all kinds of sandstones is 2.35% to 2.9% total iron. Free (extractable) iron in the ferric oxide pigment averages about 0.67%. Normally both, total iron and free iron, increase with decreasing grain size; mudstones and matrix-rich sandstones have more of their iron in the clay fraction. Nevertheless, the amount of iron in the pigment is very small compared with that in opaque grains, dark silicates, and iron-bearing clay minerals (Van Houten, 1973). In addition, Fe is a common impurity in other sedimentary minerals.

Red beds and sedimentary iron ores are groups of Fe-containing sediments whose iron oxides have attracted a lot of interest. Red beds are widespread all over the world and sedimentary iron ores worth mining comprise about 80% of the world's iron-ore production and ca. 90% of the world reserves. Both types of sediments contain iron-rich deposits, which are defined as those of at least 15% Fe. This amount is much greater than the average for mudrocks, sandstones or limestones but all these three groups of rock can, however, grade laterally into an iron-rich deposit (Blatt, 1982). Some iron formations consist largely of iron oxide. Of these hematite, $\alpha$-$Fe_2O_3$, is the most important. Sedimentary hematities are found throughout the Appalachian region and form important deposits of iron ore in the Birmingham district of Alabama. The oolites consist of a nucleus of quartz which may be very minute or a not so small quartz sand grain, around which successive layers of iron oxides, and in many cases silica, were deposited (Pettijohn, 1957).

The "red beds" are shales and sandstones with a red coloration owed to disseminated hematite. In the sandstones the hematite forms a thin film on the sand grains, although in a few cases it may constitute the cement. Less commonly the iron oxides occur as an alteration product of siderite or other ferrous iron compounds (Pettijohn, 1957). Nonmarine desert sandy red beds are found in Colorado, eastern Canada, central Europe, Great Britain, southern and Baja California and in the central Sahara. Extensive, well-sorted and fine-grained red beds include those ones in Texas, New Mexico and Wyoming. Red beds can also be found in India and northern Spain (Van Houten, 1973).

Hematite and goethite (α-FeOOH) are the main Fe-bearing minerals in sedimentary red beds. Hematite is abundant in ancient red beds whereas goethite is abundant in younger yellow-brown colored deposits (Gualtieri and Venturelli, 1999). Goethite in iron stones may have formed primarily in oxygenated coastal zones; formation may also be secondary, resulting from oxidation of siderite or other FeII minerals. Ferriferous spherules largely of goethite are forming at the present time in Lake Chad, West Africa, and $Fe^{3+}$-rich oolitic grains occur on the Amazon inner shelf. Sub-recent coated grains (oncoids) of goethite occur on the Cameroon shelf. Goethite "ooids" and pisoids are forming in lateritic soils of tropical regions (Tucker, 2001).

Therefore, the $CO_2$ sequestering potential of Fe-bearing sediments is worthy of research studies. Furthermore, Fe(III) – bearing sediments, including red beds, generally present great thickness and high porosity and permeability values as well as a widespread geographic distribution (Palandri et al., 2005), making them potential sites for underground $CO_2$ sequestration in carbonate form.

## 1.2. Reaction of $CO_2$-$SO_2$ gas mixtures with ferric iron and water

In this section several geochemical reactions are explained in order to get an understanding of the chemical aspects behind the reaction of $CO_2$-$SO_2$ gas mixtures with ferric iron and water. The overall reaction would lead to iron carbonate and sulfuric acid formation (reaction [1-1] for hematite and [1-2] for goethite). Hematite (α-$Fe_2O_3$) and goethite (α-FeOOH) were used as a proxy for Fe (III) in sediments. The thermodynamics associated with reactions below

(Table 1-1) show they are both spontaneous ($\Delta G_R^0 < 0$) and exothermic ($\Delta H_R^0 < 0$).

$Fe_2O_3$ (hematite) + 2 $CO_2$ + $SO_2$ + $H_2O$ ↔ 2 $FeCO_3$ (siderite) + $H_2SO_4$ [1-1]

2FeOOH (goethite) + $2CO_2$ + $SO_2$ ↔ $2FeCO_3$ + $H_2SO_4$ [1-2]

Table 1-1. Gibbs Energy of reaction ($\Delta G_R^0$) and Heat of reaction ($\Delta H_R^0$) for reactions [1-1] and [1-2]. Thermodynamic data was taken from (Stumm and Morgan, 1996) and (Weast, 1984).

| *Iron mineral* | $\Delta G_R^0$*(KJ/mol)** | $\Delta H_R^0$*(KJ/mol)** |
|---|---|---|
| Hematite (α-$Fe_2O_3$) | -16.31 | -196.61 |
| Goethite (α-FeOOH) | -18.68 | -188.72 |

*The values of thermodynamic properties are calculated at 1bar and 25°C.

The first step in reactions [1-1] and [1-2] is the dissolution of the gases and their conversion to their respective aqueous forms, eg., $HCO_3^-$, $CO_3^{2-}$, $H_2CO_3$, $HS^-$ and $H_2S$ (reactions [1-3] to [1-7]). Upon injection, the $SO_2$ would partition into the pore waters, as $SO_2$ is extremely soluble in the aqueous phase, according to a disproportionation reaction (reaction [1-3]) that yields dissolved sulfide ($H_2S$) and sulfuric acid ($H_2SO_4$). $CO_2$ would also dissolve in the pore waters to form bicarbonate and carbonate ions (reactions [1-4] to [1-7]).

$4\ SO_2(g) + 4\ H_2O \leftrightarrow H_2S + 3\ H_2SO_4$ [1-3]

$CO_{2\,(g)} \leftrightarrow CO_{2(aq)}$ [1-4]

$CO_{2(aq)} + H_2O \leftrightarrow H_2CO_3$ [1-5]

$H_2CO_3 \leftrightarrow HCO_3^- + H^+$ [1-6]

$HCO_3^- \leftrightarrow CO_3^{2-} + H^+$ [1-7]

After this initial step, dissolved sulfide will reduce $Fe^{III}$ to $Fe^{II}$ as the sulfide is oxidized to sulfate (reaction [1-8]), and $Fe^{II}$ would be then available for further precipitation as iron carbonate, i.e. siderite (reaction [1-9]).

$8\ Fe^{3+} + HS^- + 4\ H_2O \leftrightarrow 8\ Fe^{2+} + SO_4^{2-} + 9\ H^+$ [1-8]

$H_2CO_3 + Fe^{2+} \leftrightarrow FeCO_3 + 2H^+$ [1-9]

In natural environments, reductive dissolution is by far the most important dissolution mechanism (protonation and complexation are the others) (Cornell and Schwertmann, 2003). In the reductive dissolution of iron oxides (reaction [1-8]), the detachment of Fe is likely to be rate determining, but it can not be ruled out that, as suggested for Mn oxides, electron transfer is, in some cases, rate limiting (Cornell and Schwertmann, 2003). Reduction of $Fe^{III}$ to $Fe^{II}$ destabilises the coordination sphere of the iron both, as a result of the loss of charge and because of the larger size of the bivalent $Fe^{II}$ (0,078 vs 0.064 nm), and thus induces detachment of iron as $Fe^{2+}$ from the structure. Thereby, reductive dissolution involves the transfer of electrons from the environment, through a reducing ligand or reductant, to an oxide surface, followed by dissolution (Biber et al., 1994, Cornell and Schwertmann, 2003). Because the reducing ligand is (usually) a charged species, pH will, through its effect on extent of ligand adsorption, have a strong effect on the rate of reductive dissolution. This will be a function of both pH and the concentration of ligand in solution (Cornell and Schwertmann, 2003).

If the only sink to trap $CO_2$ is the ferric iron contained in the sediments, then reactions [1-1] and [1-2] show the gas composition required is 2/3 $CO_2$ and 1/3 of $SO_2$. The flue gas derived from the combustion of fossil fuel typically contains between 0.15 and 2 vol.% of $SO_2$, when deliberately recovered and incorporated with $CO_2$ in the injectate (Apps, 2006). This amount would not be high enough to trap all the ferric iron in siderite, provided that sufficient $Fe^{III}$ is present. Hence, one of the following options could be undertaken in order to effectively trap $CO_2$ in carbonate minerals using ferric-iron bearing sediments:

a) Usage of sediments containing additional divalent metals (e.g., Ca, Mg, etc) for further precipitation of their respective carbonates.

b) Addition of sulfur-bearing gas to the waste gas stream, like $H_2S$ from sour natural gas processing.

c) Burning of coals with higher sulfur concentrations: nowadays coals with high sulfur content are not prone to be used due to the Emission Limit Values (ELVs) for $SO_2$ being lowered down since the Large Combustion Plants Directive (LCPD). The latter one aims to reduce acidification, ground level ozone, and particles throughout Europe by controlling emissions of $SO_2$, nitrogen oxides ($NO_x$), and dust (particulate matter) from large (above 50MW thermal) combustion plants (OJ, 2001).

## 1.3. Contributions of this research work

Mineral trapping experimental studies with $CO_2$-$SO_2$ gas mixtures are very scarce (Summers et al., 2004, Palandri et al., 2005, Mandalaparty et al., 2009) and only one has been found that targeted ferric iron-bearing sediments as potential host repositories for underground $CO_2$ storage (Palandri et al., 2005). Thereby, no extensive laboratory studies directed at the sequestration of $CO_2$ in iron oxides-brine-$CO_2$-$SO_2$ systems have been conducted so far. This novel concept could also be applied to a new range of technologies currently under study to develop integrated pollutant removal systems for coal combustion (Chiesa et al., 2005, IPCC, 2005).

The previous experimental study with iron-bearing sediments was carried out with hematite at 150°C and 300 bar (Palandri et al., 2005). In that work, hematite was reacted in a 1.0m NaCl, 0.5m NaOH brine with a $CO_2$-$SO_2$ gas stream containing 88.9 and 11.1% (by volume) of $CO_2$ and $SO_2$ respectively, and 66.7 g/L as the tested value of solids concentration. The addition of NaOH aimed to mimic the natural mineral buffering of pH, thereby increasing the degree of siderite supersaturation and its precipitation rate.

This work expands Palandri and co-workers' one (Palandri et al., 2005) by the systematic, theoretical and experimental, study of the influence of reaction variables in the same reactive system, i.e. hematite, brine and gases. In this case, the baseline experiment for the hematite analysis was chosen to be more representative of a real-case scenario, i.e. 100°C and 250 bar vs 150°C and 300 bar. Although the pressure (250 bar) is within the range typically found in sedimentary formations, the temperature (100°C) is at the high end of the common range. However, it was selected to increase reaction rates in the experiment.

Solids particle size, reaction time, gas composition ($CO_2/SO_2$), reactor pressure and temperature, concentration of solids and brine composition are the reaction variables experimentally assessed in the hematite-brine-$CO_2$-$SO_2$ system.

Selection of three fine fractions (-38, 38-150 and 150-300 μm) for the experimental work aimed to speed up the carbonation reaction as well as to study the influence of the particle size of the solids in the reaction. Reaction time ranged from 24 to 264 h and longer experiments were excluded due to time constraints. Three different $CO_2$:$SO_2$ gas concentrations, more representative of real-case scenarios than the one tested before (Palandri et al., 2005), were tested in laboratory experiments: the common one in a flue gas stream derived from the combustion of fossil fuels (99.6:0.4) and two additional ones with increasing amounts of $SO_2$ (99.1:0.9 and 98.8:1.2). The former ones were chosen because they are still representative of real-case scenarios (for instance, in flue gas derived from oxyfuel combustion) and, at the same time, increasing amounts of $SO_2$ would favour siderite supersaturation and its precipitation in the experiments. Reaction conditions of temperature (75, 100, 125 and 150°C) and pressure (120, 180, 250 and 320 bar) were selected in order to cover a whole range of depths within sedimentary basins. In some experiments, for instance those at temperatures relatively high for injection sites (125 and 150°C), conditions were an attempt to enhance reaction kinetics. The values of solids concentration to be tested (10, 25, 50 and 100 g/L) were arbitrary chosen, aiming to cover a broad range of rock-to-brine ratios. However, in a real-case scenario a high rock-to-brine ratio is expected.

Adittionally, this work evaluates for first time whether goethite could be a potential repository for $CO_2$ storage by mineral trapping. The experiment reported by Palandri and co-workers (Palandri et al., 2005) is duplicated with goethite under the same experimental conditions and in the same experimental set-up in order to compare the sensitivity of the reaction to the host rock.

The influence of reaction variables (solids particle size, reaction time and gas composition) in the carbonation reaction is also evaluated for goethite. The chosen values for reaction variables are the same ones as for the hematite case, following criteria explained above. Reaction pressure, temperature, solids-to-liquid ratio and buffering effect have not been evaluated for the goethite specimen because of time constraints, but are expected to have similar effects as reported ones for hematite.

## 1.4. Implementation of geological storage of $CO_2$-$SO_2$ gas streams: legal and regulatory aspects

The legal framework needed for the implementation of long-term geological storage of $CO_2$ is one of the most challenging areas. Important developments have taken place in recent years like the amendment to the London Protocol (Anon., 2006), which entered into force on February 2007, by which "$CO_2$

streams from $CO_2$ capture processes" could be stored beneath the seabed in certain circumstances[1]. The OSPAR (Oslo-Paris) Convention for the protection of the marine environment of the North-East Atlantic against pollution is another international marine treaty that was amended in June 2007 to allow the storage of $CO_2$ in geological formations under the seabed (Haszeldine et al., 2007, de Coninck et al., 2009).

Like the amendments to the London Protocol and the OSPAR Convention, a European Union Directive on the geological storage of $CO_2$ (2009/31/EC) was published on 23 April 2009 (OJ, 2009). Some issues are addressed in the Directive, for instance, the right of Member States to determine the areas within their territory from which storage sites may be selected. It also states that the responsibility for the long-term management of storage sites post-closure is transferred to the competent authorities of Member States. The Directive entered into force on May 13 2009; Member States have until June 25 2011 for its transposition into national legislation. In the European scenario, there are also a few directives that could influence national legislation with regards to CCS: the framework directive on water (2000/60/EC), the framework directive on waste materials (2008/98/EC) and the landfill directive (1999/31/EG) (Lenstra and van Engelenburg, 2002).

Schemes where emissions of $SO_2$ are included within the $CO_2$ stream may require a review of existing legislation. The amendment to the London Protocol

---

[1] "$CO_2$ streams from $CO_2$ capture processes for sequestration are permitted: 1) only if these are injected into a sub seabed geological formation; 2) only if these consist overwhelmingly of $CO_2$, although these may contain incidental associated substances derived from the source material and capture and sequestration processes used; 3) only if no wastes or other matter are added for the purpose of disposal".

states that only $CO_2$ streams consisting overwhelmingly of $CO_2$ could be considered for disposal. Likewise, the European Directive defines a $CO_2$ stream acceptance criteria and procedure. According to this criterion "a $CO_2$ stream may contain incidental associated substances from the source, capture or injection process and trace substances added to assist in monitoring and verifying $CO_2$ migrations". Based on that statement, $SO_2$ could be considered a legitimate associate substance derived from the source material in a fossil fuel-fired power plant. Hence, this work and its suggested use would not be in conflict with that Directive since the $CO_2$ stream would consist mainly of $CO_2$, and $SO_2$ would be only present as an incidental substance derived from the source material. However, further clarification of the "overwhelmingly" concept as well as the concentration and type of impurities allowed in the $CO_2$ streams would be helpful to address co-injection of contaminants along with $CO_2$ in a CCS system.

## 1.5. Aim and objectives

The overall ***aim*** of this research project is to assess both, theoretically and experimentally, the conditions under which mineral trapping would take place in iron oxides, provided that the injected stream is a $CO_2$-$SO_2$ gas mixture, and how this concept could be considered as a geological storage option to be pursued in order to meet greenhouse emissions reductions.

The specific ***objectives*** of this research project are:

1- To develop a high pressure-high temperature system adequate for short-term (≤ 24 h) as well as long-term carbonation experiments and reaction with $CO_2$-$SO_2$ gas mixtures.

2- To predict, by geochemical modelling, which phases (gaseous, liquid and solid) would be present at equilibrium in $CO_2$-$SO_2$-brine-iron oxide systems reacted under different conditions of temperature, pressure, gas composition, solids-to-liquid ratio and brine composition.

3- To empirically study the mineral trapping capacity of iron oxides for underground $CO_2$ storage over a wide range of operating conditions including particle size of the solids, pressure, temperature, reaction time, gas composition, solids-to-liquid ratio and brine composition.

4- To assess whether the empirical system is moving towards the predicted equilibrium through the validation of geochemical modeling results against the observed experimental trends.

An off-the-shelf geochemical code, CHILLER, will be used to compute the equilibrium distribution of thermodynamic components among aqueous species, minerals and gases under different reaction conditions. The equilibrium is computed by changing one of the systems variables incrementally with re-calculation of the equilibrium phase assemblage, mineral and aqueous composition at each step.

A stirred-high pressure-high temperature reactor will be used to allow $CO_2$-$SO_2$ gas mixtures, brine and hematite samples react with each other. Series of experiments will be conducted with increasing values of one of the following variables: solids particle size, pressure, temperature, reaction time, $SO_2$ content and solids concentration. The buffering effect of the brine will be also investigated. For experiments with goethite the variables that will be studied are particle size of the solids, reaction time and $SO_2$ content. The rest of variables are expected to play a similar role as for experiments with hematite and will not be studied here. The reacted brine and collected solids from the experiments will be characterised and compared to the unreacted brine and parent samples using various analytical techniques. The initial and final pH values will also be measured to determine changes in pH after reactions. The geochemical model will be then validated through comparison with empirical results from laboratory experiments.

## 1.6. References

Anon. (2006) $CO_2$ sequestration in Sub-Seabed Formations: Consideration of Proposals to Amend Annex 1 to the London Protocol. Available from: <http://www.aph.gov.au/house/committee/jsct/co2sequestration/treaties/co2_text.pdf> (accessed 15 October 2008).

Apps, J. A. (2006). A review of hazardous chemical species associated with $CO_2$ capture from coal-fired power plants and their potential fate during $CO_2$ geological storage, Lawrence Berkeley National Laboratory, Berkeley, CA, USA.

Bergman, P. D. & Winter, E. M. (1995) Disposal of carbon dioxide in aquifers in the U.S. *Energy Conversion and Management,* 36, 523-526.

Biber, M. V., dos Santos Afonso, M. & Stumm, W. (1994) The coordination chemistry of weathering: IV. Inhibition of the dissolution of oxide minerals. *Geochimica et Cosmochimica Acta,* 58, 1999-2010.

Blatt, H. (1982) *Sedimentary Petrology,* Oxford, Freeman, W.H.

Brownlow, A. H. (1979) *Geochemistry,* New York, Prentice-Hall.

Chiesa, P., Consonni, S., Kreutz, T. & Robert, W. (2005) Co-production of hydrogen, electricity and $CO_2$ from coal with commercially ready technology. Part A: Performance and emissions. *International Journal of Hydrogen Energy,* 30, 747-767.

Cornell, R. M. & Schwertmann, U. (2003) *The Iron Oxides. Structure, Properties, Reactions, Occurrences and Uses,* Weinheim, Wiley-VCH.

de Coninck, H., Flach, T., Curnow, P., Richardson, P., Anderson, J., Shackley, S., Sigurthorsson, G. & Reiner, D. (2009) The acceptability of $CO_2$ capture and storage (CCS) in Europe: An assessment of the key determining factors: Part 1. Scientific, technical and economic dimensions. *International Journal of Greenhouse Gas Control,* 3, 333-343.

Gualtieri, A. F. & Venturelli, P. (1999) In sity study of the goethite-hematite phase transformation by real time synchrotron powder diffraction. *American Mineralogist,* 84, 895-904.

Haszeldine, R. S., Reiner, D. M., Shackley, S. & Kendall, M. (2007) Regulation for CCS beneath the UK offshore and onshore: deep geological storage and sequestration of $CO_2$. *International Risk Governance Council (IRGC) workshop on regulation of geological storage of $CO_2$.* Washington DC.

IPCC (2005). IPCC Special Report on Carbon Dioxide Capture and Storage, Prepared by Working Group III of Intergovernmental Panel on Climate Change, Cambridge, United Kingdom and New York, NY, USA.

Lenstra, W. J. & van Engelenburg, B. C. W. (2002) Legal and policy aspects: impact on the development of $CO_2$ storage. *Workshop on Carbon Dioxide Capture and Storage.* Canada, Working Group III of Intergovernmental Panel on Climate Change (IPCC).

Mandalaparty, P., Deo, M., Moore, J. & McPherson, B. (2009). Carbon dioxide sequestration: effect of the presence of sulfur dioxide on the mineralogical reactions and on the injectivity of $CO_2$+$SO_2$ mixtures, University of Utah, Salt Lake City.

OJ No. L309, Directive 2001/80/EC of the European Parliament and of the Council on the limitation of emissions of certain pollutants into the air from large combustion plants, 27.11.2001, p.1.

OJ No. L140, Directive 2009/31/EC of the European Parliament and of the Council on the geological storage of carbon dioxide, 5.6.2009, p.114.

Palandri, J. L. & Kharaka, Y. K. (2005) Ferric iron-bearing sediments as a mineral trap for $CO_2$ sequestration: Iron reduction using sulfur-bearing waste gas. *Chemical Geology,* 217, 351-364.

Palandri, J. L., Rosenbauer, R. J. & Kharaka, Y. K. (2005) Ferric iron in sediments as a novel $CO_2$ mineral trap:$CO_2$-$SO_2$ reaction with hematite. *Applied Geochemistry,* 20, 2038-2048.

Pettijohn, F. J. (1957) *Sedimentary rocks*, Harper & Brothers New York.

Pruess, K., Xu, T., Apps, J. & Garcia, J. (2001) Numerical modeling of aquifer disposal of $CO_2$. Proceedings of the SPE/EPS/DOE Exploration and Environmental Conference, San Antonio,TX.

Reichle, D., Houghton, J., Kane, B., Ekmann, J. & others (1999). Carbon sequestration research and development, DOE, US.

Rosenbauer, R. J., Koksalan, T. & Palandri, J. L. (2005) Experimental investigation of $CO_2$-brine-rock interactions at elevated temperature and pressure: Implications for $CO_2$ sequestration in deep-saline aquifers. *Fuel Processing Technology,* 86, 1581-1597.

Stumm, W. & Morgan, J. J. (1996) *Aquatic chemistry: chemical equilibria and rates in natural waters,* New York, Wiley-Interscience.

Summers, C. A., Dahlin, D. C. & Ochs, T. L. (2004) The effect of $SO_2$ on mineral carbonation in batch tests. Proceedings of the 29th International Technical Conference on Coal Utilization and Fuel Systems, Gaithersburg, MD.

Tucker, M. E. (2001) *Sedimentary petrology : an introduction to the origin of sedimentary rocks,* Hoboken, NJ, Wiley-Blackwell.

Van Houten, F. B. (1973) Origin of red beds : a review -1961-1972. *Annual Review of Earth and Planetary Sciences,* 1, 39-61.

Weast, R. C. (Ed.) (1984) *CRC Handbook of Chemistry and Physics,* Florida,USA, CRC Press, Inc.

# CHAPTER 2

# LITERATURE REVIEW

# 2. Literature review

## 2.1. $CO_2$ emissions and carbon management

Steady increases in world carbon dioxide emissions (Solomon et al., 2007) have raised legitimate concerns about global warming and imbalances in the terrestrial carbon cycle. The global atmospheric concentration of $CO_2$ has increased by 37.1% from a pre-industrial value of about 280 ppm to 384 ppm in 2009 (NOAA-ESRL, 2009). New and strong evidences attribute most of the warming observed over the past fifty years to human activities and those will continue affecting the atmospheric composition throughout the 21st century (Metz et al., 2007).

A number of gases (water vapour ($H_2O$), carbon dioxide ($CO_2$), methane ($CH_4$), nitrous oxide ($N_2O$), chlorofluorocarbons ($CF_xCl_x$) and tropospheric ozone ($O_3$)) are involved in the anthropogenic enhancement of the greenhouse effect (Houghton et al., 2001, Metz et al., 2007). Of these gases, the single most important gas is $CO_2$, which accounts for about 55% of the change in the intensity of the earth's greenhouse effect (Pidwirny, 2006). Greenhouse gas (GHG) emissions are reported as volume of $CO_2$-equivalent ($CO_2$-eq) emissions in order to have a common unit that enables comparison between the different GHG. $CO_2$-eq is defined as the amount of $CO_2$ emission that would cause the same radiative forcing[1] (RF) as an emitted amount of a well mixed GHG or a mixture of well mixed GHG, all multiplied with their respective

---

[1] RF is a measure of the influence that a factor has in altering the balance of incoming and outcoming energy in the Earth-atmosphere system. Positive forcing tends to warm the surface while negative forcing tends to cool it.

global warming potential (GWP) to take into account the different times they remain in the atmosphere (Metz et al., 2007). GHG have different GWP that are calculated by a given time horizon (Solomon et al., 2007). Anthropogenic $CO_2$ emissions have grown between 1970 and 2004 by about 80% and represented 77% of total anthropogenic GHG emissions in 2004 (Metz et al., 2007). $CO_2$ can be released into the atmosphere by combustion of fossil fuels and other carbon-containing materials, burning of forests during land clearance and from certain industrial and resource extraction processes.

The primary source of the increased atmospheric concentration of $CO_2$ since the pre-industrial period results from fossil fuel use (Figure 2-1); they provide about 80 % of global primary energy and this leads to anthropogenic emissions from combustion of fossil fuels of about 26 $GtCO_2$/year (Holloway, 2001, Dooley et al., 2006), with land-use change providing another significant but smaller contribution (Solomon et al., 2007).

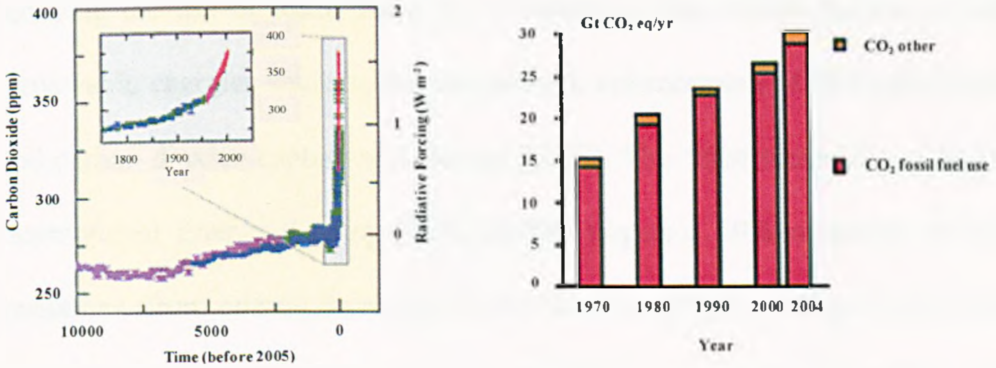

Figure 2-1. Atmospheric concentrations of carbon dioxide over the last 10,000 years (large panel) and since 1750 (inset panel) (left): modified from (Solomon et al., 2007); $CO_2$ emissions from energy production and others (right): modified from (Metz et al., 2007).

It has been asserted by the UN Framework Convention on Climate Change that a reduction on $CO_2$ emissions needs to be addressed in order to prevent dangerous interferences with the climate system although the specific target level of concentration in the atmosphere has not yet been quantified (IPCC, 2005). The global economy is set to grow four-fold between now and 2050 and a ten-fold growth could be approached in developing countries like India and China, which will involve much more use of energy (IEA, 2008b). Although as a result of current financial and economic crisis the global energy use is set to fall in 2009 (for the first time since 1981 on a significant scale), if current energy policies are maintained, it would quickly resume its long-term upward trend once economic recovery is underway (IEA, 2009). Hence, the global energy economy will need to be transformed over the coming decades. The way energy is supplied and used needs a global revolution; it seems clear that a single option is not the solution to tackle the problem and a broad portfolio of options should be taken into account in order to properly address the issue and meet the reduction requirements.

A wide variety of mitigation options include energy efficiency improvements, reducing the use of fossil fuels, by switching to less carbon intensive fuels (renewable energies sources, nuclear power), enhancement of biological sinks and carbon dioxide capture and storage (CCS). The "blue scenario" set by the International Energy Agency (IEA, 2008b) targets a 50% reduction in $CO_2$ emissions (from current levels) by 2050. Sources of $CO_2$ savings in the "blue map scenario" are compared to a "baseline scenario" where the $CO_2$ atmospheric concentration stabilises at a "safe" value of 450 ppm (Figure 2-2): energy efficiency improvements represent the largest and least costly savings.

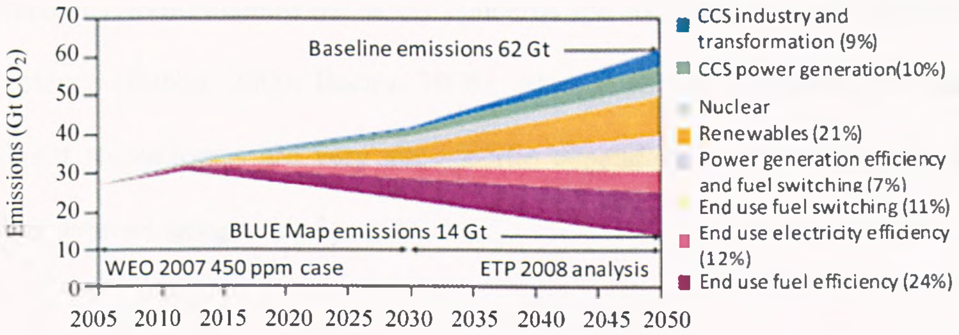

Figure 2-2. Comparison of the BLUE map scenario with the baseline 450 ppm case scenario, 2005-2050 (IEA, 2008b).

Decarbonising power generation and energy from fossil fuels (i.e., nuclear power, renewables and use of CCS at fossil fuel plants) comes next in the hierarchy of importance and it will be imperiously needed since fossil fuels are projected to maintain their dominant position in the global energy mix to 2030 and beyond (Metz et al., 2007). The IEA stabilisation scenario is based on the stabilisation wedges proposed by Pacala and Socolow (Pacala and Socolow, 2004). They claimed fossil fuel emissions could be stabilised at 7 GtC/year[2] over 50 years (2004-2054) by selecting seven wedges out of 15 potential ones. Each wedge represents a strategy to reduce the carbon emission rate by 1 GtC/year so the total avoided emissions per wedge are 25 GtC over the 50-years period. CCS technologies were proposed as 3 out of the 15 wedges. Whichever the final target in $CO_2$ emissions, action in all the areas indicated in Figure 2-2 is urgent and necessary.

The feasibility of CCS compared to the other options will depend on several factors such as time that $CO_2$ will remain stored, possibility of leakages, means of transport to the storage site, cost, rate at which the technology can be

---

[2] To convert Gt of carbon to Gt of $CO_2$, multiply by 3.67

introduced, environmental and safety concerns and social factors such as public acceptance (Bachu, 2000, Bachu, 2008). Also, it should be pointed out that different technologies are very site-specific depending on the availability of energy sources, geographic location, etc.

## 2.2. Carbon capture and storage (CCS)

Carbon capture and storage (CCS) has the potential to reduce overall mitigation costs and maintain the use of fossil fuels as an energy source in the short-term whilst future non- fossil based fuel energy systems are developed and implemented (Lackner et al., 1998, IPCC, 2005, Mazzotti et al., 2009). CCS as a mitigation approach can be applied to large point sources and it will imply capturing the $CO_2$ (separation from the flue gas and further compression), transport to a storage site and isolation there from the atmosphere. Some of the risks associated with $CO_2$ capture and geological storage are similar to, and comparable with, any other industrial activity for which extensive safety and regulatory frameworks are in place. Specific risks associated with $CO_2$ storage relate to the operational (injection) phase and to post-operational phase, of which the risks of most concern are those posed by the potential for acute or chronic $CO_2$ leakage from the storage site. Hence, local risks to health and safety, environment and equity need to be properly assessed and managed (Bachu, 2008).

### 2.2.1. Impurities from different $CO_2$ capture processes

Flue gases from combustion of fossil fuels contain a wide variety of compounds, mainly $CO_2$, $NO_x$ and volatile organic compounds. Typical flue gas composition from coal-fired (PC) and gas-fired power plants (CCGT) is shown in Table 2-1 (CCP, 2007). $CO_2$ concentration by volume is much higher in the flue gas coming from the stack of a PC power plant than from a CCGT one.

Table 2-1. Typical flue gas constituents (major) for coal and gas fired power plants. Adapted from (CCP, 2007).

| **Flue gas constituent** | **PC (% vol)** | **CCGT (%vol)** |
|---|---|---|
| Carbon dioxide ($CO_2$) | 14 | 4 |
| Nitrous oxides($NO_X$) | 80-85 | 85-95 |
| Sulphur oxides ($SO_X$) | 1-3 | < 0.1 |
| Carbon monoxide (CO) | 1-3 | 1-3 |
| Hydrogen sulphide ($H_2S$)* | - | - |
| Elemental oxygen ($O_2$) | 1-3 | 1-3 |
| Elemental nitrogen (N) | < 1% | < 1% |
| Moisture ($H_2O$) | 1-2 | 1-2 |

* may be present in reducing conditions under poor operating conditions

Three main capture processes are considered currently to separate $CO_2$ from the flue gas stream:

- *Post-combustion*: $CO_2$ is separated from the flue gases derived of combustion of a primary fuel in air.

- *Oxyfuel combustion*: $O_2$ is used in the combustion instead of air and the gas stream will contain mainly $CO_2$ and $H_2O$.

- *Pre-combustion*: the primary fuel is processed in a reactor where two separate streams of $CO_2$ (captured for storage) and $H_2$ (which will be used as the fuel) are generated.

Hence, the composition of the $CO_2$ stream to be compressed, transported and stored is dependant upon several factors such as source, capture technologies and detailed plant design. The main impurities in the gas stream after the different capture processes are shown in Table 2-2.

Table 2-2. Concentration of impurities in dried $CO_2$, % by volume (IPCC, 2005).

| | $SO_2$ | $NO$ | $H_2S$ | $H_2$ | $CO$ | $CH_4$ | $N_2/Ar/O_2$ | *Total* |
|---|---|---|---|---|---|---|---|---|
| **Coal Fired Plants** | | | | | | | | |
| Post-combustion capture | <0.01 | <0.01 | 0 | 0 | 0 | 0 | 0.01 | 0.01 |
| Pre-combustion capture (IGCC) | 0 | 0 | 0.01-0.6 | 0.8-2.0 | 0.03-0.4 | 0.01 | 0.03-0.6 | 2.1-2.7 |
| Oxyfuel | 0.5 | 0.01 | 0 | 0 | 0 | 0 | 3.7 | 4.2 |
| **Gas Fired Plants** | | | | | | | | |
| Post-combustion capture | <0.01 | <0.01 | 0 | 0 | 0 | 0 | 0.01 | 0.01 |
| Pre-combustion capture | 0 | 0 | <0.01 | 1.0 | 0.04 | 2.0 | 1.3 | 4.4 |
| Oxy-fuel | <0.01 | <0.01 | 0 | 0 | 0 | 0 | 4.1 | 4.1 |

*Coal with a sulphur content of 0.86%. $SO_2$ concentration for oxy-fuel and the maximum $H_2S$ concentration for pre-combustion capture are for cases where these impurities are deliberately left in the $CO_2$ to reduce the capture costs.
*Oxyfuel case includes cryogenic purification.

In post-combustion capture, absorption technologies using amines are considered to be the ones more likely to be used in a near future, with a very pure $CO_2$ stream produced. Typically, the content of impurities is around 1-2%

$H_2$, CO, traces of $H_2S$ and other sulfur compounds from pre-combustion physical solvent scrubbing processes, whereas a combined stream of $CO_2$ and sulfur compounds could be generated in a IGCC plant with pre-combustion capture (IPCC, 2005). For oxyfuel combustion, the possible ranges of impurities mole fraction (dry basis) for the case when no purification of the $CO_2$ stream has been undertaken are: Ar (0-5%), $N_2$ (0-15%), $O_2$ (0 – 7%) and $SO_2$ (0-1.5%) (Li et al., 2009).

Most of existing coal-fired power plants remove $SO_x$ from exit gases, but next-generation plants may simultaneously treat $CO_2$, $SO_x$ and other flue gas components. If these can be tolerated, then the potential to simultaneously remove multiple pollutants from the flue gas within the mineral-trapping process needs to be investigated.

### 2.2.2. Available options for $CO_2$ storage

Following the capture and transport of $CO_2$, its storage can be performed in a variety of scenarios: ocean, mineral carbonates, for use in industrial processes or in geological formations. Regardless of the chosen technology, this should be able to permanently store amounts of $CO_2$ significantly high, i.e., orders of magnitude similar to the fluxes currently emitted in the atmosphere (~ 26 $GtCO_2$/year from fossil fuel use) (Holloway, 2001, Dooley et al., 2006, Metz et al., 2007).

*Ocean storage* provides a means of avoiding $CO_2$ emissions to the atmosphere by injecting the captured $CO_2$ directly into the ocean where it is expected to remain isolated for centuries. However, ocean storage is still in the research phase. Besides, some adverse effects are fairly predictable in the long-term scene such as gradual trend of the ocean to reach equilibrium with the atmosphere over time and different hazards to marine organisms and associated ecosystems (Adams et al., 1997, IPCC, 2005).

*Mineral sequestration* was first mentioned by Seifritz in 1990 (Seifritz, 1990) and refers to the fixation of the $CO_2$ using binary oxides such as magnesium oxide (MgO) and calcium oxide (CaO). However, calcium and magnesium are rarely available as binary oxides in nature and they are present in silicate rocks such as serpentine ($Mg_3Si_2O_5(OH)_4$) and olivine ($Mg_2SiO_4$). Chemical reactions between these minerals and $CO_2$ lead to formation of different carbonates that store $CO_2$ in a stable, benign and immobile form. This technology is currently in the research stage (Lackner et al., 1997, Lackner et al., 1998, Teir et al., 2005, Teir et al., 2009) and the key technical challenge is how to speed up the reaction (extremely slow in nature) in order to be able to design an economically feasible process (Herzog, 2002).

*Industrial uses* of captured $CO_2$ as gas or liquid or as a feedstock in chemical processes are possible and contribute to keeping $CO_2$ out of the atmosphere by storing it in the "carbon chemical pool" (i.e. the stock of carbon-bearing manufactured products). The contribution of this approach to climate change mitigation is expected to be small since the magnitude of anthropogenic $CO_2$ emissions from fossil fuel use (~ 26 $GtCO_2$/year) is significantly higher than the scale of $CO_2$ utilization (approximately 115 Mt/year). Moreover, the stored carbon will be later on degraded to $CO_2$ and emitted back to the atmosphere (IPCC, 2005).

*Geological storage* of $CO_2$ is applicable in a variety of geological settings, such as depleted oil and gas fields, deep un-mineable coal seams and deep saline formations. Geological storage of $CO_2$ is covered in detail in section 2.3.

### 2.2.3. Economics of carbon capture and geological storage

The cost of employing a full CCS system is dominated by the cost of capture, that ranges from 15-75 US\$/t$CO_2$ net captured for coal- or gas-fired power plants (including the cost of compression). Typical costs for transportation would range from 1-8 US\$/t$CO_2$ transported[3] and geological storage from 0.5-8 US\$/t$CO_2$ net injected, plus 0.1-0.3 US\$/t$CO_2$ injected for monitoring and verification (IPCC, 2005). The storage cost varies for the different storage options. Storage in saline formations is less attractive compared to EOR and ECBM because the former ones provide an economic benefit (see sections 2.3.2.1, 2.3.2.2 and 2.3.2.3 for further details). Representative estimates of the cost for storage in saline formations typically falls between 0.5-7.7 US\$/t$CO_2$ stored, with higher costs for offshore storage options compared to the onshore ones (Allinson and Nguyen, 2002, Allinson et al., 2003, Bock et al., 2003, IPCC, 2005).

---

[3] Per 250 km pipeline or shipping for mass flow rates of 5 to 40 Mt$CO_2$/year

## 2.3. Geological storage of $CO_2$

Geological storage of $CO_2$ provides a way to avoid emitting $CO_2$ into the atmosphere by injecting it into suitable deep rock formations. The main geological settings (sedimentary basins) considered so far as suitable for the underground $CO_2$ storage are oil fields, depleted gas fields, deep coal seams and saline formations (Figure 2-3)(Holloway, 2001, IPCC, 2005). Geological sinks for $CO_2$ are immediately available and do not really need any major technological development because the injection process uses off-the-shelf technology from the hydrocarbon industry and can be deployed at a useful scale (Friedmann, 2007).

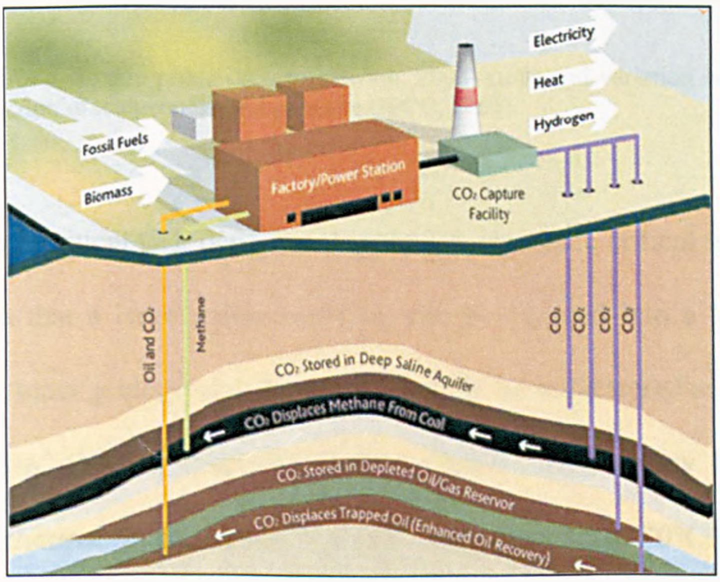

Figure 2-3. Options for the geological storage of carbon dioxide (VGB, 2007).

Prior to understanding the different carbon geological sequestration options it is important to know the physical properties of $CO_2$ because they are relevant to its underground storage. $CO_2$ is an odourless and colourless gas at normal temperature and pressure and occurs naturally in the atmosphere. Figure 2-4 (left) shows how $CO_2$ can be present on three separate phases depending on pressure and temperature. At a temperature of 31.1 °C and a pressure of 7.38 MPa (73.8 bar) $CO_2$ reaches what is so-called its supercritical state (dense phase condition). A supercritical fluid behaves as a gas but it has liquid-like densities (IPCC, 2005).

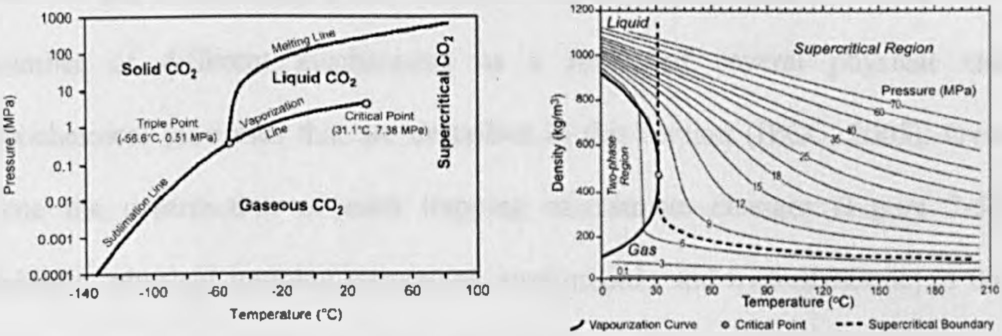

Figure 2-4. Carbon dioxide phase diagram (Bachu, 2008) (left) and variation of $CO_2$ density (right) as a function of temperature and pressure (IPCC, 2005).

The high supercritical $CO_2$ densities (Figure 2-4, right) are critical to successful storage such that a large volume of $CO_2$ can be injected into a limited pore volume. For most geological settings, $CO_2$ would be sequestered at densities of 600-800 kg/m$^3$ (Bachu, 2003, Friedmann, 2007). Sedimentary basins have average geothermal gradients that typically vary from 15 to 30°C/km, with an average value of 25°C/km (Pruess, 2005). However, in some instances, the geothermal gradient can vary significantly from site to site and even within a single reservoir (Bachu, 2003). Fluid pressure also increases with depth according to a typical hydrostatic gradient of ~ 100 bar/km (Pruess, 2005). Based on average gradients, injection depths are expected to be approximately

800 m below the surface in order to take advantage of $CO_2$'s supercritical state and high density at those depths.

### 2.3.1. $CO_2$ storage mechanisms in geological formations

Upon injection of $CO_2$ into deep geological formations (well-drilling and injection technologies would be similar to those ones developed previously by oil and gas companies), it can remain trapped underground by virtue of a number of different mechanisms as a result of several physical and geochemical processes that are described in this section (IPCC, 2005). Over time the contribution of each trapping mechanism changes (Figure 2-5). Initially, physical trapping (structural, stratigraphic and hydrodynamic) is the dominant mechanism for retaining $CO_2$ in aquifers.

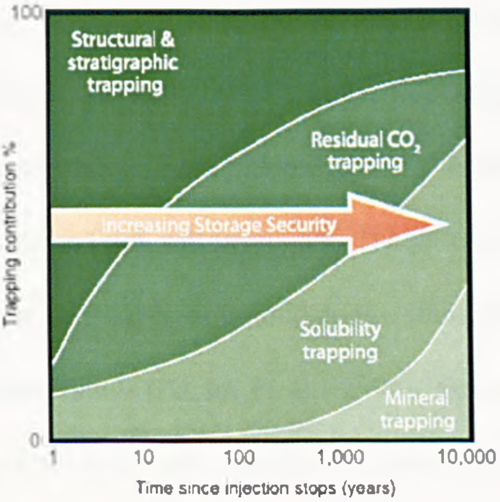

Figure 2-5. Contribution of different $CO_2$ trapping mechanisms in geological media to storage security (IPCC, 2005).

As $CO_2$ migrates through aquifers, residual gas (physical) and solubility trapping (geochemical) tend to be significant mechanisms. Over longer time scales (hundreds to thousand of years), mineral trapping (geochemical) will lock the $CO_2$ in carbonate minerals. Geochemical trapping mechanisms enhance storage security because the risk of $CO_2$ leakage does not depend directly on the integrity of the cap rock on which physical trapping relies (Suekane et al., 2008).

#### *2.3.1.1. Physical trapping*

Physical trapping allows underground storage of $CO_2$ by confining it below an impermeable or very-low-permeability seal defined as a caprock (*structural and stratigraphic trapping*). $CO_2$ injected into saline aquifers migrates upwards unevenly, until it reaches the cap rock, as a result of buoyancy caused by the density differences between $CO_2$ and formation water (30 – 50%). The caprock acts as a barrier and causes the buoyant $CO_2$ to migrate laterally along the inclination of the layer, filling any structural or stratigraphic traps it encounters (Flett et al., 2005, Holloway, 2005, IPCC, 2005, Suekane et al., 2008). Two categories of caprocks have been identified: 1) aquicludes: essentially impermeable strata such as thick salt layers and 2) aquitards: those with a very-low-permeability such as shales and mudstones through which fluids can migrate albeit extremely slow (Bachu et al., 1996). Some of these traps are formed by folded or fractured rocks that could cause them to leak so special care must be taken in order to avoid exceeding the allowable pressure that would lead to fracturing the caprock or reactivating the faults (Streit et al., 2005, Bachu, 2008).

Another means of physical trapping can be *hydrodynamic trapping,* whereby $CO_2$ is captured in saline formations as a fluid that can migrate very slowly with the natural flow regime once outside the injection-well radius of influence. Thus, hydrodynamic trapping depends on the hydrodynamic regime of the formation waters. Some studies performed in the Alberta Basin show regional-scale velocities of the order of 1 to 10 cm/year and calculations predict that in a timeframe of millions of years, the $CO_2$ will still be found within tens of kilometres of the injection site (Bachu et al., 1994, Gunter et al., 1997). The most critical issue concerning hydrodynamic trapping is the potential for $CO_2$ leakage due to imperfect confinement.

Additionally, at the pore scale, capillary forces will immobilize a substantial fraction of a $CO_2$ bubble (*residual trapping*); this fraction is determined by the interfacial tension angle, the wettability angle of the pore surfaces, and the effective diameter of the pore throat (Gladkikh and Bryant, 2003, Kovscek and Radke, 2003). $CO_2$ in then trapped as a residual phase in the pores of the solid (Kovscek and Radke, 2003, Juanes et al., 2006).

In the case of organic mineral frameworks such as coals, the $CO_2$ can physically adsorb onto the rock surface, sometimes displacing other gases (e.g. methane, nitrogen), so *adsorption* would be another means of physical trapping (Friedmann, 2007).

### 2.3.1.2. *Geochemical trapping*

Two different mechanisms are included within geochemical trapping: 1) solubility trapping and 2) mineral trapping. Firstly, *solubility trapping* occurs when $CO_2$ dissolves in formation water, being trapped as an aqueous component ($CO_2(aq)$, $H_2CO_3$, $HCO_3^-$, $CO_3^{2-}$) (Hitchon et al., 1999, Xu et al., 2004a, IPCC, 2005, Bachu, 2008). The major benefit of solubility trapping is that once the $CO_2$ is in its aqueous form, the buoyant forces that drive it upwards are eliminated but the most critical concern is the limited $CO_2$ solubility in brine.

Reactions of the following type occur when $CO_2$ dissolves in formation waters:

$$CO_{2\,(g)} \leftrightarrow CO_{2(aq)} \qquad [2\text{-}1]$$

$$CO_{2(aq)} + H_2O \leftrightarrow H_2CO_3 \qquad [2\text{-}2]$$

$$H_2CO_3 \overset{Ka_1}{\longleftrightarrow} HCO_3^- + H^+ \qquad [2\text{-}3]$$

$$HCO_3^- \overset{Ka_2}{\longleftrightarrow} CO_3^{2-} + H^+ \qquad [2\text{-}4]$$

Firstly, $CO_2$ gas dissolves in water (reaction [2-1]). Once it reaches its aqueous form, it can react with water to form carbonic acid (reaction [2-2]) that will further dissociate to bicarbonate (reaction [2-3]) and carbonate ions (reaction [2-4]). $Ka_1$ and $Ka_2$ are the acid dissociation constants for reactions [2-3] and [2-4] respectively. For a closed system they can be easily calculated if the total carbon concentration is known. For example, $Ka_1$ and $Ka_2$ values at standard conditions[4] are $10^{-6.35}$ and $10^{-10.33}$ respectively for a system containing 0.001M of total carbon (Hill, 2006). Reaction [2-2] has been reported as the rate-limiting step of the above series of reactions for solutions with low to mid pH values ($pH<pKa_2$ and $pK_a=-\log K_a$) (Dreybrodt et al., 1996, Stumm and Morgan, 1996, Liu et al., 2005). The rate of dissolution depends on how well the $CO_2$ mixes with the formation water once it is injected into the reservoir (Holloway, 2005). Carbon dioxide may mix with, and then dissolve in, formation water through three different processes: diffusion (an extremely slow process), dispersion and convection (Bachu, 2008).

The $CO_2$ solubility in formation water decreases as temperature and salinity increase and conversely, increases as pressure increases (Holloway, 2005, Bachu, 2008). Many experimental and theoretical studies have focused on the influence of those parameters in $CO_2$ solubility (Drummond, 1981, Nighswander et al., 1989, Enick and Klara, 1990, Nicolaisen, 1994, Rumpf et al., 1994, Suto et al., 2000, Duan and Sun, 2003, Portier and Rochelle, 2005, Bahadori et al., 2009). There is a range of temperatures and pressures (Figure 2-6) at which the solubility of $CO_2$ in water is not so low at high temperatures (>100°C). Deep host rocks could be then suitable for underground $CO_2$ injection despite the high temperatures because of the enhanced solubility of $CO_2$ at high pressures (Suto et al., 2007).

---

[4] Standard conditions are 1atm and 25°C.

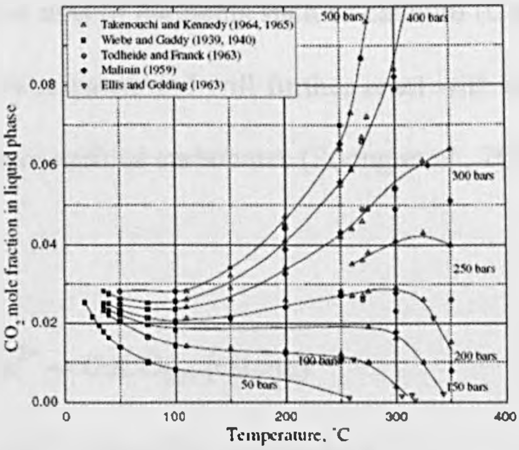

Figure 2-6. Solubility of $CO_2$ in distilled water. Solid lines are based on data from previous studies (Suto et al., 2007).

In *mineral trapping* $CO_2$ is converted to stable carbonate minerals by a series of reactions with aqueous ions found in the saline aquifer. These carbonate minerals, such as calcite (calcium carbonate), magnesite (magnesium carbonate), dolomite (calcium-magnesium carbonate) and siderite (iron carbonate), can be stored underground for millions of years (Bergman and Winter, 1995, Hitchon et al., 1999, Reichle et al., 1999).

The reactions that take place underground and will further lead to carbonates formation can be described as follows: after $CO_2$ dissolution in the aqueous phase, it will react with water to form carbonic acid (reaction [2-2]) and some of the $CO_2$, after dissociation of the acid, will be held in aqueous phase as bicarbonate (reaction [2-3]) and carbonate ions (reaction [2-4]). An acidity increase in the water is observed as a result of protons generation (reactions [2-3] and [2-4]) and therefore dissolution of silicate minerals present in the aquifer is favoured. The dissolution of silicate minerals is considered to be the rate-limiting step of the entire mineral trapping process. Following the attack on the silicate minerals, free ions of elements such as calcium (Ca), magnesium (Mg) and iron (Fe) will be released and will further react with either bicarbonate or carbonate ions to form various carbonates (Soong et al., 2003, Xu et al., 2004a, Bachu, 2008):

$$CO_3^{2-}{}_{(aq)} + Ca^{2+} \rightarrow CaCO_{3(s)} \text{ (calcite)} \qquad [2\text{-}5]$$

$$CO_3^{2-}{}_{(aq)} + Mg^{2+} = MgCO_{3(s)} \text{ (magnesite)} \qquad [2\text{-}6]$$

$$CO_3^{2-}{}_{(aq)} + Fe^{2+} = FeCO_{3(s)} \text{ (siderite)} \qquad [2\text{-}7]$$

$$CO_3^{2-}{}_{(aq)} + Ca^{2+} + Mg^{2+} = CaMg(CO_3)_{2(s)} \text{ (dolomite)} \qquad [2\text{-}8]$$

Thus, $CO_2$ is permanently fixed as a mineral. However, conversion of $CO_2$ to stable carbonate minerals is expected to be slow (hundreds to thousands of years). This fact suggests that mineral trapping may contribute significantly to $CO_2$ sequestration within saline aquifers but only in the very long term (Bachu et al., 1996). Carbon dioxide mineral traps are most effective when the aquifer contains minerals that are proton sinks, that is, the basic silicate minerals such as the feldspars and clay minerals. Consequently, mineral trapping of $CO_2$ is favoured in aquifers containing an abundance of clay minerals; typically, siliciclastic (sandstone) aquifers are favoured over carbonate aquifers (Hitchon et al., 1999).

In a similar way as the pH of the brine affects solubility, it affects precipitation of secondary carbonate minerals. Since $HCO_3^-$ (bicarbonate) and $CO_3^{2-}$ (carbonate) dominates at mid pH ($pKa_1<pH<pKa_2$) and high pH ($pH>pKa_2$)

respectively, carbonate precipitation is favoured under more basic conditions and solubility is favoured under acidic conditions (Soong et al., 2003).

Like solubility trapping, mineral trapping is very dependent on the chemical composition of formation waters and of the rock matrix, and on temperature and pressure. In addition, it depends on the contact surface between the mineral grains and the formation water containing dissolved $CO_2$, and on the flow rate of fluids past the interface. The flow rate depends on rock permeability, hydraulic gradients and water viscosity, which itself depends on water temperature and salinity, and much less so on pressure (IPCC, 2005).

### 2.3.2. Geological media for $CO_2$ storage

Three main characteristics need to be present in geological media to be suitable for $CO_2$ storage (Figure 2-7): a) the porosity needed to provide a capacity large enough to accept the intended volume of $CO_2$; b) the permeability required for injectivity, to take in $CO_2$ at the rate that is supplied by the $CO_2$ emitters; and c) confinement, to prevent the migration and/or leakage of the buoyant and mobile $CO_2$ out of the intended storage unit (Bachu, 2008).

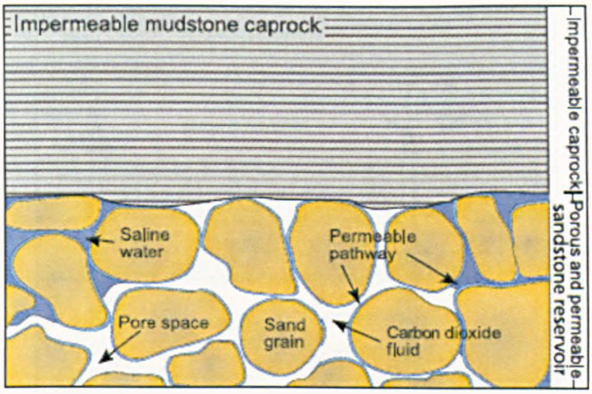

Figure 2-7. Cartoon illustrating porosity, permeability and confinement within the reservoir volume (SCCS, 2009).

Three different types of reservoirs are potential candidates for $CO_2$ storage: oil and gas reservoirs, deep coal seams and saline aquifers. They are explained in detail below.

#### 2.3.2.1. *Oil and gas reservoirs*

Both depleted and active fossil fuel reservoirs are potential sites for $CO_2$ in underground formations for several reasons: reservoir integrity and safety are demonstrated after secure accumulations of oil and gas, in some cases for many millions of years; very well known and characterised geological structures and physical properties; the development of computer models in the oil and gas industry has made possible to predict the movement, displacement behaviour and trapping of hydrocarbons and finally, some of the current structure and technology may be used for handling $CO_2$ storage operations (IPCC, 2005).

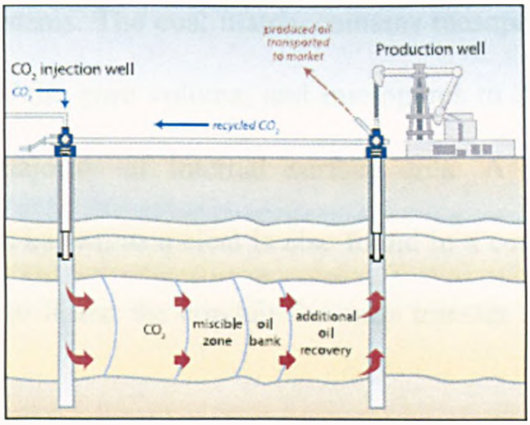

Figure 2-8. Simplified diagram of a $CO_2$-enhanced oil recovery (EOR) operation (IPCC, 2005).

Injection into depleted or inactive reservoirs does not aim to get any further oil or gas production, whereas injection into producing oil and gas reservoirs (Figure 2-8), commonly known as enhanced oil recovery, EOR, and enhanced gas recovery, EGR, respectively, will provide an additional economic benefit that would help to offset the costs of capturing, processing and transporting of anthropogenic $CO_2$ (Voormeij and Simandl, 2002). $CO_2$ injected into suitable, depleted oil reservoirs could enhance oil recovery by typically 10-15% of the original oil in place in the reservoir (IPCC, 2005). Injection of substantial quantities of both natural and anthropogenic $CO_2$ already occurs in the U.S. The storage potential of oil and gas fields is from 675-900 $GtCO_2$ (IPCC, 2005).

### 2.3.2.2. *Deep coal seams*

Also called unmineable coal seams, these are composed of organic materials and are potential media for $CO_2$ underground storage since they can physically adsorb many gases. Coalbeds contain both primary (coal matrix) and secondary (cleats) porosity systems. The coal matrix contains mesopores 20-500 Å, that account for most of the pore volume, and micropores to 20 Å diameter, that account for the majority of internal surface area. A natural system of orthogonal fractures known as a cleat is also found in a coal bed and provides some permeability to it and the conduit for mass transfer to production wells (Holloway, 2001).

A natural gas commonly known as coalbed methane is formed during the process of coalification and adsorbed onto the surfaces of the micropores in the coal. Small amounts of higher hydrocarbons, $CO_2$ and nitrogen ($N_2$) are also present. Figure 2-9 shows that coal has a higher affinity to adsorb gaseous $CO_2$ than methane.

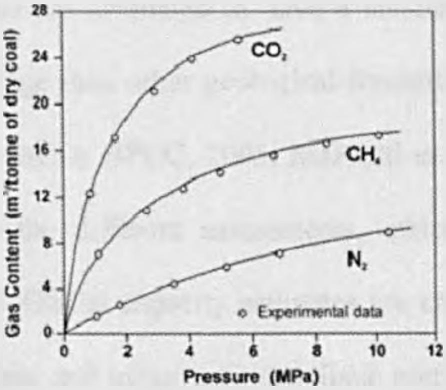

Figure 2-9. Adsorption isotherms for carbon dioxide ($CO_2$), methane ($CH_4$) and nitrogen ($N_2$) on coal (Voormeij and Simandl, 2002).

If $CO_2$ is injected into coal seams, it will flow through the cleat system of the coal, diffuse into the coal matrix and be adsorbed onto the coal micropore surfaces, displacing methane and thereby enhancing coal bed methane (CBM) recovery (Bachu, 2008, Mazzotti et al., 2009). Therefore, $CO_2$ injected into coal seams preferentially displaces methane that exists in the coal, which might then be recovered as free gas.

Carbon dioxide-ECBM will potentially increase the amount of methane produced to nearly 90% of the gas, compared to conventional recovery of only 50% by reservoir-pressure depletion alone (Stevens et al., 1996). This will help to offset the costs of the process as well as a trapping media for $CO_2$. However, critical factors to bear in mind in order to develop an economic feasible technology are the permeability of the coal seams (only high permeability ones appear to be appropriate for injection), suitable coal geometry (a few, thick seams rather than multiple, thin seams), simple structure (minimal faulting and folding), homogeneity and confinement of coal seams, adequate depth, suitable gas saturation conditions and ability to dewater the formation (IPCC, 2005). Unminable coal seams are estimated to have a smaller, but still significant, potential for $CO_2$ storage than other geological formations with an estimated capacity of 3 to 200 $GtCO_2$ (IPCC, 2005, Mazzotti et al., 2009). This figure varies depending on the different assessments, which can be based upon different assumptions. Global capacity estimates are commonly calculated by simplifying assumptions and using very simplistic methods so there is a high degree of uncertainty in reported values.

### 2.3.2.3. *Saline aquifers*

$CO_2$ injection into saline aquifer formations is one of the most promising geologic $CO_2$ sequestration options. Saline formations are deep porous sedimentary rocks saturated with formation waters that contain a total dissolved solids (TDS) concentration greater than 10,000 mg/L (DOE, 2007), and are considered unsuitable for human consumption or agricultural or industrial use.

Deep saline aquifers are found worldwide in most of the sedimentary basins and they have the highest potential capacity globally for $CO_2$ storage, up to 10,000 Gt of $CO_2$ (IPCC, 2005), which is equivalent to many centuries of $CO_2$ emissions at the current rate of 26 Gt/year (Obi and Blunt, 2006). Additionally, they underlie most existing large $CO_2$ point sources making $CO_2$ transportation costs minimal (IPCC, 2005). An schematic of an integrated CCS system with deep (> 800m) $CO_2$ injection is depicted in Figure 2-10. A $CO_2$ capture system, ancillary systems like $CO_2$ compressors, booster pumps, surge tanks, etc., transport, injection and measuring, monitoring and verification (MMV) technologies are crucial elements of a complete CCS system. However, although the component technologies work well independently, they need to work well within an integrated CCS system. Furthermore, they need to work at a scale far larger than any of the systems in operation today.

Some sedimentary rocks have up to 35% porosity. Porosity in rocks can be filled with different fluids depending on the depth of the rock within the formation. Thus, if the rock is very shallow or very close to the ground surface, its porosity is commonly filled with air. However, at greater depths (of a few centimetres to several tens of meters in most cases) rocks usually contain fresh water, being known as fresh or potable water aquifers that are generally used for water supply. Saline water aquifers are present at greater depths or beneath the sea, in which the pore space is filled by saline water. These can show varying salinity which tends to increase with depth. Less commonly, the pore space at high depth is occupied by oil or natural gas (Holloway, 2001).

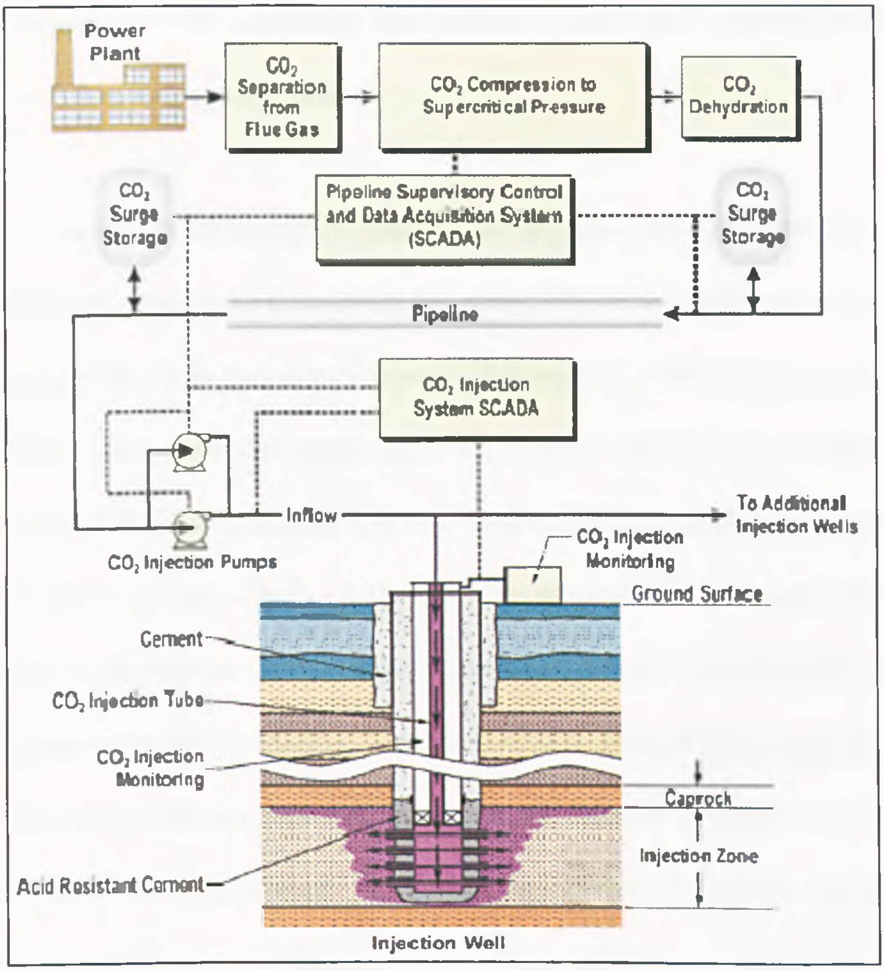

Figure 2-10. Schematic of an integrated CCS system with geologic $CO_2$ sequestration (Dooley et al., 2006).

Not all the deep aquifers are suitable for $CO_2$ disposal. They need to meet some basic requirements such as an overlying caprock, which should not contain any fractures or uncompleted wells (Bachu et al., 1994), and a minimum depth for the top of the aquifer of 800 m, ensuring in that way that injected $CO_2$ will be stored in supercritical state. Ideally, near-well permeability of the formation should be high for injection purposes versus regional-scale permeability that should be low to ensure long-term disposal of $CO_2$ (Bachu et al., 1994).

### 2.3.3. Status of $CO_2$ injection into saline formations: experience from existing storage operations

The first operations injecting $CO_2$ into saline aquifers were acid-gas ($H_2S$ and $CO_2$) disposal projects in Canada in the early 1990's for both, economic and geologic reasons. Acid gas is a mixture of $H_2S$ and $CO_2$ with minor amounts of hydrocarbon gases than can result from petroleum production or processing. It is also co-produced with natural gas in a number of large fields throughout the world (Brosse et al., 2005). Although the purpose of acid gas injection operations is to dispose of $H_2S$, significant quantities of $CO_2$ (14-98% of the total volume) are also co-injected because it results uneconomic a separation of the two gases. Acid gas injection occurs at 44 different locations across the Alberta Basin in the provinces of Alberta and British Columbia and over a wide range of formation and reservoir types, acid gas compositions and operating conditions (IPCC, 2005). However, injection rates are relatively low and very limited subsurface monitoring is done (Michael et al., 2009a).

A selection of other pilot, demo and commercial $CO_2$ storage projects in saline aquifers are currently underway or proposed (Table 2-3). The most popular and well known is that undertaken in Norway (Sleipner). The Sleipner project, operated by Statoil (currently StatoilHydro since both companies, Statoil and Hydro's oil and energy business merged in October 2007) in the North Sea, is the first commercial-scale project dedicated to store $CO_2$ in a saline formation in the world. $CO_2$ injection started in 1996 and will continue for the life of the field in order to avoid payment of taxes due to $CO_2$ emissions. The Sleipner West gas field is situated right in the middle of the North Sea, near the border between Norway and United Kingdom and more than 200 km from land. The natural gas is produced with 9% $CO_2$ and this is removed offshore by an amine process since the $CO_2$ content needs to be 2.5% for marketable purposes. The $CO_2$ (~1 Mt/year) is then injected into a large, deep sandstone reservoir (Utsira formation), approximately 150-200 m thick, 2.5 km away from the Sleipner field and about 800-1000 m below the sea floor. 4D seismic monitoring of the Utsira formation is mapping the behaviour of the $CO_2$ and has shown that $CO_2$ appears to stay in place. A theoretical model has been developed by Bickle and co-workers to analyse growing accumulations of $CO_2$ imaged by seismic reflection surveys at the Sleipner field (Bickle et al., 2007). The Saline Aquifer $CO_2$ Storage (SACS) project jointly funded by the EU, industry, and national governments was established to monitor and research the storage of $CO_2$ (Kongsjorden et al., 1997, Kongsjorden et al., 1998, Lindeberg et al., 2000, Torp and Gale, 2004, Laate, 2008).

Table 2-3. A selection of current and planned geological storage projects in saline aquifers.

| **Current Projects** | | | | |
|---|---|---|---|---|
| | | | | |
| ***Project*** | ***Country*** | ***Scale of project*** | ***Injection start date*** | ***Total storage*** |
| Alberta Basin (Acid Gas) | Canada | Commercial | 1990 | NA** |
| Sleipner | Norway | Commercial | 1996 | 20 Mt planned |

| | | | | |
|---|---|---|---|---|
| In Salah | Algeria | Commercial | 2004 | 17 Mt |
| Snøhvit | Norway | Commercial | 2008 | 23 Mt |
| Ketzin | Germany | Demo | 2008 | 60,000 t |
| Nagaoka | Japan | Pilot | 2003 | 10,000 t planned |
| Frio | USA | Pilot | 4-13 Oct 2004 | 1600 t |
| Otway | Australia | Demo | 2008 | 1 Mt |
| **Planned Projects** | | | | |
| | | | | |
| Gorgon* | Australia | Commercial | 2009 | 125 Mt |
| Zerogen* | Australia | Demo & Commercial | 2012-2017 | NA |
| Vattenfall | Germany | Pilot & Demo | NA | NA |
| * more advanced projects on the storage side in Australia ( for others refer to text)<br>** Not Available | | | | |

The In Salah Gas Project started injection in 2004 of $CO_2$ obtained from natural gas production. In Salah Gas is a joint venture project between BP (33%), Sonatrach (35%) and Statoil (32%). The Krechba Field at In Salah produces natural gas containing $CO_2$ concentrations ranging between 1 to 9% of $CO_2$ and delivers it to markets in Europe, after processing and stripping the $CO_2$ to meet commercial specifications (0.3%). The $CO_2$ stream is re-injected back into the aquifer zone (a sandstone reservoir) of one of the shallow gas producing reservoirs, at a depth of 1800 m. The top seal is a succession of mudstones up to 950 m thick. The project includes a comprehensive monitoring programme that involves a range of technologies, including noble gas tracers, pressure surveys, tomography, etc (IPCC, 2005, Riddiford et al., 2005).

Carbon storage in Snøhvit field is StatoilHydro's second largest carbon storage project in Norway. This is the first of its kind in an arctic climate; injection and storage started in April 2008 (Laate, 2008, Statoil, 2008). The gas is produced subsea and then transported to an onshore gas processing and Liquefied Natural Gas (LNG) facility in Melkøya, outside Hammerfest, where $CO_2$ content in the gas is reduced from 5-8% to 50 ppm by amine absorption. The $CO_2$ is dried, transported in a pipeline and stored in a saline aquifer that underlies the gas-bearing formation in the Snøhvit field, 2600 m beneath the seabed. At full capacity, 0.7 Mt/year of dry $CO_2$ can be stored in the field. The liquid $CO_2$ transportation by pipeline (152 km length and 0.2 m diameter) to the subsea aquifer is one of the most challenging tasks in the project due to the multhiphase fluid character of $CO_2$ when it is close to its supercritical point, requiring extensive process control training of the operators.

The EU $CO_2$SINK project, which was officially started in April 2004, aimed to develop an "in-situ" laboratory for $CO_2$ storage in Europe (Juhlin et al., 2008). As part of the project, injection into and storage of $CO_2$ in a deep saline aquifer at Ketzin, located just outside Berlin (Germany), will be examined for first time in Europe. The aim of the project is to store up to 60,000 t of $CO_2$ and will continue for a period of two years. One injection well and two observation wells have been drilled to depths of 800 m and the $CO_2$ will be pumped at a rate of about 100 t/day. Injection started in June 2008 and intensive monitoring is involved to try to develop a better understanding of the fate of underground

$CO_2$ and evaluate reservoir's stability and integrity (CCJ, 2008b, Juhlin et al., 2008). Also in Europe, the Swedish state-owned company Vattenfall has constructed a 30 MW thermal oxyfuel combustion pilot plant as part of a CCS project at Schwarze Pumpe, in Germany. The plant has been operational from the middle of 2008, with an initial testing programme of three years, after which it will eventually become a backup test for the future demonstration plant testing programme. Sequestered $CO_2$ will be stored underground upon identification of a suitable storage site. A 250-350 MW electricity demonstration plant is planned to be commissioned by 2015, after a pre-feasibility stage which started in 2006. The location for the power plant and storage site are being studied, with both onshore and offshore storage options being considered and pipelines and/or shipping considered as the main transport alternatives (Vattenfall, 2008).

An on-shore pilot scale $CO_2$ injection project in Nagaoka, 200 km north of Tokio (Japan) was agreed in 2000. Experimental injection and monitoring of $CO_2$ started in July 2003 and finished in January 2005 with a total of 10,400 t of purchased $CO_2$ (99.9 % purity) injected in a supercritical state and a maximum injection rate of 20 to 40 t per day. The saline aquifer was situated at a depth of 1.1 km and a 20 m thick layer was selected as the injection target because of its favourable values of porosity and permeability and its horizontal homogeneity. A series of geophysical techniques were chosen to monitor the $CO_2$ at both the surface and within three observation wells; geochemical reactions between the injected $CO_2$, the formation water and the aquifer rocks were also studied. Fluid samples were collected at three different depths (1109, 1114, 1118 m); at the depth of 1118 m an increase in the concentration of $HCO_3^-$ was observed due to the dissolution process of the injected $CO_2$. Concentrations of several cations (Ca, Mg, Fe and Mn) also increased probably as a result of the dissolution of different components of the host rock: calcite, gypsum, plagioclase, pyroxenes, chlorite and biotite. Batch experimental tests were performed using rock and water samples obtained from the test site that supported the above inferred geochemical reactions (Mito et al., 2007, IEA, 2008a).

In the Frio Brine pilot test (Texas, US) 1,600 t of $CO_2$ were injected for 10 days ( in 2004) at ~1,500 m depth into a 24 m well characterized as a relatively homogeneous high permeability sandstone section of the Frio Formation - a regional reservoir in the U. S. Gulf Coast. Saturation and transport properties were measured horizontally, vertically and through time using multiple tools (Doughty et al., 2008). Chemical analysis of formation water and gas samples obtained from the injection and observation well were performed during and after $CO_2$ injection. The outcomes of the study also improved conceptual models and numerical inputs.

The CO2CRC Otway Project is Australia's most advanced storage demonstration project, located in the southeast (Victoria). $CO_2$-rich gas (80% $CO_2$, 20% methane) is extracted from an existing well, compressed and processed for further injection, originally into a depleted gas field (Waarre C formation) located at a depth of 2050 m. $CO_2$ is expected to migrate up-dip within a 31 m thick reservoir sandstone that is capped by Belfast mudstone. Injection began in April 2008 and 100,000 t are the injection target for a period of over two years. An extensive monitoring and verification programme has also been implemented (CCJ, 2008a, CO2CRC, 2008b). Several other CCS demonstration projects targeting injection into a saline aquifer are planned in Australia such as the Callide Oxyfuel Project (Queensland), Coolimba Power Project (Western Australia), FuturGas Project (South Australia), Gorgon Project (Western Australia), Monash CTL Project (Victoria) and ZeroGen Project (Queensland) (CO2CRC, 2008a). Amongst them, the Gorgon and ZeroGen Projects are the most advanced in the storage side.

In the Gorgon Project, it is planned that $CO_2$ will be injected on the central eastern coast of Barrow Island, located 60km offshore north Western Australia to a depth of about 2.3 km after being separated from the proposed LNG processing plant. The storage site was selected to limit the environmental impact on areas nearby as well as to maximise the migration distance from the major faults. The project is planned to commence around 2009 with injection of 3.3 Mt of $CO_2$ per year and a target of 125 Mt over the life of the project. A major study of the subsurface is underway (CCJ, 2008c, Chevron-Australia, 2008).

The Zerogen is a two-stage project aiming to integrate the low-emission technologies of Integrated Gasification Combined Cycle (IGCC) with CCS. Stage 1 (demonstration) will be a 120 MW (gross) power plant located near Rockhampton in central Queensland, where up to 75% of the $CO_2$ will be captured for partial sequestration in deep underground reservoirs in the Northern Denison Trough, an on-shore sedimentary basin located 220 km west of the facility. This demonstration plant is expected to be operational by 2012.

In stage 2, a commercial IGCC-CCS plant is proposed to be deployed by 2017, where a 400MW (gross) power plant will capture up to 90% of $CO_2$ for full sequestration. The specific location in Queensland has not been determined yet and is subject to pre-feasibility studies of all suitable sites (Zerogen, 2008).

The seven Regional Carbon Sequestration Partnerships (RCSPs) is an initiative of the US Department of Energy (DOE) to determine the most suitable technologies, regulations and infrastructure needs for $CO_2$ carbon capture and storage in different regions of US and Canada. State agencies, universities and private companies are part of this programme to place carbon sequestration technologies on the path to commercialization. Three different phases, characterization (2003-2005), validation (2005-2009) and deployment (2008-2017), are to be accomplished by 2017 and will provide the data needed for sequestration knowledge in each of the regions as well as large-scale field-test experience within the $CO_2$ geological storage scenario. After accomplishment of the characterization phase, validation has taken place, when the partnerships have implement a portfolio of small scale geologic sequestration projects (Ball and Gupta, 2008, Finley, 2008, Hill, 2008, McPherson, 2008, Myer, 2008, Steadman, 2008). Table 2-4 shows a summary of the geologic field tests carried out during the validation phase.

Table 2-4. Validation Phase Geologic Field Tests performed by the RCSPs in saline formations. Adapted from the "Carbon Sequestration Atlas of the US and Canada" (DOE, 2007).

| **Partnership** | **Geologic province** | **Total $CO_2$ injection (tons $CO_2$)** | **Approximate depth (feet)** |
|---|---|---|---|
| | | | |
| MGSC | Illinois Basin | 10,000 | 7,000-8,600 |
| MRCSP | Cincinnati Arch | 1,000-3,000 | 3,200-3,500 |
| MRCSP | Michigan Basin | 3,000-20,000 | 3,200-3,500 |
| MRCSP | Appalachian Basin | 1,000-3,000 | 5,900-8,300 |
| SECARB | Gulf Coast | 30,000 | 10,300 |
| Big Sky | Columbia Basin | 3,000 | 3,255-3,335 & 3,600-3,755 |
| SECARB | Missisipi Salt Basin | 3,000 | 8,600 |
| SWP | Paradox Basin, Aneth Field | 20,000 | 6,900 |
| WESTCARB | Thorton Gas Field | 1,000 | 3,400-3,500 |
| WESTCARB | Colorado Plateau | 2,000 | 5,000 |

The last phase of this government/industry effort will consist of several large-volume sequestration tests in different formation types, including saline formations, to demonstrate the possibility that CCS of over 1 Mt of $CO_2$ can be done in an economic, safe and permanent manner. Currently, six out of the seven large-volume field tests have been awarded by the DOE. Undoubtedly, the experience to be gained from all the above sequestration tests will help to develop a "template" for future commercial-scale sequestration as well as demonstrate meaningful and effective monitoring, risk and mitigation protocols.

The European Commision announced in January 2007 the development of up to 12 flagship CCS demonstration projects in the EU, which will be operational by 2015 (Gibbins and Chalmers, 2008, EU, 2009). UK has recently been awarded £266 million from the EU to build its first CCS demonstration plant at Hatfield, Yorkshire. A 900 MW coal-fired electricity plant with the use of pre-combustion CCS technology to capture the $CO_2$, piping of captured $CO_2$ and its storage in an offshore gas field 100 miles away could be operating as early as 2014 (CCJ, 2009). Arrangements for the remaining projects are yet to be agreed.

The experience gained from $CO_2$ injection at pilot and existing commercial projects described above shows that $CO_2$ geological storage in saline aquifers is technologically feasible although some needs still remain: storage projects covering a wide range of subsurface environments as well as different monitoring strategies, regulation requirements and economics are needed to successfully deploy CCS in saline aquifers (Michael et al., 2009a).

### 2.3.4. Experimental work on mineral trapping in saline formations

Experimental work addressing specific aspects of geochemical trapping is considered one of the remaining knowledge gaps to be addressed by the research community to improve the quantification of $CO_2$ stored by the different storage mechanisms as well as numerical simulations (Michael et al., 2009b). Some researchers have reported experimental data on a laboratory-scale for mineral trapping studies and a review of the main findings is presented below.

#### 2.3.4.1. *Experimental work with pure $CO_2$ streams*

Assessment of rock/water/$CO_2$ interactions under a range of temperatures from 100 to 350 °C (which constitutes the range of reservoir temperatures common to many active hydrothermal systems) using two different types of rocks (granite and sandstone) indicated that acid conditions ($pH < 5$) increases dissolution rate of the rock, that will further lead the solution to be supersaturated and further deposition of secondary minerals (Suto et al., 2001, Liu et al., 2003, Suto et al., 2007). The temperature range of 150-250°C was suggested as the most suitable for $CO_2$ injection into granite rock masses due to kinetics of the overall granite reaction, which were not too slow within that temperature range. Potential calcite precipitation was also suggested but no carbonates were observed in their experimental tests (Suto et al., 2007). Glauconite (iron-rich clay) and anorthite (calcium-rich plagioclase feldspar) were also tested for 30 or 34 days as potential host rocks for $CO_2$ injection. They were allowed to react with synthetic brine solutions at two different temperatures, 50 and 150°C and two different $CO_2$ partial pressures, 600 and 2000 psi. Surface spectroscopic techniques (e.g. XPS) indicated that elemental composition at mineral surfaces was modified as a result of the experiments, showing progress towards carbonate precipitation. Those changes agreed with equilibrium modeling calculations, although carbonate precipitation was not observed in laboratory experiments due to time constraints, which prevented the system from reaching equilibrium (Sass et al., 2001).

A system comprised of arkose (consisting of a mixture of quartz and silicate minerals), shale and a synthetic brine was reacted at 200°C (selected to enhanced kinetic rates of silicate reactions) and 200 bars (chosen for consistency with and accessibility for sequestration scenarios) for 59 days to approach steady-state and then, injected with $CO_2$ and allowed to react for another 80 days. Shale was used as an aquitard, representing the confining layer of the repository. The experimental setup used therein was a flexible gold-titanium reaction cell contained within a hydrothermal apparatus. Upon conclusion of the experiment magnesite precipitation was observed when reacted sample was analysed through Scanning Electron Microscopy (SEM). Iron carbonate, i.e. siderite, was seen growing on the shale surface; halite (NaCl) and analcime ($NaAlSi_2O_6{\cdot}H_2O$) crystals were also identified and changes in brine chemistry indicated significant reaction of silicate minerals in the system (Kaszuba et al., 2003).

Several authors (Bruant Jr. et al., 2002, Giammar et al., 2005) have studied the high pressure-high temperature interaction between supercritical $CO_2$, brine and forsteritic olivine ($Mg_2SiO_4$). Two different systems were used for the study: a flow-through system where the effect of pressure on forsterite olivine dissolution rate was investigated, and a batch system where the effect of temperature and surface area was studied. The average olivine dissolution rate was ~ 1.8 times greater at 100 bar than at atmospheric pressure. The extent of olivine dissolution was also enhanced at increasing temperatures and olivine surface area. Five ten-day experiments were also conducted at 100 bar and 95°C with increasing initial magnesite ($MgCO_3$) saturation indices. A minimum value of 1.64 for the saturation index was needed to precipitate magnesite on reacted olivine (Bruant Jr. et al., 2002). Giammar et al. (Giammar et al., 2005) also identified the rate of nucleation as a barrier for magnesite precipitation. Thus, when solution compositions were manipulated in order to simulate conditions resulting from extensive forsterite dissolution, magnesite precipitation did occur. When forsterite is present, magnesite nucleation appeared to occur heterogeneously on the surface of forsterite particles but the presence of forsterite did not significantly accelerate magnesite nucleation relative to solid-free systems.

Experimental studies on mineral trapping of $CO_2$ with brine samples collected from the Oriskany Formation (Indiana County, PA) were reported by Soong and co-workers (Soong et al., 2004). They studied the effects of pH (3.6-11), reaction time (1-6 h), $CO_2$ pressure (0.34-7.63 MPa) and temperature (50-170°C) on brine carbonation in a 1/2 litre autoclave reactor manufactured in Hastelloy C-276. The amount of calcite ($CaCO_3$) precipitated as a result of the hydrothermal reaction depended primarily on the pH of the brine. Mineral trapping is also controlled by $CO_2$ pressure and temperature but by a lesser extent when compared to pH. An optimum reaction time between 4 and 6h was also reported as the optimum one for calcite precipitation when reaction conditions are set at 155°C, 6.87 MPa of $CO_2$, pH 11.0 and stirring speed 800 rpm. The importance of pH to form carbonates was also reported by Druckenmiller and co-workers (Druckenmiller et al., 2006). They induced and characterized calcite formation by reacting natural gas brine with $CO_2$ and identified optimal initial pH conditions of at least 9.0 for carbonate precipitation in reactions of 18 h. The tested ranges of temperature and pressure were 75-150°C and 600-1500 psi respectively. Temperature seemed to have a greater influence on carbonate formation than pressure.

Rosenbauer et al. (Rosenbauer et al., 2005) carried out $CO_2$-brine-rock experiments at 25 and 120°C from 100 to 600 bar and up to 80 days reaction time. Experiments reacted supercritical $CO_2$ with natural (shallow ground water high-sulfate brine from Paradox Valley, Colorado, United States) and synthetic low-sulfate brines (synthetic solution of a deep-aquifer brine also from Paradox Valley and a predominantly NaCl solution equivalent in ionic strength to the natural brine) in the presence and absence of limestone (carbonate rock) and plagioclase-rich arkose sandstone (silicate rock). Precipitation of anhydrite ($CaSO_4$) and dolomitization of limestone was the result of the interaction of limestone with the high-sulfate brine, with a final decrease in porosity of 4.5%. However, the reaction between $CO_2$-saturated low-sulfate brine and limestone increased rock porosity by 2.6% because of dissolution of 10% of the original calcite. Solubility of $CO_2$ is reported to be enhanced in the presence of both rocks but in limestone formations storage of $CO_2$ is limited to ionic and hydrodynamic trapping whereas mineral trapping occurs in brine-supercritical $CO_2$-arkose systems.

Bateman et al. (Bateman et al., 2005) provided a long-term (7.5 months) laboratory experiment reacting known quantities of minerals (a prepared mixture based on that of the Utsira sand and containing mainly quartz, 80%, and minor amounts of labradorite, k-feldspar, albite, calcite, dolomite, muscovite and chlorite) with $CO_2$-rich fluid at 70°C and 100 bar. Their aim was to use the experimental results as a test case with which to help validate predictive geochemical computer models. Samples of the reactant fluid were collected at interim times. Changes were seen on the carbonates present in the starting material, which matched well with observed trends in fluid chemistry. That was not the case for changes in silica concentration, which did not correlate to any pitting or etching in the silica-bearing phases. They reported a clear overestimation of the degree of reaction according to model predictions compared to experimental results. For instance, dawsonite was predicted to form in large quantities and it was not detected at all in the experiments. Differences between simulations and experimental results were thought to be a reflection of the data quality (equilibrium and kinetic constants) used for the predictions rather than failure of the models themselves.

Recent studies on in-situ carbonation of peridotite (composed largely of the minerals olivine, $(Mg,Fe)_2SiO_4$, and pyroxene, $(Ca,Mg,Fe)_2Si_2O_6$), a type of rock found at or near the surface in Oman and other areas around the world, suggest that the process could be speeded up by multiple orders of magnitude with simple drilling and injection methods (Kelemen and Matter, 2008). Initial injection of heated water containing pressurized $CO_2$ would trigger the carbonation process, which naturally generates heat that would in turn hasten and self-sustain the reaction. Rapid reaction rates could be then attained at depth with little expenditure of energy.

#### 2.3.4.2. *Experimental and modeling work with non-pure $CO_2$ streams*

The effect of gas impurities derived from the $CO_2$ gas stream in the rock/water/gas interactions upon co-injection deep underground is attracting a lot of interest, because there might be cost savings in co-storage of $CO_2$ and other flue gas constituents (the $CO_2$ capture process is by far the most expensive part of the whole carbon capture and storage system – see section 2.2.3).

Acid gas ($CO_2$+$H_2S$) injection activities into deep geological formations have been taking place over the last decade (see section 2.3.3). Although the purpose of acid gas injection operations is the disposal of $H_2S$ so the produced natural gas meets the pipeline and market specifications, significant quantities of $CO_2$ (14-98% of the total volume) are also co-injected because it is costly to separate the two gases. Actually, a higher amount of $CO_2$ than $H_2S$ has been injected to date into deep geological formations. In the context of current efforts to reduce anthropogenic $CO_2$ emissions, these acid-gas injection operations represent a commercial-scale analogue for large-scale $CO_2$ geological sequestration (Bachu, 2008). Hence, the necessary technology for underground $CO_2$ storage already exists; the high cost of $CO_2$ capture and the identification of geological sinks of $CO_2$ are the main barriers for its large-scale implementation (Bachu et al., 2003).

Several reaction transport simulations and geochemical modeling studies on injection of $CO_2$, together with $H_2S$ and/or $SO_2$ have been reported previously (Gunter et al., 2000, Bachu et al., 2003, Xu et al., 2004b, Knauss et al., 2005, Palandri and Kharaka, 2005, Xu et al., 2007). Results show that co-injection of $H_2S$ with $CO_2$ would not negatively impact injectivity or sequestration compared to injection of $CO_2$ alone. However, co-injection of $SO_2$ could produce significantly different results: pH appears to be a key factor to determine a zonal distribution of mineral alteration and formation of carbon and sulfur trapping minerals (Xu et al., 2004b). Precipitation of carbonates would occur within a higher pH ($> 5$) peripheral zone, whereas secondary sulfates would precipitate within the acidified zone (pH $< 5$) adjacent to the injection well (Xu et al., 2007). Siliciclastic aquifers seem to be better host rocks for mineral trapping than carbonate aquifers, especially with regard to $CO_2$ (Gunter et al., 2000).

Experimental studies on the reactivity of $H_2S$+$CO_2$-brine-solid systems under high pressure and high temperature (500 bar and 200°C) were reported by Jacquemet and co-workers (Jacquemet et al., 2005). The experiments tried to simulate the interactions that occur at reservoirs-well interfaces of acid gas geological storage. They run two experiments for 15 days each: reactants of the first experiment were cement+steel+brine and reactants of the second one were cement+steel+brine+$CO_2$+$H_2S$. The presence of the $CO_2$-$H_2S$ gas mixture induced a pH decrease and a reductive environment. As a result of the former conditions, partial cement carbonation (calcite formation around the cement) and sulfidation of iron-bearing phases (steel), i.e. formation of pyrites within the cement and around the steel, was also observed.

Very few experimental studies have been reported on co-injection of non-pure $CO_2$ streams ($CO_2$-$SO_2$ gas mixtures) into different host rocks (Summers et al., 2004, Palandri et al., 2005, Mandalaparty et al., 2009) because to date, $CO_2$ is expected to be separated from the flue gas prior to its underground injection.

Mineral carbonation tests were performed at 10 atm, 185°C and for 1 and 6 h with olivine from the Twin Sisters deposit (Washington State) and basalt from an outcrop of the Columbia River Basalt Group, Oregon (Summers et al., 2004). Minerals were combined with a 0.64M $NaHCO_3$ and 1M NaCl carrier solution in a 15% solids slurry and fed to a high pressure-high temperature autoclave. Experiments were conducted with pure $CO_2$ gas and with a $CO_2$-$SO_2$ gas stream. Results showed that 1.5% (by volume) of $SO_2$ in the mixed gas did not hinder the carbonation reaction when compared with the experiment with pure $CO_2$; $SO_2$ may actually have enhanced slightly the carbonation process by probably increasing the solubility of magnesium from the rock. In this case, solid sulfates precipitation was not observed.

A long-term experiment (~1400 h) was conducted with hematite ($\alpha$-$Fe_2O_3$), a 1mNaCl, 0.5mNaOH brine and a $CO_2$-$SO_2$ gas mixture at 150°C and 300 bar to validate siderite ($FeCO_3$) precipitation predicted by geochemical modeling (Palandri et al., 2005). The concentration of $SO_2$ in the gas mixture was of 11% (by volume). The experiment aimed to proof the concept that iron-bearing minerals could be considered as potential repositories for underground $CO_2$ storage, provided that the injected gas stream is a $CO_2$-$SO_2$ mixture. $SO_2$ acts as a reductant to reduce $Fe^{3+}$ from hematite and convert it to $Fe^{2+}$, which will further precipitate as iron carbonate and, at the same time, $SO_2$ can be trapped along with $CO_2$. Precipitation of siderite ($FeCO_3$) was verified, although to a much lesser extent than the predicted one by geochemical modeling, and the presence of other metastable phases such as pyrite and elemental sulfur was also observed. The former ones were expected to re-dissolve if given sufficient time for the reaction to reach equilibrium.

An experimental investigation was conducted with brine and a prepared arkose (comprised of equal proportions of calcite, $CaCO_3$, dolomite, $CaMg(CO_3)_2$, quartz, $SiO_2$, microcline, $KAlSi_3O_8$, andesine, $Na_xCa_yAlSi_2O_8$, and chlorite, $(Fe,Mg,Al)_6(Si,Al)_4O_{10}(OH)_8$) at temperatures ranging from 50 to 200°C, pressures from 600 to 2000 psia and reaction times up to 134 days (Mandalaparty et al., 2009). Baseline experiments were carried out with only $CO_2$ and compared with experiments carried out with gas mixtures containing 10% (by volume) of $SO_2$. The base case $CO_2$ experiments showed layers of calcite growing on the surface of the arkose, and analcime ($NaAlSi_2O_6 \cdot H_2O$) deposits occuring either as large connected aggregates or as deposits on the surfaces of other minerals. When $SO_2$ was present in the gas, continued dissolution of calcite and growth of anhydrite ($CaSO_4$) crystals was observed. However, numerical simulations did not show significant differences in injectivity between the $CO_2$ and $CO_2$+$SO_2$ case.

Should the approach of treating multiple pollutants in the $CO_2$ capture process become implemented in the future, thermodynamic and kinetic data will need to be available in order to accurately predict the gas-rock-brine behaviour in a geological $CO_2$ storage scenario. Moreover, those data need to be obtained under appropiate conditions of pH, chemical composition of the brine, temperature, pressure, etc. Thus, it is very important to have laboratory or test cases against which models can be validated; hence, a broad field is open ahead for further research. If conducted, that research will undoubtely resolve many unknowns regarding the geochemistry of trapping mechanisms and would also help in acquisition of enhanced storage capacity estimates.

## 2.4. References

Adams, E., Caulfield, J., Herzog, H. J. & Auerbach, D. I. (1997) Impacts of reduced pH from ocean $CO_2$ disposal: Sensitivity of zooplankton mortality to model parameters. *Waste Management,* 17, 375-380.

Allinson, G. & Nguyen, V. (2002) $CO_2$ geological storage economics. Proceedings of the Sixth International Conference on Greenhouse Gas Control Technologies (GHGT-6), 1-4 October, Kyoto, Japan.

Allinson, W. G., Nguyen, D. N. & Bradshaw, J. (2003) The economics of geological storage of $CO_2$ in Australia. *Australian Petroleum Production and Exploration Association (APPEA) Journal,* 43, 623-636.

Bachu, S. (2000) Sequestration of $CO_2$ in geological media: criteria and approach for site selection in response to climate change. *Energy Conversion and Management,* 41, 953-970.

Bachu, S. (2003) Screening and ranking sedimentary basins for sequestration of $CO_2$ in geological media in response to climate change. *Environmental Geology,* 44, 227-289.

Bachu, S. (2008) $CO_2$ storage in geological media: role, means, status and barriers to deployment. *Progress in Energy and Combustion Science,* 34, 254-273.

Bachu, S., Adams, J. J., Michael, K. & Buschkuehle, B. E. (2003) Acid gas injection in the Alberta Basin: a commercial-scale analogue for $CO_2$ geological sequestration in sedimentary basins. Proceedings of the Second Annual Conference on Carbon Dioxide Sequestration May 5-8, Alexandria, VA.

Bachu, S., Gunter, W. D. & Perkins, E. H. (1994) Aquifer Disposal of $CO_2$ - Hydrodynamic and Mineral Trapping. *Energy Conversion and Management,* 35, 269-279.

Bachu, S., Gunter, W. D. & Perkins, E. H. (1996) Carbon dioxide disposal. IN HITCHON, B. (Ed.) *Aquifer disposal of carbon dioxide, hydrodynamic and mineral trapping-proof of concept.* Sherwood Park, Alberta, Canada, Geoscience Publishing Ltd.

Bahadori, A., Vuthaluru, H. B. & Mokhatab, S. (2009) New correlations predict aqueous solubility and density of carbon dioxide. *International Journal of Greenhouse Gas Control,* 3, 474-480.

Ball, D. & Gupta, N. (2008) Midwest Regional Carbon Sequestration Partnership (MRCSP) - Overview and Update. Proceedings of the Seventh Annual Conference on Carbon Capture & Sequestration, Pittsburgh, PA.

Bateman, K., Turner, G., Pearce, J. M., Noy, D. J., Birchall, D. & Rochelle, C. A. (2005) Large-scale column experiment: study of $CO_2$, porewater, rock reactions and model test case. *Oil & Gas Science and Technology,* 60, 161-175.

Bergman, P. D. & Winter, E. M. (1995) Disposal of carbon dioxide in aquifers in the U.S. *Energy Conversion and Management,* 36, 523-526.

Bickle, M., Chadwick, A., Huppert, H. E., Hallworth, M. & Lyle, S. (2007) Modelling carbon dioxide accumulation at Sleipner: Implications for underground carbon storage. *Earth and Planetary Science Letters,* 255, 164-176.

Bock, B., Rhudy, R., Herzog, H., Klett, M., Davison, J., De La Torre Ugarte, D. G. & Simbeck, D. (2003). Economic Evaluation of $CO_2$ Storage and Sink Enhancement Options, TVA Public Power Institute, US.

Brosse, E., Bildstein, O. & Swennen, R. (2005) Gas-Water-Rock interactions induced by reservoir exploitation, $CO_2$ sequestration, and other geological storage. *Oil & Gas Science and Technology* 60, 9-18.

Bruant Jr., R. G., Giammar, D. E., Myneni, S. C. B. & Peters, C. A. (2002) Effect of Pressure, Temperature, and Aqueous Carbon Dioxide Concentration on Mineral Weathering as Applied to Geologic Storage of Carbon Dioxide. Proceedings of the Sixth International Conference on Greenhouse Gas Control Technologies (GHGT-6), 1-4 October, Kyoto, Japan.

CCJ (2008a) CO2CRC launches first $CO_2$ storage project in Southern Hemisphere. Available from: <www.carboncapturejournal.com> (accessed 16 October 2008).

CCJ (2008b) Germany begins $CO_2$ storage at Ketzin. Available from: <www.carboncapturejournal.com> (accessed 13 August 2008).

CCJ (2008c) The Gorgon LNG Project. Available from: <www.carboncapturejournal.com> (accessed 16 October 2008).

CCJ (2009) Britain's first Carbon Capture and Storage plant to be built in Yorkshire. Available from: <www.carboncapturejournal.com> (accessed 24 November 2009).

CCP (2007). Regulatory treatment of $CO_2$ impurities for CCS, $CO_2$ Capture Project, Policy Position paper.

Chevron-Australia (2008) Gorgon Project. Available from: <http://www.gorgon.com.au/index.html> (accessed 16 October 2008).

CO2CRC (2008a) CCS activity in Australia 2008. Available from: <http://www.co2crc.com.au/about/> (accessed 16 October 2008).

CO2CRC (2008b) CO2CRC Otway Project - Australia's first demonstration of geosequestration. Available from: <http://www.co2crc.com.au/dls/A2_posters_web/poster_otway_overview.pdf> (accessed 16 October 2008).

DOE (2007). Carbon Sequestration Atlas of the United States and Canada, U.S. Department of Energy, Office of Fossil Energy, National Energy Technology Laboratory (NETL), US.

Dooley, J. J., Dahowski, R. T., Davidson, C. L., Wise, M. A., Gupta, N., Kim, S. H. & Malone, E. L. (2006). Carbon dioxide capture and geologic storage - A core element of a global energy technology strategy to address climate change, Batelle Memorial Institute, US.

Doughty, C., Freifeld, B. M. & Trautz, R. C. (2008) Site characterization for CO2 geologic storage and vice versa: the Frio brine pilot, Texas, USA as a case study. *Environ. Geol.,* 54, 1635-1656.

Dreybrodt, W., Lauckner, J., Zaihua, L., Svensson, U. & Buhmann, D. (1996) The kinetics of the reaction $CO_2 + H_2O \rightarrow H^+ + HCO_3^-$ as one of the rate limiting steps for the dissolution of calcite in the system $H_2O$---$CO_2$---$CaCO_3$. *Geochimica Et Cosmochimica Acta,* 60, 3375-3381.

Druckenmiller, M. L., Maroto-Valer, M. M. & Hill, M. (2006) Investigation of Carbon Sequestration via Induced Calcite Formation in Natural Gas Well Brine. *Energy & Fuels,* 20, 172-179.

Drummond, S. E. (1981) Boiling and mixing of hydrothermal fluids: chemical effects on mineral precipitation, PhD, Pennsylvania State University.

Duan, Z. & Sun, R. (2003) An improved model calculating $CO_2$ solubility in pure water and aqueous NaCl solutions from 273 to 533 K and from 0 to 2000 bar. *Chemical Geology,* 193, 257-271.

Enick, R. M. & Klara, S. M. (1990) $CO_2$ solubility in water and brine under reservoir conditions. *Chemical Engineering Communications,* 90, 23-33.

EU (2009) CCS in Europe. Available from: <http://ec.europa.eu/environment/climat/ccs/work_en.htm> (accessed 22 November 2009).

Finley, R. (2008) Midwest Geological Sequestration Consortium (MGSC) - Overview and Update. Proceedings of the Seventh Annual Conference on Carbon Capture & Sequestration, Pittsburgh, PA.

Flett, M. A., Gurton, R. M. & Taggart, I. J. (2005) Heterogeneous saline formations: long-term benefits for geosequestration of greenhouse gases. Proceedings of the Seventh International Conference on Greenhouse Gas Control Technologies, 5-9 September Vancouver, Canada.

Friedmann, S. J. (2007) Geological carbon dioxide sequestration. *Elements,* 3, 179-184.

Giammar, D. E., Bruant Jr., R. G. & Peters, C. A. (2005) Forsterite dissolution and magnesite precipitation at conditions relevant for deep saline aquifer storage and sequestration of carbon dioxide. *Chemical Geology,* 217, 257-276.

Gibbins, J. & Chalmers, H. (2008) Carbon capture and storage. *Energy Policy,* 36, 4317-4322.

Gladkikh, M. & Bryant, S. (2003) Prediction of interfacial areas during imbibition in simple porous media. *Advances in Water Resources,* 26, 609-622.

Gunter, W. D., Perkins, E. H. & Hutcheon, I. (2000) Aquifer disposal of acid gases: modelling of water-rock reactions for trapping of acid wastes. *Applied Geochemistry,* 15, 1085-1095.

Gunter, W. D., Wiwchar, B. & Perkins, E. H. (1997) Aquifer disposal of $CO_2$-rich greenhouse gases: Extension of the time scale of experiment for $CO_2$-sequestering reactions by geochemical modelling. *Mineralogy and Petrology,* 59, 121-140.

Herzog, H. (2002) Carbon Sequestration via Mineral Carbonation: Overview and Assessment. MIT Laboratory for Energy and the Environment

Hill, G. (2008) Southeast Regional Carbon Sequestration Partnership (SECARB) - Overview and Update. Proceedings of the Seventh Annual Conference on Carbon Capture & Sequestration, Pittsburgh, PA.

Hill, M. A. (2006) Investigation of the pH and chemical influence of a typical host rock on carbon sequestration in brine, PhD thesis, The Pennsylvania State University.

Hitchon, B., Gunter, W. D., Gentzis, T. & Bailey, R. T. (1999) Sedimentary basins and greenhouse gases: a serendipitous association *Energy Conversion and Management,* 40, 825-843.

Holloway, S. (2001) Storage of fossil fuel-derived carbon dioxide beneath the surface of the earth. *Annual Review of Energy and the Environment,* 26, 145-66.

Holloway, S. (2005) Underground sequestration of carbon dioxide-a viable greenhouse gas mitigation option. *Energy,* 30, 2318-2333.

Houghton, J. T., Ding, Y., Griggs, D. J., Noguer, M., van der Linden, P. J., Dai, X., Maskell, K. & Johnson, C. A. (Eds.) (2001) *Climate Change 2001: The Scientific Basis,* Cambridge, United Kingdom and New York, NY, USA, Cambridge University Press.

IEA Fact sheet - Storing $CO_2$ in Unminable Coal Seams. Available from: <http://www.ieagreen.org.uk/8.pdf> (accessed 19/01 2009).

IEA (2008a) $CO_2$ Capture and Storage. Available from: <http://www.co2captureandstorage.info/project_specific.php?project_id=105> (accessed 11 August 2008).

IEA (2008b) *Energy Technology Perspectives.*

IEA (2009) *World Energy Outlook.*

IPCC (2005). IPCC Special Report on Carbon Dioxide Capture and Storage, Prepared by Working Group III of Intergovernmental Panel on Climate Change, Cambridge, United Kingdom and New York, NY, USA.

Jacquemet, N., Pironon, J. & Caroli, E. (2005) A New Experimental Procedure for Simulation of $H_2S$ + $CO_2$ Geological Storage. Application to Well Cement Aging. *Oil & Gas Science and Technology,* 60, 193-206.

Juanes, R., Spiteri, E. J., Orr Jr., F. M. & Blunt, M. J. (2006) Impact of relative permeability hysteresis on geological $CO_2$ storage. *Water Resources Research.* American Geophysical Union.

Juhlin, C., Giese, R., Zinck-Jorgensen, K., Cosma, C., Hazemeini, H., Juhojuntti, N., Luth, S., Norden, B., Forster, A. & Yordkayhun, S. (2008) Seismic monitoring at the CO2SINK project site, Ketzin, Germany: Past, present and future. *Geophysical Research Abstracts.*

Kaszuba, J. P., Janecky, D. R. & Snow, M. G. (2003) Carbon dioxide reaction processes in a model brine aquifer at 200°C and 200 bars: implications for geologic sequestration of carbon. *Applied Geochemistry,* 18, 1065-1080.

Kelemen, P. B. & Matter, J. (2008) In situ carbonation of peridotite for $CO_2$ storage. *Proceedings of the National Academy of Science,* 105, 17295-17300.

Knauss, K. G., Johnson, J. W. & Steefel, C. I. (2005) Evaluation of the impact of $CO_2$, co-contaminant gas, aqueous fluid and reservoir rock interactions on the geologic sequestration of $CO_2$. *Chemical Geology,* 217, 339-350.

Kongsjorden, H., Karstad, O. & Torp, T. A. (1997) Saline aquifer storage of carbon dioxide in the Sleipner project. *Waste Management,* 17, 303-308.

Kongsjorden, H., Karstad, O. & Torp, T. A. (1998) Saline aquifer storage of carbon dioxide in the Sleipner Project. *Waste Management,* 17, 303-308.

Kovscek, A. R. & Radke, C. J. (2003) Pressure-driven capillary snap-off of gas bubbles at low wetting-liquid content. *Colloids and Surfaces A: Physicochemical and Engineering Aspects,* 212, 99-108.

Laate, M. (2008) StatoilHydro's R&D on $CO_2$ Storage and Capture - 12 years of $CO_2$ Storage. Proceedings of the Seventh Annual Conference on Carbon Capture & Sequestration, 5-8 May, Pittsburgh, PA.

Lackner, K. S., Butt, D. P., Wendt, C. H., Goff, F. & Guthrie, G. (1997). Carbon dioxide disposal in mineral form: keeping coal competitive, Los Alamos National Laboratory,

Lackner, K. S., Butt, D. P., Wendt, C. H. & Ziock, H. (1998). Mineral Carbonates as Carbon Dioxide Sinks, Los Alamos National Laboratory,

Li, H., Yan, J., Yan, J. & Anheden, M. (2009) Impurity impacts on the purification process in oxy-fuel combustion based $CO_2$ capture and storage system. *Applied Energy,* 86, 202-213.

Lindeberg, E., Van der Meer, E., Moen, A., Wessel Berg, D. & Ghaderi, A. (2000). Saline Aquifer CO2 Storage (SACS): Task 2: Fluid and core properties and reservoir simulation,

Liu, L., Suto, Y., Bignall, G., Yamasaki, N. & Hashida, T. (2003) $CO_2$ injection to granite and sandstone in experimental rock/hot water systems. *Energy Conversion and Management,* 44, 1399-1410.

Liu, Z., Yuan, D. & Dreybrodt, W. (2005) Comparative study of dissolution rate-determining mechanisms of limestone and dolomite. *Environmental Geology,* 49, 274-279.

Mandalaparty, P., Deo, M., Moore, J. & McPherson, B. (2009). Carbon dioxide sequestration: effect of the presence of sulfur dioxide on the mineralogical reactions and on the injectivity of $CO_2$+$SO_2$ mixtures, University of Utah, Salt Lake City.

Mazzotti, M., Pini, R. & Storti, G. (2009) Enhanced coalbed methane recovery. *The Journal of Supercritical Fluids,* 47, 619-627.

McPherson, B. J. (2008) Southwest Regional Carbon Sequestration Partnership (SWP) - Overview and Update. Proceedings of the Seventh Annual Conference on Carbon Capture & Sequestration, Pittsburgh, PA.

Metz, B., Davidson, O. R., Bosch, P. R., Dave, R. & Meyer, L. A. (Eds.) (2007) *Climate Change 2007: Mitigation of Climate Change,* Cambridge, United Kingdom and New York, NY, USA, Cambridge University Press.

Michael, K., Allinson, G., Golab, A., Sharma, S. & Shulakova, V. (2009a) $CO_2$ storage in saline aquifers II - experience from existing storage operations. *Energy Procedia,* 1, 1973-1980.

Michael, K., Arnot, M., Cook, P., Ennis-King, J., Funnell, R., Kaldi, J., Kirste, D. & Paterson, L. (2009b) $CO_2$ storage in saline aquifers I - current state of scientific knowledge. *Energy Procedia,* 1, 3197-3204.

Mito, S., Xue, Z. & Ohsumi, T. (2007) Evaluation of $CO_2$ geochemical reactions at an onshore saline aquifer, Nagaoka, Japan. *European Geosciences Union (EGU).* Vienna, Austria.

Myer, L. (2008) West Coast Regional Carbon Sequestration Partnership (WESTCARB) - Overview and update. Proceedings of the Seventh Annual Conference on Carbon Capture & Sequestration, Pittsburgh, PA.

Nicolaisen, H. (1994) Phase equilibria in aqueous electrolyte solutions, PhD, Technical University of Denmark Lyngby.

Nighswander, J. A., Kalogerakis, N. & Mehrotra, A. K. (1989) Solubilities of carbon dioxide in water and 1 wt% NaCl solution at pressures up to 10 MPa and temperatures from 80 to 200 °C. *Chemical Engineering Data,* 34, 355-360.

NOAA-ESRL (2009) Earth's $CO_2$ home page. Available from: <http://co2now.org> (accessed 19th November 2009).

Obi, E.-O. I. & Blunt, M. J. (2006) Streamline-based simulation of carbon dioxide storage in a North Sea aquifer. *Water Resources Research.* American Geophysical Union.

Pacala, S. & Socolow, R. (2004) Stabilization wedges: solving the climate problem for the next 50 years with current technologies. *Science,* 305, 968-972.

Palandri, J. L. & Kharaka, Y. K. (2005) Ferric iron-bearing sediments as a mineral trap for $CO_2$ sequestration: Iron reduction using sulfur-bearing waste gas. *Chemical Geology,* 217, 351-364.

Palandri, J. L., Rosenbauer, R. J. & Kharaka, Y. K. (2005) Ferric iron in sediments as a novel $CO_2$ mineral trap:$CO_2$-$SO_2$ reaction with hematite. *Applied Geochemistry,* 20, 2038-2048.

Pidwirny, M. (2006) Introduction to the atmosphere: the greenhouse effect. Available from: <www.physicalgeography.net/fundamentals> (accessed 15 June 2006

Portier, S. & Rochelle, C. (2005) Modelling $CO_2$ solubility in pure water and NaCl-type waters from 0 to 300 °C and from 1 to 300 bar. Application to the Utsira Formation at Sleipner. *Chemical Geology,* 217, 187-199.

Pruess, K. (2005) Numerical studies of fluid leakage from a geologic disposal reservoir for $CO_2$ show self-limiting feedback between fluid flow and heat transfer. *Geophysical Research Letters,* 32, L14404.

Reichle, D., Houghton, J., Kane, B., Ekmann, J. & others (1999). Carbon sequestration research and development, DOE, US.

Riddiford, F., Wright, I., Bishop, C., Espie, T. & Tourqui, A. (2005) Monitoring geological storage in the In Salah Gas $CO_2$ storage project. Proceedings of the 7th International Conference on Greenhouse Gas Control Technologies, September 2004, Vancouver, Canada.

Rosenbauer, R. J., Koksalan, T. & Palandri, J. L. (2005) Experimental investigation of $CO_2$-brine-rock interactions at elevated temperature and pressure: Implications for $CO_2$ sequestration in deep-saline aquifers. *Fuel Processing Technology,* 86, 1581-1597.

Rumpf, B., Nicolaisen, C., Öcal, C. & Maurer, G. (1994) Solubility of carbon dioxide in aqueous solutions of sodium chloride:experimental results and correlation. *Ber.Bunsenges.Phys.Chem.,* 1, 431-447.

Sass, B. M., Gupta, N., Ickes, J. A., Engelhard, M. H., Baer, D. R., Bergman, P. & Byrer, C. (2001) Interaction of rock minerals with carbon dioxide and brine: a hydrothermal investigation. Proceedings of the First National Conference on Carbon Sequestration, 15-17 May Washington DC.

SCCS (2009). Opportunities for $CO_2$ storage around Scotland - an integrated strategic research study, Scottish Centre for Carbon Storage, Edinburgh.

Seifritz, W. (1990) $CO_2$ disposal by means of silicates. *Nature,* 345, 486.

Solomon, S., Qin, D., Manning, Chen, Z., Marquis, M., Averyt, K. B., Tignor, M. & Miller, H. L. (Eds.) (2007) *Climate Change 2007: The Physical Science Basis,* Cambridge, United Kingdom and New York, NY, USA, Cambridge University Press.

Soong, Y., Goodman, A. L., McCarthy-Jones, J. R. & Baltrus, J. P. (2004) Experimental and simulation studies on mineral trapping of $CO_2$ with brine. *Energy Conversion and Management,* 45, 1845-1859.

Soong, Y., Jones, J. R., Harrison, D. K., Hedges, S. W., Goodman, A. L. & Baltrus, J. P. (2003) Mineral Trapping of $CO_2$ with Oriskany Brine. Proceedings of the Second Annual Conference on Carbon Sequestration, 5-8 May Alexandria, VA, USA.

Statoil (2008) Carbon storage started on Snohvit. Available from: <http://www.statoilhydro.com/en/NewsAndMedia/News/2008/Pages/CarbonStorageStartedOnSn%C3%B8hvit.aspx> (accessed 22 November 2009).

Steadman, E. (2008) Plains CO2 Reduction Partnership (PCOR) - Overview and Update. Proceedings of the Seventh Annual Conference on Carbon Capture & Sequestration, Pittsburgh, PA.

Stevens, S. H., Kuuskraa, J. A. & Schraufnagel, R. A. (1996) Technology spurs growth of U.S. coalbed methane. *Oil and Gas Journal,* 94, 56-63.

Streit, J., Siggins, A. & Evans, B. (2005) Predicting and monitoring geomechanical effects of $CO_2$ injection. IN BENSON, S. M. (Ed.) *Geologic storage of carbon dioxide with monitoring and verification.* London, Elsevier Science.

Stumm, W. & Morgan, J. J. (1996) *Aquatic chemistry: chemical equilibria and rates in natural waters,* New York, Wiley-Interscience.

Suekane, T., Nobuso, T., Hirai, S. & Kiyota, M. (2008) Geological storage of carbon dioxide by residual gas and solubility trapping. *International Journal of Greenhouse Gas Control,* 2, 58-64.

Summers, C. A., Dahlin, D. C. & Ochs, T. L. (2004) The effect of $SO_2$ on mineral carbonation in batch tests. Proceedings of the 29th International Technical Conference on Coal Utilization and Fuel Systems, Gaithersburg, MD.

Suto, Y., Liu, L., Hashida, T., Tsuchiya, N. & Yamasaki, N. (2001) Experimental study of rock/water/$CO_2$ interaction at temperatures of 100-350 °C. Proceedings of the Tenth International Symposium on Water-Rock Interaction (WRI-10), 10-15 July, Villasimius, Italy.

Suto, Y., Liu, L., Hashida, T. & Yamasaki, N. (2000) Measurement of $CO_2$ solubility in simulated underground water at depth for the carbon dioxide sequestration. Proceedings of the Proceedings of Joint ISHR & ICSTR, Kochi, Japan.

Suto, Y., Liu, L., Yamasaki, N. & Hashida, T. (2007) Initial behavior of granite in response to injection of $CO_2$-saturated fluid. *Applied Geochemistry,* 22, 202-218.

Teir, S., Eloneva, S., Fogelholm, C. J. & Zevenhoven, R. (2009) Fixation of carbon dioxide by producing hydromagnesite from serpentinite. *Applied Energy,* 86, 214-218.

Teir, S., Eloneva, S. & Zevenhoven, R. (2005) Production of precipitated calcium carbonate from calcium silicates and carbon dioxide. *Energy Conversion and Management,* 46, 2954-2979.

Torp, T. A. & Gale, J. (2004) Demonstrating storage of CO2 in geological reservoirs: The sleipner and SACS projects. *Energy,* 29, 1361-1369.

Vattenfall (2008) Vattenfall's Project on CCS. Available from: <http://www.vattenfall.com/www/co2_en/co2_en/index.jsp> (accessed 16 October 2008).

VGB (2007). Facts and figures - Electricity generation 2007, VGB Powertech, Essen, Germany.

Voormeij, D. A. & Simandl, G. J. (2002). Geological and Mineral $CO_2$ Sequestration Options: A Technical Review, British Columbia Geological Survey, US.

Xu, T., Apps, J., Pruess, K. & Yamamoto, H. (2007) Numerical modeling of injection and mineral trapping of $CO_2$ with $H_2S$ and $SO_2$ in a sandstone formation. *Chemical Geology,* 242, 319-346.

Xu, T., Apps, J. A. & Pruess, K. (2004a) Numerical simulation of $CO_2$ disposal by mineral trapping in deep aquifers. *Applied Geochemistry,* 19, 917-936.

Xu, T., Apps, J. A., Pruess, K. & Yamamoto, H. (2004b) Injection of $CO_2$ with $H_2S$ and $SO_2$ and Subsequent Mineral Trapping in Sandstone-Shale Formation. Available from: <http://repositories.cdlib.org/lbnl/LBNL-57426 > (accessed 16 January 2006

Zerogen (2008) The Zerogen Project: Project overview. Available from: <http://www.zerogen.com.au/project/overview.aspx> (accessed 16 October 2008).

# CHAPTER 3

# METHODOLOGY

# 3. Methodology

Two solid samples were utilised in this research project: an iron oxide, hematite ($\alpha$-$Fe_2O_3$), and an iron oxyhydroxide, goethite ($\alpha$-FeOOH). The hematite sample proceeds from South Africa and was kindly donated by Prof. Sam Kingman of the National Centre for Industrial Microwave Processing (NCIMP), at the University of Nottingham (NCIMP, 2009). The goethite sample is original from El Paso County (Colorado) and was purchased from Ward's Natural Science Establishment (Ward's, 2009).

This chapter describes: a) the procedures and analytical methods employed to characterise the parent solid samples and reaction products (section 3.1); b) the procedure followed in modelling studies (section 3.2); c) the experimental procedure followed in the short-term ($\leq$ 264 h)[1] experiments conducted in the high pressure-high temperature system designed at the University of Nottingham (section 3.3); d) finally, the long-term (24 days) experiment conducted in the flexible gold-titanium reaction cell at the United Stated Geological Survey (USGS) is described in section 3.4.

## 3.1 Characterisation of parent solid samples and reaction products

### 3.1.1 Characterisation of solid samples

---

[1] For the purpose of this thesis short-term experiments are defined as those ones conducted for reaction times $\leq$ 264 h, and long-term experiments are those conducted for reaction times > 264h.

### *3.1.1.1 Particle size analysis/grain-size distribution*

Particle size analysis for the individual size fractions was performed by laser diffraction to verify the composition of the parent samples obtained for the experimentation. The technique relies on the fact that the diffraction angle is inversely proportional to particle size. A Malvern Mastersizer instrument uses this principle to provide completely accurate results over a large size range (typically 0.02 -2000 µm). Particles are measured in suspension by recirculation of the sample in front of the laser beam. In a cell, particles of the sample (~ 40-60 mg) are suspended in water (dispersion medium) and stirring is used to facilitate proper dispersion of particles in the liquid. Liquid level in the sample cell should be approximately 2 cm below the top edge of the cell. The particles concentration in the dispersion should be above a minimum level (~ 5% obscuration) in order to produce an acceptable signal-to-noise ratio in the detector. Likewise, it should be below a maximum level (~ 35% obscuration) in order to avoid multiple scattering. The measurement starts with the proper alignment of the optical part of the instrument, followed by a blank measurement with water (particle-free dispersion medium) which will be further subtracted from data obtained with the sample. A measuring time of approximately 3 s is used to allow for a large number of detector scans or sweeps at short time intervals, and an average signal is calculated. For each sample, results were averaged over four to six measurements (BS, 1999).

### *3.1.1.2 Surface area analysis*

Surface area measurements of parent solid samples were carried out using a standard ASAP 2010 (Micromeritrics, USA), which utilises $N_2$ adsorption at -196°C as a standard method. Prior to the analysis, samples (~ 0.2 g) were degassed at 115°C under vacuum. Isotherms are recorded by the stepwise introduction of known amounts of adsorbate, i.e. $N_2$, and the recording of the equilibrium pressure; from the isotherm produced, the BET (Brunauer, Emmett and Teller) surface area can be calculated using the BET equation (Brunauer et al., 1938, Brunauer et al., 1940, Gregg and Sing, 1982). The former equation is applied in the region of relative pressures near completed monolayers ($0.05 \leq P/P_0 \leq 0.35$)[2] because it is where the BET theory and experimental isotherms agree very well, leading to a powerful and extremely useful method of surface area determination.

### *3.1.1.3 Inductively Coupled Plasma – Atomic Emission Spectroscopy (ICP-AES) analysis*

Elemental analysis of parent solid samples was performed using a Perkin Elmer Optima® 3300 DV inductively coupled plasma – atomic emission spectrometer (ICP-AES). ICP-AES is a technique for analysing the concentration of metallic elements in solid and liquid samples. The analyte is excited and some of the excitation energy is released in the form of electromagnetic radiation, of a wavelength that is characteristic of the emitting

---

[2] $P_0$ is the saturation pressure of the adsorbate at the temperature of the analysis.

species (Günzler and Williams, 2001). The intensities of these characteristic wavelengths are detected, measured and compared to intensities for known standards to provide quantitative analysis (Settle, 1997). Detection limits of the instrument vary for each cation between 0.0001 and 0.5 µg/L. Each parent solid sample was analysed for the following elements: Fe, Al, Mg, Mn, Ti, Ca, S, P, Na, K and Si.

The ICP-AES was equipped with autosampler (AS-90 Plus®) and controlled with the Perkin Elmer Winlab software. The solids (~ 0.2 g) were prepared for analysis via a three-stage digestion procedure: a) 10 ml nitric acid (69%) are added to the weighed sample, which is further heated up to 190°C over 20 min and hold there for 30 min, followed by cooling to < 50°C; b) 3 ml of concentrated HCl + 5 ml 40% HF are added; the sample is heated up to 190°C over 20 min and hold there for 20 min, followed by cooling to < 50°C; c) 30 ml of 4% boric acid solution are added, the sample is heated up to 180°C over 20 min and hold there for 10 min, followed by cooling to < 50°C. Finally, the digestate solution is transferred to a 100 ml volumetric flask and diluted to mark with Milli-Q water, shaked and transferred to a prepared polythene bottle for the analysis. In the analysis, three replicate readings are taken for each sample.

#### *3.1.1.4 X-ray diffraction (XRD) analysis*

XRD analyses of unreacted and selected reacted samples were carried out on a 1050 XRD (Philips Analytical, Netherlands) attached to a 3 kW X-ray generator (Hilton Brooks, UK) producing copper Kα radiation at a wavelength of 0.15418 nm. XRD is one of the most common analytical techniques used for qualitative and quantitative analysis of crystalline compounds. Every crystalline material will give a characteristic diffraction pattern (Warren, 1990, Shriver and Atkins, 1999). Proper X-ray powder diffraction specimens should be flat, densely packed and very fine-grained powders. This is achieved by pressing the sample powder (~2 g) into a cavity without causing preferential orientation of the crystallites. Each cavity mount can then be numbered and placed in the relevant position inside a 36 position sample holder magazine, ready for XRD analysis. The XRD analyses were conducted over an angle range of 5 to 65 or 80 degrees 2θ with a scan speed of 2 degrees 2θ per minute. A single crystalline phase must have a concentration of approximately 5 wt% in order to be detected.

### *3.1.1.5 Thermo-gravimetric analysis (TGA)*

Thermogravimetric analysis (TGA) is the study of weight changes of a specimen as a function of temperature; weight changes observed at specific temperatures correlate to different reactions (oxidation/reduction, combustion, etc.), volatilisation of sample components, decomposition or other changes (Speyer, 1994, MEE, 2001). The TGA analyses of parent and reacted samples were recorded in a Q500 Thermogravimetric Analyzer from TA Instruments. Analyses were run under atmospheric pressure. Samples (~ 20-40 mg) placed in Pt crucibles were first equilibrated at 30°C and then heated under a $N_2$ atmosphere at 10°C/min from 30 to 900°C, with one stop at 105°C for 15 min.

Reacted samples were ground in a pestle and mortar for the TGA analyses so the effects derived from a different particle size of the samples will be negligible.

### *3.1.1.6 X-ray Photoelectron Spectroscopy (XPS) analysis*

X-ray photoelectron spectroscopy (XPS) provides qualitative and quantitative information on the surface of the samples (approximately the top 10 nm) and can be very useful for looking for compositional changes at mineral surfaces after the reactions of interest. Qualitatively, the detected binding energies of core shell electrons ejected by X-rays are used to identify compositional elements. Quantitatively, peak areas in the XPS spectrum are used to calculate the relative abundance of the atoms present in the area analysed. Hydrogen and helium are the only elements that can not be detected by XPS analysis (Moulder et al., 1995, Watts and Wolstenholme, 2003, Briggs and Beamson, 2006).

XPS spectra of parent and selected reacted samples were recorded using a Kratos Axis Ultra spectrometer, employing a monochromatic Al Kα X-ray source (hν = 1486.6 eV), hybrid (magnetic/electrostatic) optics, a hemispherical analyzer, a multichannel plate, and a delay line detector (DLD) with a collection angle of 30° and a takeoff angle of 90°. Kratos VISION II software was used to record all XPS spectra and the data files were translated to VAMAS format and processed using the CASAXPS software package version 2.3.2. Typically, samples (~20 mg) were mounted on standard Kratos stainless steel bar holders using double sided sticky tape and presented like this for analyses. Two points linear and Shirley background subtractions were used depending upon the shape of the spectrum to account for inelastically scattered electrons that contribute to the background. Peaks were fitted using GL(30) lineshapes; a combination of a Gaussian (70%) and Lorentzian (30%) profiles. The full width half maximum (FWHM) of each component was initially constrained to be in between 0.8 and 1.5 eV. Typically, samples were run under the charge neutralisation conditions (Kratos AXIS Nove charge neutralisation system) and charge correction was normally achieved by setting the aliphatic carbon peak to 285.0 eV (normally coming from adventitious carbon surface contamination). A ± 0.1 eV error in the acquisition of binding energies is quoted by the instruments manufacturer. The transmission corrected Reference Sensitivity Factors (RSF) used to determine relative atomic percentages were taken from the Kratos Library (Kratos, 2009) (RSF of F 1s = 1). An atomic relative percentage error of 10 to 20% depending on signal to noise ratio and a detection limit of 0.1 to 0.01 depending on the atom are quoted by the instrument's manufacturer. The reproducibility of the XPS measurements is typically ± 10%.

### 3.1.2 Characterization of liquid samples

#### *3.1.2.1 pH measurements*

The pH of brine samples is measured and recorded at ambient temperature before and after the experiments. A benchtop ThermoOrion pH/mV/Temperature meter with a glass electrode probe is used for short-term experiments at the University of Nottingham, and a Oakton 500 series pH-meter with an Orion 8103 Ross combination pH probe is used in the long-term experiment at USGS. Prior to any pH measurements of the brines, the pH-meter is calibrated at ambient temperature using three pH buffer solutions with pH values of 4.0, 7.0, and 10.0. The pH-meters are accurate to ± 0.01 pH units.

### *3.1.2.2 Salinity measurements*

A VWR hand-held or portable refractometer (SW series) (VWR, 2009) is used to measure the salt concentration (0-28%) of brine samples collected over the duration of the long-term carbonation experiment conducted at USGS. Only a couple of drops of the brine solution are needed for the measurement. The instrument actually measures the refractive index of the solution, which is defined as the ratio of the speed of light travelling through a vacuum to the speed of light in the solution being tested. The refractive index varies with salinity so any changes in salt concentration would be detected.

### *3.1.2.3 Molecular absorption spectroscopy analysis*

Determination of dissolved iron in brine samples collected after the experiments was performed following the 1-10 phenanthroline spectrophotometric method. The method is based on the Beer's law, a very simple relationship by which the absorbance of a solution is linear with the concentration of the absorbing substance, if the wavelength, the pathlength and other experimental conditions are kept constant (Skoog et al., 2000, Harris, 2003). 1-10 phenanthroline is a tryciclic nitrogen heterocyclic compound that reacts with iron to form a very stable and deeply coloured red complex. The intensity of the colour is independent of pH in the range 2 to 9.

A computer controlled UV-VIS spectrophotometer from Shimadzu with an accuracy of ± 1 nm was employed for the measurements, where a standard cuvette is filled with the sample. Samples were prepared for analysis in 100 ml volumetric flasks. To each flask reactives were pipetted in the following order: 0.8 ml of brine solution (it may vary depending on the dilution factor); 1 mL of hydroxylamine hydrochloride solution (reducing agent); 10 mL of the 1-10 phenanthroline solution (complexing agent) and 8 mL of sodium acetate solution (buffer). Then, each solution is diluted to 100 mL, mix thoroughly and let stand for 10 min to fully develop the colour. This method proofed to be an excellent and sensitive one (in the order of ppm) for determining iron concentration in aqueous solution.

#### *3.1.2.4 Ion chromatography analysis*

A Dionex (model DX500) Ion Chromatograph (IC) (Dionex, 2009) was used to quantify sulfate, sulfite and thiosulfate concentration in brine samples collected over the course of the long-term experiment conducted at the USGS. The IC is comprised of a chromatographic column (IonPac AS9-HC, 4x250 mm) for separation and a conductivity cell for detection, and allows the separation of ions and polar molecules based on their charge properties (Settle, 1997, Günzler and Williams, 2001). Samples were diluted to 1:500 with distilled water so the ions concentration would fall within the range of the calibration curves previously obtained for each of the anions.

### 3.1.2.5 Total inorganic carbon analysis

The concentration of dissolved $CO_2$ in brine samples collected during the long-term experiment was measured with a UIC, Inc. Model 5014 $CO_2$ Coulometer (UIC, 2009). This total inorganic carbon analyser provides a highly accurate (in the range of 0.01 μg to 100 mg) determination of carbon in any $CO_2$-containing gas stream. A relative standard deviation of better than 0.20% is common for samples containing 1000 μg to 3000 μg of carbon. For smaller carbon concentrations, an absolute deviation of ± 1 μgC is typical (UIC, 2007b, UIC, 2009). This particular coulometer consists of two modules: the electrochemical coulometric cell and the UIC, Inc. CM5130 acidification module.

The acidification module is capable of analysing either solid or liquid samples and these are acidified in a heated reaction vessel to evolve forms of inorganic carbon (including dissolved $CO_2$, carbonate ion, bicarbonate ion and carbonic acid) as carbon dioxide. A $CO_2$-free carrier gas sweeps the reaction products through a scrubbing system, which removes $H_2S$, $SO_x$ and other gases that may result from the acidification of some materials, and into the $CO_2$ coulometer for detection (UIC, 2007a). As a $CO_2$ gas stream passes into the coulometric cell, the $CO_2$ is quantitatively absorbed, reacting with a monoethanolamine

($HOCH_2CH_2NH_2$) solution to form a titratable acid, which causes the color indicator to fade. Photodetection monitors the change in color of the solution as percent transmittance (%T) and a titration current is automatically activated. The current (in coulombs) used to bring the solution back to its original acidity level is then converted into a digital readout of micrograms of carbon – i.e., each electron used corresponds to one $CO_2$ molecule within the gas stream, which in turn corresponds to one atom of carbon in the original sample of interest. A $CaCO_3$ standard was run in addition to the samples of interest to verify the results generated by the instrument. The instrument is based on the principles of Faraday's Law, hence it requires no calibration (UIC, 2007b).

## 3.2 Thermodynamic/Modeling studies

Thermodynamic simulations were computed to predict how a system containing either an iron oxyhydroxide, goethite (FeOOH), or an iron oxide, hematite ($Fe_2O_3$), $CO_2$-$SO_2$ gas mixtures and 1.0m NaCl, 0.5m NaOH brine, behaves at equilibrium for a range of temperature, pressure, gas concentration, brine composition and solids concentration conditions. Validation of the obtained theoretical results would be further performed experimentally.

The computer program CHILLER was the modeling tool used for calculating equilibria in aqueous systems. For a given temperature, pressure and total composition of a chemical system, CHILLER computes multi-component heterogeneous chemical equilibria among solids, gases and an aqueous phase (Reed and Spycher, 2006). The mineral is first equilibrated with the fluids at the stated conditions and then, $SO_2$ is incrementally added to the system so the program recalculates equilibrium after each of these steps.

## 3.3 Study of high pressure-high temperature carbonation reactions: short-term experiments

A whole set of experiments at different temperature, pressure, varying amounts of $SO_2$ in the gas phase, particle size of solid material, solids concentration, brine composition and reaction time were run for hematite and goethite in a high pressure-high temperature apparatus designed and assembled at the University of Nottingham.

### 3.3.1 Experimental apparatus.

Short-term ($\leq$ 264 h) carbonation experiments were conducted in a 600mL autoclave (Hastelloy C-276) manufactured by Parr Instrument Company. A schematic and photo of the employed system are depicted in Figure 3-1 and Figure 3-2 respectively, and the design and optimisation of the experimental setup as well as its components is discussed in Chapter 4.

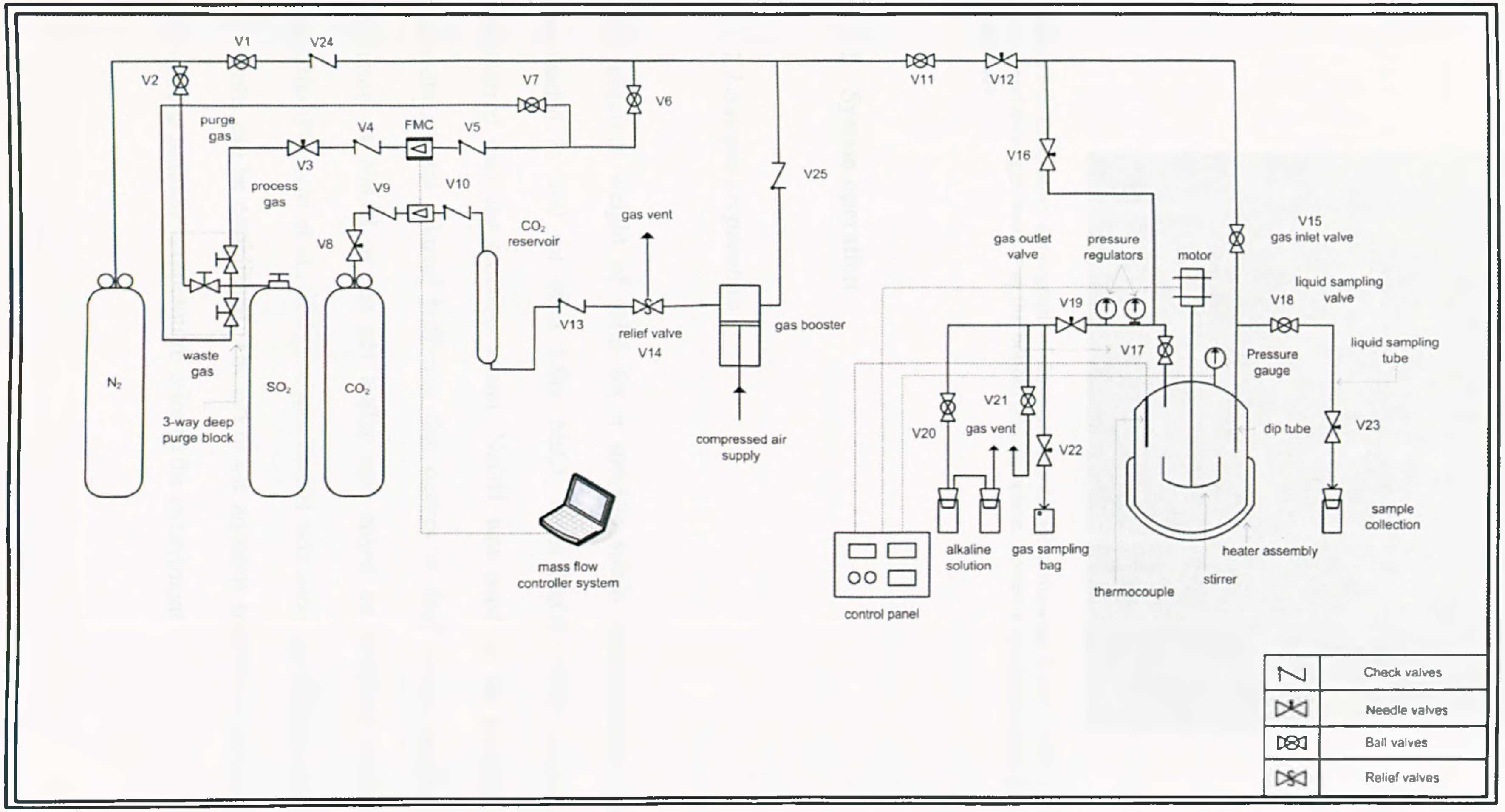

Figure 3-1. Schematic of the high pressure-high temperature system designed for carbonation experiments.

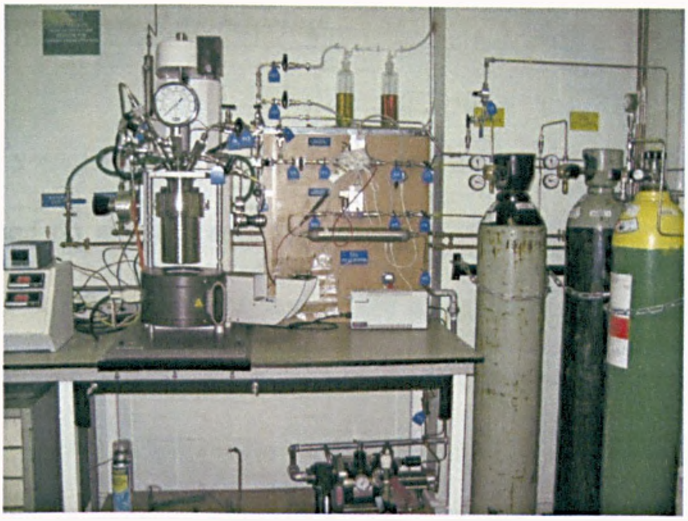

Figure 3-2. Laboratory photograph of the experimental setup showing the gas cylinders on the right hand-side, gas booster at the bottom and autoclave, heater and control panel on the left hand-side.

### 3.3.2 System operation

#### *3.3.2.1 Sample preparation*

The required weight of solid for a specific solids concentration value is suspended in 400 ml of a 1.0m NaCl, 0.5m NaOH brine solution and transferred into the reaction vessel. NaOH was used in the experiment to simulate natural mineral buffering that occurs in deep saline aquifers. The selection of NaOH as the pH buffer was based on previous studies with hematite (Palandri et al., 2005), where NaOH was used, so further comparison of results can be established. The pH of the aqueous solution is measured and recorded at ambient temperature prior to the experiment.

### *3.3.2.2 Reactor setup and monitoring*

The reaction vessel is place in the cradle and slide up to be assembled. The stirrer is turned on and the aqueous solution-rock mixture is agitated at 750 rpm from this point on until the end of the experiment. The reactor is purged with $N_2$ for 5 min and a predetermined amount of $SO_2$ is then admitted into the system via the digital $SO_2$ mass flow controller at a rate of 1.5ln/min[3]. Next and to avoid any likely condensation of $SO_2$ gas remaining in the inlet line of the reactor, this latter one is purged with $N_2$ for approximately 5 min. A predetermined amount of $CO_2$ is then pumped into the autoclave via the digital $CO_2$ mass flow controller and the compressed-air driven gas booster. The injection rate is 10 ln/min. The heating mantle is secured to the vessel and the heating process takes place until the desired temperature is reached in the system. At that point, pressure will reach a stable value and it is then when the reaction is assumed to start.

Evolution of the reactor pressure in a representative experiment can be seen in Figure 3-3, where segment 1 represents the purging of the system with $N_2$ for ~ 5-6 min (inner graph) followed by the pressurization and heating processes; Segment 2 represents the reaction time considered for the experiment, and segment 3 represents the depressurization process at the end of the experiment.

---

[3] litres per min at normal conditions of temperature (0°C) and pressure (1bar).

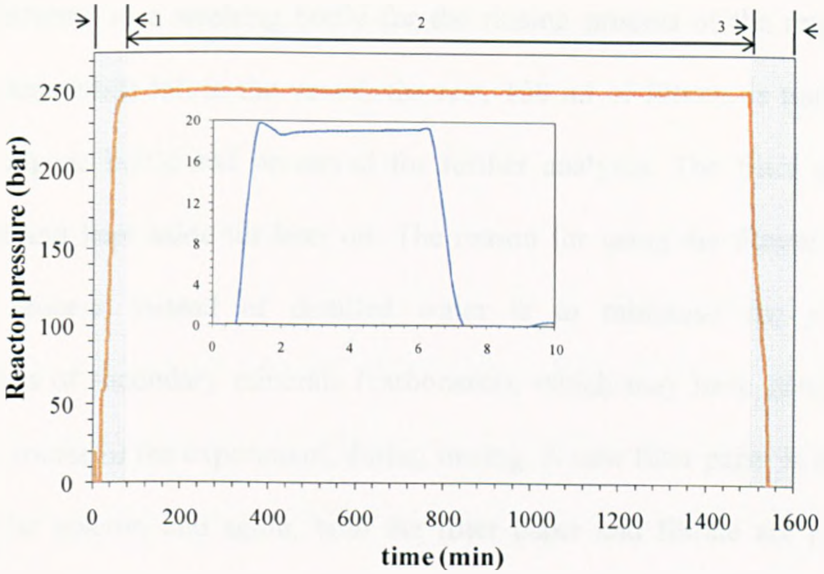

Figure 3-3. Evolution of reactor pressure in a representative experiment.

Reaction temperature and pressure are monitored and recorded every 20 s with two different softwares, Picolog Player and Calgrafix respectively, and the safety mechanisms put in place allow the researcher to leave the system unattended in the case of a long-term experiment (days or months).

### *3.3.2.3 Experiment shutdown*

At the completion of each test, the agitation ceases and the slurry is cooled down to a temperature of ~35°C via the cooling coil. The remaining gases in the reactor are vented through the depressurization system and bubbled through an alkaline solution; the slurry is then removed from the reaction vessel. The pH of this slurry is measured and recorded, again at ambient temperature, and the solution is vacuum-filtered to separate the solids from the aqueous solution. A glass microfibre Whatman filter paper with a pore size of 0.7 μm is used for the filtration process. After filtration, part of the filtrate (250 ml) is collected and transferred to a washing bottle for the rinsing process of the reactor, to recover any solids left in the vessel; the rest, 150 ml of filtrate, is transferred into a nalgene bottle and preserved for further analyses. The filter paper is removed and kept aside till later on. The reason for using the filtrate for the rinsing process instead of distilled water is to minimise the potential dissolution of secondary minerals (carbonates), which may have precipitated over the course of the experiment, during rinsing. A new filter paper is used for rinsing the reactor, and again, both the filter paper and filtrate are properly collected and saved for analyses. The iron in solution is measured immediately by taking an aliquot of 0.8 ml from each of the filtrates and following an established procedure for iron determination with 1.10-phenanthroline and molecular absorption spectroscopy. The two collected filter papers are dried overnight in an oven at 110°C, and then solids are collected, weighed and saved for XRD, TGA and XPS analyses.

## 3.4 Study of a high pressure-high temperature long-term carbonation reaction in a flexible gold-titanium reaction cell

Iron oxyhydroxide, goethite ($\alpha$-FeOOH), was reacted with a 1.0m NaCl, 0.5m NaOH solution and a $CO_2/SO_2$ gas mixture in a 24 day experiment at a temperature of 150°C and pressure of 300 bar at the US Geological Survey (USGS) in a flexible Au-Ti reaction cell with ~ 181 ml total volume. The purpose of this experiment was to learn the technology and become familiar with the operation of these well-known flexible reaction cells, used mostly in hydrothermal experiments, and to compare new results to those previously published for the same experimental setup.

### 3.4.1 Experimental apparatus

A full description of the flexible gold-titanium reaction cell is discussed in Chapter 4 but a schematic and photo of the experimental apparatus used to carry out the high-pressure-high temperature experiment at USGS can be seen in Figure 3-4 below.

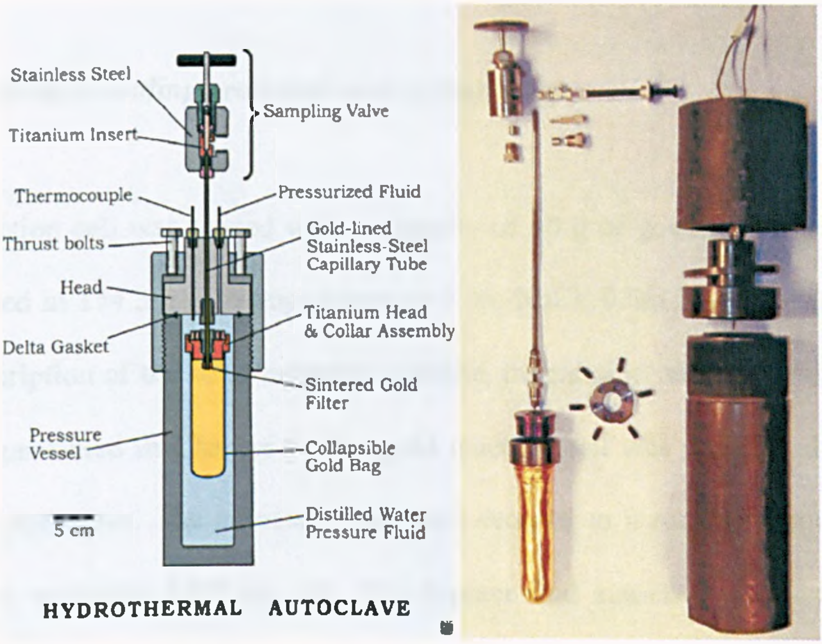

Figure 3-4. Schematic and photo of the gold-titanium flexible reaction-cell system used at USGS.

### 3.4.2 System operation

#### *3.4.2.1 Pre-loading procedure*

Prior to loading fluid and solid reactants into the flexible reaction cell for the experiment, the cell must be assembled and leak tested by pressuring with $N_2$ or Ar up to ~15 psi. One important aspect in determining the amount of reactants to add to the cell is to take into account the thermal expansion and volume increase from ambient conditions to experimental conditions of non-compressible fluids.

#### *3.4.2.2 Sample loading procedure and system setup*

The reaction cell was loaded with a quantity of 10 g of goethite (75-150 μm) suspended in 154.5 g of nitrogen-purged 1.0m NaCl, 0.5m NaOH solution. A full description of the solid material, goethite, preparation and characterisation will be presented in Chapter 5. The gold reaction cell was sealed and loaded into the autoclave. The autoclave was then secured to a rocking furnace that oscillates vertically 180° on axis. The furnace and autoclave containing the reaction cell is rotated 1) to maintain temperature stability and homogeneity and 2) to ensure that the reactants are well mixed and thus enhance reaction kinetics. The pressure vessel was initially pressurized slowly to 200 bar by adding water to its annular space via a compressed air-driven hydraulic pump, causing the reaction cell to collapse gradually. The sampling valve is left open during this operation to allow displacement of the remaining air or purge gas from the headspace of the reaction cell into a gas-tight syringe. The sampling valve is closed at the first indication of fluid entering the syringe. 14 g of $CO_2$ were then added through the sampling valve of the reaction cell with a syringe pump (ISCO Corp.) to supersaturation, followed by the addition of 1 ml of distilled water to ensure that all $CO_2$ in the line entered the cell. The assemblage was heated to 150°C and the pressure adjusted to 300 bar. Next, $SO_2$ was added to the experiment, again through the sampling valve of the reaction cell, via syringe pump and further addition of 1 ml of distilled water also followed to force the gas left behind in the line to enter the reaction cell. However, the amount of $SO_2$ gas is likely somewhat less than the intended amount of 3 g due to an equipment failure. Temperature was maintained by a proportional controller and measured with a type K thermocouple calibrated to a platinum resistance temperature detector (RTD). Pressure was measured with analogue gauges and digital transducers (Heise).

#### *3.4.2.3 Sampling of fluids*

Aqueous samples were withdrawn periodically during the course of the experiment for chemical analyses to determine changes in fluid composition over time. During sampling, the sampling-valve was opened gradually allowing internally filtered clear fluid to pass from the reaction cell through the chemically inert sampling-valve into an appropriate sample container, either a plastic or gas-tight glass syringe. The pressure in the pressure vessel is maintained via the hydraulic pump that adds enough fluid to accommodate the decreasing volume of the flexible reaction-cell. Sampling and pressurizing of the pressure vessel can be performed simultaneously so sampling is both, an isothermal and isobaric process. The employed analytical scheme involved withdrawal of three separate fluid aliquots from the reaction cell at every sample interval, with an average of ~ 3 g of withdrawn fluid per sample. The first aliquot, around 0.2-1.0 g, is discarded since its only purpose was to flush the high-pressure sample tube. The second one, approximately 0.5 g, was withdrawn into ~ 1 ml of 17% NaOH solution and taken to a total-carbon analyzer to measure the total dissolved $CO_2$. The third one, approximately 2 g, is for pH, salinity and analyses of major cations and anions. Fluid pH and salinity are measured immediately with a few drops from the aliquot. The rest of it is filtered (0.2 µm) and preserved for batch analyses of sulfate, sulfite and thiosulfate by ion chromatography as well as determination of iron by a spectrophotometric method.

The analytical scheme used for sampling and analysing the aqueous samples withdrawn over the course of the experiment is shown in Table 3-1.

Table 3-1. Summary of the analytical scheme used for sampling and analysing aqueous samples.

| *Sample size* | *Procedure for sampling* | *Results obtained* |
|---|---|---|
| *0.2-1.0 g in 20-mL plastic syringe* | Discard | Cleanout exit tube |
| *0.5 g in 5-ml gas-tight glass syringe* | Extract $CO_2$ with NaOH. Aliquot injected in a total-carbon analyzer. | Total dissolved $CO_2$ |
| *2 g in 20-mL plastic syringe* | A couple of drops are used to determine the refraction index (RI). | Fluid salinity |
| | pH measured by pH-meter. | pH (25°C) |
| | 0.1 mL processed with a spectrophotometric method. | $Fe^{2+}$, total Fe and $Fe^{3+}$ in solution |
| | 0.01 mL of sample diluted with distilled water and injected into an ion chromatograph (Dionex model DX500). | $SO_4^{2-}$, $SO_3^{2-}$, $S_2O_3^{2-}$ |
| | Save residual fluid in a vial. | Further analyses if needed |

### *3.4.2.4 Experiment shutdown*

At the end of the experiment, pressure was lowered to 200 bar and the setpoint on the temperature controller was lowered to 80°C in order to cool down the reactor. A compressed air stream was directed within the annular space between the reactor and the furnace to help cooling while the pressure was kept constant at 200 bar. When temperature reached 80°C, the reactor was vented again and taken under the water tap for quenching and venting of the remaining gas inside. At T ~ 30°C and ambient pressure, the system was taken apart and the solution was filtered with a Buchner funnel and Whatman paper filters (fine) to separate and recover the solids. The filtrate and filter paper were collected and the different aliquots explained in the previous section were taken from the filtrate. Next, the reaction cell was rinsed with distilled water that was also filtered and collected until all the solids were removed from the reaction cell. A 4ml aliquot was collected from the new filtrate to measure the iron in solution due to quench effects related retrograde dissolution; the remaining filtrate was also preserved for later analyses. The gold reaction cell was then cleaned, by washing it with a heated and diluted nitric acid solution. Both filter papers were dried overnight in an oven at 110°C, and then solids were collected from the filter papers, weighed and saved for analyses.

## 3.5 References

Brunauer, S., Deming, L. S., Deming, W. E. & Teller, E. (1940) On a theory of the van der Waal adsorption of gases. *Journal of the American Chemical Society,* 62, 1723-1732.

Brunauer, S., Teller, E. & Emmett, P. H. (1938) Adsorption of gases multimolecular layers. *Journal of the American Chemical Society,* 60, 309-319.

British Standard, 1999. BS ISO 13320-1:1999. Particle size analysis - Laser diffraction methods.

Dionex (2009) Dionex corporation. Available from: <http://www.dionex.com> (accessed 4 December 2009).

Gregg, S. J. & Sing, K. S. W. (1982) *Adsorption, Surface Area and Porosity,* London, Academic Press Inc. Ltd.

Günzler, H. & Williams, A. (Eds.) (2001) *Handbook of analytical techniques,* Weinheim, Germany, Wiley-VCH.

Harris, D. C. (2003) *Quantitative chemical analysis,* New York, W.H. Freeman.

MEE (2001) *Handbook of analytical methods for materials*, Materials Evaluation and Engineering (MEE), Inc.

NCIMP (2009) The National Centre for Microwave Industrial Processing. Available from: <http://www.nottingham.ac.uk/ncimp/> (accessed 25 November 2009).

Palandri, J. L., Rosenbauer, R. J. & Kharaka, Y. K. (2005) Ferric iron in sediments as a novel $CO_2$ mineral trap:$CO_2$-$SO_2$ reaction with hematite. *Applied Geochemistry,* 20, 2038-2048.

Reed, M. H. & Spycher, N. F. (2006). Users guide for CHILLER: A program for computing water-rock reactions, boiling, mixing and other reaction processes in aqueous-mineral-gas systems and minplot guide (Third Edition), University of Oregon, Eugene.

Settle, F. A. (Ed.) (1997) *Handbook of instrumental techniques for analytical chemistry,* New Jersey, Prentice-Hall, Inc.

Shriver, D. F. & Atkins, P. W. (1999) *Inorganic chemistry,* New York, W.H. Freeman and Co.

Skoog, D. A., West, D. M., Holler, F. J. & Crouch, S. R. (2000) *Analytical chemistry: an introduction,* Philadelphia, Saunders College Pub.

Speyer, R. F. (1994) *Thermal analysis of materials,* New York, Marcel Dekker, INC.

UIC (2007a) Instruction manual - CM5130 Acidification Module. UIC, Inc.

UIC (2007b) Operation manual - CM5014 $CO_2$ Coulometer. UIC, Inc.

UIC (2009) Carbon dioxide coulometer. Available from: <http://www.uicinc.com/CANs/CarbAppNote_01.pdf> (accessed 4 December 2009).

VWR (2009) VWR products. Available from: (accessed 4 December 2009).

Ward's (2009) Available from: <http://wardsci.com/> (accessed 25 November 2009).

Warren, B. E. (1990) *X-ray Diffraction,* New York, Dover.

# CHAPTER 4

# DEVELOPMENT OF A HIGH PRESSURE-HIGH TEMPERATURE SYSTEM FOR GAS-ROCK-BRINE REACTIONS WITH $CO_2$-$SO_2$ MIXTURES

# 4. Development of a high pressure-high temperature system for gas-rock-brine reactions with $CO_2$-$SO_2$ mixtures

Experimental investigation of mineral trapping reactions requires facilities that must operate under extreme conditions of temperature and pressure in a routine and reliable way. Each project has different objectives and tolerances and therefore, the appropriate equipment needs to be designed to enable the experimentalist to accurately assess the response of a particular chemical system to a range of physical and chemical variables.

High pressure-high temperature reactors have been used in the past for mineral carbonation studies (Druckenmiller et al., 2006, Huijgen et al., 2006, Alexander et al., 2007) but very scarce experimental research can be found in the literature concerning mineral trapping reactions. Most of the latter ones have been carried out in rocking autoclaves for hydrothermal experiments (Kaszuba et al., 2003, Rosenbauer and Koksalan, 2003, Palandri et al., 2005, Rosenbauer et al., 2005) and in continuous stirred tank reactors (CSTR) (Sass et al., 2001, Bruant Jr. et al., 2002, Soong et al., 2004); the flexible reaction-cell system (rocking autoclave) has been used in this research project, so a description of the system and its background would be described in the first section of this chapter.

The high cost of a flexible reaction cell-system as well as the nature of the experiments to be conducted in this research project, i.e. mostly short-term (24 h) tests, required the development of an appropriate apparatus for the experimentation. The flexible reaction cell-system, although it is a widely used, flexible, optimised and well-known set-up, is not convenient for short-term (24 h) experiments due to the long time (~12 h) required for its assemblage and reaction conditions stabilisation. Therefore, in this work a novel high pressure-high temperature system had to be developed in order to carry out mainly short-term (24 h) experimental tests but also experiments for longer reaction times than 24 h.

A second section will describe the novel high pressure-high temperature system designed and optimised in this project for the experimental studies. The main challenge of the design was the operation of the system with a mixture of gases ($CO_2$ and $SO_2$) instead of a single gas ($CO_2$). Very little has been done before on experimental co-injection of several gases for underground $CO_2$ sequestration studies (Jacquemet et al., 2005, Palandri et al., 2005, Mandalaparty et al., 2009). The challenge and complexity of integrating the co-injection of various gases in the experimental set-up is described in this chapter as well as the system optimisation.

## 4.1. The flexible reaction-cell system

Flexible reaction cells have been used with hydrothermal experimental equipment to study high-temperature rock-water interactions (Rosenbauer et al., 1993). This apparatus, which was initially described by Dickson and co-workers (Dickson et al., 1963), is uniquely designed for serial on-line sampling of complex liquid-vapor-solid systems under any conditions of temperature and pressure up to 500°C and 600 bars pressure, without disturbing temperature or pressure. This eliminates time-delays and other problems associated with quenching. The equipment employs a collapsible reaction-cell of Teflon, titanium, or gold, housed within a pressure vessel and rotating furnace, with separate valves for sample and pressure fluids. As samples are extracted via a gas-tight syringe, the cell contracts and its decreased volume is offset by an equivalent volume of pressure fluid (distilled water) that is automatically pumped into the surrounding jacket. Total cell-volume is typically about 240 ml, of which about 120 ml can be extracted. Early pressure vessels were constructed of stainless steel with Bridgeman seals and had ~600 ml volume (Dickson et al., 1963). Later pressure vessels were composed of a chrome-vanadium alloy with a volume of ~800 ml and utilized delta gaskets for sealing (Seyfried et al., 1987). The delta gasket closure utilizes the slight change in angle produced as a consequence of the pressure rise in the pressure vessel to force the "delta" ring against its seat, ensuring a self-energized closure.

The reaction cell contains the fluid and solid reactants for an experiment and is isolated from the pressure fluid contained within the annular space of the autoclave. A schematic illustration of the hydrothermal solution equipment and the flexible reaction-cell system is shown in Figure 4-1. Internally filtered aqueous samples can be withdrawn from the reaction cell during the course of the experiment. Since the volume of sample removed is displaced by the water (pressure fluid) surrounding the cell, sampling is accomplished at constant pressure and temperature.

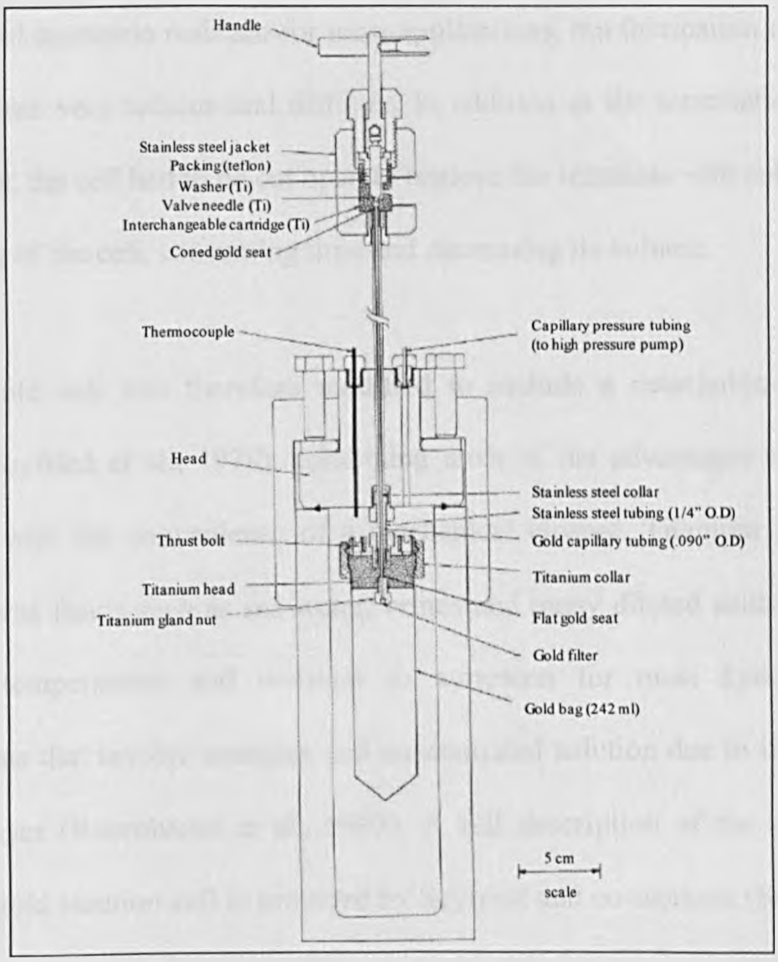

Figure 4-1. Schematic of the hydrothermal solution equipment and flexible reaction-cell system (Seyfried et al., 1987).

The suitability of a reaction cell for hydrothermal experiments is a function of its chemical inertness, physical integrity and deformability. Historically, Teflon, gold, titanium, and iridium in their pure form and in combination have been used in the design and construction of flexible reaction-cells. The first cells were composed of Teflon and useful for low temperature applications but were limited to 285°C were increasingly permeable to dissolved molecular species, such as $H_2O$, and dissolved silica and gases, so they can migrate between the pressure vessel and the reaction cell (Seyfried et al., 1979, Seyfried et al., 1987). All gold- reaction cells were welded to circumvent the problems associated with the Teflon. Gold is highly deformable, impermeable to gases and corrosion resistant for most applications, but fabrication of the all gold-cell was very tedious and difficult. In addition at the termination of an experiment, the cell had to be cut open to retrieve the reactants with subsequent re-welding of the cell, consuming time and decreasing its volume.

The all gold cell was therefore modified to include a detachable titanium closure (Seyfried et al., 1979), combining most of the advantages of the all gold cell with the convenience of a mechanical closure. Titanium is highly inert to most fluids such as sea water, brines and many diluted acids, even at elevated temperatures and resistant to corrosion for most hydrothermal applications that involve complex and concentrated solution due to its passive surface layer (Rosenbauer et al., 1993). A full description of the combined titanium-gold reaction cell is provided by Seyfried and co-workers (Seyfried et al., 1979, Seyfried et al., 1987). The major advantage of this system is the easy and quick removal of the titanium top from the gold body at the end of the experiment. The gold body for this reaction cell, with a hemispherical bottom, is commercially available from several suppliers (Seyfried et al., 1987). The titanium closure consists of three basic parts (Figure 4-2): the head or cap, the collar and the retainer plate. The 6 thrust bolts threaded into the retainer plate establishes the pressure seal between the titanium head and the gold-titanium collar by forcing the titanium head against the collar and into the top of the gold cell. A further variation of the system was the all titanium cell, in an effort to ameliorate amalgamation problems of Cu and possibly Pb with Au in extreme reducing environments. However, the utility of this all titanium cell is limited due to ductility constraints and contamination potential under some experimental conditions and with repeated use (Rosenbauer et al., 1993). A further evolution of the gold cell includes a detachable gold cap with iridium seal rings.

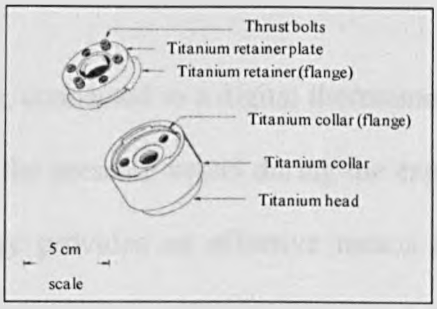

Figure 4-2. Titanium closure for gold-titanium reaction cell (Seyfried et al., 1979).

After the reaction cell has been loaded with the experimental reactants and secured within the autoclave, the system is pressurized by an automatic, compressed air-driven hydraulic diaphragm pump. Slight decreases in vessel pressure, for example when sampling the reaction-cell, automatically triggers the hydraulic pump to provide water to the vessel via high-pressure, capillary tubing, thereby maintaining a constant pressure. Even with manual hydraulic pumps, pressure can be maintained to within 5 bars of the desired pressure (Seyfried et al., 1987). Distilled water is used as the medium for the pressure fluid.

Two pressure gauges are utilised to measure and monitor pressure. One gauge is attached directly to a rotating furnace containing the pressure vessel and reaction cell, and is used to continuously monitor the pressure during the course of the experiment. It is equipped with dual contacts that can be set to maximum and minimum pressures as a safety mechanism to shut down the experiment if the electronics fail. A second highly sensitive Heise gauge monitors the pressure of the pressure fluid during sampling (Seyfried et al., 1987).

A type K thermocouple, connected to a digital thermometer is used to measure the temperature within the pressure vessel during the experiment. This flexible reaction cell technology provides an effective means for carrying out high pressure-high temperature rock-gas-fluid interactions because it permits a contamination-free operation over a wide range of independently controlled pressure and temperature operating conditions. Furthermore, the system is applicable to studies where the chemistry of the aqueous phase needs to be monitored over time.

## 4.2. Development of a high pressure – high temperature experimental system for gas-brine-rock reactions with $CO_2$-$SO_2$ mixtures

Ideally, the experimental setup needed for the experiments should be inert, and should in no way participate in the reaction under investigation; furthermore, it should be convenient to operate and allow the researcher to monitor the progress of the reaction, and all of this without compromising safety (Seyfried et al., 1979).

Continuous stirred tank reactors (CSTR) had been used in the past for most mineral carbonation studies (Sass et al., 2001, Bruant Jr. et al., 2002, Soong et al., 2003, Druckenmiller et al., 2006, Alexander et al., 2007). Therefore, the design of this system aimed the use of such reactors under a range of pressures and temperatures representative of underground geological conditions and with a mixture of feed gases. A whole system of valves, pipes and fittings would also be needed to mimic gas ($CO_2$-$SO_2$ mixture)-water-rock underground reactions. A basic schematic of the original designed experimental set-up is shown in Figure 4-3. All the single elements in the diagram are explained in detail below.

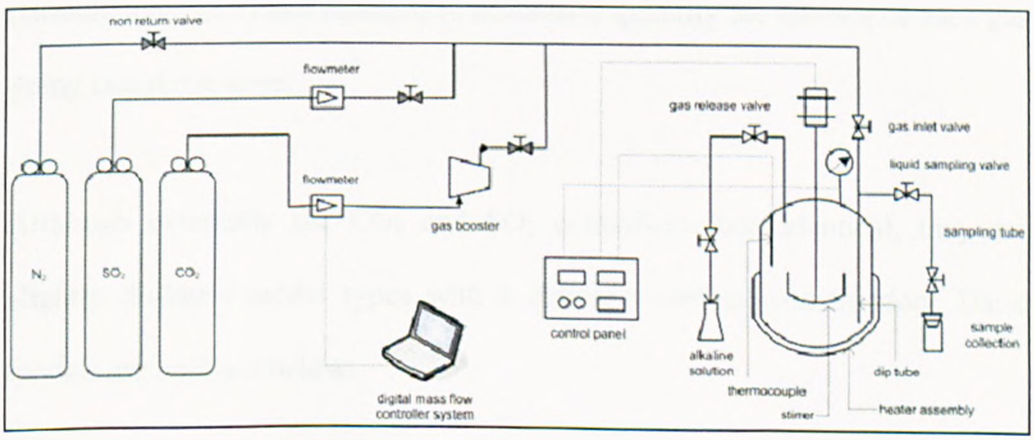

Figure 4-3. Schematic of the original designed experimental set-up.

### 4.2.1. Gas cylinders

Three gases ($CO_2$, $SO_2$ and $N_2$) are delivered into the system from three different cylinders supplied by Air Products. $CO_2$ and $SO_2$ are provided as the reactive gases in the experiments. They come out from two different cylinders, each of them with a technical grade quality (~ 99.5% purity). Maximum delivery pressure from the $CO_2$ cylinder is around 30 bar, whereas from the $SO_2$ cylinder is ~ 2.1 bar. $N_2$ (technical grade) is provided to purge the system and not as a reactive gas so it is not necessary to control its flow.

### 4.2.2. Digital mass flow controllers (MFC)

Since the $CO_2/SO_2$ ratio is one of the key variables to be investigated, two digital mass flow controllers (MFC) were supplied by Bronkhorst Ltd. (Bronkhorst, 2009) and installed to accurately quantify the amount of each gas going into the reactor.

Although externally the $CO_2$ and $SO_2$ controllers look identical, they are slightly different model types with a different internal construction. These models are outlined below:

1/ Model F-201CV, range from 1 to 50 mln*/min $CO_2$, with an accuracy of ±0.8% of reading plus ±0.2% of full-scale or better.

---

* The flowrate given by the MFC is at normal conditions (P = 1 bar and T = 0°C).

2/ Model F-201 DV, range from 1 to 50 mln*/min $SO_2$, with an accuracy of ±1% of full-scale or better.

As both instruments have a percentage of full-scale component in their expected accuracy, the error does increase the lower down the range the instrument operates. The F-201CV series ($CO_2$ one) is much more accurate working at the bottom of its range than the F-201 DV one; however, the F-201DV was selected for the $SO_2$ application based on the gas type, i.e, it was the recommended one for use on $SO_2$ based on operational experience.

For both models the repeatability is better than ±0.2% so the experimental error should be within ±0.2% given the same operating conditions (gas type, pressure, temperatures, etc) (Davison, 2006).

According to the experimental procedure, a predetermined amount of $SO_2$ is first charged into the reactor and followed by injection of a predetermined amount of $CO_2$ to achieve the desired operating pressure.

### 4.2.3. Gas booster

Pressure is supplied to the system by means of $CO_2$ pressurization with a compressed air-driven gas booster. The booster was selected taking into account the maximum desirable pressure in the system (300 bar) as well as the delivery pressure from the $CO_2$ cylinder (30 bar). An air driven gas booster was supplied by Haskel International, Inc. (Haskel, 2009). Booster dimensions are shown in Figure 4-4.

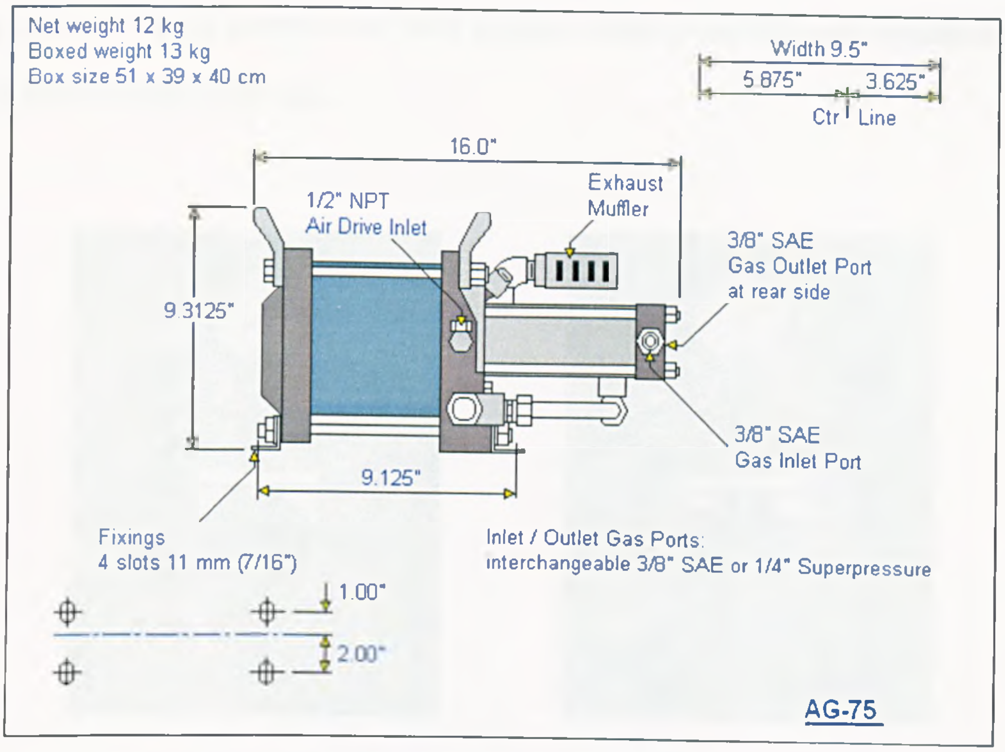

Figure 4-4. Gas booster dimensions (Haskel, 2009).

The selected system is specific for the $CO_2$ flow and any operation with $SO_2$ would ruin the equipment (due to its corrosive nature). The reason for choosing a booster for the standalone $CO_2$ flow was the higher cost for a $SO_2$ operating one.

### 4.2.4. Autoclave

The selected reactor was a 600 mL Parr reactor supplied by Scientific and Medical Products Ltd (S&M, 2009). Figure 4-5 shows a photo of the reactor. It is a bench stand stirred one, manufactured in Alloy C276 and fitted with high torque sealed magnetic stirrer drive unit in Alloy C276 and 1/8 hp variable speed electric motor. It is supplied with a 3-term P.I.D. temperature controller and motor speed control unit, with pressure display module and tachometer display module (230 volt).

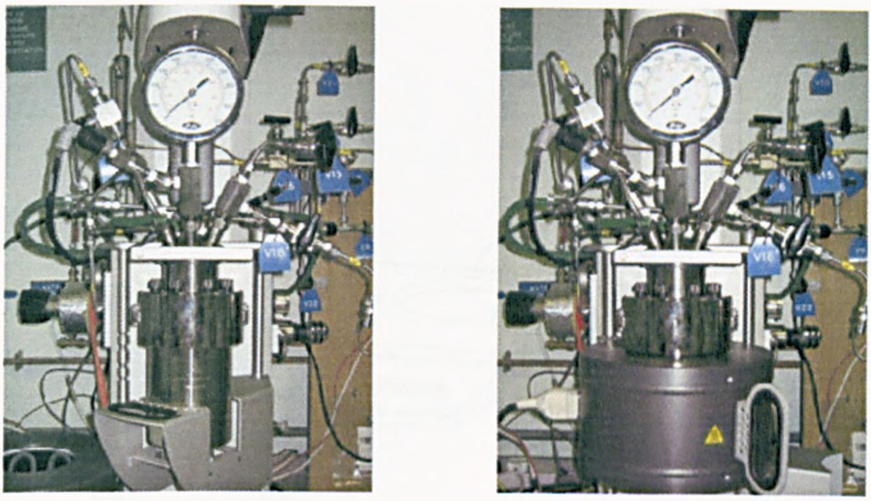

Figure 4-5. Front view of reactor with cradle (left) and heating mantle (right).

The reactor is mounted on a bench stand unit with attached stirrer drive motor, heater and a cradle system to aid in reactor assemblage. A schematic of the bench stand system is shown in Figure 4-6. It has a fixed-head design and the head is fitted with: pressure gauge (0-10000 psi), pressure transducer, safety rupture disc (5000 psi), gas outlet valve, gas inlet valve and liquid sampling valve via internal dip tube, thermo well with control thermocouple, gas entrainment stirrer and serpentine cooling coil. Figure 4-7 shows a detailed schematic of the reactor's head with all the attached fittings.

Generally, undiluted (dry) $SO_2$ is not corrosive to ordinary metals; however, when small amounts of moisture are present, sulphur dioxide will attack most metals. Therefore, stainless steel would be corroded under operations with $SO_2$. To avoid that, the reactor material had to be carefully selected so the alloy

C276, a nickel chromium-molybdenum alloy, was chosen to prevent from corrosion. All valves and adapters on the head, pressure gage internals and pressure transducer are built in 316 SS (Stainless Steel) since they are not in contact with the corrosive solution.

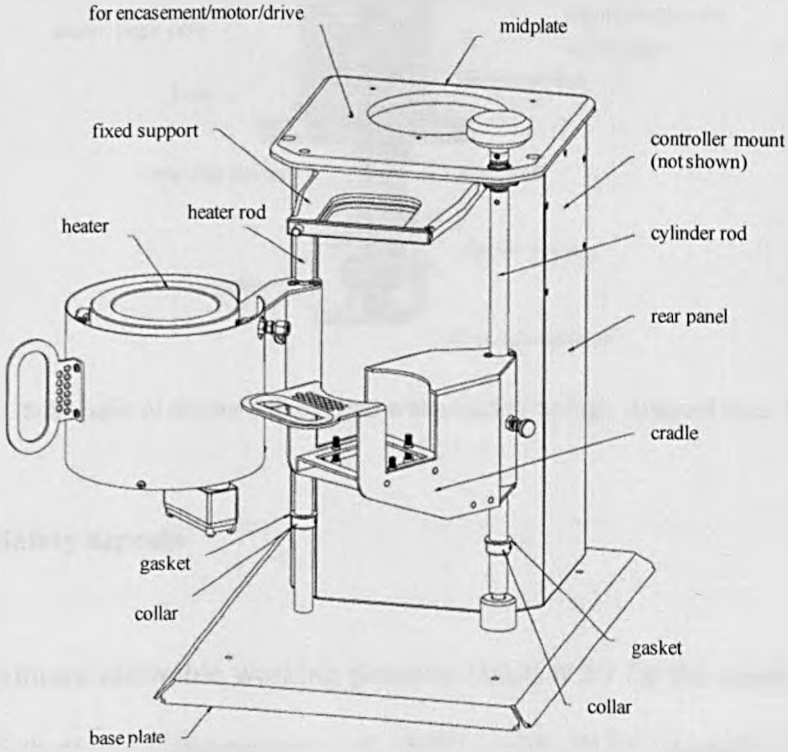

Figure 4-6. Schematic of bench-stand system on which the reactor is mounted. Adapted from (Parr, 2009).

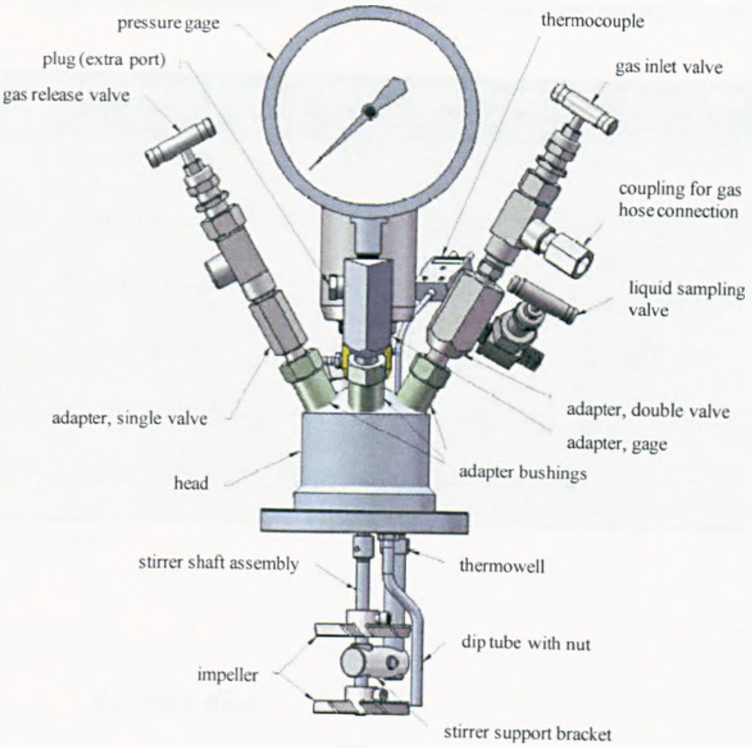

Figure 4-7. Schematic of reactor's fixed head with attached fittings. Adapted from (Parr, 2009).

### 4.2.5. Safety aspects

The maximum allowable working pressure (M.A.W.P) for the reactor is 5000 psi (345 bar) at a temperature of 350°C, with PTFE (tetrafluoroethylene polymer) flat gasket, i.e., teflon®. PTFE teflon® gaskets are desirable because they can be used multiple times. For the majority of the experiments pressure did not exceed 250 bar. All fittings and pipes used were rated for values of pressure and temperature as high as required for the system operation. Temperature and pressure rating for the main fittings and piping system of the experimental set-up can be seen below in Table 4-1.

Table 4-1. Temperature and pressure rating for main fittings and piping system (Swagelok, 2009).

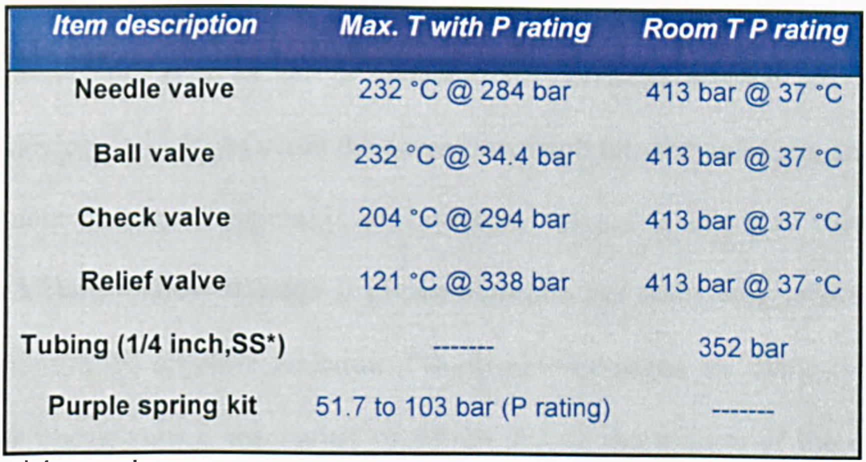

| Item description | Max. T with P rating | Room T P rating |
|---|---|---|
| Needle valve | 232 °C @ 284 bar | 413 bar @ 37 °C |
| Ball valve | 232 °C @ 34.4 bar | 413 bar @ 37 °C |
| Check valve | 204 °C @ 294 bar | 413 bar @ 37 °C |
| Relief valve | 121 °C @ 338 bar | 413 bar @ 37 °C |
| Tubing (1/4 inch,SS*) | ------- | 352 bar |
| Purple spring kit | 51.7 to 103 bar (P rating) | ------- |

*stainless steel

### 4.2.5.1. *Rupture disc*

A safety rupture disc was attached to the head of the pressure vessel to protect the equipment and the operator from unexpected overpressure. The disc is intended to rupture and release the pressure before it reaches a dangerous level; it is also furnished with a metal tag which identifies the burst rating of the disc at a particular temperature as well as the material of the disc. It is important that this tag remains on the apparatus so that present and future operators are always aware of the disc rating. The bursting pressure of the disc is 362 bar at 22.2 °C.

The material of the disc must be compatible with the environment in which it is used so an alloy 600 disc with gold face on the process side was the one chosen for the disc. Although the alloy 600 will resist most chemical vapours, the gold facing is needed due to operation with $CO_2$ and $SO_2$ because corrosion becomes a problem.

#### *4.2.5.2. Check valves*

Three non-return (check) valves were initially installed in each gas line as safety devices in order to avoid the gases flow back into the cylinders and their subsequent damage. Essentially, a non-return valve is a one-way valve that allows a fluid to flow through it in one direction but completely prevents its movement in the opposite direction. Two common designs are swing-type and lift-type check valves, the names of which denote the motion of the closure member. In the forward direction, flow forces overcome the weight of the member or a spring to open the flow passage. With reverse pressure conditions, flow forces drive the closure member into the valve seat, thus providing shutoff (Green and Perry, 2008).

#### *4.2.5.3. Pressure and temperature limiting system*

The pressure gage fitted in the reactor's head continuously monitors pressure inside the vessel during an experiment and the digital pressure display module is equipped with a safety cut-out feature. This feature offers excellent protection against accidental overpressure by allowing the user to set a maximum pressure which, if reached, will activate the high limit relay and turn-off the heater immediately. In effect, the pressure-gage set point acts as a back-up temperature controller to prevent the system from achieving a pressure much greater than that desired.

This sort of pressure and temperature-limiting system is a requisite safety feature for any fluid-filled pressure vessel at elevated temperatures and pressures, particularly for long and therefore at least partially unattended operation (Seyfried et al., 1987).

#### *4.2.5.4. Safety screen*

The reactor was protected by a bullet-resistant glass (known by the brand name Lexan®) safety screen which provides extra protection in case of catastrophic leakage or rupture. The screen's glass, Lexan®, is basically made by layering a polycarbonate material (which is a tough transparent plastic) between pieces of ordinary glass in a process called lamination, which creates a glass-like material that is thicker than normal glass (GE, 2004).

Signs were also placed around the apparatus at all times in order to inform other workers that the apparatus was in operation.

### 4.2.6. Design optimization

Various preliminary tests were carried out to verify the performance of the equipment. Some problems were encountered and had to be solved for successful operation of the whole system. A description of those problems is explained below as well as the modifications and optimization needed in the original design.

#### *4.2.6.1. Pressurization process*

Preliminary tests aimed to pressurize the system along with detection of potential leaks; only $CO_2$ was used for this task due to its less toxic character than $SO_2$. The pressure increase observed within the reactor was almost negligible after 15 minutes and the pressurization process turned out to be extremely slow because of the allowed flow by the MFC and the booster operation. The $CO_2$ MFC range was too small for a relatively quick pressurization since the flow given by the controller was at normal conditions (P=1 bar, T=0°C), and the pressure increase would cause a significant decrease in the real flow let through. Hence, the final amount of gas going into the reactor was so small that a long period of time (over 24 h) was needed to reach high pressures (300 bar). Also, due to the piston-like behaviour of the booster the flowrate value read by the MFC software was very variable, showing a spiky behaviour, due to fluctuations of the flow.

Two different modifications were then needed to solve the encountered problems explained above:

1/ Re-range of the $CO_2$ flow mass controller. The model F-201CV was re-ranged to cover 1 to 10 ln/min $CO_2$. This modification significantly decreases the time needed to pressurise the system (~ 20-30 min). Accordingly, the $SO_2$ MFC was also re-ranged to supply a flowrate between 0 and 1,5 ln/min.

2/ An intermediate reservoir between the MFC and the booster to soften flow fluctuations: a double-ended stainless steel sample cylinder was chosen, with a volume of 500 ml and rated up to 100 bar. To prevent damage of the cylinder due to backpressure from the gas booster, a stainless steel high pressure relief valve (rated up to 413 bar at 37°C) was placed between both elements. Depending on the relief pressure, a different spring is needed to be fitted in the relief valve. Different spring colours correspond to different relief pressures. A purple spring met the requirement, covering a range from 51.7 to 103 bar (adjustable). Relief pressure then would be adjusted to a value lower than the maximum pressure hold by the sample cylinder.

### *4.2.6.2. Depressurization system*

In the depressurization process $CO_2$ undergoes an adiabatic expansion which cools it, also known as Joule-Thomson effect, which relates the pressure drop to the temperature drop for real gases: $\Delta T = \mu \cdot \Delta P$, where $\mu$ is the Joule-Thompson coefficient and $\Delta P = P_{final} - P_{initial}$. Given the experimental value of $\mu_{CO2} = 1.11\ K \cdot atm^{-1}$ (Atkins and de Paula, 2006) and a pressure drop of ~ 100 atm, $CO_2$ would undergo a cooling of about 162°C, passing from a temperature of around 35°C to a temperature well below its freezing point of -78.8°C. As a result of this process, dry ice (solid $CO_2$) formation was observed in the vessel, pipeline and gas release valve, therefore preventing the experimentalist from running a controlled and safe operation.

The depressurization system had to be modified to a safer and controlled manner. In order to successfully control the operation, two pressure regulators were fitted in the line to sequentially decrease the outlet pressure. The specifications of each of them are outlined below:

a) Line stainless steel regulator: this regulator is specifically designed for high inlet and outlet pressure applications. It can take up to 415 bar of inlet pressure and recommended outlet pressure ranges between 5 and 70 bar (Air-Products, 2007b). Its temperature range is from -40°C to 75°C.

b) Drop point regulator: this stainless steel regulator is a low inlet pressure and single stage one. Each model offers exceptional pressure and flow control with a maximum inlet pressure of 55 bar and maximum outlet pressure of 8 bar (Air-Products, 2007a). Temperature ranges between -20°C to 60°C.

The adiabatic expansion highlighted before will take place mainly in the line regulator so heating cord was used and wrapped around it to keep it warm enough to avoid dry ice formation. Temperature was maintained at approximately 60°C during the regulator operation and could not exceed 75°C due to the regulator specifications.

The gas coming out from the autoclave at the end of the experiment is washed in two consecutive glass gas bubblers containing a 1.0 M NaOH solution with a few drops of universal acid-base indicator. The colour of the solution will change and fade depending upon its pH (a green colour is observed at pH ~ 8-9 and a yellowish colour at pH ~ 5-6); this change of colour gives the experimentalist an indication of when the basic solution has been consumed and needs to be replaced. Hence, acid gases are retained in the solution and the clean gas is vented outside.

#### *4.2.6.3. Corrosion*

Corrosion of valves and inner parts of the $SO_2$ MFC was observed in preliminary tests with $SO_2$ flowing through the system. $SO_2$ has a vapour pressure of ~ 1.8 bar at 15°C and it is very likely that the gas expansion through the cylinder regulator (Joule-Thomson effect) was producing a temperature decrease and gas condensation within the regulator and downstream of the regulator.

A nitrogen purge system was present in the experimental set-up design but it only hooked into the $SO_2$ system downstream of the $SO_2$ MFC. This was adequate for purging the actual reaction chamber but a deep purge was needed in addition to this and therefore connected to the system at the $SO_2$ cylinder end. This would enable purging of the cylinder end for cylinder changing purposes and also, and more importantly, allow purging of the whole $SO_2$ process line in-between runs. Hence, $SO_2$ would be removed from the system and any $SO_2$ condensation in the components would be prevented.

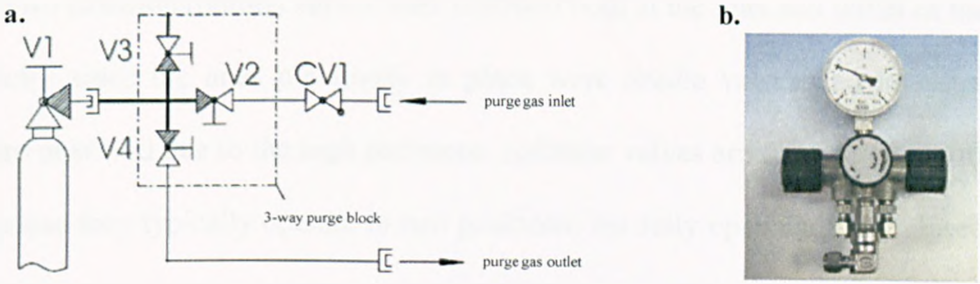

Figure 4-8. Schematic of a 3-way deep purge block at the $SO_2$ cylinder end (a): the purging gas is $N_2$ and CV1 is a non-return valve installed on inlet to purge gas valve. Picture of the 3-way deep purge block installed in the system (b). Adapted from (Bridge, 2007).

The existing $N_2$ line was easily connected to a 3-way deep purge block at the $SO_2$ cylinder end and the $SO_2$ cylinder regulator removed from the system. A schematic of the purge block and its photo is shown in Figure 4-8. The block's body is made up of 316L with an internal volume of 1.3 $cm^3$ and three high pressure diaphragm type isolation valves (process isolation, purge inlet and vent). Also, to avoid further difficulties with liquid carry-over and as an extra-safety feature, heating tape was placed around the $SO_2$ MFC to maintain its temperature at ~ 30°C.

#### 4.2.6.4. *Other fittings, sampling and venting systems*

The schematic and pictures of the final experimental system are shown in Figure 4-9, Figure 4-10 and Figure 4-11. Several valves were added as well as a gas sampling system and two extra venting systems. Description of these elements follows:

a) Two isolation (on/off) valves were installed both at the inlet and outlet of the reactor since the ones previously in place were needle valves and leakages were observed due to the high pressures. Isolation valves are considered on/off because they typically operate in two positions; the fully open and fully closed position (thus on/off). Valves made specifically for on/off service are designed with tight reliable shutoff in the closed position and little restriction in the open position.

b) A gas sampling system was installed at the reactor outlet to enable the experimentalist to perform a quantitative analysis of the gas mixture contained within the autoclave. The initial gas composition is set up with the MFC and the final one can be then determined by collecting a gas sample from the system and feeding it into a gas chromatographer.

c) Venting systems: Installation of the relief valve upstream the gas booster required an extra gas vent at that point should the valve blow off. Also, an extra gas venting line at the reactor outlet provided a way out for the non-hazardous gases ($N_2$) which do not have to be bubbled and neutralised before going into the atmosphere.

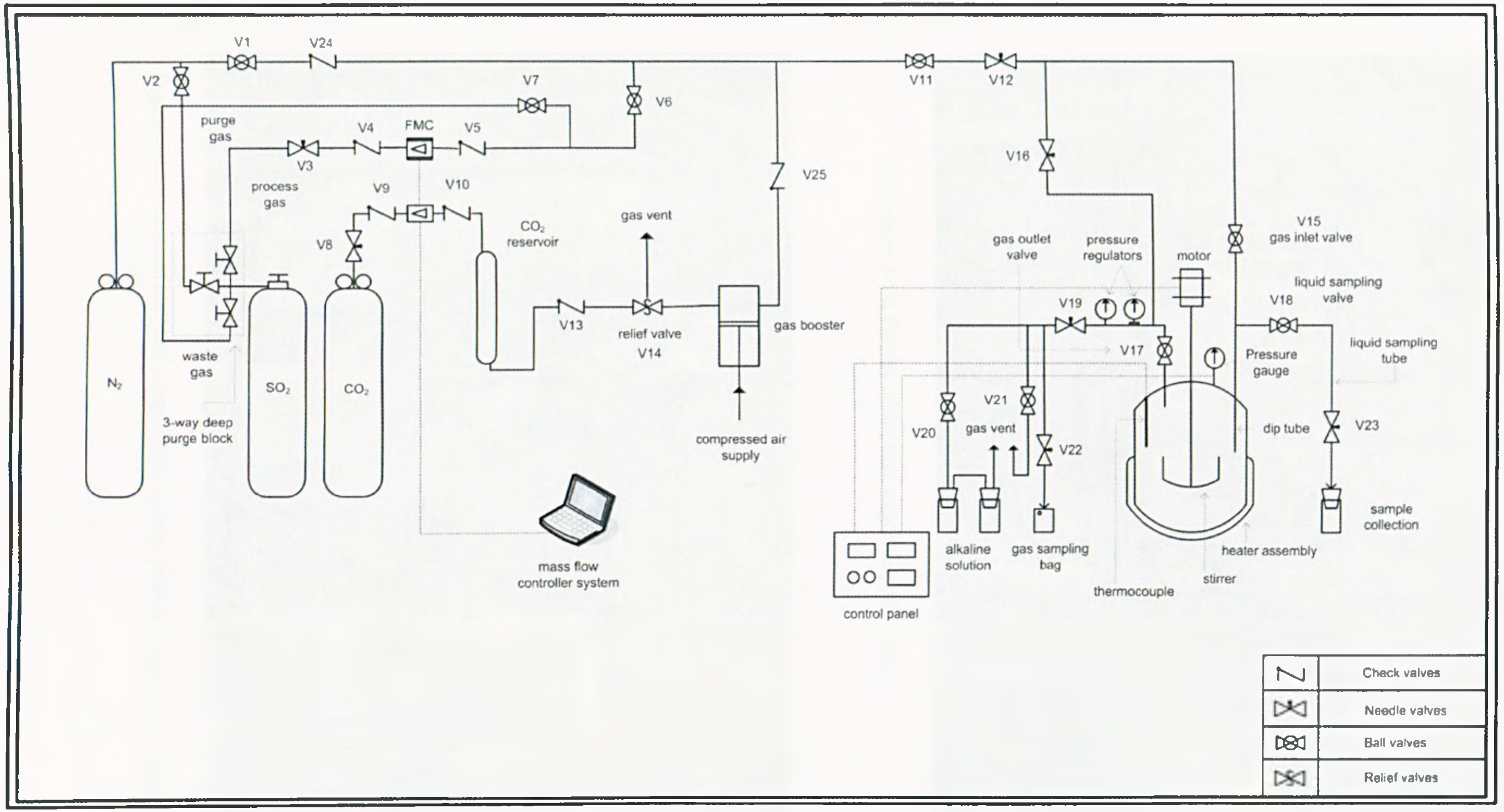

Figure 4-9. Schematic of the final experimental set-up.

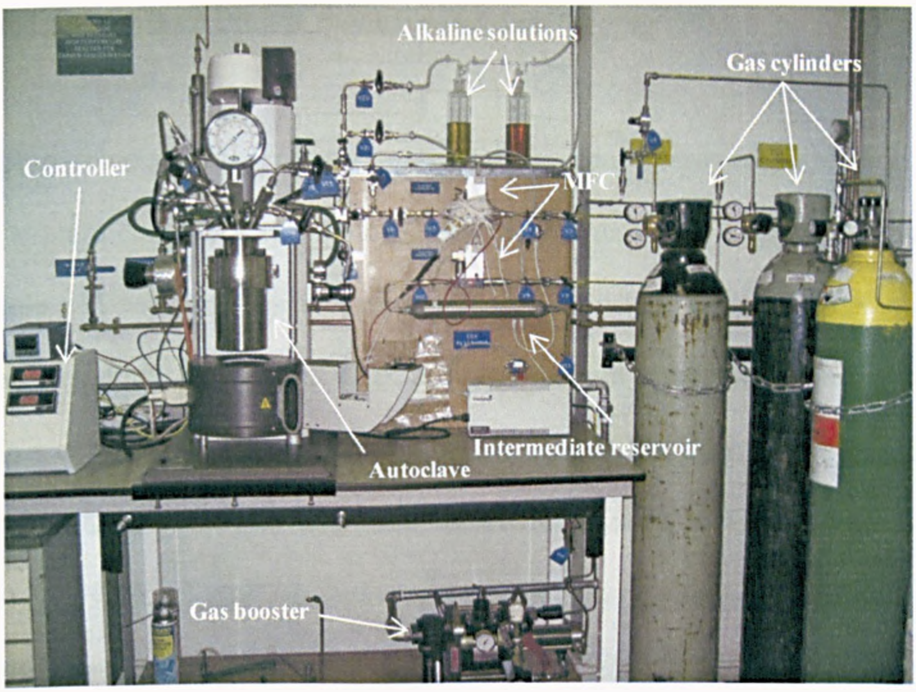

Figure 4-10. Picture of the final experimental system.

Figure 4-11. Picture of the final experimental system with safety screen on place.

#### *4.2.6.5. Data display modules and data logging*

Reactor temperature, pressure and stirring speed are displayed on the temperature controller and motor speed control unit. The tachometer display module (TDM) provides a means for continuously monitoring the stirring speed in the reactor. It consists of a digital readout mounted in the controller cabinet connected to an optical sensor installed in the over arm drive on the reactor; the digital display will show the stirring speed over a range from 0 to ~ 1600 rpm with a 1 rpm resolution and +/- 10 rpm accuracy (Parr, 2009). The digital pressure display module (PDM) provides a digital readout for continuously monitoring the pressure within the reactor, plus the backup safety feature mentioned in section 4.2.5.3, which will terminate the power to the heater if a preset maximum is reached. Pressure is displayed with 1 bar resolution and 1% full scale accuracy (Parr, 2009). The signal for the pressure display is generated by a transducer in a stainless steel housing mounted on the reactor, in the side port of the gage adapter. The transducer must not be heated above 120°C; a water cooling sleeve attached to the transducer mounting body is used to keep the transducer below this limit when operating the reactor.

Reactor temperature and pressure are also logged during the entire duration of the experiment to record any variation. The data converter used for logging the reactor pressure was a ADC 16 (Pico, 2009) and pressure and temperature records could be depicted with the Picolog Player and Calgrafix softwares respectively. Pressure and temperature data were recorded every 20 s to ensure all changes were kept track of.

The temperature of the two heating tapes placed in the system, one around the $SO_2$ MFC and the other one around the line pressure regulator, was also displayed in two different units: one of them controlled the $SO_2$ MFC temperature and was set to 30°C; the other unit was only a display to show the temperature of the pressure regulator connected to the reactor outlet gas valve, but no control could be performed.

#### *4.2.6.6. Reproducibility evaluation*

The equipment reproducibility was required to allow meaningful comparison of results with independent studies. Pressure was reached in the system by means of a compressed air-driven $CO_2$ gas booster and final pressure in the autoclave was highly influenced by the booster operation and heating process. These two had to be carefully controlled, i.e. calibrated, in order to minimise the data disparities due to their inconsistent operation. Calibration of the equipment was then performed so different $CO_2$:$SO_2$ gas compositions could produce the desired reaction pressures and temperatures.

Experiment duplicates were run to assess the reproducibility of the equipment. Experiment conditions were: hematite reacted at 100°C for 24h with a $CO_2$:$SO_2$ gas composition of 99.6:0.4 (% by volume) and three different particle size values (-38, 38-150 and 150-300 μm); the targeted pressure was 250bar. Researched and measured variables were iron in dissolution (ferrous, ferric and total), initial and final pH, solids weight uptake (%) and reactor pressure. The main reason for running duplicates with different particle size of the solids was the assessment of the reproducibility of measured weight uptake values, since the difficulty of collecting the solids from the vessel might vary depending on their particle size. Results from these reproducibility studies are presented in Figure 4-12 below.

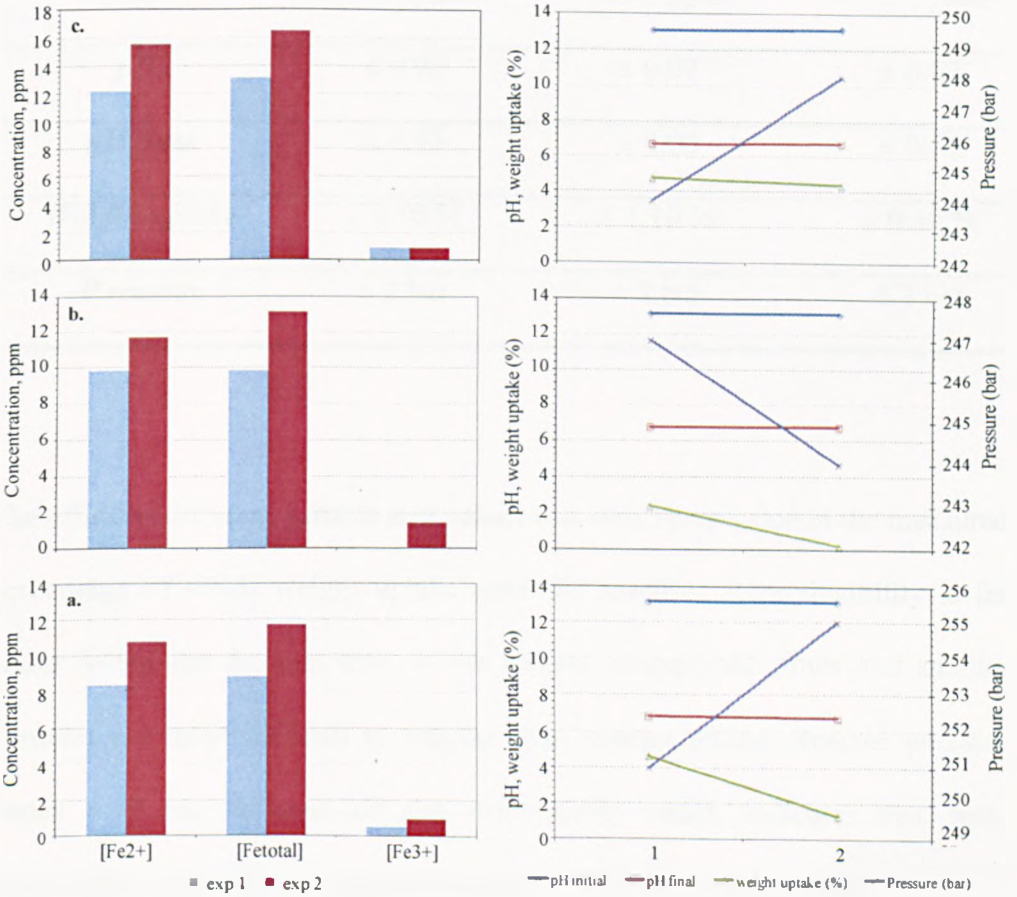

Figure 4-12. Results of reproducibility tests for different particle size ranges : -38 (a), 38-150 (b) and 150-300 (c); iron in solution (left) and pH, initial and final, weight uptake, %, and reactor pressure, bar, (right) are shown.

Table 4-2 shows the reproducibility values for the different parameters to be studied in the experimental section. Reproducibility of the initial pH value was included because final pH is strongly dependant upon the initial one so it is important to get the same starting pH in duplicate experiments.

Table 4-2. Reproducibility values for experimental tests.

| | Reproducibility results | | |
|---|---|---|---|
| ***Particle size (μm)*** | ***-38*** | ***38x150*** | ***150x300*** |
| ***[$Fe^{2+}$]*** | ± 1.2 ppm | ± 0.9 ppm | ± 1.7 ppm |
| ***[Fe total]*** | ± 1.4 ppm | ± 1.7 ppm | ± 1.7 ppm |
| ***[$Fe^{3+}$]*** | ± 0.2 ppm | ± 0.7 ppm | ± 0.0 ppm |
| ***$pH_0$*** | ± 0.02 | ± 0.02 | ± 0.02 |
| ***pH final*** | ± 0.05 | ± 0.00 | ± 0.03 |
| ***Weight uptake*** | ± 1.70 % | ± 1.10 % | ± 0.19 % |
| ***P reactor*** | ± 2 bar | ± 2 bar | ± 2 bar |

The effect of different particle size values was only remarkable in the measured percentage of solids weight uptake after the reaction. Reproducibility is far better in the top fraction than in the others; as expected, fines and smaller particles are more difficult to recover than coarser grains. Reactor pressure varies ± 2 bar between all the experiments which indicates that both, experimental procedure and apparatus, are reliable and reproducible.

## 4.3. Summary

A novel high pressure-high temperature experimental system has been developed for the study of gas-brine-rock reactions that mimic underground geological processes when injecting a $CO_2/SO_2$ mixture of gases. The high complexity of integrating the equipment operation at high temperatures and pressures with the injection of several gases (one of them, $SO_2$, being very corrosive) has been overcome and successfully resolved. The procedure and system have been evaluated and optimised in order to provide to highest degree of repeatability of the measurements.

Monitoring reaction progress is essential and this requirement has been met with the different data logging systems and ability for periodic sampling of fluids from the experimental set-up. In addition, the developed experimental facility is convenient and safe to operate, permitting an appropriately trained individual to initiate and dismantle experiments with a high degree of efficiency.

## 4.4. References

Air-Products (2007a) Drop point regulators Series DP70. Available from: <www.airproducts.co.uk> (accessed 18 June 2007).

Air-Products (2007b) Line Regulator R2400 Series. Available from: <www.airproducts.co.uk> (accessed 18 June 2007).

Alexander, G., Maroto-Valer, M. M. & Gafarova-Aksoy, P. (2007) Evaluation of reaction variables in the dissolution of serpentine for mineral carbonation. *Fuel,* 86, 273-281.

Atkins, P. & de Paula, J. (2006) *Atkins' Physical Chemistry,* Oxford University Press.

Bridge, S. (2007) FTI - controlling pressure and vacuum.

Bronkhorst (2009) Mass flow and pressure measurement and control. Available from: <http://www.bronkhorst.co.uk/> (accessed 1 December 2009).

Bruant Jr., R. G., Giammar, D. E., Myneni, S. C. B. & Peters, C. A. (2002) Effect of Pressure, Temperature, and Aqueous Carbon Dioxide Concentration on Mineral Weathering as Applied to Geologic Storage of Carbon Dioxide. Proceedings of the Sixth International Conference on Greenhouse Gas Control Technologies (GHGT-6), 1-4 October, Kyoto, Japan.

Davison, J. (2006) Bronkhorst mass flow controllers.

Dickson, F. W., Tunell, G. & Blount, C. W. (1963) Use of Hydrothermal Solution Equipment to Determine Solubility of Anhydrite in Water from 100 Degrees C to 275 Degrees C and from 1 Bar to 1000 Bars Pressure. *American Journal of Science,* 261, 61-78.

Druckenmiller, M. L., Maroto-Valer, M. M. & Hill, M. (2006) Investigation of Carbon Sequestration via Induced Calcite Formation in Natural Gas Well Brine. *Energy & Fuels,* 20, 172-179.

GE (2004) General Electric (GE) advanced materials. Plastics: Lexan® PC resin product brochure. Available from: <http://www.plastoplan.com/download/ge_plastics_pdf_downloads/gep_Lexan_2004_eng.pdf> (accessed 2 December 2009).

Green, D. W. & Perry, R. H. (2008) *Perry's chemical engineers' hanbook,* McGraw-Hill.

Haskel (2009) High pressure gas and liquid engineering. Available from: <www.haskel.com> (accessed 1 December 2009).

Huijgen, W. J. J., Witkamp, G.-J. & Comans, R. N. J. (2006) Mechanisms of aqueous wollastonite carbonation as a possible $CO_2$ sequestration process. *Chemical Engineering Science,* 61, 4242-4251.

Jacquemet, N., Pironon, J. & Caroli, E. (2005) A New Experimental Procedure for Simulation of $H_2S$ + $CO_2$ Geological Storage. Application to Well Cement Aging. *Oil & Gas Science and Technology,* 60, 193-206.

Kaszuba, J. P., Janecky, D. R. & Snow, M. G. (2003) Carbon dioxide reaction processes in a model brine aquifer at 200°C and 200 bars: implications for geologic sequestration of carbon. *Applied Geochemistry,* 18, 1065-1080.

Mandalaparty, P., Deo, M., Moore, J. & McPherson, B. (2009). Carbon dioxide sequestration: effect of the presence of sulfur dioxide on the mineralogical reactions and on the injectivity of $CO_2$+$SO_2$ mixtures, University of Utah, Salt Lake City.

Palandri, J. L., Rosenbauer, R. J. & Kharaka, Y. K. (2005) Ferric iron in sediments as a novel $CO_2$ mineral trap:$CO_2$-$SO_2$ reaction with hematite. *Applied Geochemistry,* 20, 2038-2048.

Parr (2009) Parr Instrument Company. Available from: <http://www.parrinst.com/> (accessed 1 December 2009).

Pico (2009) Pico Technology. Available from: <http://www.picotech.com/> (accessed 2 December 2009).

Rosenbauer, R. J., Bischoff, J. L. & Potter, J. M. (1993) A Flexible Au-Ir Cell with Quick Assembly for Hydrothermal Experiments. *American Mineralogist,* 78, 1286-1289.

Rosenbauer, R. J. & Koksalan, T. (2003) Experimental $CO_2$-saturated brine-rock interactions at elevated temperature and pressure: Implications for $CO_2$ sequestration in deep-saline aquifers. *Abstracts of Papers of the American Chemical Society,* 226, U603-U603.

Rosenbauer, R. J., Koksalan, T. & Palandri, J. L. (2005) Experimental investigation of $CO_2$-brine-rock interactions at elevated temperature and pressure: Implications for $CO_2$ sequestration in deep-saline aquifers. *Fuel Processing Technology,* 86, 1581-1597.

S&M (2009) Scientific & Medical Products Ltd. Available from: <http://www.scimed.co.uk/> (accessed 1 December 2009).

Sass, B. M., Gupta, N., Ickes, J. A., Engelhard, M. H., Baer, D. R., Bergman, P. & Byrer, C. (2001) Interaction of rock minerals with carbon dioxide and brine: a hydrothermal investigation. Proceedings of the First National Conference on Carbon Sequestration, 15-17 May Washington DC.

Seyfried, W. E., Gordon, P. C. & Dickson, F. W. (1979) New Reaction Cell for Hydrothermal Solution Equipment. *American Mineralogist,* 64, 646-649.

Seyfried, W. E., Janecky, D. R. & Berndt, M. E. (1987) Rocking autoclaves for hydrothermal experiments II. The flexible reaction-cell system. IN ULMER, G. C. & BARNES, H. L. (Eds.) *Hydrothermal Experimental Techniques.* New York, Wiley.

Soong, Y., Goodman, A. L., McCarthy-Jones, J. R. & Baltrus, J. P. (2004) Experimental and simulation studies on mineral trapping of $CO_2$ with brine. *Energy Conversion and Management,* 45, 1845-1859.

Soong, Y., Jones, J. R., Harrison, D. K., Hedges, S. W., Goodman, A. L. & Baltrus, J. P. (2003) Mineral Trapping of $CO_2$ with Oriskany Brine. Proceedings of the Second Annual Conference on Carbon Sequestration, 5-8 May Alexandria, VA, USA.

Swagelok (2009) Swagelok - Fluid Systems Technologies. Available from: <http://www.swagelok.com/> (accessed 1 December 2009).

## CHAPTER 5

# MODELLING MINERALOGICAL CHANGES

# 5. Modelling mineralogical changes

## 5.1. Theory of computed multi-component equilibrium

CHILLER is a FORTRAN computer program and the most advanced member in a series of programs that have been developed since the mid-1970's to compute multi-component thermodynamic chemical equilibria in aqueous systems. Its name is derived from its original function of calculating the cooling of an aqueous phase but since 1976, the program has been updated to include several capabilities, including rock titration (Reed and Spycher, 2006). A wide range of geochemical codes (Geochemist's Workbench, GWB, TOUGHREACT, PHREEQC, etc.) is available to compute multi-component equilibrium. CHILLER was chosen as the one for this research project because the only experimental work previously reported with iron oxides (Palandri et al., 2005) was simulated with CHILLER; thereby, comparison of simulation results and predictions can be established.

CHILLER computes the equilibrium distribution of thermodynamic components among aqueous species, minerals and gases, using equilibrium constants for aqueous, solid and gas reactions at selected temperature and pressure (Palandri and Reed, 2004). The program applies the Newton-Raphson numerical method to solve a set of simultaneous non-linear polynomial equations of mass balance and mass action that describe the chemical equilibrium in the system. Mass action equations are substituted into the mass balance equations, which are originally linear but are made non-linear via the substitution. The calculation takes account of oxidation-reduction equilibria, aqueous ion complexing, activity coefficients, non-unit water activity and solid solutions (Reed, 1982). The heterogeneous equilibrium calculations produces the gas species mole fractions and the mass and composition of each additional phase in the system including solid or liquid solutions, at overall equilibrium (Symonds and Reed, 1993).

CHILLER is used to model geochemical processes by changing one of the system variables incrementally, e.g., composition, temperature, pressure or enthalpy, with re-calculation of the equilibrium phase assemblage, mineral compositions and aqueous composition at each step. The aqueous activity coefficients are computed using the extended Debye-Hückel equation of Helgeson and co-workers (Helgeson et al., 1981), as modified by Tanger and Hegelson (Tanger and Helgeson, 1988) and gas fugacities using a virial equation as discussed by Spycher and Reed (Spycher and Reed, 1988). The accurate calculation of aqueous activity coefficients in the method requires that NaCl be the dominant solute at ionic strength greater than ~ 1 molal, and that the total salinity not exceed ~ 3 molal (Palandri and Reed, 2004).

SOLTHERM is the thermodynamic database of equilibrium constants for minerals, gases and aqueous species used by CHILLER. Most of the equilibrium constants were calculated using the software package SUPCRT92 (Johnson et al., 1992), modified with a four term heat capacity regression equation, to use an internally consistent mineral thermodynamic dataset for silicates, oxides, hydroxides, carbonates and gases from Holland and Powell

(Holland and Powell, 1998). SUPCRT92 was also used to compute equilibrium constants for non-silicate minerals and gases using data from Helgeson and co-workers (Helgeson et al., 1978) that was not duplicated in Holland and Powell data. The database also contains equilibrium constants for minerals and aqueous species from more than 50 additional different sources referenced in the database. Shock et al. (Shock et al., 1997) reported the thermodynamic data used for water and aqueous species used in both versions of SUPCRT. There are two versions of SOLTHERM depending on the pressure regime: one of them contains data for constant pressure at 1000 bar from 25 to 600 °C, and the other one applies to the water liquid-vapor saturation curve from 25 to 350 °C (Palandri and Reed, 2001).

### 5.1.1. Limitations of the method

Theoretical equilibrium calculations performed with CHILLER do not account for absolute rates of mineral dissolution and precipitation, nor of aqueous speciation, which could be more significant with decreasing temperature. Therefore, it is worth to bear in mind that precipitation and persistence of metastable phases is always a possibility even if the products of a chemical reaction are favoured thermodynamically. Also, alteration of primary minerals may proceed at different rates. In spite of this, natural alteration assemblages observed in the field are commonly in good agreement with those alteration assemblages computed with the software, even at temperatures as low as 25°C (Palandri and Reed, 2004). Mineral texture and geometry, i.e., size, shape and distribution of mineral grains relative to each other are not addressed in the simulations.

It is common that equilibrium between a fluid and primary minerals is absent (and in some cases cannot be attained); in many sedimentary basins and volcanic-hosted hydrothermal systems however, it is widely and validly assumed that local chemical equilibrium exists among fluids and alteration minerals if temperatures are high enough, or, if fluid flow rates are sufficiently slow, permitting equilibration at temperatures as low as 75-80°C (Palandri and Reed, 2004).

Further limitations refer to the quality of the thermodynamic data used by the code: there are cases where thermodynamic data is not available for the minerals or phases of interest and a similar mineral could be then used as a proxy, e.g. chrysotile serpentine as a proxy for lizardite serpentine; in other instances, the thermodynamic parameters are based on empirical data for which there is a degree of uncertainty, hence the results are considered to be approximations (Palandri and Reed, 2004). It is also important not to deviate significantly from conditions corresponding to water liquid-vapor saturation curve since the equilibrium constants used for the simulations correspond to those conditions.

### 5.1.2. Thermodynamic relations and system calculations

The computer program applies the Newton-Raphson method to solve a set of mass-balance into which mass-action equations are substituted. For a gas-solid-liquid chemical system at a specified temperature, T, pressure, P, and composition, this is defined by the total number of moles $M_i^t$ of each thermodynamic component, designated by subscript i. A set of $N_i$ mass-balance equations, one for each thermodynamic component, and a set of $N_k$ mass-action equations, one for each saturated solid, solid solution endmember and liquid are defined (Symonds and Reed, 1993). "Derived" species are defined as those whose compositions are expressed as linear combinations of the component species. Their corresponding terms in the mass-balance equations can be replaced by the appropriate secondary mass-action expressions (those written for the "derived" species), thereby the number of primary equations to be simultaneously solved is reduced to a minimum number $N_i$.

Typically, the trial values to begin the Newton-Raphson method need to be within five or ten orders of magnitude of the values when solved; trial values smaller than the final solution values work better than do ones larger. The numerical solution obtained after each iteration of the method is judged so, a convergence test is performed for each of the component species, i, defining the chemical system. Determination of supersaturated phases as a consequence of the previous change of $M_i^t$ (T, or P where applicable) is carried out after each increment in the calculation, upon evaluation of the saturation index. Mineral saturation indices are defined as:

$$SI = \frac{AP}{K}$$

where *AP* is the activity product and *K* is the equilibrium constant. For a given analysis of formation water, if a mineral saturation index is higher than 1, then that mineral is supersaturated with respect to the fluid whereas if SI < 1, it will remain undersaturated. Among the supersaturated minerals (log (AP/K) < 0), the mineral that is most supersaturated, as indicated by the most negative value of log(AP/K), is included in an initial heterogeneous equilibrium calculation, after which the solution is checked again for supersaturated minerals. This procedure is repeated until there are no supersaturated minerals (Reed, 1982). Temperature change calculations simply require re-calculation for each segment of the equilibrium constants, using a power function that expresses logarithm of the equilibrium constant as a function of the temperature (Symonds and Reed, 1993).

## 5.2. Results and discussion

### 5.2.1. Reactions in a hematite-brine-$CO_2$-$SO_2$ system

This section presents modelling (i.e. equilibrium) results obtained for the hematite-brine-$CO_2$/$SO_2$ gas reactions. Theoretical calculations were performed in the early stages of this research study, where a 100% pure hematite sample was targeted for the experimental studies conducted later on. Hence, the modelling does not consider the influence of aluminium in the hematite sample. However, the obtained hematite sample happened to be a non 100% pure one, and kaolinite was identified as a minor component in the sample (see details in Chapter 6). Therefore, and to illustrate the effect of Al on the modelling, reactions in a hematite-kaolinite-brine-$CO_2$-$SO_2$ system are presented in the Appendix, and uncertainties arising from this are discussed in the sample analysis performed in Chapter 7.

Solids particle size, reaction time, gas composition ($CO_2$/$SO_2$), reactor pressure and temperature, concentration of solids and brine composition are the reaction variables experimentally assessed in the hematite-brine-$CO_2$-$SO_2$ system. Predicted equilibrium based on computer simulations do not address mineral texture and geometry aspects and does not account for kinetics; hence, the effects of particle size and reaction time on the overall reaction have only been assessed experimentally. The sensitivity of the reaction to the rest of variables has been studied both, theoretically and experimentally, and modelling results are presented here.

#### 5.2.1.1. *Results for the baseline case*

The thermodynamic equilibrium simulation at 100°C and 250 bar (baseline case) was constructed to establish the thermodynamically favored phase. In the simulations, a 1.0m NaCl brine is first equilibrated with a 0.5m NaOH solution (the input file for CHILLER is shown in Table 5-1) at the desired pressure (250 bar), followed by heating of the brine up to the desired temperature (100 °C) and further equilibration with 10 g of hematite. Equilibration with excess $CO_2$

(165 g) was performed next and further incremental $SO_2$ addition (up to 70 g) completed the simulation. Equilibrium is computed after each increment of $SO_2$ gas added to the system, so that the effects of varying amounts of $SO_2$ in a $CO_2$-dominated flue gas can be studied. This simulation with a pH buffer aims to mimic the natural mineral buffering of pH, thereby increasing the degree of siderite supersaturation and its precipitation rate.

Computed equilibrium mineral/gas phase assemblage (Figure 5-1) for increasing amounts of $SO_2$ gas added indicate siderite is the stable phase over a wide range of $SO_2$ gas added, from -5.40 (off-scale left) to 1.21 log g ( from 4 μg to 16.4 g). Further addition of $SO_2$ will yield dissolution of siderite and after all of the hematite has dissolved, pyrite precipitation. In a very acidic environment, native sulfur will replace pyrite.

Table 5-1. Initial test file for CHILLER: $CO_2$-$SO_2$ reaction at 100°C and 250 bar with 10 g of hematite in 400 mL of 1.0mNaCl, 0.5mNaOH brine using 165g (excess) $CO_2$. Parameters in the table are defined in CHILLER's manual (Reed and Spycher, 2006).

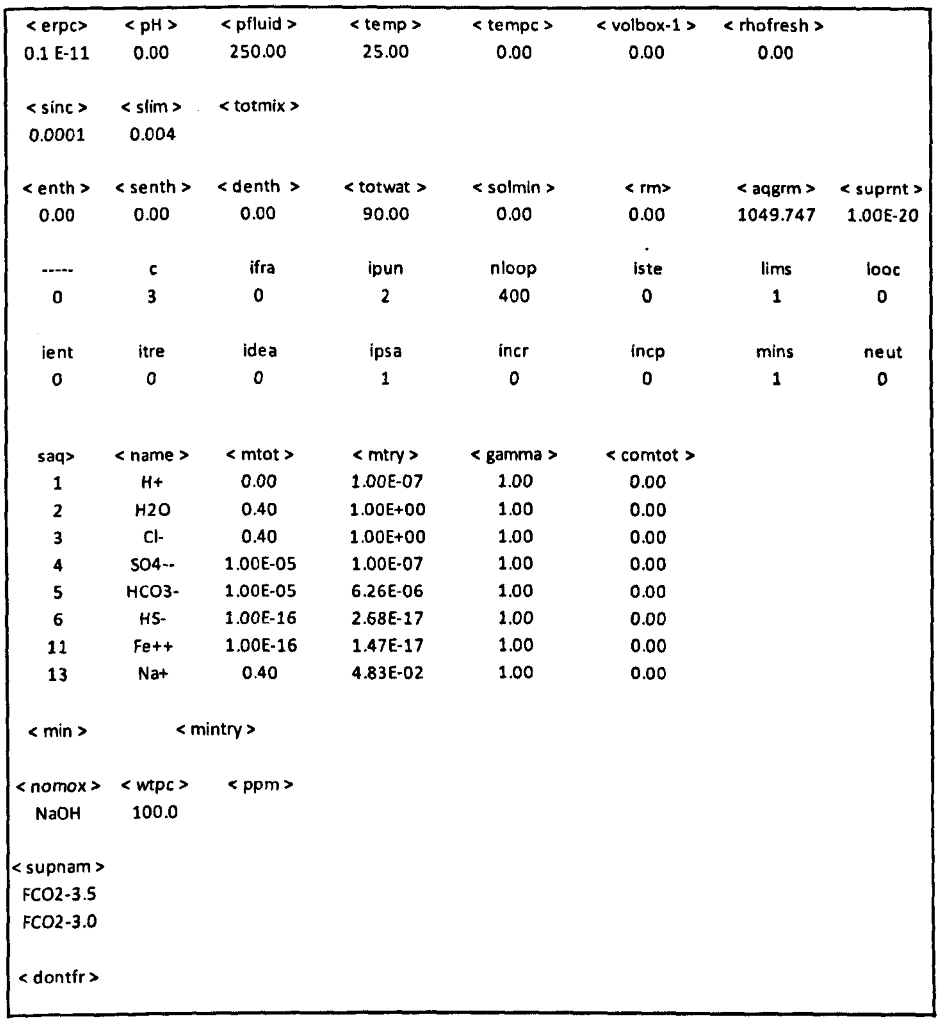

```
< erpc>    < pH >    < pfluid >    < temp >    < tempc >    < volbox-1 >   < rhofresh >
0.1 E-11   0.00      250.00        25.00       0.00         0.00           0.00

< sinc >   < slim >  < totmix >
0.0001     0.004

< enth >   < senth > < denth >     < totwat >  < solmin >   < rm>          < aqgrm >    < suprnt >
0.00       0.00      0.00          90.00       0.00         0.00           1049.747     1.00E-20

-----      c         ifra          ipun        nloop        iste           lims         looc
0          3         0             2           400          0              1            0

ient       itre      idea          ipsa        incr         incp           mins         neut
0          0         0             1           0            0              1            0


saq>       < name >  < mtot >      < mtry >    < gamma >    < comtot >
1          H+        0.00          1.00E-07    1.00         0.00
2          H2O       0.40          1.00E+00    1.00         0.00
3          Cl-       0.40          1.00E+00    1.00         0.00
4          SO4--     1.00E-05      1.00E-07    1.00         0.00
5          HCO3-     1.00E-05      6.26E-06    1.00         0.00
6          HS-       1.00E-16      2.68E-17    1.00         0.00
11         Fe++      1.00E-16      1.47E-17    1.00         0.00
13         Na+       0.40          4.83E-02    1.00         0.00

< min >         < mintry >

< nomox >  < wtpc >  < ppm >
NaOH       100.0

< supnam >
FCO2-3.5
FCO2-3.0

< dontfr >
```

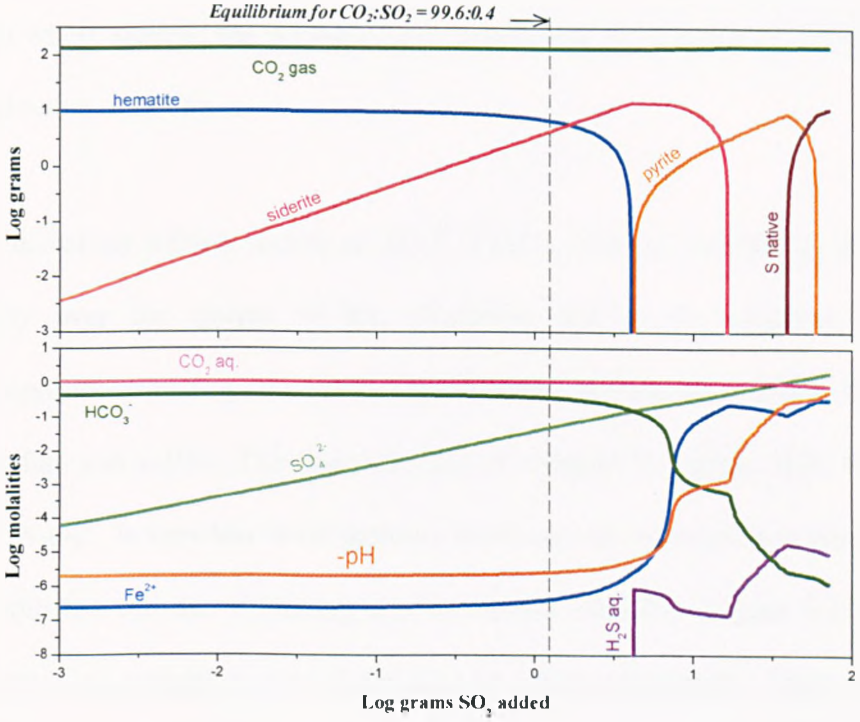

Figure 5-1. Results from simulation at 100°C and 250 bar of the $CO_2$-$SO_2$ reaction with 10 g of hematite in 400 mL of 1.0mNaCl, 0.5mNaOH brine using 165g (excess) $CO_2$: mineral/gas phase assemblage (top) and fluid composition (bottom).

The graph for computed fluid composition at equilibrium (Figure 5-1) shows that at very small amounts of $SO_2$ added, the pH is nearly constant, buffered by hematite dissolution, which consumes $H^+$, whereas both addition of $SO_2$ and siderite precipitation, generate acidity. After ~ 0.25 g of $SO_2$ added, the pH begins to decrease because the amount of $H^+$ generated becomes greater than that consumed by hematite dissolution. The slope of the pH curve decreases as siderite begins to dissolve and consume $H^+$, followed by a further steep decrease when pyrite precipitates. The formation of native sulfur causes a plateau in pH until pyrite dissolves completely, after which the pH declines again in response to the precipitation of native sulfur as the only active process. The total dissolved iron concentration, present mainly as $Fe^{2+}$, $FeCl^+$, $FeCl_2$, FeO, $FeOH^+$ and $FeSO_4$, remains almost constant and very low (~$10^{-7}$ mol/kg solvent) until the curve steepens in response to a more acidic pH, reaching 0.24m where siderite has dissolved out, continuing to increasing slightly until a final value of 0.32m.

Total dissolved sulfate, mostly as $SO_4^{2-}$, $FeSO_4$, $NaSO_4^-$ and $HSO_4^-$, increases steadily over the course of the simulation due to the addition of gas. Disproportionation $SO_2$ reaction produced sulfate and sulfide and only traces of thiosulfate and sulfite. The concentration of reduced S species, $H_2S$, $HS^-$, $S^{2-}$, $SO_3^{2-}$, $S_2O_3^{2-}$, is very low until hematite dissolves out, increasing in response to $SO_2$ addition. All the S-bearing species behave similarly (Figure 5-2), with a very low concentration until hematite dissolves completely. Then, a sharp increase is observed for all of them; concentrations level off when pyrite becomes the stable phase because S is going in pyrite rather than in the fluid (reaction [5-3]). Next, an increase in the $H_2S$ and $S_2O_3^{2-}$ concentrations and subsequent decrease in $HS^-$, $SO_3^{2-}$ and $S^{2-}$ concentrations is observed due to $SO_2$ disproportionation (reaction [5-4]), until sulfur saturation is reached in response to increasing sulfate, sulfide and decreasing pH (reaction [5-3]).

$$4Fe^{2+} + SO_4^{2-} + 7HS^- + H^+ \leftrightarrow 4FeS_2\text{ (pyrite)} + 4H_2O \qquad [5\text{-}1]$$

$$4SO_2(g) + 4H_2O(l) \leftrightarrow H_2S(aq) + 3H_2SO_4(aq) \qquad [5\text{-}2]$$

$$3H_2S + H_2SO_4 \leftrightarrow 4S(\text{native}) + 4H_2O \qquad [5\text{-}3]$$

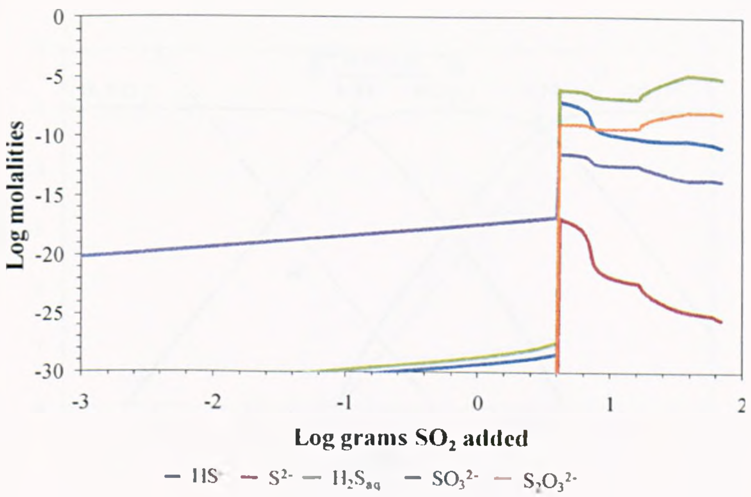

Figure 5-2. Equilibrium sulfur species concentration for the simulation at 100°C and 250 bar with hematite.

The trend of bicarbonate concentration in Figure 5-1 clearly follows the one for pH, reflecting how a closed carbonate system is strongly linked to the composition and pH of the brine (Stumm and Morgan, 1996). The Bjerrum plot, log concentration vs pH, for a closed carbonate system at standard conditions and a fixed value of the total carbonate concentration is shown in Figure 5-3, and clearly exemplifies the latter statement. Depending on the pH of the medium, the concentration of the different carbonate species varies favoring one versus the others. This plot is an important reference for above-ground $CO_2$ mineral carbonation studies. In this work and although relevant T and P conditions are different and therefore the lines would be shifted, the plot helps the understanding of parallel trends for the bicarbonate concentration and pH values, since as the pH decreases a different carbonate specie is favored ($H_2CO_3$); hence, pH determinates the bicarbonate concentration in the system.

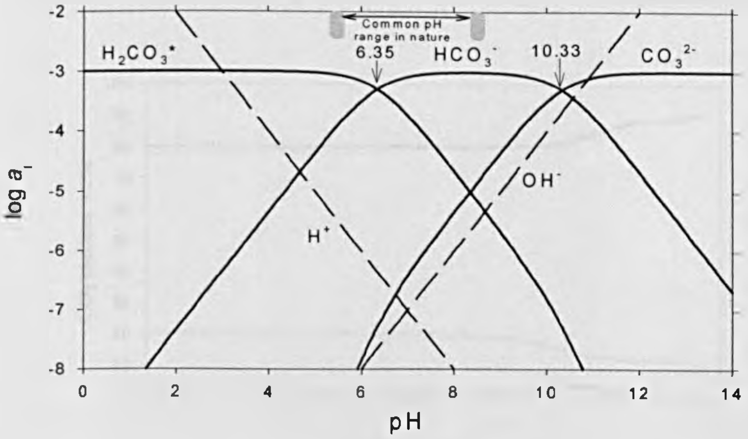

Figure 5-3. Bjerrum plot for a closed carbonate system at standard (T=25°C and P=1bar) conditions (Stumm and Morgan, 1996) .

The vertical line in Figure 5-1 denotes the equilibrium conditions for the amount of $SO_2$ used in the experiments with a $CO_2$:$SO_2$ composition of 99.6:0.4, typical of a flue gas stream, where the mineral assemblage should consist only of hematite and siderite, with a conversion of 27.9% of the Fe present in the hematite into siderite and 0.15 g of $CO_2$ sequestered in siderite per g of rock. The percentage of iron conversion into siderite is calculated according to Equation 5-1, where $\xi_{Fe}$ is the percentage of conversion and $m_{Fe}$ the mass of iron (in grams) contained in the rock. Equilibrium pH is 5.59 and dissolved iron of 0.023 ppm.

$$\xi_{Fe}[\%] = \frac{m_{Fe} \text{in } FeCO_3}{m_{Fe} \text{ in parent rock}} \times 100 \qquad \text{Equation 5-1}$$

The mass balance for the total carbon in the system showing how it partitions among the different phases (gas, siderite and brine) can be seen in Figure 5-4, where $\sum CO_3^{2-}$ denotes the total aqueous carbonate concentration and is defined as follows:

$$\sum CO_3^{2-} = [H_2CO_3] + [HCO_3^-] + [CO_3^{2-}] \qquad \text{Equation 5-2}$$

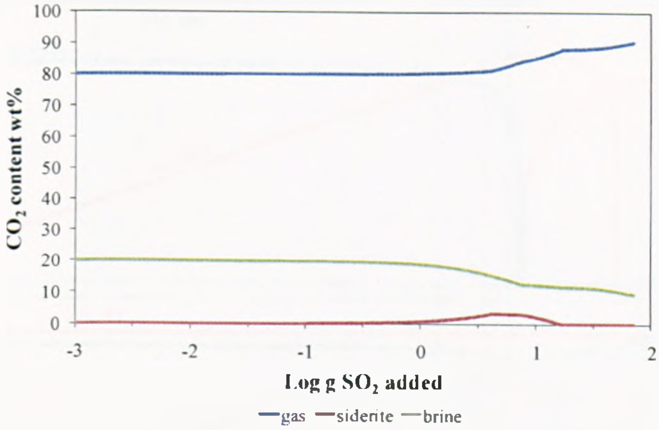

Figure 5-4. Carbon partitioning amongst the different phases.

$CO_2$ is mostly trapped in gas phase (80% or more), followed by trapping in brine (10-20%) and siderite (less than 10%). For the experimental case (see section 7.1.2 in chapter 7), denoted by vertical line in Figure 5-1, $CO_2$ content percentage in gas, siderite and brine are of 80.4, 0.9 and 18.7% respectively.

### *5.2.1.2. Effect of gas composition*

The thermodynamic equilibrium simulation constructed at 100°C and 250 bar, and explained in previous section, also gives information of the effect of varying the relative amounts of $CO_2$ and $SO_2$ in the total amount of gas added to the reactive system. Equilibrium results obtained for the gas compositions used in the experimental runs (see section 7.1.3 in chapter 7) are denoted by the vertical lines in Figure 5-5 and will be further discussed and compared with the collected experimental values in Chapter 7.

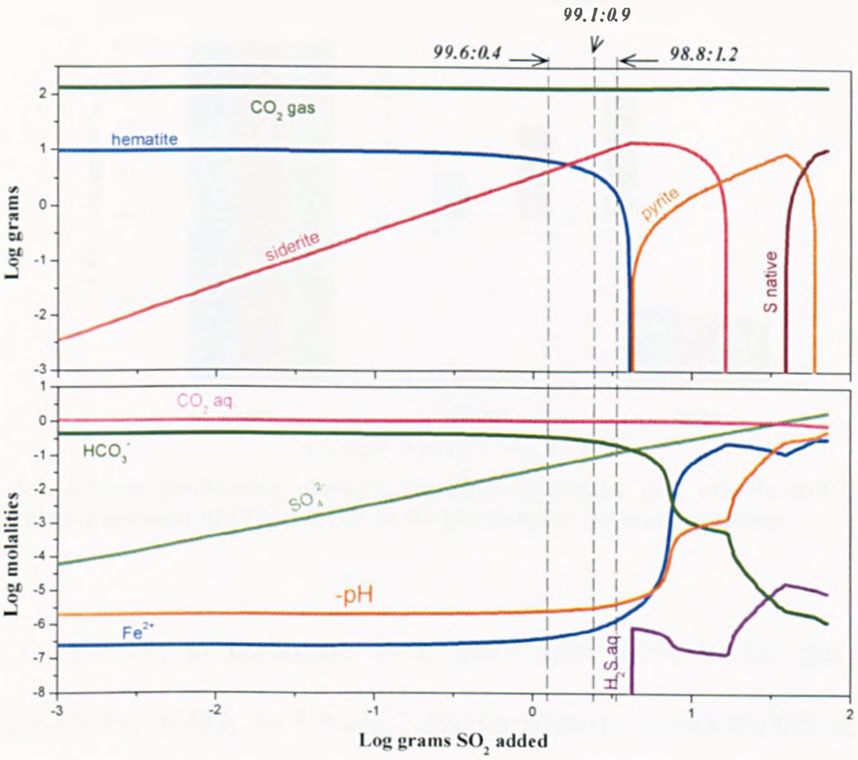

Figure 5-5. Results from the simulation at 100°C and 250 bar of the $CO_2$-$SO_2$ reaction with 10 g of hematite in 400mL of 1.0mNaCl, 0.5mNaOH brine using 165g (excess) $CO_2$ and showing mineral/gas phase assemblage (top) and fluid composition (bottom) for varying amounts of $SO_2$ in the gas added.

The main conclusion from the modelling results is the higher amount of $CO_2$ trapped in siderite as the $SO_2$ concentration increases in the gas stream added to the system. Precipitated siderite and remaining hematite are the only two stable solid phases predicted at equilibrium for the tested ratios. Figure 5-6 shows the carbon content (wt %) amongst the predicted carbon-containing phases (gas, siderite and brine) for the three studied $CO_2$:$SO_2$ gas concentrations.

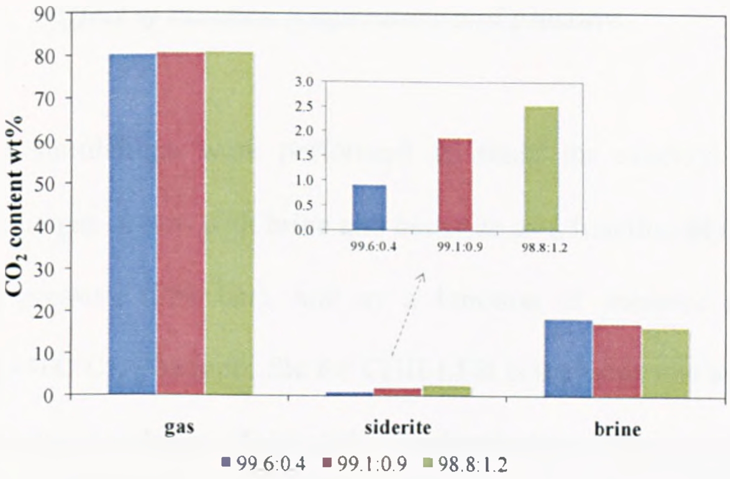

Figure 5-6. Carbon partitioning amongst the different phases, gas, siderite and brine, for varying relative amounts of $CO_2$ and $SO_2$ in the gas added to the reactive system.

The $CO_2$ content in carbonate form goes from 0.9% in the gas stream containing 0.4% of $SO_2$, to 1.9 and 2.5% for streams containing 0.9 and 1.2% respectively (Figure 5-6 inner graph). As a result, the $CO_2$ content in brine slightly decreases at higher $SO_2$ amounts and consequently, a slight $CO_2$ content increase is observed for the gas phase.

The desired stoichiometric molar ratio for $CO_2$ to $SO_2$ indicated by reaction [5-4] is 2:1, but the ratio in the simulation where all of the hematite has been consumed is ~ 9:1, excluding the $CO_2$ remaining in the supercritical gas phase, due to the large amount of $CO_2$ remaining dissolved in solution.

$Fe_2O_3$ (hematite) + 2 $CO_2$ + $SO_2$ + $H_2O$ ↔ 2 $FeCO_3$ (siderite) + $H_2SO_4$ [5-4]

### *5.2.1.3. Effect of reaction temperature and pressure*

A series of simulations were performed to study the reaction of a $CO_2$ dominated flue gas stream with brine and hematite as a function of temperature at constant pressure (250 bar), and as a function of pressure at constant temperature (100°C). The input file for CHILLER is the same one as shown for the baseline case simulation (Table 5-1). Qualitatively, graphs are very similar to the ones obtained in section 5.2.1.1 so they are not shown again here.

Obtained modelling results for both series of simulations will be compared in Chapter 7 with the experimental results obtained in those experiments carried out under the same reaction conditions.

### *5.2.1.4. Effect of solids concentration*

Simulations were constructed to test the effect of varying the rock-to-brine ratio in the mineral trapping capacity of hematite. In all simulations, the input file for CHILLER was the same one as the one shown for the baseline case simulation (Table 5-1).

The higher the solid-to-brine ratio (i.e, solids concentration), the wider the range of total amount of gas added where siderite is precipitated (Figure 5-7), due to the higher amount of iron present in the system to be carbonated.

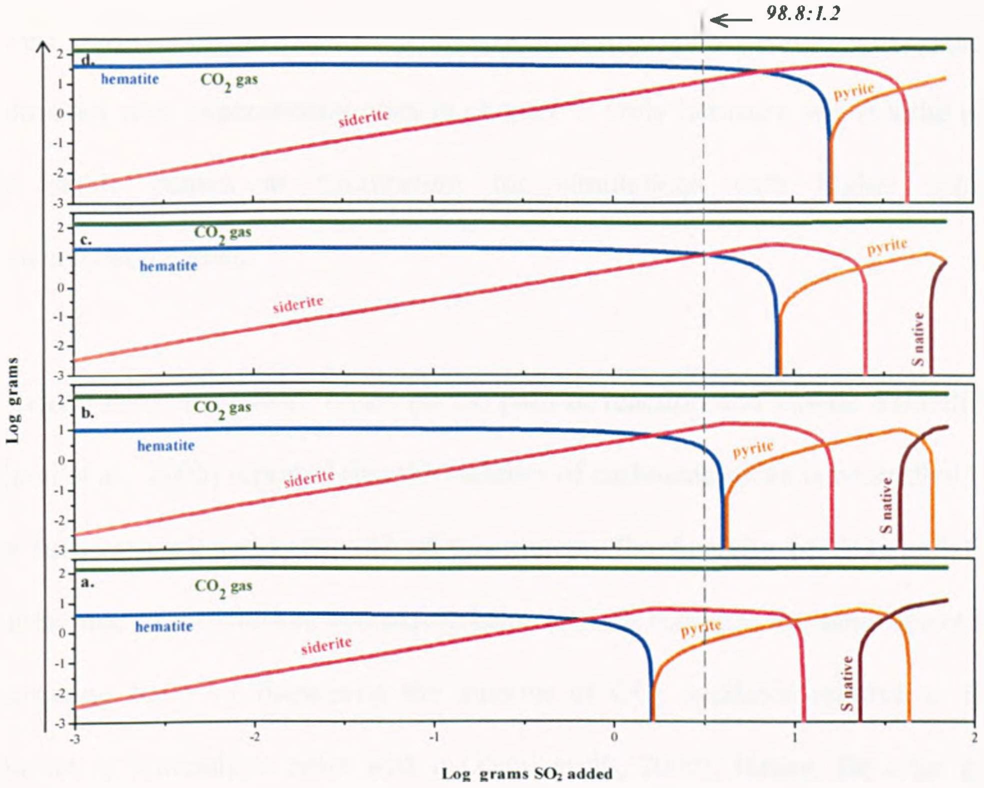

Figure 5-7. Reaction at 100°C and 250 bar of mixtures of $CO_2$ and $SO_2$ and 1.0mNaCl, 0.5mNaOH previously equilibrated with 10 g of hematite. Equilibrium mineral assemblage vs. log grams of $SO_2$ added. Solids concentration: (a.) 10 g/L; (b.) 25g/L; (c.) 50g/L; (d.) 100g/L.

Patterns of hematite dissolution and siderite, pyrite and S native formation and re-dissolution are similar for all the cases but for the highest solids concentration value (100 g/L), no S native is observed at the end of the simulation. As the solids concentration value increases, precipitation of secondary minerals is shifted to higher values of $SO_2$ gas added, due to the presence of more solid in the system to be reduced and carbonated. Precipitates that form at high $SO_2$ contents in the gas stream, i.e., pyrite and S native, would be delayed due to the wider range of siderite precipitation at higher solid-to-brine ratios. Equilibrium predictions obtained for a $CO_2$:$SO_2$ gas concentration (vol. %) of 98.8:1.2 (see vertical line in Figure 5-7) show pyrite and siderite as the only stable solid phases present in the system for a solids concentration of

10 g/L, with all the hematite been already consumed. Latter results will be then compared with experimental ones in chapter 7. Only hematite and siderite are the stable phases at equilibrium for simulations with higher solids concentration values.

Previous theoretical work based on the path of reaction and kinetic modelling (Zerai et al., 2006) reported that the stability of carbonate rocks is controlled by the brine-to-rock ratio, the pH of the system, the fugacity of $CO_2$ and the kinetic rate of dissolution. Increasing brine-to-rock ratio has the same effect as increasing $fCO_2$ by increasing the amount of $CO_2$ available relative to the amount of minerals to react with it (Zerai et al., 2006). Hence, for a set gas composition, a higher extent for the carbonation reaction is obtained for decreasing rock-to-brine ratios: 93.2% of the iron content in the unreacted material was trapped in siderite for the simulation performed with 10 g/L; this value goes down to 77.3%, 38.6% and 19.3% for the simulations with 25, 50 and 100 g/L respectively (conversions calculated by Equation 5-1).

#### *5.2.1.5. Effect of a pH buffer*

A thermodynamic equilibrium simulation was constructed at 100°C and 250 bar without the presence of a pH buffer (NaOH). This simulation establishes whether siderite is a thermodynamically favored reaction product when natural mineral buffering is not present. In the non-buffered case the input file for CHILLER was the one shown in Table 5-2. Modelling results are compared with the simulation obtained for the baseline case, which is identical except for the absence of the NaOH pH buffer.

Table 5-2. Initial test file for CHILLER: $CO_2$-$SO_2$ reaction at 100°C and 250 bar with 10 g of hematite in 400 mL of 1.0mNaCl brine using 165g (excess) $CO_2$. Parameters in the table are defined in CHILLER's manual (Reed and Spycher, 2006).

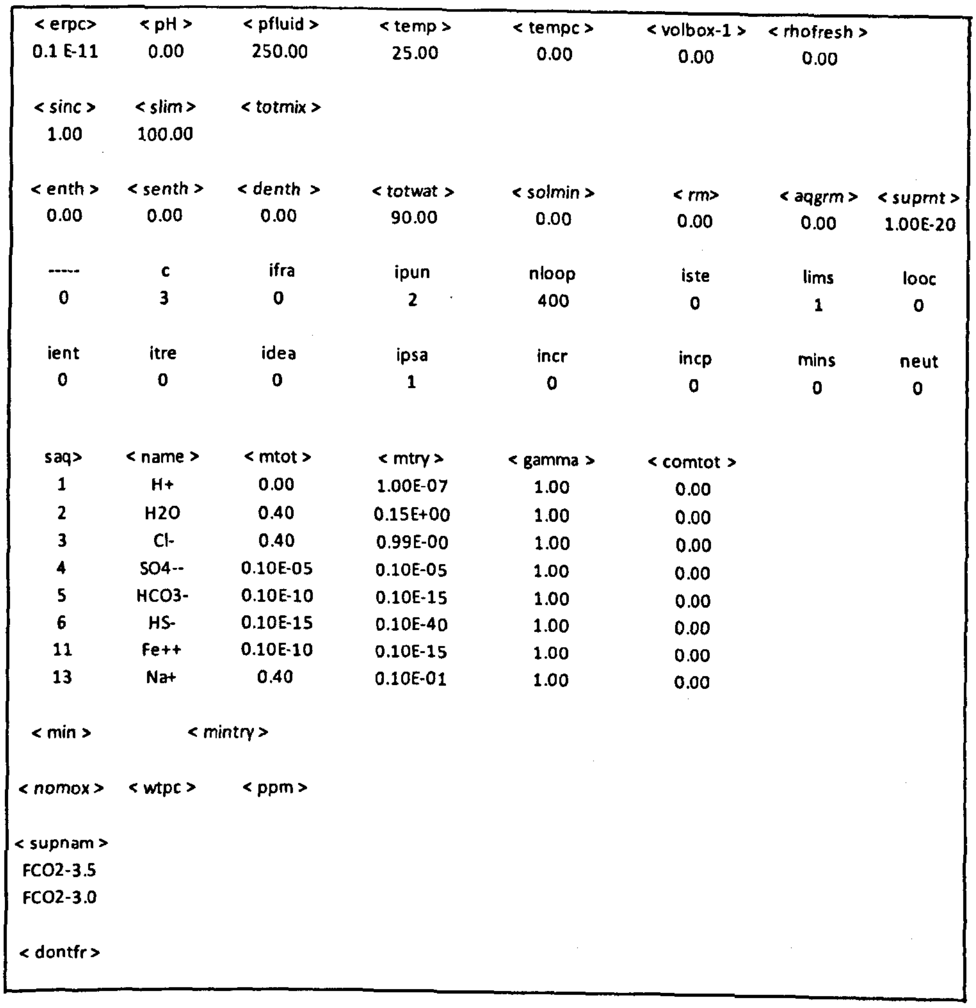

```
< erpc>    < pH >    < pfluid >   < temp >    < tempc >   < volbox-1 > < rhofresh >
0.1 E-11   0.00      250.00       25.00       0.00        0.00         0.00

< sinc >   < slim >  < totmix >
1.00       100.00

< enth >   < senth > < denth >    < totwat >  < solmin >  < rm>        < aqgrm >  < suprnt >
0.00       0.00      0.00         90.00       0.00        0.00         0.00       1.00E-20

-----      c         ifra         ipun        nloop       iste         lims       looc
0          3         0            2           400         0            1          0

ient       itre      idea         ipsa        incr        incp         mins       neut
0          0         0            1           0           0            0          0


saq>       < name >  < mtot >     < mtry >    < gamma >   < comtot >
1          H+        0.00         1.00E-07    1.00        0.00
2          H2O       0.40         0.15E+00    1.00        0.00
3          Cl-       0.40         0.99E-00    1.00        0.00
4          SO4--     0.10E-05     0.10E-05    1.00        0.00
5          HCO3-     0.10E-10     0.10E-15    1.00        0.00
6          HS-       0.10E-15     0.10E-40    1.00        0.00
11         Fe++      0.10E-10     0.10E-15    1.00        0.00
13         Na+       0.40         0.10E-01    1.00        0.00

< min >              < mintry >

< nomox >  < wtpc >  < ppm >

< supnam >
FCO2-3.5
FCO2-3.0

< dontfr >
```

In the non-buffered simulation, the desired product, siderite, is thermodynamically stable over a wide range of total $SO_2$ grams added, from -1.36 to 0.94 log g added (40 mg - 8.8 g) (Figure 5-8 b.). The main difference between this simulation and the pH-buffered one is the wider range of total gas added where siderite precipitates, where in the latter case, ranges from -5.4 to 1.21 log total grams $SO_2$ added (4 μg – 16.4 g) (Figure 5-8 a.).

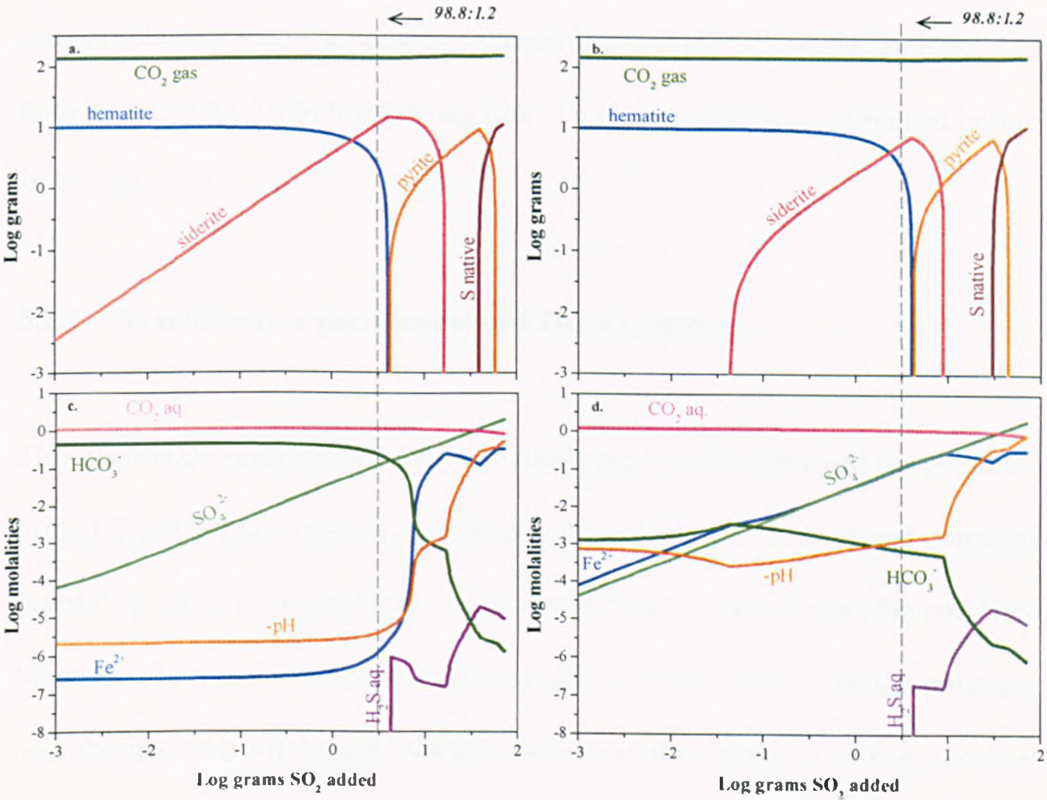

Figure 5-8. Results summary from simulations at 100°C and 250 bar of the $CO_2$-$SO_2$ reaction with 10g of hematite: buffered case (left) and un-buffered case (right). Mineral/gas phase assemblage is depicted in top graphs (a. and b.) and fluid composition in bottom ones (c. and d.).

Overall, the main differences when comparing the fluid composition for simulations with and without pH buffering are a much lower pH and higher dissolved $Fe^{II}$ concentration (Figure 5-8 c. and d.) due to a lower degree of siderite precipitation for the non pH-buffered case. The total dissolved $Fe^{II}$ concentration increases steadily over the course of the simulation, i.e. with $SO_2$ addition, for the unbuffered case. Also, brine pH increases initially due to hematite dissolution, which consumes $H^+$, to a point where siderite becomes the stable phase in the system and starts to precipitate (Figure 5-8 d.). From that point on, pH decreases due to siderite precipitation, which generates acidity. A further decrease is observed when pyrite precipitates and finally, S native formation also generates more acidity in the system. It is also remarkable how the bicarbonate concentration and pH follow the same trend in both simulations due to their strong link in a closed system, as explained before in section 5.2.1.

### 5.2.2. Reactions in a goethite-brine-$CO_2$-$SO_2$ system

This section presents modelling (i.e. equilibrium) results obtained for goethite-brine-$CO_2$/$SO_2$ gas reactions. Goethite is investigated as a novel and potential repository for $CO_2$ mineral trapping in two different cases: firstly, the goethite-brine-$CO_2$/$SO_2$ gas reaction is evaluated at 150°C and 300 bar in the presence and absence of a pH buffer (NaOH). Secondly, the influence of particle size, reaction time and gas composition on the carbonation reaction is also assessed at 100°C and 250 bar for further comparison with experimental results obtained in Chapter 8.

#### *5.2.2.1. Results in a goethite-brine-$CO_2$-$SO_2$ system at 150°C and 300bar*

Two thermodynamic equilibrium simulations were constructed at 150°C and 300 bar. The only difference between them was the presence or absence of a pH buffer (NaOH). The input files for CHILLER are the same ones as for the hematite case for the buffered (Table 5-1) and unbuffered case (Table 5-2) except for the following parameters: <pfluid> (pressure of the system), and <mtot> (total number of moles) for the component species $H_2O$, Cl- and Na+. In this case, <pfluid> = 300 and <mtot> = 0.15 for the three component species mentioned above.

In the simulation with the NaOH buffer, the computed pH of the fluid with the buffer is 13.4 compared to 5.8 for the case without the buffer. Equilibration of the fluid with goethite at the reaction conditions yields a pH of 10.9 and 5.8 for buffered and non-buffered cases respectively. Further equilibration with excess supercritical $CO_2$ yields a pH of 5.9 and 3.3 for the above cases. Finally, simulations are completed with incremental $SO_2$ addition and the obtained results are discussed below.

Figure 5-9 shows the equilibrium mineral/gas phase assemblage and fluid composition for increasing amounts of $SO_2$ gas added for the simulations with and without pH buffering. Qualitatively, graphs are very similar to the ones obtained in the simulations for hematite, previously discussed in detail in sections 5.2.1.1 and 5.2.1.5. Thereby, the graphs will not be explained again in this section.

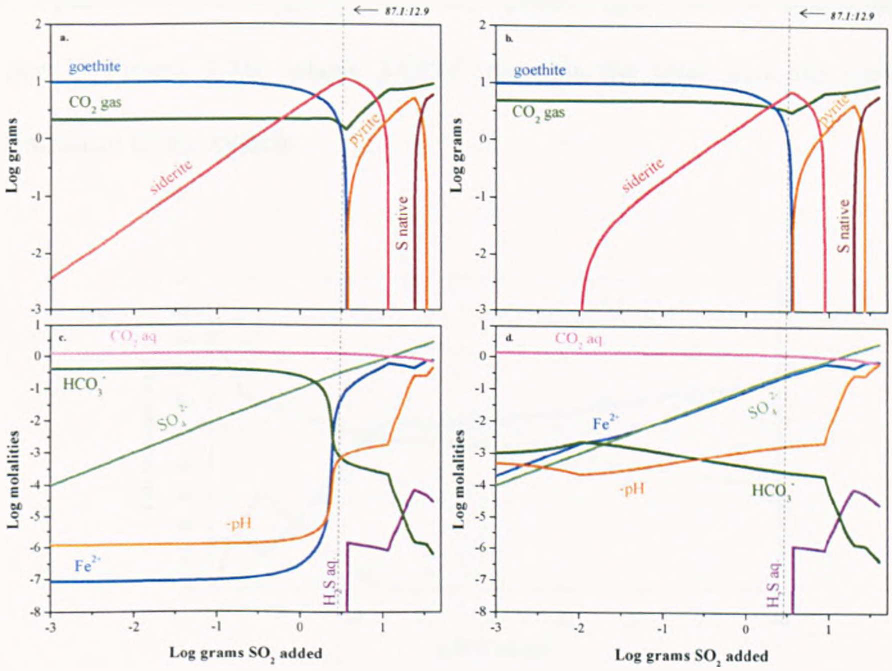

Figure 5-9. Results summary from simulations at 150°C and 300 bar of the $CO_2$-$SO_2$ reaction with 10g of goethite: buffered case (left) and un-buffered case (right). Mineral/gas phase assemblage is depicted in top graphs (a. and b.) and fluid composition in bottom ones (c. and d.).

Due to the wider range of added $SO_2$ where siderite precipitates in the system with a pH buffer, this case was selected for the experimental run, aiming to observe the desired carbonate product, siderite, on the time scale of a laboratory experiment. The vertical line in Figure 5-9 indicates the amount of $SO_2$ chosen for the experimental case, 0.48 log g (3 g) of $SO_2$ added, because at that point the amount of precipitated siderite is close to its maximum. The equilibrium mineral assemblage should consist only of goethite and siderite, with a conversion of 78.2% of the Fe present in the goethite into siderite (calculated according to Equation 5-2) and 0.39 g of $CO_2$ sequestered in siderite per g of sample.

Carbon partitioning amongst the different phases (gas, siderite and brine) can be seen in Figure 5-10, where $\sum CO_3^{2-}$ denotes the total aqueous carbonate concentration in the system.

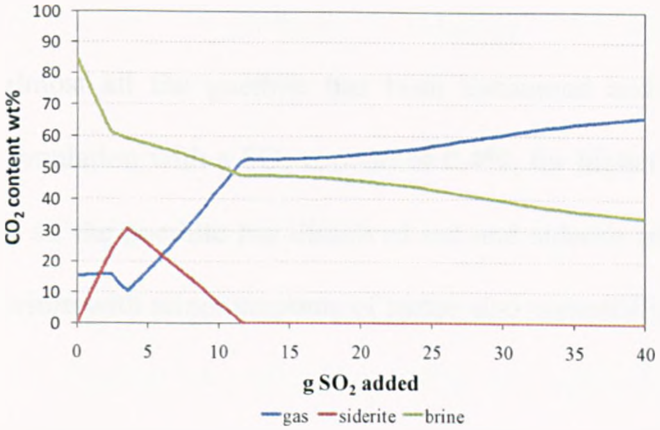

Figure 5-10. Carbon partitioning in the system for the pH-buffered simulation at 150°C and 300bar.

Siderite precipitation reaches its maximum at a gas ratio of ~ 80/20 wt% (corresponding to 3.6 g of $SO_2$ added), where ~ 30% of the $CO_2$ is contained in the carbonate. Even at that inflexion point, the pore fluid contains about 2 times (~ 60%) the amount of $CO_2$ present in the solid in a given volume of brine and solid. For a gas stream containing 12.9% $SO_2$ (experimental case), 60% of the $CO_2$ is trapped in brine followed by trapping in carbonate form (27.2%), i.e. siderite, and in supercritical gas phase (12.7%).

### 5.2.2.2. *Results in a goethite-brine-$CO_2$-$SO_2$ system at 100°C and 250 bar*

Geochemical modelling predictions are qualitatively very similar to the ones obtained for the long-term experiment (Figure 5-9) so the graphs will not be shown again here. One simulation was performed for the baseline case (100°C, 250 bar, 1.0m NaCl 0.5m NaOH and solids concentration = 10g/L) where the effect of varying amounts of $SO_2$ gas in the system can be studied. Again, the input file for CHILLER was the same one as for the hematite case (Table 5-1).

In this case, almost all the goethite has been consumed and converted to siderite in the simulation with a $SO_2$ content of 0.4%; for higher $SO_2$ contents (0.9 and 1.2%), all the goethite has dissolved out and siderite is the predicted phase at equilibrium with minor amounts of pyrite also present (Figure 5-11).

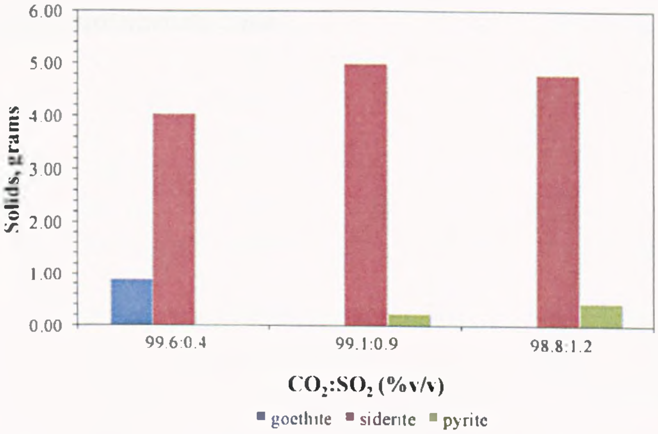

Figure 5-11. Goethite, siderite and pyrite predicted amounts (in grams) at equilibrium in experiments with varying relative amounts of $CO_2$ and $SO_2$ in the gas added.

Predicted solid phases at equilibrium differ from those obtained in the simulation with hematite because the solids concentration value was different: 25 g/L was the one used for hematite whereas 10 g/L was used for goethite instead. A lower rock-to-brine ratio in the goethite modelling work results in an increase of the amount of $CO_2$ available relative to the amount of solids to react with it. Thereby, a higher extent for goethite dissolution and carbonation reactions is obtained compared to the 25 g/L case.

The small solid-to-liquid ratio used in the simulations enhanced goethite reactivity, so most of the starting material was already consumed and successfully converted into siderite in the simulation with a 0.4% content of $SO_2$. Further $SO_2$ addition yielded some pyrite formation so siderite and pyrite are the only stable phases at equilibrium in simulations with 0.9 and 1.2% of $SO_2$ content.

Solids particle size and reaction time are not taken into account by the geochemical model so their effect in the carbonation reaction is evaluated empirically and further compared (brine chemistry and mineral assemblage) in Chapter 8 with the equilibrium case.

## 5.3. References

Fernandez Bertos, M., Simons, S. J. R., Hills, C. D. & Carey, P. J. (2004) A review of accelerated carbonation technology in the treatment of cement-based materials and sequestration of $CO_2$. *Journal of Hazardous Materials B,* 112, 193-205.

Helgeson, H. C., Delany, J. M., Nesbitt, H. W. & Bird, D. K. (1978) Summary and Critique of the Thermodynamic Properties of Rock-Forming Minerals. *American Journal of Science,* 278, 1-229.

Helgeson, H. C., Kirkham, D. H. & Flowers, G. C. (1981) Theoretical Prediction of the Thermodynamic Behavior of Aqueous-Electrolytes at High-Pressures and Temperatures .4. Calculation of Activity-Coefficients, Osmotic Coefficients, and Apparent Molal and Standard and Relative Partial Molal Properties to 600-Degrees-C and 5 Kb. *American Journal of Science,* 281, 1249-1516.

Holland, T. J. B. & Powell, R. (1998) An internally consistent thermodynamic data set for phases of petrological interest. *Journal of Metamorphic Geology,* 16, 309-343.

Johnson, J. W., Oelkers, E. H. & Helgeson, H. C. (1992) Supcrt92 - a Software Package for Calculating the Standard Molal Thermodynamic Properties of Minerals, Gases, Aqueous Species, and Reactions from 1-Bar to 5000-Bar and 0-Degrees-C to 1000-Degrees-C. *Computers & Geosciences,* 18, 899-947.

Palandri, J. L. & Reed, M. H. (2001) Reconstruction of in situ composition of sedimentary formation waters. *Geochimica Et Cosmochimica Acta,* 65, 1741-1767.

Palandri, J. L. & Reed, M. H. (2004) Geochemical models of metasomatism in ultramafic systems: Serpentinization, rodingitization, and sea floor carbonate chimney precipitation. *Geochimica Et Cosmochimica Acta,* 68, 1115-1133.

Palandri, J. L., Rosenbauer, R. J. & Kharaka, Y. K. (2005) Ferric iron in sediments as a novel $CO_2$ mineral trap:$CO_2$-$SO_2$ reaction with hematite. *Applied Geochemistry,* 20, 2038-2048.

Reed, M. H. (1982) Calculation of Multicomponent Chemical-Equilibria and Reaction Processes in Systems Involving Minerals, Gases and an Aqueous Phase. *Geochimica Et Cosmochimica Acta,* 46, 513-528.

Reed, M. H. & Spycher, N. F. (2006). Users guide for CHILLER: A program for computing water-rock reactions, boiling, mixing and other reaction processes in aqueous-mineral-gas systems and minplot guide (Third Edition), University of Oregon, Eugene.

Shock, E. L., Sassani, D. C., Willis, M. & Sverjensky, D. A. (1997) Inorganic species in geologic fluids: Correlations among standard molal thermodynamic properties of aqueous ions and hydroxide complexes. *Geochimica Et Cosmochimica Acta,* 61, 907-950.

Spycher, N. F. & Reed, M. H. (1988) Fugacity Coefficients of $H_2$, $CO_2$, $CH_4$, $H_2O$ and of $H_2O$-$CO_2$-$CH_4$ Mixtures - a Virial Equation Treatment for Moderate Pressures and Temperatures Applicable to Calculations of

Hydrothermal Boiling. *Geochimica Et Cosmochimica Acta,* 52, 739-749.

Stumm, W. & Morgan, J. J. (1996) *Aquatic chemistry: chemical equilibria and rates in natural waters,* New York, Wiley-Interscience.

Symonds, R. B. & Reed, M. H. (1993) Calculation of Multicomponent Chemical-Equilibria in Gas-Solid-Liquid Systems - Calculation Methods, Thermochemical Data, and Applications to Studies of High-Temperature Volcanic Gases with Examples from Mount St-Helens. *American Journal of Science,* 293, 758-864.

Tanger, J. C. & Helgeson, H. C. (1988) Calculation of the Thermodynamic and Transport-Properties of Aqueous Species at High-Pressures and Temperatures - Revised Equations of State for the Standard Partial Molal Properties of Ions and Electrolytes. *American Journal of Science,* 288, 19-98.

Zerai, B., Saylor, B. Z. & Matisoff, G. (2006) Computer simulation of $CO_2$ trapped through mineral precipitation in the Rose Run Sandstone, Ohio. *Applied Geochemistry,* 21, 223-240.

## CHAPTER 6

# CHARACTERISATION OF PARENT SAMPLES

# 6. Characterisation of parent samples

This chapter describes the results from the different analyses conducted on the parent samples, hematite and goethite, used in the experimental work. Characterization of the initial non-reacted material is important for further comparison with results from analyses conducted on reacted samples.

## 6.1. Particle size analysis/ grain-size distribution

The parent material was crushed, ground and sieved to different size fractions according to the following procedure: starting material was crushed to a size of about 1-3 mm by means of a jaw crusher. The material was then ground in a harden steel Tema mill (vibrating disc/ring mill) during 20s for fine powdering of the sample. This material was dry sieved to segregate three different particle size fractions (< 38 μm, 38-150 μm and 150-300 μm). After size separation, washing of the material was needed to remove the fines. The size fractions were then dried for 1h in an oven at 105°C and the material was further dry sieved for 20 min.

A particle size analysis was carried out for each fraction to ensure the desired size fractions had been prepared. Figure 6-1 and Figure 6-2 show the particle size distribution of the prepared fractions in non-cumulative and cumulative percentages, respectively. Distribution of particles within each size fraction is confirmed by the analysis although there are some discrepancies between a sieve size analysis and the use of laser light scattering. This is particularly highlighted for the prepared top size fractions of the goethite sample.

The cumulative curves (Figure 6-2) should start at zero and remain there until the lower-end of the desired size fraction interval. They should reach the value of 100% at the upper-end of such interval and above. However, there is a percentage of particles beyond the intended sieve fractions. For hematite, the different fractions contain 92.5 % (<38 µm), 75.2% (38-150 µm) and 62.5% (150-300 µm) of the material within the intended range, whereas for goethite those percentages are of 75.0, 73.4, 48.7 and 40.8% for size fractions of <38, 38-150, 75-150 and 150-300 µm respectively. The extra size fraction prepared for goethite (75-150 µm) was the one used in the long-term experiment run in the gold-titanium flexible reaction cell; this fraction had been reported as the one used in previous experimental work with hematite (Palandri et al., 2005) and was used to facilitate comparison amongst results. The percentage of particles observed below the lower-end value of each size fraction interval is probably due to the limitation of the sieving method, being almost impossible to get rid of all the fines within each fraction. Also, the washing process is a limiting factor for the presence of fines. The percentage obtained above the upper-end limit of the intended particle size range can be due to either one or several of the following reasons:

a) Agglomeration of particles in suspension during the measurement.
b) Laser diffraction provides a two dimensional particle size measurement so lack of the third dimension could lead to wrong values depending on

which dimension has been considered for the calculation. This could be notably remarkable with elongated and anomalously large particles.

c) One drawback of sieving is the fact that the longer the sieving time, the higher the probability that particles orientate themselves and fall through the sieve. Hence, particles with larger size than the top intended one could end up in the fraction for analysis.

d) The particle size fractions were not sieved successfully, probably due to too much material on the sieve (~ 50g), which could be responsible for the very wide particle size distributions.

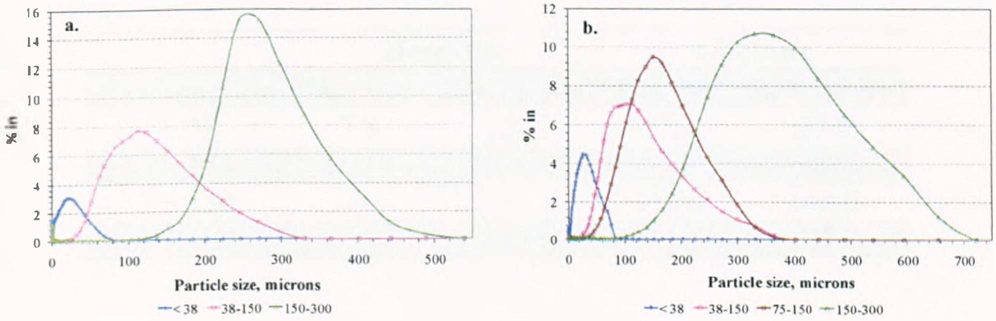

Figure 6-1. Particle size distribution of the prepared hematite (a) and goethite (b) fractions (non-cumulative percentage).

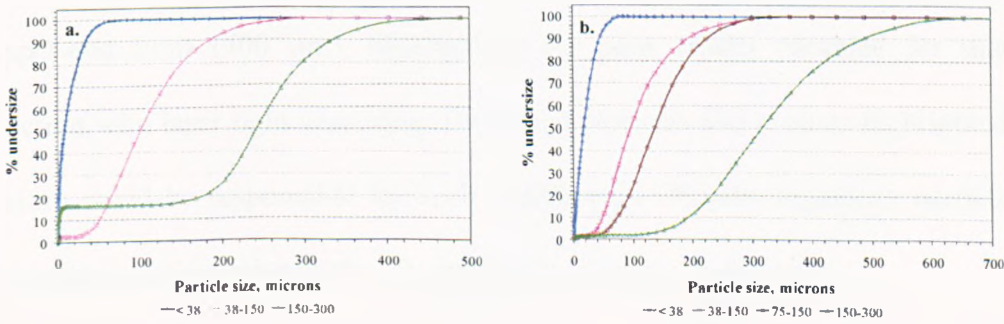

Figure 6-2. Particle size distribution of the prepared hematite (a) and goethite (b) fractions (cumulative percentage).

The equivalent volume mean (D(4,3)) and the volume median diameter (D(v,0.5), sometimes shown as $D_{50}$ or $D_{0.5}$) are reported in Table 6-1. The D(4,3) is calculated according to the following formula (Rawle, 2000):

$$D[4,3] = \frac{\sum d^4}{\sum d^3} \quad d \equiv particle\ diameter$$

This formula indicates around which central point of the frequency the particle size distribution would focus. $D_{50}$ is the value of the particle size which divides the population exactly into two equal halves i.e. there is 50% of the distribution above this value and 50% below.

Table 6-1. D50and D(4,3) values of the prepared hematite and goethite fractions.

| | Hematite | | Goethite | |
|---|---|---|---|---|
| **Fraction, µm** | **$D_{50}$, µm** | **D(4,3), µm** | **$D_{50}$, µm** | **D(4,3), µm** |
| **< 38** | 7.8 | 12.9 | 17.3 | 20.8 |
| **38-150** | 100.4 | 108.8 | 96.2 | 109.7 |
| **75-150** | ---- | ---- | 136.6 | 143.0 |
| **150-300** | 225.5 | 199.8 | 315.5 | 325.2 |

For the top fractions, disparities between particle size analysis with sieving and laser light scattering are more remarkable than for the bottom ones. For instance, the $D_{50}$ value for the 150-300 µm goethite fraction is beyond the upper-end limit (300 µm), highlighting the poor results obtained for this fraction with laser light scattering. Elongated particles and reasons highlighted before could be responsible for such a difference. Results regarding particle size remain informative as the disparities are internally consistent.

## 6.2. X-ray diffraction (XRD) analysis

Diffraction patterns from XRD analyses indicate that, as expected, the hematite sample is primarily composed of the ferric iron oxide ($Fe_2O_3$), with a minor amount of kaolinite ($Al_2Si_2O_5(OH)_4$) also present (Figure 6-3). The XRD spectra for the goethite sample (Figure 6-4) confirmed the presence of the iron oxyhydroxide only.

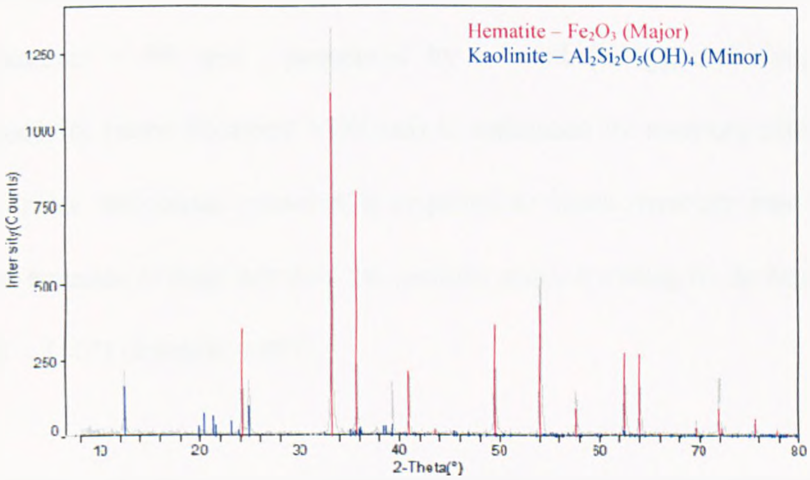

Figure 6-3. X-ray diffraction spectra for parent hematite material (<38 μm).

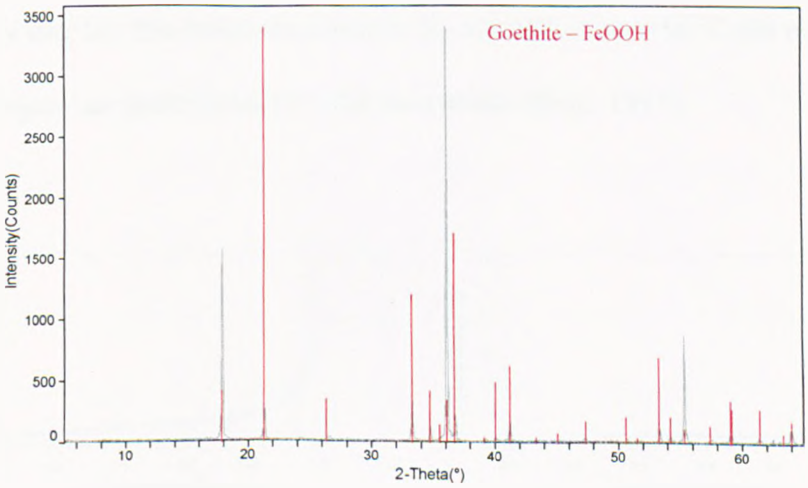

Figure 6-4. X-ray diffraction spectra for parent goethite material (<38 μm).

Kaolinite is a common hydrous aluminum silicate mineral found in sediments, soils, hydrothermal deposits, and sedimentary rocks; thereby, its presence in the hematite sample is possibly due to the natural character of the latter one.

## 6.3. Surface area analysis

BET-$N_2$ adsorption isotherms are used for estimating porosity and internal surface area. Six major types of isotherms describe the different kind of porosity, microporosity (pore diameter < 2nm) and/or mesoporosity (2 nm < pore diameter < 50 nm) , presented by a solid (Gregg and Sing, 1982). Macroporosity (pore diameter > 50 nm) is estimated by mercury porosimetry. In the former technique, pressure is required to force mercury into the solid structure because it does not wet the sample surface owing to its high contact angle ($\theta \sim 140°$) (Patrick, 1995).

The isotherms observed for parent hematite and goethite samples are presented in Figure 6-5 and can be classified as a type II isotherm. Substances that typically display this behavior towards $N_2$ adsorption at -196°C are non porous or macroporous (pore diameter > 50 nm) solids (Sing, 1995).

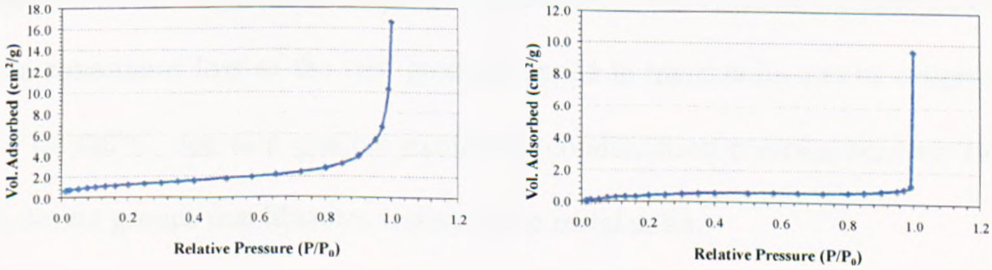

Figure 6-5. $N_2$ adsorption isotherms for hematite (left) and goethite (right) parent samples.

The internal surface area was calculated for all the different size fractions obtained for hematite and goethite using the BET (Brunauer, Emmett and Teller) equation. Values obtained ranged from 2 to 5 ± 0.1 $m^2/g$, which again highlight the non porous or macroporous character of all the prepared samples. Hence, reactivity of different size fractions and materials may be due to their external surface area and differences in reactivity due to internal surface area are not expected to be significant.

## 6.4. Thermogravimetric characterization

Thermogravimetric analysis (TGA) was used to determine the temperature regions of weight loss resulting from physical and chemical bond cleavage with release of volatile products.

### 6.4.1. Hematite analysis

Hematite thermogravimetric analysis reveals weight loss associated mainly with kaolinite since the iron oxide does not decompose at temperatures below 900°C. For kaolinite, the larger dehydroxylation phenomenon which corresponds to metakaolin ($Al_2Si_2O_7$) formation (reaction [6-1]), is limited to the 450-700°C temperature range (Castelein et al., 2001, He et al., 2003), even if a continuous loss of the $OH^-$ groups trapped in metakaolin can be observed up to 900°C, due to a gradual oxolation (condensation reaction between two hydroxyl groups that liberates water) of the metakaolin.

$$2\ Al_2Si_2O_5(OH)_4 \longrightarrow 2\ Al_2Si_2O_7 + 4\ H_2O \qquad [6\text{-}1]$$

The TGA profile of hematite (Figure 6-6) shows an initial and continuous weight loss until a temperature of around 380°C, where the dehydroxylation process takes place and therefore the loss of hydroxyl water content of the kaolinite. Assuming this weight loss is only due to the presence of kaolinite and its complete decomposition, the percentage of the latter one in the hematite sample can be calculated (similarly to calculations shown in the next section), giving a value of 17.42%.

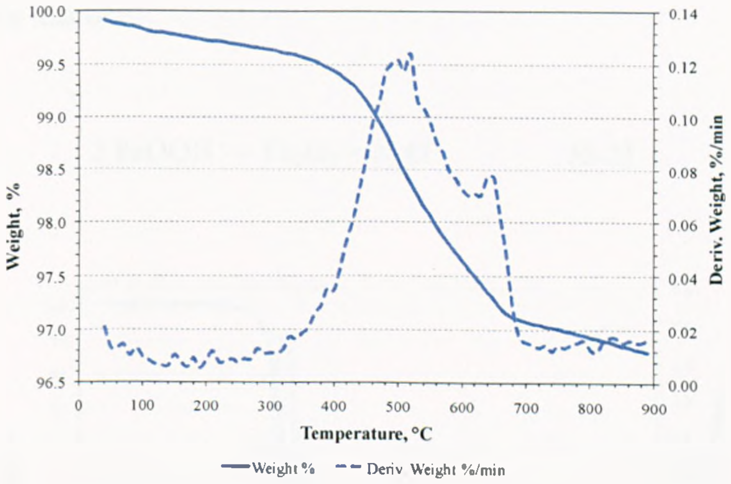

Figure 6-6. TGA decomposition temperature profile of parent hematite sample.

Even pure oxides contain some OH in the structure, if fine-grained, but this is driven off over a much wider temperature range than is that of the FeOOH forms. Fine-grained material normally contains an appreciable amount of adsorbed water which leads to a weight loss between 100 and 200°C and this can usually be distinguished from water of dehydroxilation (Cornell and Schwertmann, 2003).

### 6.4.2. Goethite analysis

Goethite thermogravimetric analysis showed only one weight loss corresponding to the dehydroxylation process of the iron oxyhydroxide (Figure 6-7). The absence of weight loss and subsequently one peak in the derivative weight curve at around 100°C, indicates that no adsorbed water is present in the sample. The weight loss starting at ~ 241°C corresponds to the dehydroxylation of the iron oxyhydroxide to α-$Fe_2O_3$ (hematite) according to the following reaction:

$$2\ FeOOH \rightarrow Fe_2O_3 + H_2O \qquad [6\text{-}2]$$

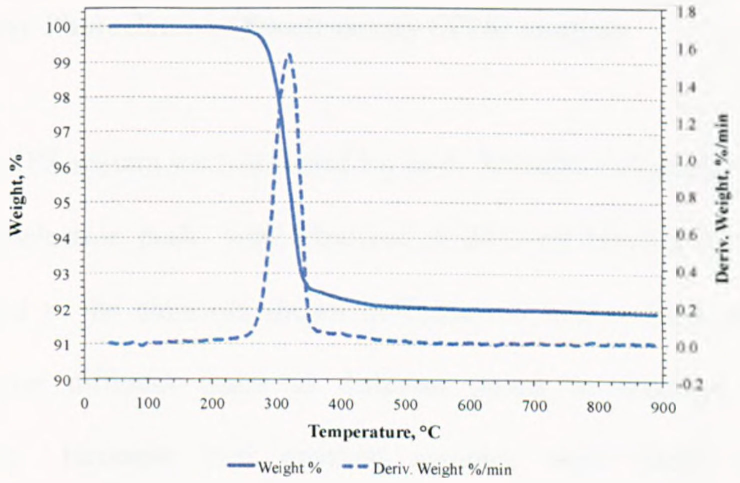

Figure 6-7. TGA decomposition temperature profile of parent goethite sample.

The theoretical mass loss ($\Delta m$) due to the above reaction can be easily calculated with the following formula:

$$\Delta m = \frac{m_i - m_f}{m_i} \qquad \text{Equation 6-1}$$

where $m_i$ and $m_f$ are the initial and final mass respectively.

The calculated mass loss value (%) for the dehydroxylation process of goethite according to Equation 6-1 is 10.13% versus the experimental value of 7.7%. The disagreement between the calculated and experimental values might be due to the fact that the goethite sample is not 100% pure and therefore, the theoretical weight loss would need to be recalculated considering the weight percentage of the iron oxyhydroxide in the parent sample. The disagreement could also be due to non-optimum conditions (lack of time for complete decomposition due to a ramp-like method) in the operation of the thermogravimetric analyser.

## 6.5. X-ray Photoelectron Spectroscopy (XPS) analysis

Wide scan XPS spectra were obtained for both, hematite and goethite samples, where photoelectron peaks were observed at different binding energies (BE) and assigned to the elements shown in Table 6-2 below. Each sample was analysed four different times in different points in order to test their homogeneity. Hematite and goethite samples were found reasonably homogeneous.

Table 6-2. Results of wide scan XPS analysis of hematite and goethite samples in atomic relative percentage. Terms in brackets next to the element symbols indicate the photoelectron emission used in the analysis. Values shown have been computed as the average value of four different measurements.

| Sample | Na [1s] | Fe [2p] | O [1s] | C [1s] | Cl [2p] | S [2p] | Si [2p] | Al [2p] | F [1s] | Cr [2p] | N [1s] |
|---|---|---|---|---|---|---|---|---|---|---|---|
| hematite | 0.04 | 5.01 | 60.40 | 11.43 | 0.22 | 0.12 | 12.49 | 8.21 | 1.21 | 0.08 | 0.80 |
| goethite | 3.1 | 7.4 | 47.7 | 22.6 | 1.6 | 1.5 | 4.3 | 1.4 | 10.4 | --- | --- |

The presence of kaolinite in the hematite material is verified with XPS, as indicated by the high atomic relative percentages of Al and Si on the surface of the sample (8.21 and 12.49% respectively), which agrees well with results from thermal analysis that also showed the presence of the silicate. Thereby, kaolinite is present in both, bulk and surface of the hematite sample. Other minor impurities are also found on the surface of both minerals such as Na, C, Cl, S, F, Cr and N; elements assigned to all the peaks obtained in the spectra are reported but some of them could be discarded due to its extremely small percentage.

The presence of $F^-$ ions on the surface of iron oxides could be due to the fluoride-hydroxyl exchange taking place on the solid surface, which has been reported in geological materials (Jinadasa et al., 1993). While the majority of the $F^-$ ions added to the soils by natural or industrial processes tend to become firmly fixed, it has been shown in percolation studies that migration through a soil column can release soluble Al and Fe species. The geochemistry of $F^-$ ion (ionic radius 1.36Å) is similar to that of the $OH^-$ ion (ionic radius 1.40 Å) and there can be easy exchange between them (Jinadasa et al., 1993).

Whenever iron oxides are formed in nature, a range of unwanted elements is normally co-precipitated (Cornell and Schwertmann, 2003) so, in natural samples presence of impurities is expected.

## 6.6. References

Castelein, O., Soulestin, B., Bonnet, J. P. & Blanchart, P. (2001) The influence of heating rate on the thermal behaviour and mullite formation from a kaolin raw material. *Ceramics International,* 27, 517-522.

Cornell, R. M. & Schwertmann, U. (2003) *The Iron Oxides. Structure, Properties, Reactions, Occurrences and Uses,* Weinheim, Wiley-VCH.

Gregg, S. J. & Sing, K. S. W. (1982) *Adsorption, Surface Area and Porosity,* London, Academic Press Inc. Ltd.

He, H. P., Guo, J. G., Zhu, J. X. & Hu, C. (2003) 29Si and 27Al MAS NMR study of the thermal transformations of kaolinite from North China. *Clay Minerals,* 38, 551-559.

Jinadasa, K. B. P. N., Dissanayake, C. B., Weerasooriya, S. V. R. & Senaratne, A. (1993) Adsorption of fluoride on goethite surfaces - implications on dental epidemiology. *Environmental Geology,* 21, 251-255.

Palandri, J. L., Rosenbauer, R. J. & Kharaka, Y. K. (2005) Ferric iron in sediments as a novel $CO_2$ mineral trap:$CO_2$-$SO_2$ reaction with hematite. *Applied Geochemistry,* 20, 2038-2048.

Patrick, J. W. (Ed.) (1995) *Porosity in carbons: characterization and applications,* London, Edward Arnold.

Rawle, A. (2000) Basic principles of particle size analysis. Malvern Instruments Limited.

Sing, K. S. W. (1995) Physisorption of gases by porous carbons. IN PATRICK, J. W. (Ed.) *Porosity in carbons: characterisation and applications*. London, Edward J. Arnold.

# CHAPTER 7

# RESULTS AND DISCUSSION: HEMATITE ANALYSIS

# 7. Results and discussion: hematite analysis

This chapter describes the assessment of an iron oxide, hematite ($\alpha$-$Fe_2O_3$), as a potential host repository for underground $CO_2$ storage in carbonate form. Firstly, the overall carbonation reaction of hematite is experimentally assessed by systematic variation of reaction variables (solids particle size, reaction time, gas composition, reaction temperature and pressure, solid-to-liquid ratio and effect of a pH buffer) in section 7.1. Comparison and discussion of equilibrium and empirical results is also included within that section. Finally, the implications for geological storage of $CO_2$ are discussed in section 7.2.

## 7.1. Study of an iron oxide, hematite, as a potential repository for $CO_2$ storage by mineral trapping

This section presents empirical results obtained for the hematite-brine-$CO_2$/$SO_2$ gas reactions. Table 7-1 summarises the experiments conducted in the high pressure-high temperature experimental set-up designed at the University of Nottingham. Solids particle size, reaction time, gas composition ($CO_2$/$SO_2$), reactor pressure and temperature, concentration of solids, brine composition and measured initial pH of each experiment are reported. The stirring rate was set to a high constant value (750 rpm), so reaction rates will be determined by reaction control rather than by processes in the boundary layer at either the solid/liquid or gas/liquid interface. Previous studies (Huijgen et al., 2006) reported conversion is not influenced by the agitation power at high stirring rates (≥ 500 rpm).

The final pH of the brine as well as dissolved (ferrous) iron in solution were analysed for all experiments. Dissolved ferric iron was also analysed but values are not reported because obtained concentrations were not significant (> 2ppm) in any of the studied cases. Weight gain or loss of reacted solids is also reported.

Preliminary 24h-experiments were conducted to investigate the influence of solid particle size fractions in the dissolution/carbonation reactions; this first set of experiments would set up the solid particle size to be used for the remaining experiments. Reaction time and gas composition are variables of particular significance and therefore a more detailed analysis is described for each of them. Next, study of the rest of reaction variables is discussed.

The gas composition used in the two first sets of experiments, those evaluating particle size and reaction time variables, is the one characteristic of a typical coal-fired power plant flue gas stream (0.4 v/v% of $SO_2$), which is more representative of a real-case scenario. For the remaining sets of experiments, a gas composition with a slightly higher $SO_2$ content (1.2 v/v%) than in a typical flue gas stream, and therefore, closer to the stoichiometric molar ratio (2:1), was chosen for the experimentation in an aim to get an extent of the dissolution and carbonation reactions good enough to be detected on the time scale of a laboratory experiment.

Depending on the studied experimental variable, different analytical techniques were employed to characterise reaction products, with bulk techniques (X-ray diffraction, XRD, or thermal analysis, TGA) being more helpful in long-term experiments than in short-term ones. Obtained XRD results were only relevant for the hematite-brine-$CO_2$-$SO_2$ experiment reacted for 264h; hence, only results for the latter sample are shown in this manuscript. TGA analysis was chosen as the bulk technique and X-ray photoelectron spectroscopy (XPS) was chosen as a surface technique in order to fully characterise the reacted solid samples (i.e. its bulk and surface composition). XPS was only used as an analytical tool in sections evaluating reaction time and gas composition on the carbonation reaction because those sections are considered the most significant ones and the analyses were highly expensive for each sample.

The absence of other analytical methods such as SEM (Scanning Electron Microscopy) or SEM/EDX is due to their failure to throw any significant results. The technique was originally considered because particle sizes are well within the size range appropriate to SEM and the facilities were available, so several samples were analysed by SEM/EDX, but new phases were not identified. Hence, those results are not presented here.

Discussion of results includes validation of the theoretical model in those cases where comparison between theoretical and empirical values is possible.

Table 7-1. Operating conditions and measured initial pH of all experiments with hematite.

| | ***Particle size (μm)*** | ***Time (h)*** | ***$CO_2$:$SO_2$ comp. (vol %)*** | ***Pressure (bar)*** | ***Temperature (°C)*** | ***Solids concentration (g/L)*** | ***Brine composition*** | ***$pH_{initial}$*** |
|---|---|---|---|---|---|---|---|---|
| 1 | **-38** | 24 | 99.6:0.4 | 250 | 100 | 25 | 1.0 m NaCl + 0.5 m NaOH | 12.8 |
| 2 | **38x150** | 24 | 99.6:0.4 | 250 | 100 | 25 | 1.0 m NaCl + 0.5 m NaOH | 12.9 |
| 3 | **150x300** | 24 | 99.6:0.4 | 250 | 100 | 25 | 1.0 m NaCl + 0.5 m NaOH | 12.9 |
| 4 | 150x300 | **62** | 99.6:0.4 | 250 | 100 | 25 | 1.0 m NaCl + 0.5 m NaOH | 13.0 |
| 5 | 150x300 | **163** | 99.6:0.4 | 250 | 100 | 25 | 1.0 m NaCl + 0.5 m NaOH | 13.0 |
| 6 | 150x300 | **264** | 99.6:0.4 | 250 | 100 | 25 | 1.0 m NaCl + 0.5 m NaOH | 12.9 |
| 7 | 150x300 | 24 | **99.1:0.9** | 250 | 100 | 25 | 1.0 m NaCl + 0.5 m NaOH | 13.0 |
| 8* | 150x300 | 24 | **98.8:1.2** | 250 | 100 | 25 | 1.0 m NaCl + 0.5 m NaOH | 13.0 |
| 9 | 150x300 | 24 | 98.8:1.2 | **120** | 100 | 25 | 1.0 m NaCl + 0.5 m NaOH | 13.1 |
| 10 | 150x300 | 24 | 98.8:1.2 | **180** | 100 | 25 | 1.0 m NaCl + 0.5 m NaOH | 13.2 |
| 11 | 150x300 | 24 | 98.8:1.2 | **320** | 100 | 25 | 1.0 m NaCl + 0.5 m NaOH | 13.0 |
| 12 | 150x300 | 24 | 98.8:1.2 | 250 | **75** | 25 | 1.0 m NaCl + 0.5 m NaOH | 12.9 |
| 13 | 150x300 | 24 | 98.8:1.2 | 250 | **125** | 25 | 1.0 m NaCl + 0.5 m NaOH | 13.0 |
| 14 | 150x300 | 24 | 98.8:1.2 | 250 | **150** | 25 | 1.0 m NaCl + 0.5 m NaOH | 12.6 |
| 15 | 150x300 | 24 | 98.8:1.2 | 250 | 100 | **10** | 1.0 m NaCl + 0.5 m NaOH | 12.7 |
| 16 | 150x300 | 24 | 98.8:1.2 | 250 | 100 | **50** | 1.0 m NaCl + 0.5 m NaOH | 12.7 |
| 17 | 150x300 | 24 | 98.8:1.2 | 250 | 100 | **100** | 1.0 m NaCl + 0.5 m NaOH | 12.6 |
| 18 | 150x300 | 24 | 98.8:1.2 | 250 | 100 | 25 | **1.0 m NaCl** | 6.4 |

*baseline experiment; stirring speed= 750rpm for all experiments.

## 7.1.1. Effect of particle size

### *7.1.1.1. Analysis of fluid chemistry and solids weight uptake*

Figure 7-1 shows how the iron in solution (left) varies depending on the particle size range as well as the final pH and solids weight uptake after the reaction (right). Iron in solution is present as ferrous iron indicating that most of the iron that leached out from hematite was successfully reduced from its ferric to its ferrous state. Iron concentration increased very slightly towards the top fractions while weight uptake clearly decreased from 11% in the finest fraction to ~ 7% in the intermediate and top fractions. This could indicate one and/or several iron-containing phases might have precipitated as a result of the experiments, with a higher contribution in the finest fraction, since a low dissolved iron concentration could indicate the iron has been trapped in a solid phase and therefore, the percentage of weight uptake is higher compared to the other fractions. However, it is very unlikely the weight uptake percentage observed in the bottom fraction is only due to an iron-containing precipitate, based on the small difference obtained for dissolved iron concentration of the three particle size ranges.

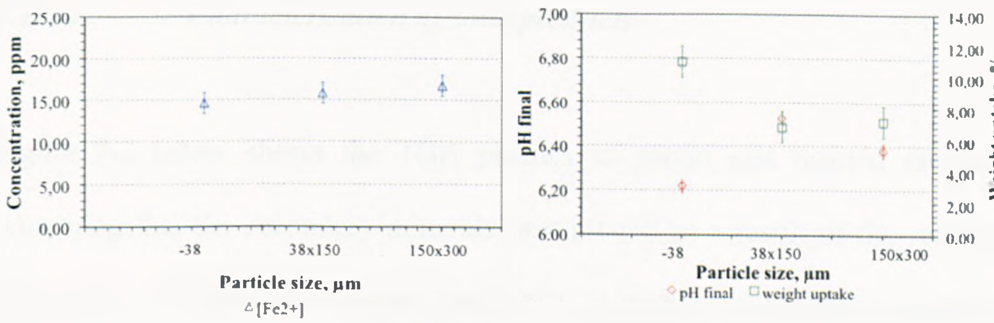

Figure 7-1. Effect of particle size on iron in solution (left) and measured final pH and solids weight uptake (%) (right).

In some instances, different reactivity between size fractions of the same material is explained as a result of their different compositions, with smaller size fractions containing a higher percentage of cations prone to be carbonated (Fernandez Bertos et al., 2004). ICP-AES analysis of the different fractions obtained upon segregation of the parent material has been performed and has shown a higher iron content in the intermediate fraction than in the other ones (Table 7-2), so the latter statement would not be accurate in this case.

Table 7-2. Major-element oxide concentrations (in wt %) of hematite fractions as determined by ICP-AES.

| Particle size, μm | $Fe_3O_4$ | $Al_2O_3$ | MgO | MnO | $TiO_2$ | CaO | $SO_3$ | $P_2O_5$ | $Na_2O$ | $K_2O$ | $SiO_2$ |
|---|---|---|---|---|---|---|---|---|---|---|---|
| **-38** | 79.22 | 9.03 | 0.06 | 0.03 | 0.29 | 0.10 | 0.29 | 0.16 | 0.04 | 0.13 | 10.40 |
| **38-150** | 87.12 | 8.37 | 0.02 | 0.04 | 0.35 | 0.08 | 0.23 | 0.10 | 0.05 | 0.11 | 10.61 |
| **150-300** | 84.83 | 9.23 | 0.02 | 0.03 | 0.36 | 0.08 | 0.22 | 0.31 | 0.05 | 0.13 | 11.57 |

Solution pH is lower in the -38 μm fraction (Figure 7-1), which corresponds with the highest weight uptake percentage. This fact would be consistent with precipitation of one and/or several phases which imply $H^+$ production such as siderite.

### *7.1.1.2. Characterisation of solid products*

Figure 7-2 below shows the TGA profiles of parent and reacted samples. Assuming that the secondary minerals precipitated as a result of the reaction decompose at temperatures lower than 900°C, a higher weight loss is expected to be observed in the finest fraction (-38 μm), since its weight uptake was the highest one.

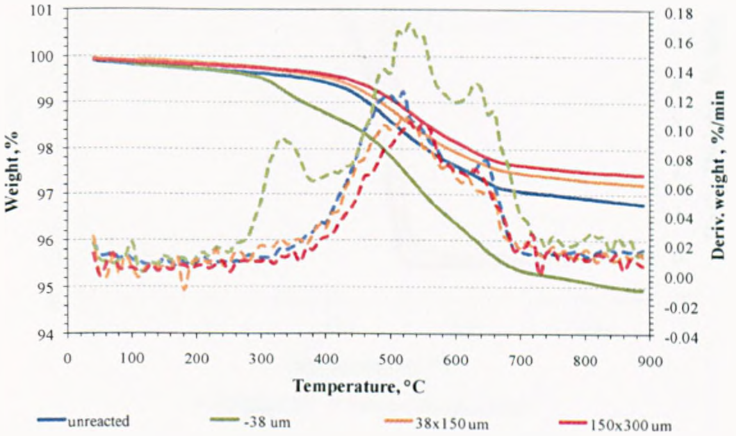

Figure 7-2. Thermogravimetric analysis of the parent and reacted samples with different particle size. Dashed lines correspond to derivative weight curves.

As expected, the main difference in the TGA profile with respect to the parent material is observed for the -38 μm fraction. Two different regions are clearly shown for its profile: one between ~250 and 400°C and another one between 400 and 700°C. The latter one corresponds to the kaolinite decomposition temperature region. A higher weight loss is observed for this region compared to the unreacted material, signaling either the amount of kaolinite present in the sample increased upon the reaction, or the presence of other phases which decompose in the same temperature range; a further weight loss occurs around 300°C, so a new phase decomposing around that temperature has precipitated as a consequence of the reaction. Siderite decomposes between 400 and 500°C, based upon the TGA profile of the standard sample (Figure 7-3), and the literature reports its decomposition temperature between 400 and 600°C (Bayliss and Warne, 1972, Kotra et al., 1982), which is a higher temperature than the one reported here. Thereby, the weight loss observed at ca. 300°C is not due to siderite precipitation.

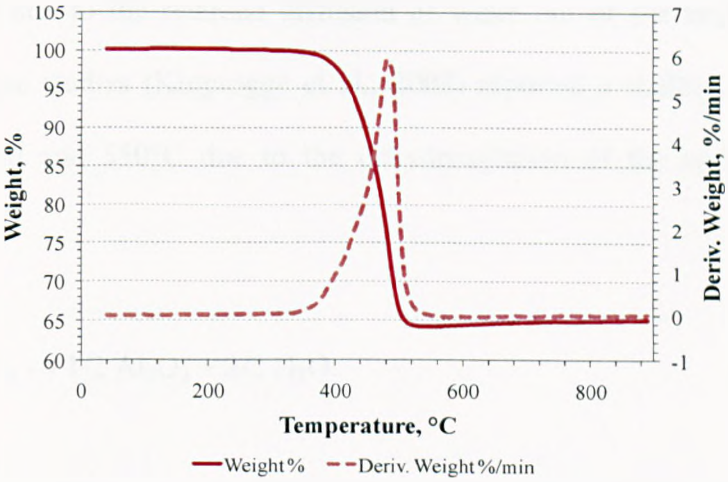

Figure 7-3. TGA curve for a standard sample of iron carbonate (siderite).

Previous researchers (Loughnan and See, 1967) have reported the decomposition of dawsonite ($NaAl(OH)_2CO_3$) between 290 and 330°C according to reaction [7-1].

$$2NaAl(OH)_2CO_3 \rightarrow Na_2CO_3 + Al_2O_3 + 2H_2O + CO_2 \qquad [7\text{-}1]$$

Previous studies (Huggins and Green, 1973) also claimed dawsonite thermal decomposition to $H_2O$, $CO_2$ and $NaAlO_2$ follows a two-step reaction: firstly, crystalline dawsonite decomposes between 300 and 375°C, where all the hydroxyl water and two-thirds of the $CO_2$ are given off. The balance of $CO_2$ is released in a second step over the range of 360 to 650°C, leaving a residue of crystalline sodium aluminate ($NaAlO_2$).

The dehydration of gibbsite ($Al(OH)_3$) (reaction 7-2) is characterised by three DTA endothermic effects at 222, 303 and 498°C (Balek et al., 2003). The main decomposition peak was previously reported around 300°C (Kloprogge et al., 2002, Balek et al., 2003), which was attributed to the formation of boehmite ($AlO(OH)$) due to the retarded diffusion of water out of the larger gibbsite grains. Those studies (Kloprogge et al., 2002) reported a shallow endotherm between 500 and 550°C due to the dehydroxylation of the earlier formed boehmite.

$$Al(OH)_3 \rightarrow 1/2\ Al_2O_3 + 3/2\ H_2O \qquad [7\text{-}2]$$

No weight loss is observed at 300°C for the intermediate and top fractions, and most likely some kaolinite dissolution has occurred based on the lower weight loss observed in the temperature range between 400 and 700°C compared to the unreacted sample. Their weight uptake can be due to new phases decomposing in the same temperature range as kaolinite does and/or new phases with decomposition temperatures higher than 900 °C, most likely some precipitated residual brine due to the experimental rinsing process.

### *7.1.1.3. Summary*

Fine powders (-38 μm) proofed to be the most reactive ones based on the observed weight uptake by the solids. This high reactivity is not probably due to the internal surface area of the different fractions, which is not expected to play an important role based on reported values of BET surface areas (see Chapter 6). At this point, it is convenient to distinguish between the external and the internal surface of the particles. The external surface can be considered as the one including all the prominences and all of those cracks which are wider than they are deep in the solid; the internal surface will then comprise the walls of all cracks, pores and cavities which are deeper than they are wide (Gregg and Sing, 1982). It has been reported (Alexander et al., 2007) that finer powders generally present a higher reactivity than coarser ones due to the structural defects imparted into the crystal lattice as a consequence of particle size reduction, as well as an increase in the external surface area, with more surfaces available to react with aqueous $CO_2$. The former statement seems to be the reason for the highest reactivity of the fine fraction (-38 μm) compared to the other ones. It is also important to bear in mind that the "external surface area" differs from the "reactive surface area". The concept of "reactive surface area" recognises that certain areas of the crystal surface are significantly more reactive than others, e.g., steps or the outcrops of dislocations. However, this concept is not easy to quantify and has inspired an intensive discussion in the field of geochemical kinetics and mineral weathering (Brantley et al., 2008).

Even in the reaction with very fine powders (-38 μm), experimental values of pH and dissolved iron are far from the predicted ones under the same conditions. Simulated equilibrium pH is 5.59, which is lower than the experimental value of 6.22; dissolved iron concentration is ~14 ppm, far higher than the 0.023 ppm predicted by geochemical modeling. As expected, these data reveal that equilibrium has not been attained after only 24 h of reaction time. Siderite precipitation could not be confirmed based on thermal analysis and either gibbsite or dawsonite formation seems to have been favored instead. Modelling results considering the influence of aluminium (see Figure A-1 in Appendix) showed dawsonite precipitation versus gibbsite one. However, gibbsite is not included in the calculation due to the lack of thermodynamic data. Therefore, both minerals, i.e. dawsonite and gibbsite, could have been precipitated. In the experiment, ferrous iron remained in solution instead of been trapped in a significant amount of siderite as in the modeled case. However, experimental solids weight uptake is of 11%, which compared to equilibrium one (12.59%), is reasonably close. It seems obvious that other metastable phases (those ones thermodynamically unstable under the reaction conditions) have precipitated and were not identified in the thermogravimetric profile, probably because their decomposition temperatures fall within the kaolinite decomposition temperature range and/or are higher than 900°C.

Despite of the high reactivity of the finest fraction (<38 μm), it would not be very representative of real-case scenarios where coarser solids are expected; hence, the top fraction was the chosen one for the experimental work. It also proofed to be very easy to work with in terms of the experimental solids recovery process upon reaction, which was also another advantage of working with this particle size.

### 7.1.2. Effect of reaction time

Geochemical modelling with CHILLER does not account for kinetics so experimental evaluation of reaction time is crucial to assess the extent of the reaction and equilibrium stage. A series of autoclave experiments (numbers 4-6 in Table 7-1) to study the effect of reaction time on formation of predicted iron carbonate were conducted. Reaction time ranged from 24 to 264 h. Experimental trends are discussed below and compared with the equilibrium predicted case.

#### *7.1.2.1. Analysis of fluid chemistry and solids weight uptake*

In the aqueous phase, no significant changes for dissolved iron and pH were observed beyond a reaction time of 62 h (Figure 7-4). Iron in solution decreased from a measured value of 17 ppm after 24 h to 12 ppm after 62 and 163 h, to further decrease slightly to 10 ppm after 264 h. Fluid pH increased from 6.38 after 24 h to a value of ~ 6.70 for the rest of the experiments. Continuous hematite dissolution might be buffering the pH throughout the experiment. The largest change in solids weight uptake (19%) was observed after 264 h, indicating precipitation of one or more secondary minerals between 163 and 264 h.

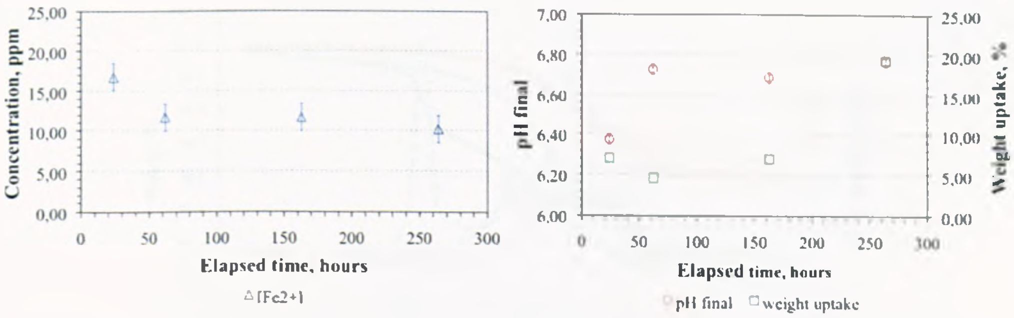

Figure 7-4. Dissolved iron (left) and measured final pH and solids weight uptake (%) (right) as a function of reaction time. Error bars size for weight uptake series is smaller than symbol size.

### *7.1.2.2. Characterisation of solid products*

A thorough analysis of reacted solids was conducted on experimental runs evaluating the influence of reaction time in the overall carbonation process. Thermal analysis, X-ray diffraction and X-ray photoelectron spectroscopy were the applied analytical techniques to elucidate the nature of precipitated phases over the course of the reactions. Results obtained from each of them are explained in detail below.

#### *7.1.2.2.a. Thermogravimetric analysis*

Thermogravimetric analysis (TGA) shows a similar behaviour of all reacted samples except for the one reacted for 264 h (Figure 7-5). The latter one shows a 1% weight loss around 300°C, which is in good agreement with the decomposition temperature of dawsonite and gibbsite (Huggins and Green, 1973, Kloprogge et al., 2002, Balek et al., 2003).

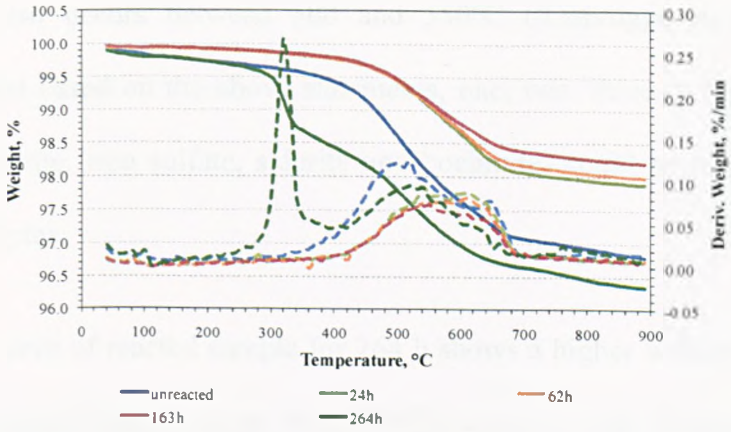

Figure 7-5. TGA curves of unreacted and reacted samples collected at different reaction times. Dashed lines correspond to derivative weight curves.

Kaolinite dissolution is inferred from the TGA profiles of samples collected after 24, 62 and 163 h, based on the weight loss associated to the kaolinite dehydroxilation process (400-700°C). Precipitation of secondary minerals in that temperature region could also contribute to the observed weight loss. Iron sulfide and siderite are potential precipitates as a result of the reaction, but their identification from the TGA profiles is not possible due to a similar decomposition temperature range: iron sulfate decomposition has been reported to initiate around 500°C, with a sharp decrease in weight at that temperature and followed by a slower decomposition at 500-600°C (Siriwardane et al., 1999); on the other hand, and as stated previously (see section 7.1.1.2), siderite decomposes between 400 and 600°C. An additional challenge for the detection of siderite is due to its inhibition by the superposition of its peaks and kaolinite peaks in the temperature range of 500-600°C. Even though the siderite detection limit is improved with a controlled $N_2$ atmosphere in the furnace, 30% of well-crystallised siderite may be overlooked by thermal analysis in mixtures with kaolinite (Bayliss and Warne, 1972). Decomposition of boehmite also occurs between 500 and 550°C (Kloprogge et al., 2002). Thereby, and based on the above statements, one, two, three or four of those solids (kaolinite, iron sulfate, siderite and boehmite) could be present in the reacted samples.

The TGA curve of reacted sample for 264 h shows a higher weight loss in the kaolinite decomposition range (400-700°C) than the one observed in the unreacted sample. Additionally, a further weight loss at ca. 800°C is noted for this reacted sample, which agrees well with the decomposition temperature of sodium carbonate (Figure 7-6).

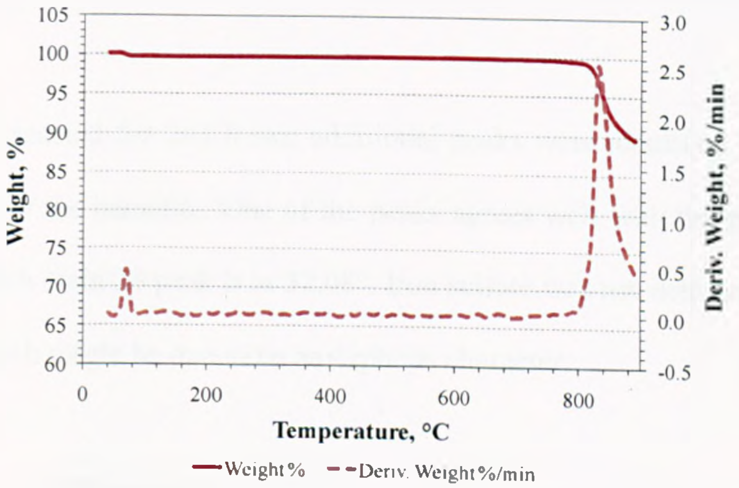

Figure 7-6. TGA curve for a standard sample of sodium carbonate.

### 7.1.2.2.b. X-ray diffraction analysis

X-ray diffraction (XRD) was also conducted to identify the bulk crystalline phases formed during the reaction. Changes were not observed in the XRD diffractograms of recovered solids after 24, 62 and 163 h so their diffractograms are not shown. The XRD diffractograms of unreacted and reacted sample for 264 h can be seen below in Figure 7-7.

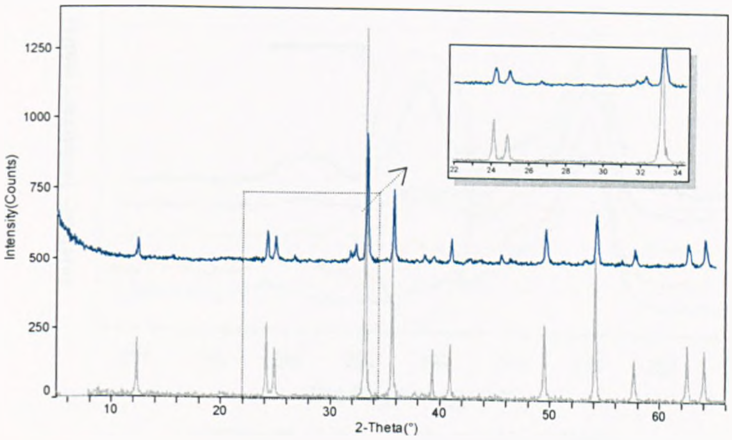

Figure 7-7. XRD diffractograms of unreacted (grey line) and reacted (green line) hematite sample (264 h).

For sample reacted for 264 h two additional peaks were identified before the main peak for the hematite. One of the peaks agrees well with the presence of siderite which main 2θ peak is at 32.08°. Iron sulfate was not detected by XRD analysis which might be due to an amorphous character.

### 7.1.2.2.c. XPS analysis

Reacted solids were analysed in detail by XPS to determine whether surface composition had been altered as a result of the experiments and reactions had taken place on the hematite surface.

First, a detailed analysis of the C signal was conducted based on its high resolution scan (Figure 7-8). XPS data for the different samples clearly indicates that a peak with a BE associated to a carbonate compound had developed quite significantly after 264 h. Thereby, carbonate formation did occur and is enhanced with longer reaction times.

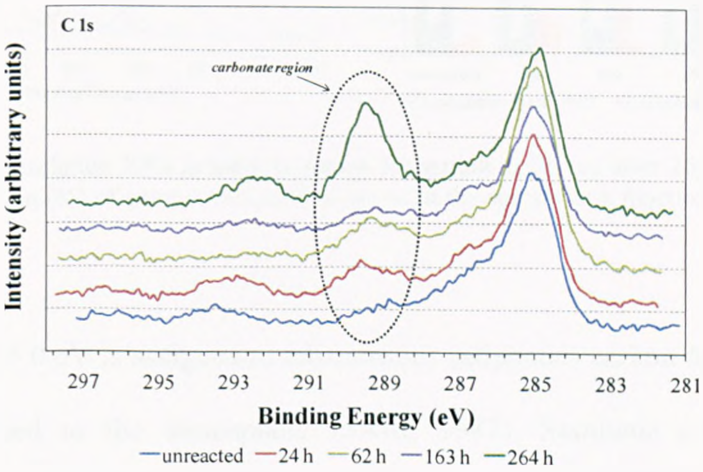

Figure 7-8. XPS C1s spectra of hematite solid samples collected at different reaction times.

Deconvolution of the experimental C 1s spectra profile was performed to study the contribution of the different peaks to the total curve. The solid black line represents experimental data and the total calculated fitting is shown in grey with circular markers. The other curves represent components used to curve fit the spectra. An example of the deconvolution process is depicted in Figure 7-9 (left) and the atomic concentration (%) of the different components for samples collected at different reaction times is also shown in Figure 7-9 (right).

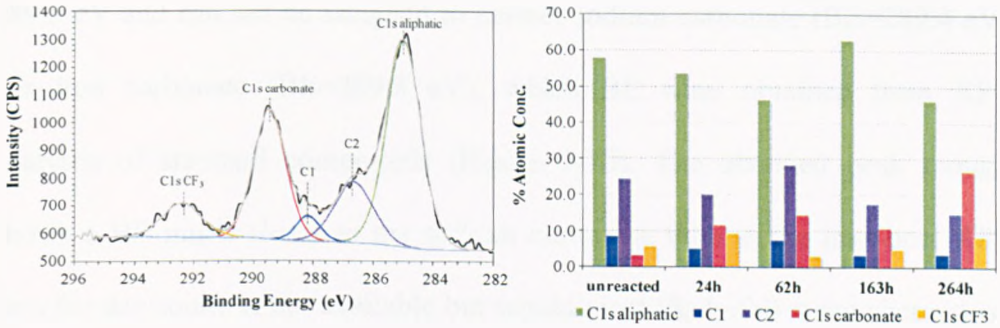

Figure 7-9. High resolution XPS in the C1s region for sample collected after 264h (left) and atomic concentration (%) of components used to curve fit the spectra as a function of reaction time.

The peak at 285.0 eV is assigned to adventitious (aliphatic) carbon found in all samples exposed to the atmosphere (Swift, 1982). Synthetic components defined as C1 and C2 correspond to carbon atoms of the type C=O and C-OH respectively of unknown origin, most of it probably related to the adventitious contamination (Swift, 1982, Moulder et al., 1995, Briggs and Beamson, 2006). The carbon peak due to a $CF_x$-containing phase does not disappear in the reacted samples but, bearing in mind the surface F content in the parent hematite is only 1.21 atomic % (see section 6.5 in Chapter 6) this contribution is not significant. The component with a BE that relates to carbonate carbon atoms, increases its atomic concentration to a maintained value ranging from 11 to 14% in collected solids reacted for 24, 62 and 163 h. A substantial increase (26.7%) is observed though in sample collected after 264h, which is again a clear evidence of carbonate precipitation.

The carbonate peak in the sample collected after 264 h (Figure 7-9 left) was further analysed to identify which carbonate had been formed over the course of the experiment. The BE for the peak related to carbonate carbon atoms is

289.5 eV and can not be assigned to neither sodium carbonate (BE=289.4 eV) nor iron carbonate (BE=289.8 eV), which BE were obtained from XPS analyses of standard compounds (Figure 7-10). The obtained peak though shows a BE much closer to the sodium carbonate than to the iron one. XPS data for dawsonite is not available but would most likely fall somewhere close to reference data for sodium carbonate.

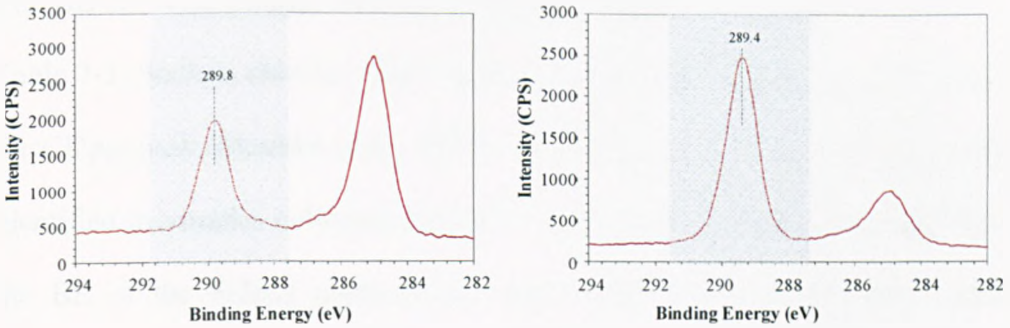

Figure 7-10. XPS C1s spectra of standard iron carbonate, i.e. siderite (left), and sodium carbonate (right).

High resolution scans were also performed for the rest of the elements aiming to elucidate potential solid phases precipitated on the hematite surface. The most significant difference in the O1s high resolution scans is the presence of new O1s peaks at BE of 536.1 and 531.8 eV in the sample reacted for 264h, which are comparable to the BE of the O1s peaks observed in the reference spectra for sodium and iron carbonates respectively (Figure 7-11). Iron sulfate precipitation occurred after 62 and 264 h as verified by the BE of the $S2p_{3/2}$ peak (168.9 eV) (Moulder et al., 1995).

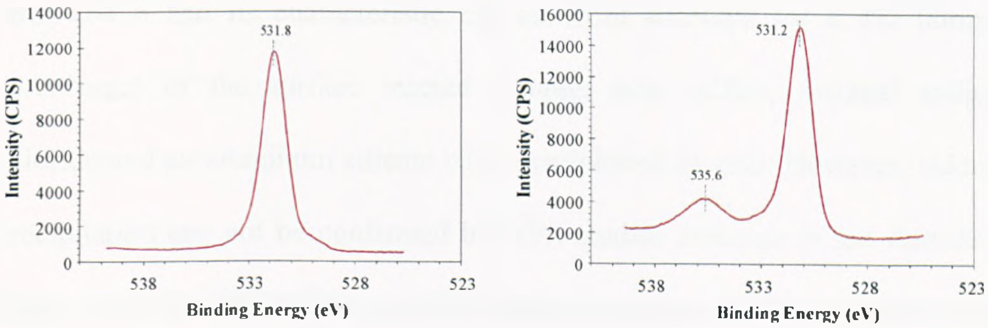

Figure 7-11. XPS O1s spectra of standard iron carbonate (left) and sodium carbonate (right).

The BE of Na1s, $Cl2p_{3/2}$, $Al2p_{3/2}$ and $Si2p_{3/2}$ photoelectron peaks are shown in Table 7-3. Sodium chloride seems to have precipitated according to the BE of the $Cl2p_{3/2}$ peak (Moulder et al., 1995). An aluminium silicate ($Al_2SiO_5$) is also identified in samples collected after 62, 163 and 264 h, which is supported by the BE of the $Si2p_{3/2}$ photoelectron peak (103.0 eV). Na1s and $Al2p_{3/2}$ photoelectron peaks have contributions from different compounds, probably dawsonite, sodium carbonate and sodium chloride for Na1s, and dawsonite and aluminium silicate for $Al2p_{3/2}$.

Table 7-3. Binding Energies of Na1s, $Cl2p_{3/2}$, $Al2p_{3/2}$ and $Si2p_{3/2}$ photoelectron peaks for samples collected at different reaction times.

| Sample | Na1s | $Cl2p_{3/2}$ | $Al2p_{3/2}$ | $Si2p_{3/2}$ |
|---|---|---|---|---|
| **unreacted** | ---- | ---- | 75.0 | 103.2 |
| **24h** | 1072.0 | 198.7 | 74.9 | 103.2 |
| **62h** | 1071.8 | 198.8 | 74.7 | 103.0 |
| **163h** | 1071.7 | 198.7 | 74.7 | 103.0 |
| **264h** | 1071.6 | 198.8 | 74.6 | 103.0 |

A quantitative analysis could not been performed confidently with XPS due to the high complexity of the samples and the potential numerous possibilities, but ***some conclusions*** can be withdrawn: carbonate precipitation has occurred after 264 h and its characteristic carbon atom accounts for a 4% (atomic percentage) of the surface reacted sample; Iron sulfate, residual sodium chloride and an aluminum silicate have precipitated as well. However, siderite precipitation can not be confirmed by XPS studies although is not dismissed either, since the BE of O1s and S2p photoelectron peaks are coincident with those for ferrous sulfate.

#### *7.1.2.3. Summary*

The effect of reaction time on the overall mineral trapping reaction with hematite showed reaction progress was made and siderite was identified by XRD as a reaction product after 264 h, which is in good agreement with results from modeling studies. XPS analysis also indicated the potential presence of other carbonate, dawsonite, which decomposition temperature at ca. 300°C agrees well with results from thermal analysis. In the simulation of a hematite-kaolinite-brine-$CO_2$-$SO_2$ system, the equilibrium mineral assemblage consisted of hematite, dawsonite, siderite and quartz (see Figure A-1 in Appendix) so, assuming dawsonite precipitation took place (based on TGA and XPS results), a 3.6% of dawsonite is present in the reacted sample for 264h provided that decomposition of dawsonite was complete.

Residual sodium chloride and iron sulfate were detected only on the surface of the sample and had not been predicted by the simulations. Sodium chloride presence was probably due to the experimental procedure because the rinsing process of the solids was carried out with the collected brine from the experiment. On the other hand, iron sulfate precipitation occurred after 62 and 264 h as verified by the BE of the S2p peak; this is in good agreement with dissolved iron analyses, where iron concentration decrease was also observed after 62 and 264 h.

Experimental values of pH and dissolved iron are again far from the equilibrium ones. Measured fluid pH was higher than the theoretical (in-situ) one due to limitations of the experimental procedure and $CO_2$ evolving from the brine upon the reactor depressurization process. As for measured dissolved iron, the higher value compared to the predicted one owes to ferrous iron being left dissolved. The percentage of weight uptake was higher though (19.36%) in the experiment than in the simulation (12.59%), and alteration minerals included siderite, dawsonite, iron sulfate, sodium carbonate and sodium chloride.

The presence of iron sulfate in reacted solids is likely due to the quenching process rather than to the experiment: the solubility of ferrous sulfate reaches a maximum of ca. 4 mol/kg at 55°C and, although it decreases to $4.2 \cdot 10^{-3}$ mol/kg at 350°C (Cameron, 1930, Rudolph et al., 1997), it is still quite soluble at elevated temperatures and even more in the presence of an excess of sulfuric acid (Rudolph et al., 1997). Thereby, its presence at high temperature (100°C) is highly unlikely.

The likely presence of dawsonite in the reacted solids might be due to the moderately basic solution that enhances dawsonite precipitation (Benezeth et al., 2007) as well as to the high $CO_2$ fugacities:

$$Na^+ + Al(OH)_4^- + HCO_3^- + H^+ \rightarrow NaAlCO_3(OH)_{2(s)} + 2H_2O(l)$$

Previous equilibrium modeling studies in a $CO_2$-brine-sandstone system (Zerai et al., 2006), where dawsonite and siderite are identified as reaction products, indicate that dawsonite does not precipitate in the final equilibrium assemblage for simulations under a whole range of initial $fCO_2$ and model temperatures, with siderite being present as the stable phase; However, the path of reaction modeling and kinetic modeling indicates that for all the initial $fCO_2$ studied, dawsonite does precipitate during the initial stages of the reaction, but dissolves as the reaction proceeds to completion. Siderite patterns of formation and dissolution are similar to those for dawsonite, but siderite is more stable than dawsonite at lower $CO_2$ fugacities and higher pH, and at higher temperatures.

Based on all the above, dawsonite precipitation over in the experiments has been favored due to dawsonite's increasing stability at high $CO_2$ fugacities. This would be representative of a near injection well and immediately following injection case. In a real scenario, however, as time goes by, $CO_2$ fugacity is expected to decrease with increasing distances from the injection site and, over longer periods of time after injection, due to $CO_2$ dispersion, migration and/or leakage. It would be then when siderite becomes the stable phase, taking up some of the re-released $CO_2$ from dawsonite dissolution.

A comparison can be established between results reported here and those from previous studies with hematite, brine and a $CO_2$-$SO_2$ mixture (Palandri et al., 2005). Although the experimental conditions were not the same (pure hematite with minor amounts of Al, 150°C, 300 bar, ~67 g/L and 11.1 vol. % of $SO_2$ as opposed to reaction conditions of a hematite sample containing some kaolinite, 100°C, 250 bar, 25 g/L and 0.4% vol. of $SO_2$ in this research), dawsonite was also identified as a reaction product by Palandri and co-workers. However, its formation was presumably due to the experimental procedure just prior to quenching the experiment, which involved the addition of NaOH to the system. Siderite precipitation was confirmed in that case after ~ 611 h as well as some metastable pyrite and S. Studies presented here, where the reaction time was 264h, verified the presence of siderite and probably dawsonite, so they are in good agreement with those reported by Palandri and co-workers (Palandri et al., 2005).

### 7.1.3. Effect of gas composition

Three different $CO_2$:$SO_2$ gas concentrations were tested in laboratory experiments (exp. numbers 3, 7 and 8 in Table 7-1): Equilibrium results obtained for those ratios are discussed and compared with the collected experimental values.

### 7.1.3.1. Analysis of fluid chemistry and solids weight uptake

Experimental trends for dissolved iron, final pH and solids weight uptake (%) observed after the reaction, were compared to the predicted (i.e. equilibrium) ones given by geochemical modeling.

Ferrous iron in solution increased as a result of increasing amounts of $SO_2$ in the reactive gas stream in both, predicted and experimental tests (Figure 7-12). Higher amounts of $SO_2$ would yield a higher amount of hydrogen sulfide due to the $SO_2$ disproportionation reaction (reaction [7-3]) and, consequently, reduction of ferric iron contained in the starting material by hydrogen sulfide is driven to the right side (reaction [7-4]) and more ferrous iron is obtained in solution.

$$4SO_2 + 4H_2O \leftrightarrow H_2S + 3H_2SO_4 \qquad [7\text{-}3]$$

$$8Fe^{3+} + HS^- + 4H_2O \leftrightarrow 8Fe^{2+} + SO_4^{2-} + 9H^+ \qquad [7\text{-}4]$$

However, the amount of dissolved iron measured experimentally is three orders of magnitude higher than the equilibrium one predicted by the simulations. As expected, equilibrium was not reached after a 24h experiment, and most likely, reaction time was not long enough to promote siderite nucleation and precipitation.

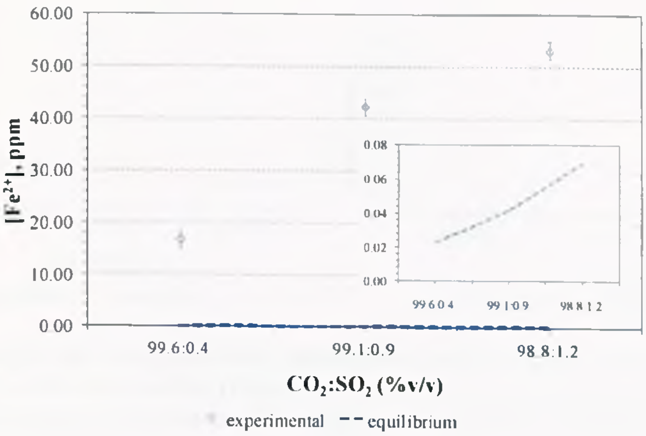

Figure 7-12. Comparison of experimental and predicted results for dissolved iron as a function of varying relative amounts of $CO_2$ and $SO_2$ in the gas added.

As for the pH values and according to reaction [7-3], brine acidity is higher when the amount of $SO_2$ added to the system is also higher. Thereby, the more $SO_2$ present in the gas stream, the lower the pH of the brine. Measured experimental values are higher than the equilibrium ones and incongruently, measured pH for the experiment with a 1.2% content of $SO_2$ is slightly higher than the one with a 0.9% of $SO_2$. Experimental pH was recorded as quickly as possible upon depressurization and opening of the reactor, but the elapsed time prior to the measurement might have been slightly longer for the last point, so the $CO_2$ would have had more time to evolve from the brine and consequently, the measured brine pH would be slightly higher. Also, hematite dissolution might be buffering the pH in the experiment.

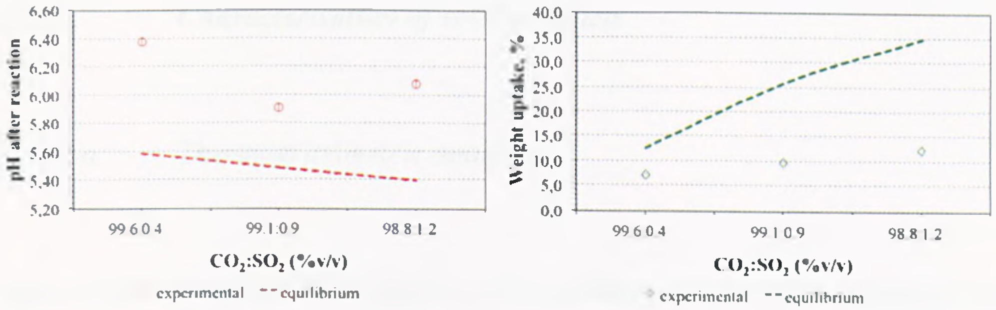

Figure 7-13. Comparison of experimental and predicted results for brine pH (left) and solids weight uptake (%) after the reaction (right) as a function of varying relative amounts of $CO_2$ and $SO_2$ in the gas added. Error bars size for weight uptake series is smaller than symbol size.

Predicted weight uptake by the solids increases following reaction with increasing amounts of $SO_2$ in the gas stream; this is due to more dissolved iron available for nucleation and precipitation of siderite, driving reaction [7-5] to the right.

$$H_2CO_3 + Fe^{2+} \leftrightarrow FeCO_3 + 2H^+ \qquad [7\text{-}5]$$

A similar trend is observed for the percentage of solids weight uptake in the theoretical and experimental results but the values are not of the same order of magnitude. The solids weight uptake in the experiments is not as high as the predicted ones but, this is due to the fact that the simulation is predicting results under equilibrium conditions, while the data from the autoclave experiments is obtained after only 24h of reaction.

### 7.1.3.2. *Characterisation of solid products*

#### 7.1.3.2.a. *Thermogravimetric analysis*

Figure 7-14 shows the TGA profiles of the parent and reacted samples with different amounts of $SO_2$ added to the reactive gas stream. Kaolinite dissolution is enhanced with higher contents of $SO_2$ in the gas added; thereby, a lower weight loss is observed in samples with increasing $SO_2$ contents in the temperature range where kaolinite decomposes (400-700°C). Dissolution of kaolinite increases directly with increased proton concentrations (Biber et al., 1994). Hence, as the $SO_2$ content increases and the brine gets more acidic, so does the degree of protonation. Protons promote dissolution by attacking a particularly vulnerable point in the crystal structure, namely the oxygen atom of the corner shared by the aluminum and silicate polyhedra. The lone pair of electrons on the oxygen atoms in the kaolinite structure undergo protonation as the proton concentration increases. The protonation of the oxygen atoms polarises and weakens the Al-O-Si bonds, thereby facilitating the removal of aluminium atoms from the crystal lattice (Stumm and Morgan, 1996) according to the following reaction:

$$Al_2Si_2O_5(OH)_4 + 6\,H^+ \leftrightarrow 2Al^{3+} + 2H_4SiO_4 + H_2O \qquad [7\text{-}6]$$

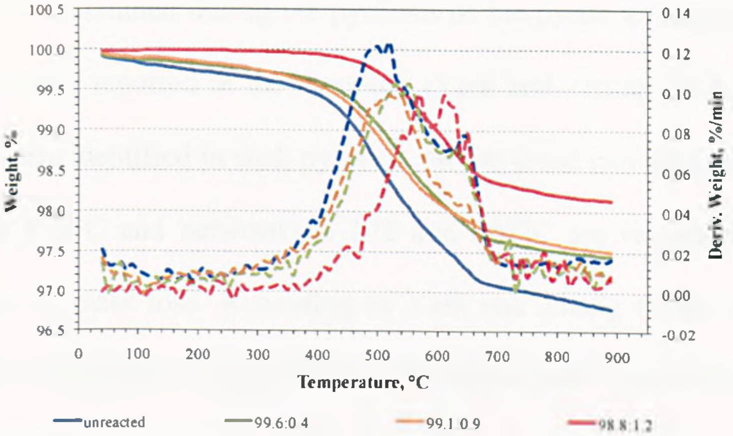

Figure 7-14. TGA curves of unreacted and reacted samples with varying relative amounts of $CO_2$ and $SO_2$ in the gas added. Dashed lines correspond to derivative weight curves.

The rate of mass loss profile is significantly different for the sample reacted with a gas mixture containing 1.2% of $SO_2$. The latter sample happens to be thermally more stable than the others since its decomposition temperature is higher than the rest. The weight loss could be due to some remaining kaolinite as well as one and/or more precipitated phases with decomposition temperatures ranging from ca. 500 to 700°C. On one hand, with further addition of $SO_2$, increasing concentrations of $Fe^{2+}$, sulfate and sulfide drive reaction [7-7] to the right, so pyrite could be a potential phase formed as a result of the reaction.

$$4Fe^{2+} + SO_4^{2-} + 7HS^- + H^+ \leftrightarrow 4\ FeS_2\ (\text{pyrite}) + 4H_2O \qquad [7\text{-}7]$$

On the other hand, experimental results (Palandri, 2000) have shown precipitation of amorphous iron sulfide as the one favoured kinetically (reaction [7-8]):

$$Fe^{2+} + HS^- \leftrightarrow FeS\ (\text{amorphous}) + H^+ \qquad [7\text{-}8]$$

The TGA curve obtained during the pyrolisis of the pyrite mineral in nitrogen has been recently reported in the literature (Yani and Zhang, 2009). Broadly, four stages were identified in such pyrolisis, where those two occuring between ca. 447 and 572°C and between ca. 572 and 667°C are responsible for the highest rates of mass loss. According to Yani and Zhang (Yani and Zhang, 2009) pyrite decomposes via a multi-step sequential and kinetically controlled process as follows:

$$FeS_2 \rightarrow FeS_x \rightarrow FeS \rightarrow Fe$$

Gaseous sulfur in the form of a mixture of allotropic species, $S_n$ (n=1-8), is released during the thermal decomposition of pyrite.

Iron sulfate and boehmite also decompose between 500 and 600°C (Siriwardane et al., 1999, Kloprogge et al., 2002). Hence, precipitation of pyrite, iron sulfate, boehmite and/or amorphous iron sulfide may have occurred in the sample reacted with the highest content of $SO_2$ in the gas (1.2%) phase.

Due to the high number of possibilities, a quantitative analysis can not be performed based on TGA results because of the potential overlapping of the TGA curves for kaolinite, iron sulfate, boehmite and iron sulfide in the same range of temperatures.

### *7.1.3.2.b. XPS analysis*

In order to assist in the interpretation of reacted solid products, analyses of reacted hematite samples were performed using XPS.

A wide scan and high resolution scans of all the elements were conducted, and the atomic relative percentage difference for the different elements related to the starting material are plotted (Figure 7-15) for the varying relative amounts of $CO_2$ and $SO_2$ in the gas added to the reactive system. It can be noted that the atomic relative percentage difference for C1s related to carbonate carbon atoms is only positive when the $SO_2$ content in the gas is characteristic of a typical flue gas stream (99.6:0.4). The BE of this C1s photoelectron peak is 289.6 eV, which is right in between the values of BE corresponding to siderite (289.8 eV) and sodium carbonate (289.4 eV). Only around 1% (atomic) of carbonate atoms is detected on the surface of the reacted hematite sample when compared with the unreacted one. Hence, no weight loss could be clearly assigned to any carbonate compound in the corresponding TGA curve (Figure 7-14). Based on the BE of the C1s peak, either siderite, sodium carbonate, dawsonite or a mixture of one, two or three of those phases could be present due to the reaction.

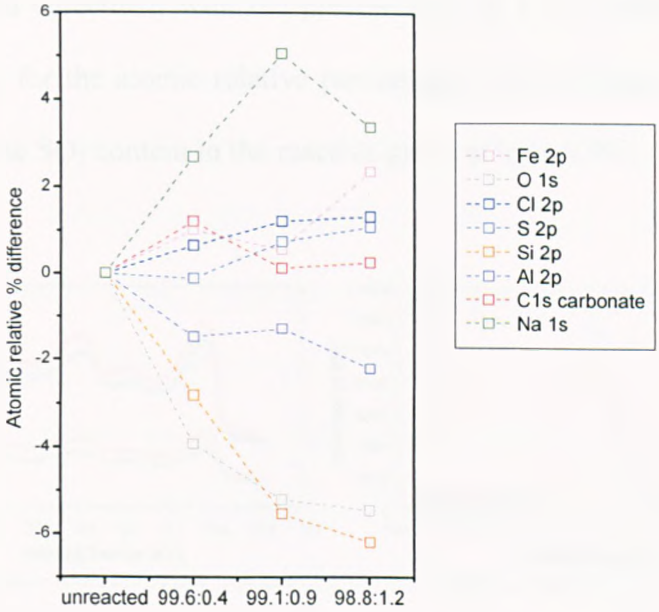

Figure 7-15. Atomic relative percentage difference of different elements as a function of varying relative amounts of $CO_2$ and $SO_2$ in the gas added.

Sulfur atomic concentration started to be significant (1% or more) when the $SO_2$ content was equal or higher than 0.9% as can be seen in Figure 7-15. The BE of sulfur for Fe(II) sulfate is around 169.0 ± 0.2 eV (Siriwardane et al., 1999, Descostes et al., 2000), which corresponds to the BE of sulfur in the reacted samples. Thereby, sulfur seems to be bond to the hematite surface in the sulfate form.

The Fe2p high resolution XPS spectra also indicates a mixture of Fe(III) and Fe(II) compounds with increasing amounts of $SO_2$ in the gas added: for reacted samples with 0.9% of $SO_2$ content or higher (Figure 7-16), the satellite of $Fe2p_{3/2}$ constitutes a shoulder in the photoelectron peak (more characteristic of Fe(II) compounds) whereas, for the unreacted and reacted sample with 0.4% of $SO_2$, this same satellite is very distinctive from the photoelectron peak, indicating the Fe (+III) character of the compound (Grosvenor et al., 2004).

This is in good agreement with the precipitation of Fe(II) sulfate, since the observed trend for the atomic relative percentage of S2p (Figure 7-15) is not positive until the $SO_2$ content in the reactive gas is at least 0.9%.

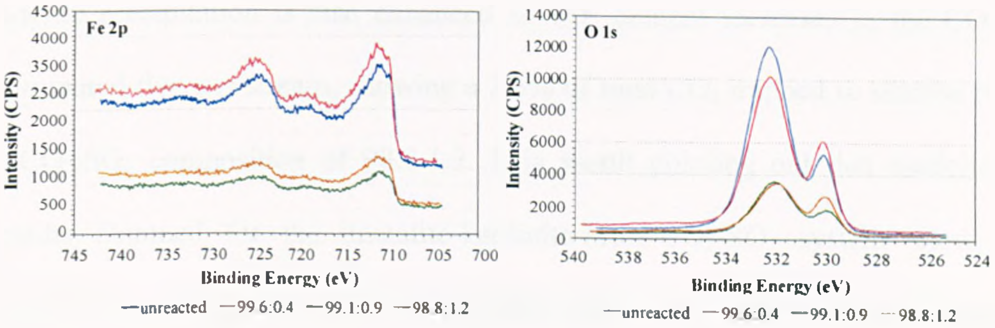

Figure 7-16. High resolution XPS in the Fe 2p (left) and O 1s regions (right) for unreacted and reacted samples with varying relative amounts of $CO_2$ and $SO_2$ in the gas added.

The high resolution XPS spectra of O1s peak can also be seen in Figure 7-16. It is clear how the intensity ratio between the O1s peak corresponding to kaolinite (532.2 eV) and hematite (530.1 eV) gets smaller as the $SO_2$ content is higher in the gas stream, enhancing kaolinite dissolution. For the reacted samples with 0.9 and 1.2% of $SO_2$ content, the kaolinite peak also broadens, which is consistent with the presence of the O1s peak at the BE characteristic of Fe(II) sulfate (531.8 eV) (Siriwardane et al., 1999).

The presence of residual brine, i.e. NaCl, and an aluminum silicate might be also possible based on BE of Na1s (1071.8 eV), $Cl2p_{3/2}$ (198.9 eV), $Al2p_{3/2}$ (74.7 eV) and $Si2p_{3/2}$ (102.9 eV) photoelectron peaks (Moulder et al., 1995), which are present in all the reacted samples.

### *7.1.3.3. Summary*

Geochemical modeling simulations predict that, under modeled conditions, $CO_2$ is mainly trapped as a free gas phase and as ionic $CO_2$ species in the brine; siderite precipitation is also enhanced as $SO_2$ content increases in the $CO_2$-dominated flue gas stream, showing a 2.5% of total $CO_2$ trapped in siderite for a $CO_2$:$SO_2$ composition of 98.8:1.2. It is worth pointing out that modeling results obtained for the hematite-kaolinite-brine-$CO_2$-$SO_2$ system show a mineral assemblage consisting of hematite, dawsonite, siderite, kaolinite and quartz for a $CO_2$:$SO_2$ composition of 98.8:1.2 (see Figure A-1 in Appendix).

Experimentally, dissolved iron values are again significantly higher (three orders of magnitude) than predicted ones. Equally, percentages of weight uptake by the solids are not as high as the modeled values but do follow the same thermodynamically predicted trend, indicating higher precipitation for increasing $SO_2$ contents in the experiment. The higher the $SO_2$ content in the gas stream, the higher the brine acidity is, according to the model. Experimentally measured pH does not quite follow that trend since its empirical value is not the lowest one for the experiment with a highest $SO_2$ content. Either the limitations of the experimental procedure or the pH buffering as a result of hematite dissolution might be responsible for the latter statement.

Thermal analysis results were not conclusive in the identification of precipitates from the reactions due to potential precipitated phases decomposing over the same range of temperatures. Surface spectroscopic techniques (e.g. XPS) indicate dehydroxilation and dissolution of kaolinite is promoted in more acidic environments as well as the iron sulfate, residual brine and an aluminum silicate presence on the surface of the sample as a result of the brine-rock-gases interaction. A very small amount of carbonate atoms (~ 1%) was confirmed in the reacted sample with the lowest $SO_2$ content (0.4%) but the identity of the precipitated carbonate and/or carbonates could not be verified.

In high $SO_2$ content experiments, as the one reported by Palandri and co-workers (Palandri et al., 2005), initially highly reducing conditions could lead to precipitation of undesirable phases, such as iron sulfide, that could persist metastably later on. However, precipitated iron sulfide phases should re-dissolve as time goes by to allow siderite precipitation and confirm the geochemical modeling predictions. As more time elapses, carbon in the fluid will eventually become trapped as mineral carbonates as the acidic character due to $SO_2$ is neutralised through hematite dissolution.

### 7.1.4. Effect of reaction temperature and reaction pressure

A series of autoclave experiments were conducted to study the reaction of a $CO_2$ dominated flue gas stream with brine and hematite as a function of temperature (experiments 8, 12, 13 and 14; see Table 7-1) at constant pressure (250 bar), and as a function of pressure (experiments 8-11; see Table 7-1) at constant temperature (100°C). Predictions based on computer simulations are compared with empirical trends and results are discussed below.

### *7.1.4.1. Analysis of fluid chemistry and solids weight uptake*

Dissolved iron, pH after the reaction and weight uptake (%) curves for increasing values of temperature and pressure are depicted in Figure 7-17. It is worth noting how the trend is the opposite for all measured variables when comparing experiments with different temperatures and different pressures, which is consistent with the opposite effect that temperature and pressure have in a reaction.

Predicted dissolved iron concentration decreases and modeled pH increases with increasing temperatures. This is due to the combined effect of the following: a) $CO_2$ reacts with water to form $H_2CO_3$ which dissociates to $H^+$ and $HCO_3^-$, more so at lower temperatures (Holloway, 2005, Bachu, 2008). Thereby, higher temperatures will inhibit $CO_2$ dissolution compared to lower ones and the fluid pH will become less acidic, i.e., fluid pH will be higher and dissolved iron lower (hematite dissolution is enhanced in more acidic environments) than in low temperatures experiments; b) $SO_2$ disproportionation reaction (reaction [7-9]) is exothermic ($\Delta H_R^0<0$) and according to Le'Chatelier's principle, an increase in temperature decreases the equilibrium constant of the reaction. Thereby, less amounts of $H_2S$ will be yielded in reactions with increasing temperatures. $H_2S$ concentration would affect brine pH as well as ferrous iron concentrations in solution: the more $H_2S$

produced, the lower the brine pH, and the more dissolved ferrous iron since $H_2S$ is the reductant agent responsible for reducing $Fe^{3+}$ contained in the oxide to $Fe^{2+}$.

$$4SO_2(g) + 4H_2O(l) \leftrightarrow H_2S\ (aq) + 3H_2SO_4\ (aq) \quad \Delta H_R^0 = -104.4\ \text{kcal/mol}\ [7\text{-}9]$$

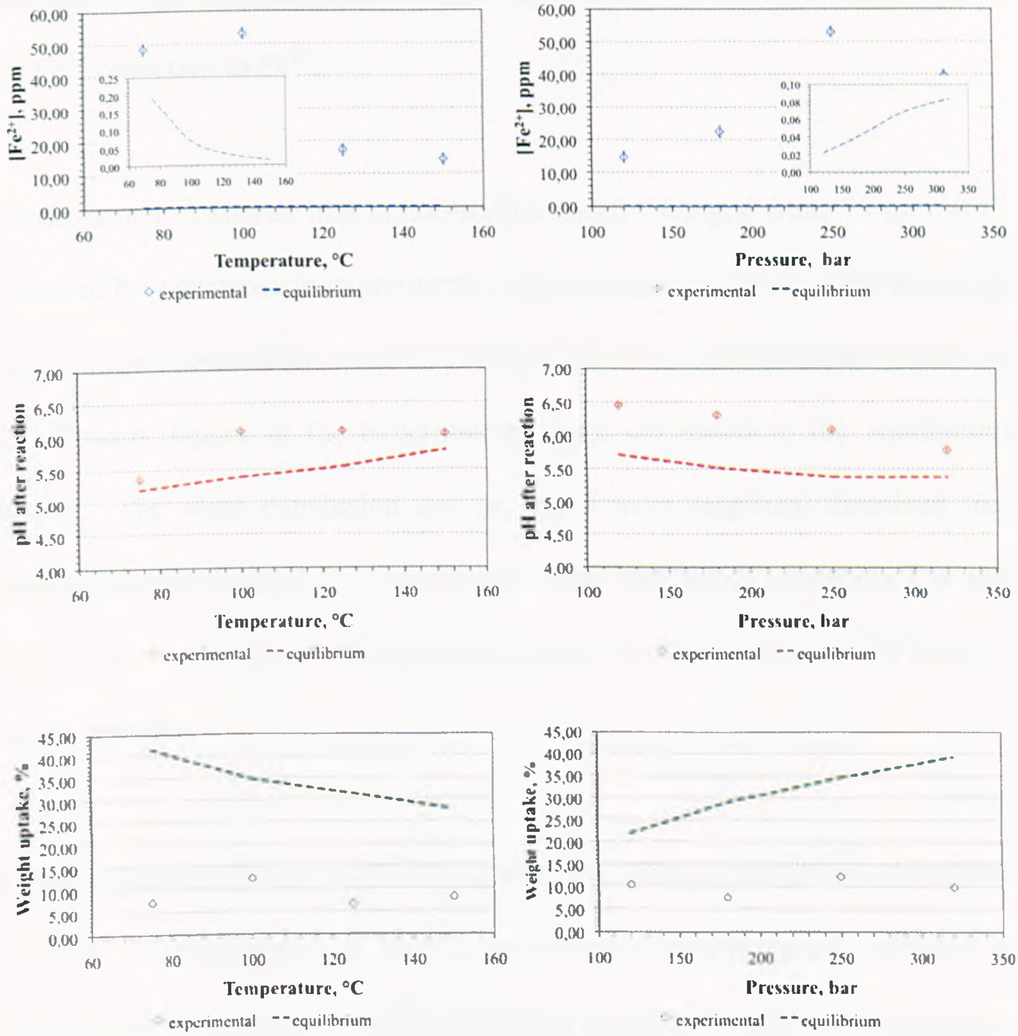

Figure 7-17. Comparison of experimental and predicted results for dissolved iron, brine pH and solids weight uptake (%) after the reaction as a function of temperature (at constant pressure) and pressure (at a constant temperature). Error bars size for weight uptake series is smaller than symbol size.

Conversely, the opposite trend is observed for the modeled dissolved iron and brine pH curves from simulations with increasing reaction pressures. Increasing pressures would enhance $CO_2$ solubility (Bachu, 2008) as well as would increase the equilibrium constant of the $SO_2$ disproportionation reaction according to Le'Chatelier's principle. As a result of the above statement, acidity of the brine will be higher in experiments with higher reaction pressures and dissolved iron concentration will also be higher due to more $H_2S$ available for $Fe^{3+}$ reduction to $Fe^{2+}$.

Experimental dissolved iron concentration barely changed from 75 to 100°C, followed by a decrease in experiments reacted at 125 and 150°C. The empirical trend follows reasonably well the modeled one, but concentration values are significantly higher in the experimental work compared to the simulations results. The same conclusion can be stated from empirical dissolved iron concentrations obtained in experiments with increasing pressures. For this latter case, concentration of dissolved iron is almost the same for 250 and 320 bar of pressure.

Empirical brine pH does increase, as predicted, when moving from experiment at 75°C to experiment at 100°C, but remains approximately constant in experiments at higher temperatures (125 and 150°C). The effect of temperature on the rate constant of a reaction is described by the Arrhenius equation (equation [7-10]) where $k$ is the reaction rate constant, $A$ is referred to as the preexponential factor, $E_a$ as the activation energy of the reaction, $R$ is the gas constant and $T$ is the absolute temperature (Stumm and Morgan, 1996).

$$k = Ae^{-E_a/RT} \qquad [7\text{-}10]$$

According to the Arrhenius equation, the higher the reaction temperature, the higher the reaction rate constant. Kinetic considerations might be then responsible for such observations and precipitation of secondary minerals (that generate acidity) might be buffering the pH. Also, although higher temperatures decrease the solubility of $CO_2$ in water and therefore the rate of carbonation, the carbonation reaction is exothermic and the heat of reaction could promote the formation of meta-stable phases (Fernandez Bertos et al., 2004).

Observed experimental pH values for experiments with increasing values of reaction pressure do follow the theoretical trend but, as in previous sections, empirical values are higher than predicted ones due to the limitations of the pH measurement method in the laboratory (the pH of the quenched brine rebounds as the $CO_2$-charged brine degasses).

As for the predicted percentage of weight uptake, modelled results show a decreasing trend for experiments with increasing reaction temperatures and the opposite trend for experiments with increasing pressures. The amounts, in grams, of final hematite and precipitated siderite predicted by geochemical modeling are shown in Figure 7-18. Siderite precipitation follows the same trend as reported modeled weight uptake percentage and can be explained as follows: higher temperatures decrease the solubility of $CO_2$ in water, therefore decreasing the rate of carbonation. Conversely, higher pressures increase the solubility of $CO_2$ and hence, the rate of carbonation. Previous studies have already reported that the higher the amount of $CO_2$ in the gas phase, the higher is the rate of carbonation so by varying the partial pressure of $CO_2$ , the rate of carbonation can be controlled (Fernandez Bertos et al., 2004).

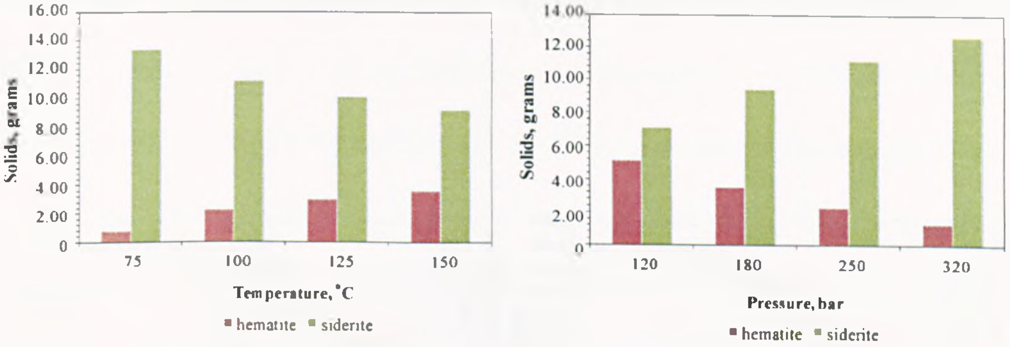

Figure 7-18. Hematite and siderite amounts (in grams) at equilibrium in experiments with different reaction temperatures and with different reaction pressures.

Experimental percentage of weight uptake increases from ~ 7% at 75°C to ~ 12% at 100°C to further decrease to a maintained value ranging between 7 and 8% for experiments at higher temperatures (Figure 7-17), signaling re-dissolution of a phase previously precipitated in the experiment and/or further dissolution of the starting material and no precipitation of secondary minerals. The opposite trend is observed for percentage of weight uptake in experiments with increasing values of reaction pressure (Figure 7-17). None of the experimental trends (neither the one for varying values of reaction temperature nor the one for varying values of reaction pressure) follow the expected theoretical trend for the percentage of weight uptake by the solids. It is obvious that kinetics play an important role on rates of dissolution of the initial solid as well as precipitation of secondary minerals, preventing the system from following the expected theoretical trend and reaching equilibrium after 24 h.

### *7.1.4.2. Characterisation of solid products*

The analysis of the precipitates was accomplished using thermal analysis to identify which compound and/or compounds were responsible for the observed percentage of weight uptake. The TGA profiles are shown in Figure 7-19 below.

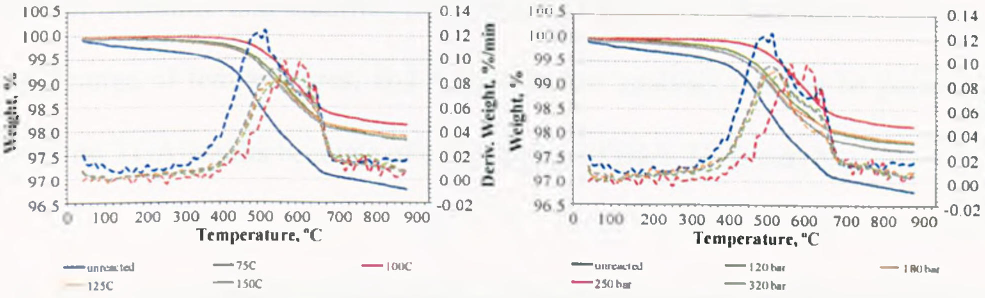

Figure 7-19. TGA curves of unreacted and reacted hematite samples at different temperatures (left) and pressures (right). Dashed lines correspond to derivative weight curves.

The TGA profiles for reacted samples at different temperatures show a weight loss in the temperature region between 400 and 800°C. This temperature range is approximately the same where kaolinite decomposes, as can be seen in the TGA profile for the unreacted sample. However, the TGA curves for the reacted hematite samples show a lower weight loss in that region compared to the parent material, indicating kaolinite dissolution and precipitation of secondary minerals. The TGA curve of the sample reacted at 100°C shows the lowest weight loss, which is in close agreement with the experimental percentage of weight uptake by the solids (the highest one of that set of experiments). It seems obvious the weight taken up by the reacted solids is due to solid phases decomposing in the temperature region ca. 400 and 800°C and/or temperatures above 900°C. Precipitation of residual brine might be responsible for some of the reported weight uptake and its associated weight loss is not observed before 900°C. Derivative weight curves indicate the maximum higher rates of weight loss at higher temperatures than the curve for the parent sample. As for experiments with varying amounts of $SO_2$ in the gas stream previously explained in section 7.1.3, several phases (iron sulfate, iron sulfide, boehmite and siderite) could have precipitated that decompose in the same range of temperatures, and a quantitative analysis can not be performed based on TGA results because of overlapping of their TGA curves.

The TGA curves for the unreacted and reacted samples at different reaction pressures can be explained in a similar manner to the set of curves obtained at different temperatures and the conclusions withdrawn would then be the same: a quantitative analysis of the precipitates is not feasible if based only on thermal analysis results.

#### *7.1.4.3. Summary*

Geochemical modeling predicts lower carbonate (i.e. siderite) precipitation with increasing temperature (at a set pressure) and, conversely, a higher carbonate formation with increasing pressure (at a set temperature). The solubility of $CO_2$ in water (i.e. the activity of bicarbonate in water) decreases with increasing temperature and increases with increasing pressure. Thereby, thermodynamically, siderite precipitation is enhanced at low temperatures and high pressures. However, temperature has an important effect on reaction kinetics and, as reaction temperature increases, so does the reaction rate constant. Hence, the result is the contribution of two opposite temperature effects and a reaction temperature of maximum conversion is normally identified. Dissolution of $CO_2$ and $SO_2$ gases in water, and precipitation of siderite are all fast relative to rate limiting hematite dissolution (Palandri et al., 2005).

Based on experimental weight uptake (%) values, temperature of maximum conversion seems to be 100°C (maximum weight uptake was observed). Precipitates at that temperature could not be identified by thermal analysis, with several phases (siderite, iron sulfate, boehmite and iron sulfide) been potential candidates as the formed ones based on the TGA profiles.

Weight uptake (%) for experiments at a constant temperature of 100°C increases with increasing reaction pressures (hence, higher $CO_2$ pressure) up to 250 bar, and no further weight uptake is observed beyond that value. Based on Soong and co-workers studies (Soong et al., 2004), pressure does not seem to have a high effect in the formation of carbonate minerals as long as a minimum $CO_2$ pressure is maintained in the reactor.

Discrepancies between experimental and predicted trends are more significant when evaluating the effect of reaction temperature and pressure compared to the effect of other variables on mineral trapping by iron oxides; overall, modeled trends are not followed by empirical ones because of the major role played by kinetics in the involved reactions.

The partial pressure of $CO_2$ and $SO_2$ are important variables because they control the concentration of dissolved gases in the brine (which would then become available to react with the host reservoir) and consequently the evolution of the pH over the course of the reaction. Temperature is of interest because it affects reaction kinetics, which could play an important role on a full-scale injection operation. Previous studies (Bachu, 2003) reported that warm basins are less favorable for $CO_2$ sequestration than cold ones because of the reduced capacity in terms of $CO_2$ mass and because of higher $CO_2$ buoyancy, which drives the upward $CO_2$ migration. In this case, experimental optimum conditions for precipitation of secondary minerals under tested parameters have been identified as 100°C and 250 bar, which would be encountered at a depth of ~ 2.5 km in a sedimentary basin with a hydrostatic pressure gradient of 100 bar/km and a geothermal gradient of ~ 40°C/km (higher than the average of 25°C/km). To date, $CO_2$ has been injected into depths ranging from 800 to deeper than 3000 m (Gale, 2009), so injection at a depth of 2.5 km would be feasible.

### 7.1.5. Effect of solids concentration

A series of autoclave experiments (experiment numbers 8, 15, 16 and 17 in Table 7-1) were conducted to validate the equilibrium trends predicted by geochemical modelling when testing the effect of varying the rock-to-brine ratio in the mineral trapping capacity of hematite. Comparison of predicted and empirical trends is performed in the same way as in previous sections.

### *7.1.5.1. Analysis of fluid chemistry and solids weight uptake*

Dissolved iron content in the system is very small (0.05 ppm) for the simulation with a solids concentration of 10 g/L, due to the iron been trapped in siderite and pyrite instead of being present as a dissolved phase in the brine (Figure 7-20, inner figure). As the solids concentration increases in the system (25, 50 and 100 g/L) the dissolved iron concentration reaches a plateau. The amount in grams of siderite precipitated is the same for the latter simulations (11.2 g), hence, dissolved iron would also be the same. As mentioned in the previous section, the reactions taking place in the system are the same; precipitation of solid phases is delayed to higher amounts of $SO_2$ added due to higher values of solids concentration used in the simulations.

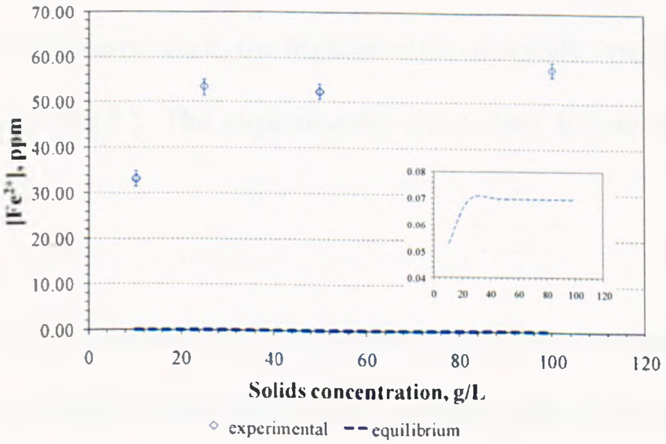

Figure 7-20. Comparison of experimental and predicted trends for dissolved iron as a function of different solids concentration values.

Equilibrium pH remains approximately the same for the different values of solids concentrations used, and for measured pH, values also remain ~ constant except for the value in the experiment with a solids concentration of 25 g/L (Figure 7-21). This is probably due to the slightly higher initial pH of the brine (13.0) compared to the rest of the experiments (~12.7) (see Table 7-1).

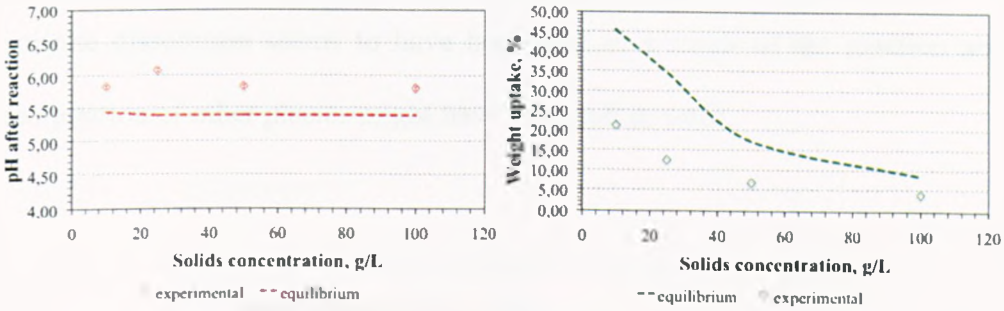

Figure 7-21. Comparison of experimental and predicted trends for brine pH and solids weight uptake (%) as a function of different solids concentration values. Error bars size for weight uptake series is smaller than symbol size.

The modelled trend observed for the weight uptake (%) is strongly linked to the dissolved iron concentration, since the predicted solid phases that precipitate in the system are $Fe^{2+}$-containing phases. Hence, the smallest value of dissolved iron corresponds to the highest value of weight uptake by the solid (experiment with 10g/L). The experimental trend does follow the theoretical one.

Measured changes in dissolved iron concentration, pH and weight uptake (%) by the solids agree well with equilibrium modeling calculations (Figure 7-20 and Figure 7-21) but, although reaction progress was made, time limitations prevented the system from reaching the equilibrium values.

### *7.1.5.2. Characterisation of solid products*

Analyses of precipitates by thermal analysis (Figure 7-22) are quite similar to those obtained in section 7.1.4.2. Again, no quantitative analysis can be made due to solid phases decomposing within the same range of temperatures. It is clear though, from comparison amongst the TGA curves of unreacted and reacted samples in the temperature range between 400 and 800°C, how kaolinite dissolution seems to have happened as a result of the reaction and precipitation of other phases might have occurred as well.

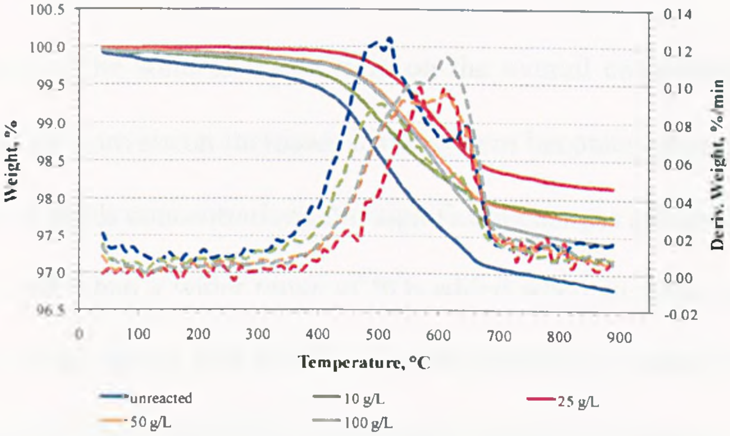

Figure 7-22. TGA curves of unreacted and reacted hematite samples with different solids concentration values. Dashed lines correspond to derivative weight curves.

Curves for rate of weight loss (dashed lines in Figure 7-22) are shifted to higher temperatures in reacted hematite samples compared to the unreacted one, indicating that precipitates in those samples are more stable thermally than unreacted powders. Predicted siderite and pyrite phases could have precipitated as a result of the reaction in sample reacted with 10g/L of solids concentration, but can not be confirmed from the TGA profiles due to overlapping of their curves. The former statement also applies to the rest of reacted samples. The high percentages (ranging from ~21% to ~7%) of weight uptake observed for experiments with a value of solids concentration of 10, 25 and 50 g/L , probably involved precipitation of solid phases that decompose at temperatures higher than 900°C and not only phases which decompose within the 400-800°C range. Residual brine is, again, a strong candidate as one of the potential phases responsible for part of the observed percentage of weight uptake in the experimental tests.

#### *7.1.5.3. Summary*

The influence of the solid to liquid ratio on the overall carbonation reaction suggests that the conversion increases if the system becomes more diluted (i.e. lower value of solids concentration). No significant changes are observed in the simulations other than a wider range of $SO_2$ added where siderite becomes the stable phase in the system and, therefore, precipitation of secondary minerals at higher values of $SO_2$ gas added for increasing solid-to-liquid ratios.

Experimental trends agree well with the theoretical ones but, again, values are of different order of magnitude for dissolved iron and weight uptake (%) data because of being far from steady-state in the experimental runs. It is uncertain whether the reaction led to carbonates precipitation or not because their presence could not been confirmed by thermal analysis.

In a real-case scenario, $CO_2$ will displace brine as it is injected, decreasing the amount of brine in the pore space; thereby, the rock-to-brine ratio would increase with approach to the injection site and a decrease in the extent of the carbonation reaction can be expected, i.e., a decrease in the mass of carbonate minerals precipitated. The rock-to-brine ratio could then play a significant role in the zone close to the injection well. As time goes by, more free $CO_2$ in the pore space will dissolve into the brine so more minerals would react with aqueous $CO_2$ and $SO_2$ and carbonate minerals precipitation would be increased.

### 7.1.6. Effect of a pH buffer

A laboratory experiment (number 18 in Table 7-1) was carried out without the pH buffer (NaOH) to be further assessed and compared with the corresponding experiment (number 8 in Table 7-1) carried out with the pH buffer.

Comparison of modeling and empirical results is discussed in section 7.1.6.1 and characterisation of solid products in section 7.1.6.2.

#### *7.1.6.1. Analysis of fluid chemistry and solids weight uptake*

As discussed in the previous section, predicted dissolved iron is much higher in the non-buffered simulation than in the buffered one due to a more acidic environment and a lower stability of siderite in the system. This trend is also observed in empirical results (Figure 7-23).

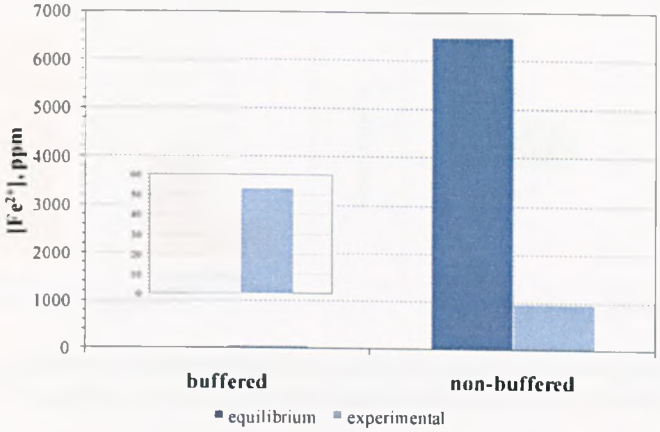

Figure 7-23. Comparison of experimental and predicted results for dissolved iron as a function of the presence or absence of a pH buffer.

Nevertheless, dissolved iron concentration is higher than predicted one for the buffered case and lower for the non-buffered case. Absence of siderite precipitation could be responsible for this observation in a buffered-experiment: measured dissolved iron is higher than predicted because iron remained in solution instead of being trapped in the carbonate rock. Time constraints prevented the system from reaching steady-state. Dissolved iron concentration is not as high as predicted in the non-buffered experiment. Again, the extent of the hematite dissolution reaction could not reach the predicted one because of the short duration of the experiment. Precipitation of Fe-bearing phases might also have happened and could contribute to trap part of the dissolved iron in the experiment.

The trend for pH values predicted by geochemical modeling is followed by experimental values and pH is always higher in the buffered case than in the non-buffered one (Figure 7-24).

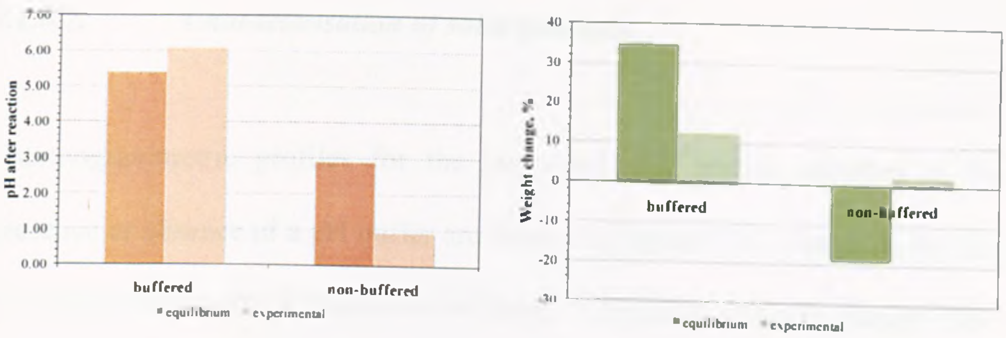

Figure 7-24. Comparison of experimental and predicted results for brine pH (left) and solids weight change (%) (right) as a function of the presence or absence of a pH buffer.

In the experiment carried out with NaOH the measured pH was 6.1 versus the 5.4 obtained for equilibrium. An extremely low pH (0.9) was measured in the non-buffered experiment, which is much lower than the predicted one (2.9), even considering reported pH values in experimental tests are always higher than theoretical ones due to experimental limitations in the pH measurement method. This result suggests hematite dissolution did not occur very extensively and therefore, pH remained extremely low due to $CO_2$ and $SO_2$ dissolving in the brine and generating acidity.

Predicted weight change was negative when no NaOH was added to the experiment because most of the starting material dissolved (only 2.3 g out of the initial 10 g remained in the system) and only 5.9 g of siderite precipitated. Experimentally, the observed weight change was positive (~ 2%), indicating the extent of hematite dissolution was not as expected because hematite was the main collected solid; however, precipitation of a minor amount of secondary minerals did occur based on the value of weight change. For the buffered case, reported weight change percentages were positive and almost three times higher for the simulation than for the empirical test.

### 7.1.6.2. Characterisation of solid products

Thermogravimetric profiles for the unreacted and reacted samples in the presence or absence of a pH buffer are shown in Figure 7-25. Based on the rate of weight loss curves (dashed lines in Figure 7-25), no significant changes have occurred in the sample reacted in absence of a pH buffer: its derivative weight curve profile follows quite well the one for the parent hematite; dissolution of kaolinite present in the starting material seems to be the only process occurring in the reaction because the observed weight loss between 400 and 700°C is not as high as in the unreacted sample. The observed weight uptake is very small (~2%) and could be only due to phases that decompose at temperatures higher than 900°C, most likely some residual brine being left behind upon the sample rinsing process. Siderite precipitation is not possible under those acidic conditions. Recent publications (Golubev et al., 2009, Testemale et al., 2009) have reported rate constant values for dissolution of siderite under acidic conditions ($pH \leq 5$). These studies claim that protonation of the mineral surface controls dissolution of siderite and $H_2CO_3$ species have no effect on the dissolution rate, so the driving factor is the acidity of the fluid in contact with the carbonate rock. Based on these studies, any potential siderite present in our reactive system would undoubtedly dissolve because of the extreme acidity of the brine (0.9).

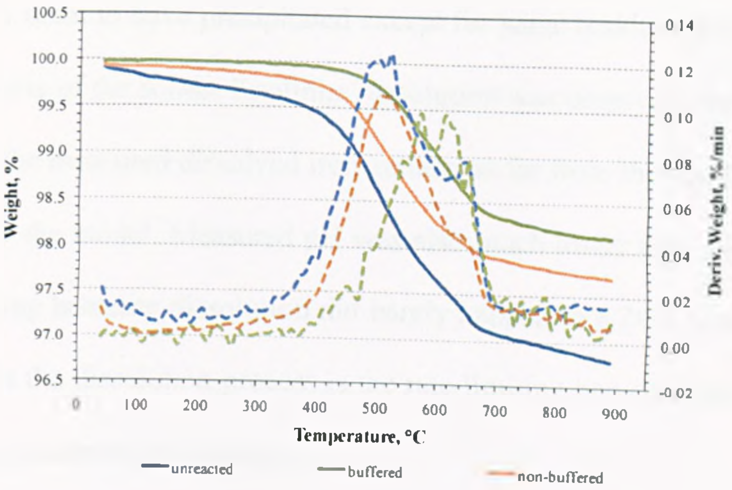

Figure 7-25. TGA curves of unreacted and reacted samples in buffered and non-buffered experiments. Dashed lines correspond to derivative weight curves.

The observed weight loss between 400 and 700°C for the sample reacted with a pH buffer is the lowest one, indicating that either kaolinite dissolved more than in the non-buffered experiment or a combination of kaolinite dissolution and secondary minerals precipitation. The derivative weight curve profile is quite different from the parent hematite one so the second option seems to be the right one. Potential phases that could have precipitated during the course of the experiment have been already discussed in section 7.1.3: iron carbonate, iron sulfate, boehmite and iron sulfide could have formed as a result of the reaction based on the TGA curves.

### *7.1.6.3. Summary*

Geochemical modeling, also considering the aluminum content of the sample (see Figure A-2 in Appendix), predicts siderite as the stable phase in the system even in the absence of some initial NaOH buffering. However, experimentally, absence of a pH buffer produces an extremely acidic brine (pH=0.9) where no solid phases seem to have precipitated except for some residual brine upon the rinsing process of the solids. Kaolinite dissolution was observed from the TGA curves and the measured dissolved iron value was far from the equilibrium one predicted by the model. Measured pH was also much lower than the predicted one, indicating hematite dissolution did barely happen in a 24 h timeframe and showing that the dissolution process is the rate-limiting one compared to gases solubility and siderite precipitation.

In a CCS scenario, most saline-aquifer sequestration targets contain a NaCl brine – siliciclastic rock system and some initial bicarbonate buffering (Newell et al., 2008). Dissolved carbonate is present in solution because of the ubiquitous presence of some carbonate minerals, as detrital grains and as secondary cements. Thereby, some degree of initial buffering is expected, which is crucial to assess because, as can be seen in results from this section, it greatly affects the speciation, pH and mineralogy of the system.

## 7.2. Implications for geological storage of $CO_2$

The precipitation of carbonate minerals is beneficial as a means of fixing anthropogenic-derived $CO_2$ in solid form, but could also modify the hydrologic properties of targeted aquifers, i.e., their porosity and permeability.

The $CO_2$ trapping capability will greatly depend on the primary mineral composition (in this case, initial abundance of hematite) of the reservoir rock. Near the injection well, most of the pores are filled with $CO_2$ and $SO_2$ as brine is displaced during the injection. Some brine will be trapped within the pore that can facilitate reaction between $CO_2$ and $SO_2$ and the host rock. Upon injection, $SO_2$ is assumed (due to its high solubility) to instantaneously interact with the aqueous phase to produce the thermodynamically more stable products, sulfuric acid and hydrogen sulfide. When $CO_2$ gas comes in contact with water, it dissolves to form $H_2CO_3$,to further dissociate into $H^+$ and $HCO_3^-$. Due to the generated acidity, it is very likely that some dissolution of the host rock near the injection site would occur, including dissolution of any cements present in the reservoir rock. However, dissolution of the host rock is accompanied by the precipitation of secondary minerals, like dawsonite, gibbsite and siderite. This will greatly affect porosity and permeability of the aquifer. Mineral dissolution would result in an increase of porosity and permeability, as opposed to mineral precipitation that would decrease them.

The net change in porosity will depend on the quantities of phases that dissolve and precipitate and on their molar volumes (considering only volume changes). The effect on permeability depends greatly on where the dissolution and/or precipitation occur within the pore space. According to reaction [7-11], complete conversion of hematite to siderite would result in almost a doubling of mineral volume (Table 7-4), with the subsequent porosity and permeability loss.

$$Fe_2O_3 \text{ (hematite)} + 2\ CO_2 + SO_2 + H_2O \leftrightarrow 2\ FeCO_3 \text{ (siderite)} + H_2SO_4 \quad [7\text{-}11]$$

Near the well, precipitation of sulfur-bearing minerals, like pyrite, FeS and native sulfur (reactions [7-12] to [7-14]), would occur during the injection operation period, where a strong acidified zone would be generated; carbonate precipitation would occur with increasing distance from the well, within the higher pH regions. In the outermost zone, unaltered rock would probably be the only solid present in the system. Dawsonite could also precipitate immediately following injection and near the injection well, where the $fCO_2$ remains high enough for the reaction to take place. This reaction is enhanced by high ambient $Na^+$ concentrations, plume-induced $CO_2$ aqueous solubility and kaolinite dissolution according to reaction [7-15].

$$4\ Fe_2O_3\ \text{(hematite)} + 15\ H_2S + H_2SO_4 \leftrightarrow 8\ FeS_2\ \text{(pyrite)} + 16\ H_2O \qquad [7\text{-}12]$$

$$4\ Fe_2O_3\ \text{(hematite)} + 9\ H_2S \leftrightarrow 8\ FeS\ \text{(amorphous)} + H_2SO_4 + 8\ H_2O \qquad [7\text{-}13]$$

$$3H_2S + H_2SO_4 \leftrightarrow 4S\text{(native)} + 4H_2O \qquad [7\text{-}14]$$

$$Al_2Si_2O_5(OH)_4 + 2Na^+ + 2CO_2 + H_2O \leftrightarrow 2NaAl\ (OH)_2CO_3 + 2SiO_2 + 2H^+ \qquad [7\text{-}15]$$

Complete alteration of the kaolinite to dawsonite would lead to a 20% increase of the mineral volume. Therefore, in the solid sample considered in this study, i.e. hematite (~83%) and kaolinite (~17%), complete alteration to siderite and dawsonite would result in a ~ 72% increase of the sample volume. If the host reservoir had an average porosity of 20%, which is within the typical range of values for current large injection projects (Gale, 2009), a 72% increase of the sample volume would cause a 35% porosity decrease. It is important to note that dawsonite would presumably re-dissolve as soon as the $CO_2$ pressure dissipates, so some porosity would again be generated. A natural red bed would be composed of other minerals like quartz; hence, complete alteration of ferric iron-bearing minerals within the rock would lead to a lower porosity decrease than for the hematite sample considered in this research. Iron in natural sedimentary basins may also occur in many other minerals, especially phyllosilicates, which could supply other cations prone to be precipitated in secondary minerals. For instance, the presence of Ca may lead to precipitation of anhydrite ($CaSO_4$), gypsum ($CaSO_4 \cdot 2H_2O$) or ankerite ($CaFe(CO_3)_2$) instead of siderite.

There may also be a porosity and permeability loss near the injection site due to precipitation of pyrite, FeS-am or sulfur that could lead to reduction in injectivity. FeS-am, if present, is always metastable with respect to pyrite and should re-dissolve. More S will then become available for further reduction of $Fe^{3+}$ from hematite and hence further precipitation of siderite.

Table 7-4. Molar volumes for precipitates of interest in the $CO_2$-$SO_2$-brine-hematite carbonation reaction.

| Mineral | Molar Volume[†][§] (cm$^3$/mol) |
|---|---|
| Hematite ($\alpha$-$Fe_2O_3$) | 30.27±0.012 |
| Kaolinite ($Al_2Si_2O_5(OH)_4$) | 99.52±0.26 |
| Siderite ($FeCO_3$) | 29.38±0.014 |
| Dawsonite ($NaAl(OH)_2CO_3$) | 59.50*[§] |
| Pyrite ($FeS_2$) | 23.94±0.007 |
| FeS (cubic) | 24.44±0.01 |
| FeS (hex.) | 24.81±0.02 |
| Sulfur (orthorhombic) | 15.51±0.05 |
| Sulfur (monoclinic) | 16.49±0.08 |
| Sulfur (rombohedral) | 14.51±0.06 |
| Halite (NaCl) | 27.02±0.003 |

[†]Data obtained from the CRC Handbook of Chemistry and Physics (Weast, 1984); [§]at standard temperature and pressure; *calculated from dividing the compound's molecular weight (g/mol) by its density (g/cm$^3$) obtained from (Webmineral, 2009).

A net decrease in porosity has the potential to cause clogging, slowing injection or, on the positive side, can improve the cap rock sealing. Thus, the products of the $CO_2$-$SO_2$-brine-hematite reaction along with rates of dissolution and precipitation are very important for understanding the fate of injected $CO_2$ and $SO_2$ as well as the long time effect on the safety and integrity of the seal of the formation.

Additionally, some NaCl seems to be present in the collected precipitates from the experiments but its origin is not clear. Most likely, it was introduced during the rinsing process of collected samples after the experiments. Reacted slurries were filtered to separate the solids from the brine and, unrecovered solids from the reactor were rinsed away with the brine itself, trying to minimise the dissolution of any precipitate. Due to the high concentration of Na and Cl in brine, NaCl could be present following the drying of the precipitates. On the other hand, salt precipitation is likely to occur in the vicinity of the injection well, in the dry-out zone, as a result of vaporization of water along with the dissolution of $CO_2$ (Zeidouni et al., 2009). If salt precipitation occurs, porosity and permeability might be reduced as well as injectivity. The loss in injectivity will depend on the degree of reduction of formation permeability with increased salt saturation.

The particle size fraction is of interest because it can affect reaction kinetics, which could have important consequences in a real-case operation. Based on results reported in this chapter, a fine solid fraction (< 38 μm) would react much faster than a coarser one (38-150 and 150-300μm). However both, fast and slow, reactivities have advantages and disadvantages when applied to a full-scale operation. On one hand, if the reactions are extremely slow the potential for leakage of $CO_2$ into overlying formations may increase; on the other hand, fast reaction rates may adversely affect the injectivity in an injection well by decreasing the porosity and permeability close to the injection site. Ultimately, a reduction of the lifetime of the well could also happen.

Significant changes in porosity and permeability could also occur as a result of mineral dissolution and precipitation due to the acidic environment generated by the $CO_2$-$SO_2$ gas injection. As the $SO_2$ content in the gas stream increases, so does the acidity of the system; hence, the acidified zone generated in the aquifer would be stronger and probably larger than for cases with lower $SO_2$ contens in the gas stream. Mineral dissolution would probably dominate in that acidified zone with a consequent increase in porosity and permeability. Nonetheless, precipitation of sulfur-bearing phases would incur in a porosity decrease so the different rates of dissolution and precipitation reactions will ultimately determine the net change in porosity and permeability over the reaction time.

In a brine-rock system where the natural mineral buffering is not present, the medium will become more acidic than in a buffered system and the mineralogy and brine characteristics are expected to be very different. Presumably, minerals dissolution will become more important in more acidic systems, i.e. non-buffered, than in less acidic ones. This will result in a porosity and permeability increase as opposed to a buffered system where carbonate minerals precipitation would be favored and porosity and permeability would then decrease. Nonetheless, in an acidic system precipitation of secondary minerals, such as S-bearing minerals that are stable at lower pH values (pyrite, S native, anhydrite...), can also be favored; consequently, porosity and permeability would decrease. Thereby, it is very important to accurately characterise the in situ geochemistry for reliable evaluation of $CO_2$ trapping in mineral form.

## 7.3. References

Alexander, G., Maroto-Valer, M. M. & Gafarova-Aksoy, P. (2007) Evaluation of reaction variables in the dissolution of serpentine for mineral carbonation. *Fuel,* 86, 273-281.

Bachu, S. (2003) Screening and ranking sedimentary basins for sequestration of $CO_2$ in geological media in response to climate change. *Environmental Geology,* 44, 227-289.

Bachu, S. (2008) $CO_2$ storage in geological media: role, means, status and barriers to deployment. *Progress in Energy and Combustion Science,* 34, 254-273.

Balek, V., Subrt, J., Rouquerol, J., Llewellyn, P., Zelenak, V., Bountsewa, I. M., Beckman, I. N. & Gyoryova, K. (2003) Emanation thermal analysis study of synthetic gibbsite: Evaluation of experimental ETA results by mathematical modelling. *Journal of Thermal Analysis and Calorimetry,* 71, 773-782.

Bayliss, P. & Warne, S. S. J. (1972) Differential thermal analysis of siderite-kaolinite mixtures. *American Mineralogist,* 57, 960-966.

Benezeth, P., Palmer, D. A., Anovitz, L. M. & Horita, J. (2007) Dawsonite synthesis and reevaluation of its thermodynamic properties from solubility measurements: Implications for mineral trapping of $CO_2$. *Geochimica Et Cosmochimica Acta,* 71, 4438-4455.

Biber, M. V., dos Santos Afonso, M. & Stumm, W. (1994) The coordination chemistry of weathering: IV. Inhibition of the dissolution of oxide minerals. *Geochimica et Cosmochimica Acta,* 58, 1999-2010.

Brantley, S. L., Kubicki, J. D. & White, A. F. (2008) *Kinetics of water-rock interaction,* New York, USA, Springer.

Briggs, D. & Beamson, G. (Eds.) (2006) *The XPS Database of Polymers,* SurfaceSpectra.

Cameron, F. K. (1930) The solubility of ferrous sulphate. *Journal of Physical Chemistry,* 34, 629-710.

Descostes, M., Mercier, F., Thromat, N., Beaucaire, C. & Gautier-Soyer, M. (2000) Use of XPS in the determination of chemical environment and oxidation state of iron and sulfur samples: constitution of a data basis in binding energies for Fe and S reference compounds and applications to the evidence of surface species of an oxidized pyrite in a carbonate medium. *Applied Surface Science,* 165, 288-302.

Fernandez Bertos, M., Simons, S. J. R., Hills, C. D. & Carey, P. J. (2004) A review of accelerated carbonation technology in the treatment of cement-based materials and sequestration of $CO_2$. *Journal of Hazardous Materials B,* 112, 193-205.

Gale, J. (2009) Geological storage of $CO_2$: status of CCS and challenges ahead. *Fourth International Conference on Clean Coal Technologies (CCT).* Dresden, Germany.

Golubev, S. V., Bénézeth, P., Schott, J., Dandurand, J. L. & Castillo, A. (2009) Siderite dissolution kinetics in acidic aqueous solutions from 25 to 100 °C and 0 to 50 atm $pCO_2$. *Chemical Geology,* 265, 13-19.

Gregg, S. J. & Sing, K. S. W. (1982) *Adsorption, Surface Area and Porosity,* London, Academic Press Inc. Ltd.

Grosvenor, A. P., Kobe, B. A., Biesinger, M. C. & McIntyre, N. S. (2004) Investigation of multiplet splitting of Fe 2p XPS spectra and bonding in iron compounds. *Surface and Interface Analysis,* 36, 1564-1574.

Holloway, S. (2005) Underground sequestration of carbon dioxide-a viable greenhouse gas mitigation option. *Energy,* 30, 2318-2333.

Huggins, C. W. & Green, T. E. (1973) Thermal Decomposition of Dawsonite. *American Mineralogist,* 58, 548-550.

Huijgen, W. J. J., Witkamp, G.-J. & Comans, R. N. J. (2006) Mechanisms of aqueous wollastonite carbonation as a possible $CO_2$ sequestration process. *Chemical Engineering Science,* 61, 4242-4251.

Kloprogge, J. T., Ruan, H. D. & Frost, R. L. (2002) Thermal decomposition of bauxite minerals: infrared emission spectroscopy of gibbsite, boehmite and diaspore. *Journal of Materials Science,* 37, 1121-1129.

Kotra, R. K., Gibson, E. K. & Urbancic, M. A. (1982) Release of volatiles from possible Martian analogs. *Icarus,* 51, 593-605.

Loughnan, F. C. & See, G. T. (1967) Dawsonite in the Greta coal measures at Muswellbrook, New South Wales. *American Mineralogist,* 52, 1216-1219.

Moulder, J. F., Stickle, W. F., Sobol, P. E. & Bomben, K. D. (1995) *Handbook of X-ray Photoelectron Spectroscopy: a reference book of standard spectra for identification and interpretation of XPS data*, Physical Electronics.

Newell, D. L., Kaszuba, J. P., Viswanathan, H. S., Pawar, R. J. & Carpenter, T. (2008) Significance of carbonate buffers in natural waters reacting with supercritical $CO_2$ : Implications for monitoring, measuring and verification (MMV) of geologic carbon sequestration. *Geophysical Research Letters,* 35, L23403.

Palandri, J. L., Rosenbauer, R. J. & Kharaka, Y. K. (2005) Ferric iron in sediments as a novel $CO_2$ mineral trap:$CO_2$-$SO_2$ reaction with hematite. *Applied Geochemistry,* 20, 2038-2048.

Rudolph, W., Brooker, M. H. & Tremaine, P. R. (1997) Raman spectroscopic investigation of aqueous $FeSO_4$ in neutral and acidic solutions from 25°C to 303°C: inner- and outer-sphere complexes. *Journal of Solution Chemistry,* 26, 757-777.

Siriwardane, R. V., Poston Jr., J. A., Fisher, E. P., Shen, M. & Miltz, A. L. (1999) Decomposition of the sulfates of copper, iron (II), iron (III), nickel, and zinc: XPS, SEM, DRIFTS, XRD and TGA study. *Applied Surface Science,* 152, 219-236.

Soong, Y., Goodman, A. L., McCarthy-Jones, J. R. & Baltrus, J. P. (2004) Experimental and simulation studies on mineral trapping of $CO_2$ with brine. *Energy Conversion and Management,* 45, 1845-1859.

Stumm, W. & Morgan, J. J. (1996) *Aquatic chemistry: chemical equilibria and rates in natural waters,* New York, Wiley-Interscience.

Swift, P. (1982) Adventitious carbon - the panacea for energy referencing. *Surface and Interface Analysis,* 4, 47-51.

Testemale, D., Dufaud, F., Martinez, I., Benezeth, P., Hazemann, J. L., Schott, J. & Guyot, F. (2009) An X-ray absorption study of the dissolution of siderite at 300 bar between 50°C and 100°C. *Chemical Geology,* 259, 8-16.

Weast, R. C. (Ed.) (1984) *CRC Handbook of Chemistry and Physics,* Florida,USA, CRC Press, Inc.

Webmineral (2009) Mineralogy Database. Available from: <http://webmineral.com/> (accessed 8 December 2009).

Yani, S. & Zhang, D. An experimental study into pyrite transformation during pyrolysis of Australian lignite samples. *Fuel* (2009), doi:10.1016/j.fuel.2009.07.025

Zeidouni, M., Pooladi-Darvish, M. & Keith, D. (2009) Analytical solution to evaluate salt precipitation during $CO_2$ injection in saline aquifers. *Energy Procedia,* 1, 1775-1782.

Zerai, B., Saylor, B. Z. & Matisoff, G. (2006) Computer simulation of $CO_2$ trapped through mineral precipitation in the Rose Run Sandstone, Ohio. *Applied Geochemistry,* 21, 223-240.

## CHAPTER 8

# RESULTS AND DISCUSSION: GOETHITE ANALYSIS

# 8. Results and discussion: goethite analysis

This section presents experimental results obtained for goethite-brine-$CO_2/SO_2$ gas reactions. Firstly, a long term experiment (24 days) was conducted in a flexible-gold reaction cell under the same conditions as previously tested with hematite (T = 150°C, P = 300 bar, solids concentration = 67 g/L, ~ 11% vol. $SO_2$) and compared with predicted results from geochemical modelling. Reaction time was not as long as the one used in the experiment with hematite (~ 58 days) but comparisons can still be performed (section 8.1).

Secondly, short-term experiments ($\leq$ 264 h) were conducted in the high pressure-high temperature apparatus designed at the University of Nottingham to evaluate the same sample, goethite, for $CO_2$ storage with a gas composition more representative of a real-case scenario (0.4% v/v $SO_2$). Comparison between modeling and empirical results is also discussed (section 8.2).

Implications for geological storage of $CO_2$ are discussed in section 8.3. Finally, a comparison between hematite and goethite as potential reservoirs for $CO_2$ mineral trapping is established in section 8.4.

## 8.1. Reaction in a goethite-brine-$CO_2$-$SO_2$ system at 150°C and 300 bar

### 8.1.1. Analysis of fluid chemistry

Fluid samples were taken hourly or daily near the beginning of the experiment, and at increasing longer intervals depending on fluid chemistry and approach to steady-state. Total dissolved $CO_2$, refractive index, pH and iron in solution were analysed immediately after sampling. Dissolved anions were analysed by ion chromatography at the end of the experiment.

Changes in fluid chemistry were monitored with time (Figure 8-1). Total and ferrous iron concentrations were less than 2 ppm during the entire duration of the experiment and sharply increased in the quench fluid (Figure 8-1c), likely due to the dissolution of siderite precipitated during the experiment. Siderite has a retrograde solubility (Greenberg and Tomson, 1992, Sun et al., 2009) and is less soluble and more stable at elevated temperatures (Figure 8-2). Iron in the rinsed fluid was almost three times higher than in the quench fluid indicating that the rinsing process dissolved an iron-containing phase, probably iron sulfate since it shows a high solubility in water at atmospheric pressure and temperature. Some siderite could be also dissolving but its solubility is very low under those conditions (Sun et al., 2009).

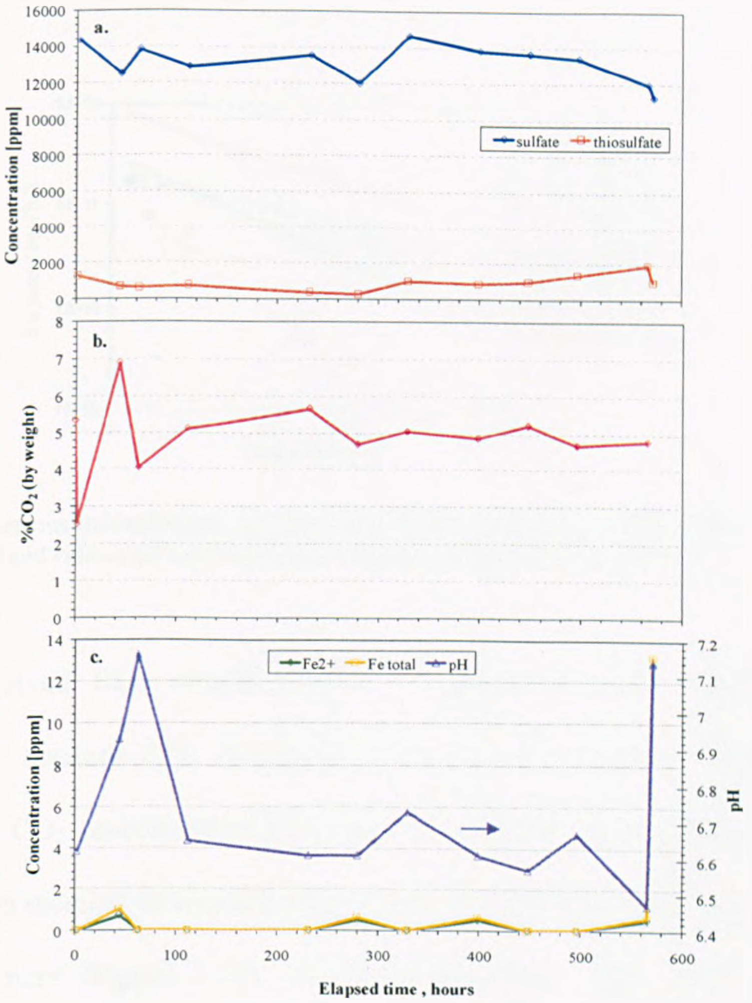

Figure 8-1. Fluid composition and pH over the course of the experiment: (a) dissolved sulfur(sulfate and thiosulfate); (b) total dissolved $CO_2$; (c) dissolved iron (total iron and ferrous iron) and fluid pH.

Changes in pH early in the experiment suggest the formation of a pH dependent precipitate. It is important to point out that pH values are maxima due to $CO_2$ degassing upon sampling and changes the distribution of carbon species in solution. The observed decrease in pH could be due to precipitation of siderite and/or other phases implying $H^+$ production:

$$H_2CO_3 + Fe^{2+} \leftrightarrow FeCO_3 + 2H^+ \qquad [8\text{-}1]$$

$$Fe^{2+} + HS^{-} \leftrightarrow FeS\ (\text{amorphous}) + H^{+} \qquad [8\text{-}2]$$

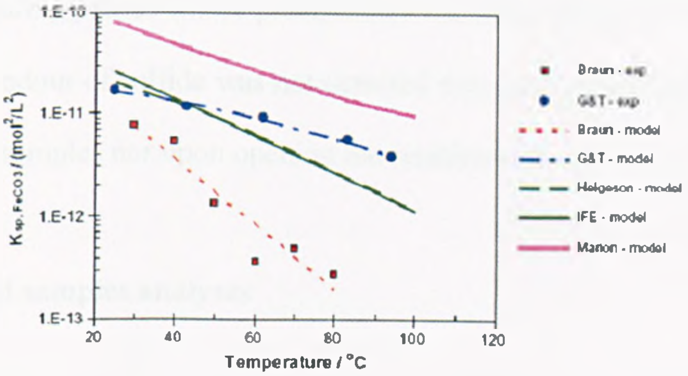

Figure 8-2. Ferrous iron carbonate (siderite) equilibrium constant vs temperature obtained from experimental and calculated solubility data- modified from (Sun et al., 2009).

Total dissolved $CO_2$ should remain ~ constant over the course of the experiment because $CO_2$ is present in excess as a separate phase. Some changes in $CO_2$ concentration were observed early in the experiment, with an initial sharp increase followed by a decrease to a constant value for the rest of the experiment (Figure 8-1b). The refractive index was found to remain constant at 7.6 throughout the experiment.

Disproportionation reaction of $SO_2$ yielded high concentrations of sulfate and thiosulfate (Figure 8-1a) along with some sulfite. The latter could not be quantified because it is rapidly oxidized; this was also observed by Palandri and co-workers (Palandri et al., 2005) in their experiment with hematite. They inferred a reaction between sulfite and sulfide (derived of the disproportionation reaction) producing thiosulfate and leaving behind a small amount of sulfite. No significant changes are observed in sulfate and thiosulfate concentrations over the course of the experiment except for a slightly decreasing trend in sulfate concentration towards the end of the experiment. This might be the result of precipitation of sulfate-bearing mineral and/or S-bearing phases whose precipitation consume sulfate such as sulfur and pyrite. The odour of sulfide was not detected throughout the experiment in any of the fluid samples nor upon opening the reaction cell.

### 8.1.2. Solid samples analyses

Analysis of the precipitate by XPS revealed that the sample surface had undergone significant alterations and confirmed the formation of carbonate species. Areas under peaks intensities were used to calculate concentrations of the elements as percentages of total intensity. First, a wide scan was performed to identify the elements according to their BE. Significant changes are seen in the surface elemental content of the unreacted, reacted and rinse-reacted samples (Table 8-1). The rinse-reacted sample had been collected from the reaction cell upon rinsing with distilled water and further filtration. Each sample was analysed four different times, targeting different points within the same sample in order to test its homogeneity, with samples been found reasonably homogeneous.

Table 8-1. Results of XPS analysis of goethite in atomic relative percentage. Terms in brackets next to the element symbols indicate the photoelectron emission used in the analysis. Values shown have been computed as the average value of four different measurements.

| Sample | Na [1s] | Fe [2p] | O [1s] | C [1s] | Cl [2p] | S [2p] | Si [2p] | Al [2p] | F [1s] |
|---|---|---|---|---|---|---|---|---|---|
| **Unreacted** | 3.1 | 7.4 | 47.7 | 22.6 | 1.6 | 1.5 | 4.3 | 1.4 | 10.4 |
| **Reacted** | 5.3 | 9.7 | 48.9 | 31.7 | 1.0 | 0.8 | 1.7 | 1.0 | 0.0 |
| **Reacted + rinsed** | 1.7 | 11.1 | 53.7 | 29.4 | 0.2 | 0.2 | 2.5 | 1.2 | 0.0 |

The unreacted sample contains 22.6% of carbon but the analysis of the C1s high resolution scan reveals that none of these carbon atoms are in the carbonate form. Based on the BE of the carbon signal, this carbon is mainly due to the contribution of the aliphatic carbon (found in all samples exposed to the atmosphere), which shows a peak intensity responsible of 58.6% of the total carbon signal; 9.2% is due to carbon associated with fluoride. A more detailed analysis of the high resolution scans for each element and the C 1s XPS spectrum will be discussed later, with a more in-depth study of the different contributions to the carbon signal. Other impurities also present in the unreacted sample are sulfur, silicon, aluminium and fluoride.

The sodium content of the solid increased as a result of the reaction and decreased very significantly upon the rinsing process, indicating that this process dissolved most of that sodium present in the solid; the increase in sodium content could result from incomplete rinsing of the brine from the reacted sample so chloride was also analysed to determine if it behaved in a similar way to sodium. It can be seen in Table 8-1 that chloride atomic % concentration was lower in the reacted sample than in the unreacted one, indicating that the increase in sodium can not be attributed entirely to residual salt. Rather, the sodium appears to be incorporated into the structure of the iron oxyhydroxide. Sulfur, silicon, aluminium and fluoride content decreased as a result of the reaction, mainly due to dissolution of phases containing such elements. The carbon content also increased after the reaction and decreased slightly with the rinsing process.

Solubility values at 1 atm and 20°C of some solid phases that may have precipitated due to the experiment and further rinsed out due to the rinsing process are shown in Table 8-2. Overall, the sodium-containing phases show high solubility values compared to almost all the iron-containing phases (except iron sulfate); a decreased atomic % concentration of sodium, carbon, chloride and sulfur is observed in the rinsed sample with respect to the reacted sample (Table 8-1). Sodium content decrease (3.6%) was almost the same as the sulfur, chloride and carbon combined content decrease (3.7%). Hence, S, Cl and C-containing sodium compounds could have been present and later dissolved, most likely NaCl, $Na_2CO_3$ and $Na_2SO_4$/$Na_2S_2O_3$. Also, $FeSO_4$ dissolution is also expected due to the significant increase of iron in solution upon the rinsing process. These phases would probably have precipitated when quenching the experiment because most of these compounds are very soluble (Lide, 1999), even at high temperature, and are likely undersaturated during the experiment. The surface iron content increased in the rinsed sample compared to the reacted sample but this would be only a result of the surface decrease content of other elements, making the iron content higher in percentage.

Table 8-2. Solubility values of some phases of interest (Lide, 1999).

| | Solubility [g/100g $H_2O$] @ 1 atm and 20°C |
|---|---|
| **$FeCO_3$*** | $6.6 \cdot 10^{-5}$ |
| **$Na_2CO_3$** | 21.5 |
| **NaCl** | 35.9 |
| **$Na_2SO_4$** | 19.5 |
| **$Na_2S_2O_3$** | 73 |
| **$FeSO_4$** | 25.6 |

* Sulfides, carbonates, sulfites, phosphates, hydroxides and oxides of Fe are considered as insoluble.

Figure 8-3 shows the obtained XPS C 1s spectra of the different samples. It can be clearly seen that a new peak centered at 289.6 eV is formed after the reaction, which is consistent with carbonate formation predicted by geochemical modeling.

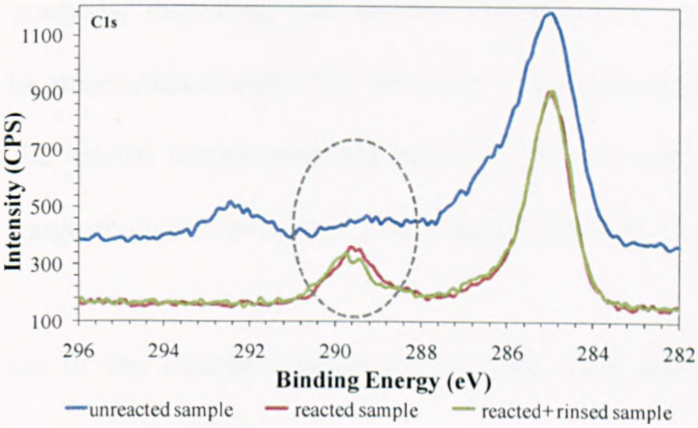

Figure 8-3. XPS C1s spectra of unreacted, reacted and reacted + rinsed samples.

Reference BE values for the carbonate peak in siderite and sodium carbonate are 289.8 and 289.4 eV respectively, as determined by XPS analysis of the reference compounds. The BE for the peak related to carbonate carbon atoms in the reacted sample is right in between the values for the iron and sodium carbonates; this could indicate the presence of both carbonates. Furthermore, the BE of the carbonate peak in the reacted + rinsed sample shifts to higher values more characteristic of siderite (Figure 8-3), which validates the latter statement since sodium carbonate was probably dissolved upon rinsing of the solids, leaving siderite behind as the only carbonate present in the rinsed sample.

Observation of the bulk samples before and after the experiment by XRD revealed no obvious change. However, thermal decomposition of unreacted, reacted and rinse-reacted samples revealed a small percentage of weight loss (~0.8%) at the decomposition temperature of siderite (ca. 400°C) in the rinse-reacted sample (Figure 8-4). This observation is in good agreement with results from XPS analyses, indicating that siderite was the only carbonate phase present in the rinse-reacted solid. The presence of sodium carbonate was not detected in the reacted sample probably because it was formed in very small amount, not large enough to be seen in a bulk sample analysis like TGA.

An estimation of the siderite content of the final solid can be computed according to reaction [8-3] below:

$$FeCO_3 \xrightarrow{\Delta} FeO + CO_2 \qquad [8\text{-}3]$$

Assuming all the remaining siderite decomposed in the TGA analysis, 2.1% of iron carbonate was present in the rinse-reacted solid. Collected solids after the experiment were 9.1 g so 8.7% of weight loss was observed versus the 18.8% weight uptake predicted by geochemical modeling. Experimentally, conversion of Fe from goethite into siderite was 1.5%, far yet from the equilibrium 78.2%.

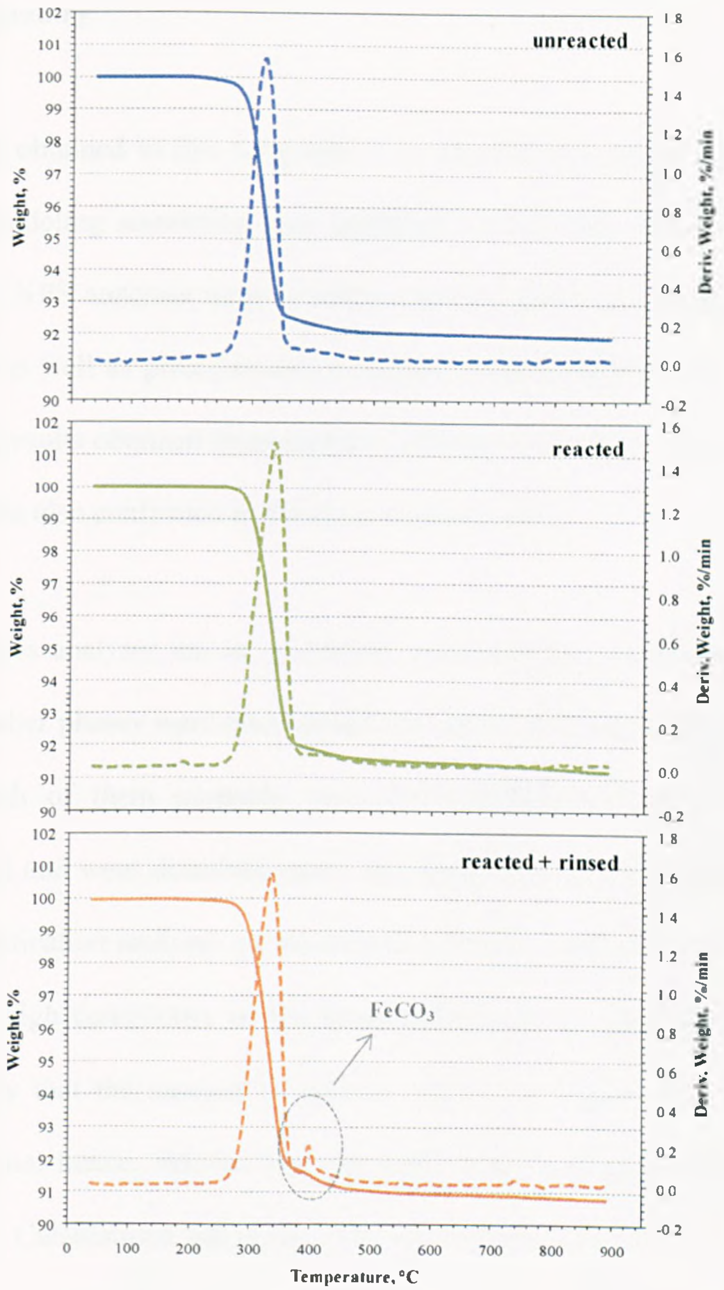

Figure 8-4. TGA curves of unreacted, reacted and rinse-reacted goethite samples. Dashed lines correspond to derivative weight curves.

Thereby, only 76 mg of $CO_2$ were sequestered in siderite per g of sample instead of predicted 0.39 g. It is important pointing out that this value is an underestimated one because some of the siderite precipitated over the course of the experiment probably dissolved in the quenched fluid, so its quantity in-situ would have been higher than the measured value in the laboratory (0.2g).

### 8.1.3. Summary

The results obtained in this long term (~ 1 month) experiment are consistent with the modeling simulation that predicted an iron-rich solid-phase should precipitate. XPS analyses largely confirmed how the rock surface underwent alterations as well as precipitation of siderite. Bulk solid thermal analysis did agree with results obtained from surface techniques, i.e., XPS, because siderite presence was also confirmed in the rinse-reacted solid.

Solid samples analyses are in agreement with changes in fluid composition; however, other phases were also identified such as sodium carbonate and iron sulfate. Both of them probably precipitated during the quenching of the reaction cell and were dissolved upon the rinsing process with distilled water. Total quantification analyses on the samples surface could not been performed due to the high complexity of the samples but relative quantitative analysis clearly show that the amount of siderite was much higher than the sodium carbonate one; hence, siderite was the main reaction product present in the experiment. Calculations based on TGA curves showed 76 mg of $CO_2$ were sequestered in iron carbonate per g of goethite.

Reaction though did not reach equilibrium after ~ 1 month but given enough time steady-state should be attained. Goethite would be then a suitable repository for $CO_2$ underground storage as long as $CO_2$-$SO_2$ gas stream is injected into the rock formation.

## 8.2. Reaction in a goethite-brine-$CO_2$-$SO_2$ system at 100°C and 250 bar

Three different sets of experiments were performed in the high pressure-high temperature apparatus designed at the University of Nottingham: a first one, evaluated the influence of the particle size of the solids on the overall reaction; a second one, evaluated the reaction time on the carbonation of goethite when the gas composition is similar to the one derived from a fossil fuel-derived combustion process; and, a the third one evaluated the influence of the $SO_2$ content in the gas stream.

Operating conditions of the different sets of experiments are described in Table 8-3. The criteria for choosing the experimental conditions are the same as for experiments with hematite. Baseline conditions of temperature (100°C), pressure (250 bar), brine composition (1.0mNaCl and 0.5mNaOH) and reaction time (24 h) remain the same as for the baseline case in experiments with hematite. The solids concentration was set to a constant value of 10g/L because of the scarce amount of parent goethite sample available for the experiments. The stirring rate was set again to a high constant value (750rpm) to ensure reaction rates are determined by reaction control rather than by processes in the boundary layer at either the solid/liquid or gas/liquid interface.

Agreement between predicted and empirical values is also discussed in the sections below.

Table 8-3. Operating conditions and measured initial pH of experiments with goethite.

| *Experiment* | *Particle size (μm)* | *Time (h)* | *$CO_2$:$SO_2$ comp. (vol. %)* | *Pressure (bar)* | *Temperature (°C)* | *Brine composition* | *$pH_{initial}$* |
|---|---|---|---|---|---|---|---|
| 1 | -38 | 24 | 99.6:0.4 | 250 | 100 | 1.0 m NaCl + 0.5 m NaOH | 12.71 |
| 2 | 38x150 | 24 | 99.6:0.4 | 250 | 100 | 1.0 m NaCl + 0.5 m NaOH | 12.66 |
| 3 | 150x300 | 24 | 99.6:0.4 | 250 | 100 | 1.0 m NaCl + 0.5 m NaOH | 12.71 |
| 4 | 150x300 | 64 | 99.6:0.4 | 250 | 100 | 1.0 m NaCl + 0.5 m NaOH | 13.29 |
| 5 | 150x300 | 165 | 99.6:0.4 | 250 | 100 | 1.0 m NaCl + 0.5 m NaOH | 12.76 |
| 6 | 150x300 | 264 | 99.6:0.4 | 250 | 100 | 1.0 m NaCl + 0.5 m NaOH | 13.22 |
| 7 | -38 | 24 | 99.1:0.9 | 250 | 100 | 1.0 m NaCl + 0.5 m NaOH | 12.64 |
| 8 | -38 | 24 | 98.8:1.2 | 250 | 100 | 1.0 m NaCl + 0.5 m NaOH | 12.59 |

Solids concentration = 10g/L and stirring speed = 750 rpm for all experiments.

### 8.2.1. Effect of particle size

#### *8.2.1.1. Analysis of fluid chemistry and solids weight uptake*

Results of the solution analysis for the three experiments conducted with different particle size (experiment numbers 1-3 in Table 8-3) indicate the same general trends as the ones observed in experiments with hematite previously discussed in Chapter 7. The concentration of dissolved iron barely changed (Figure 8-5) but it is slightly higher in the experiment conducted with the largest size fraction, i.e. 150x300 μm. In all the experiments iron concentration was much higher, approximately three orders of magnitude, than predicted one in the simulations (0.02 ppm).

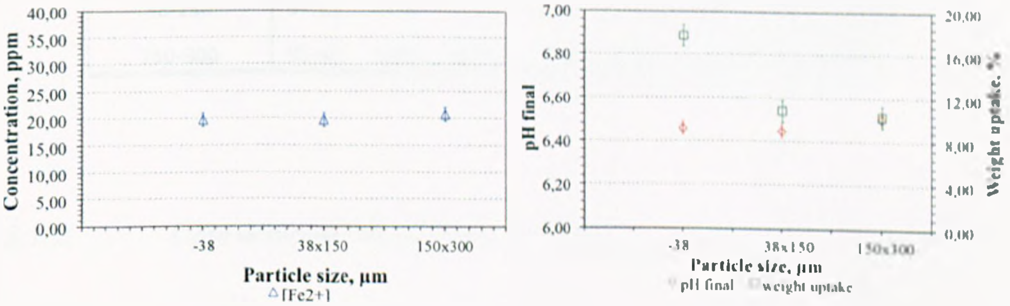

Figure 8-5. Effect of particle size on iron in solution (left) and measured final pH and solids weight uptake (%) (right) in goethite particles.

Brine pH values also remain approximately constant and higher than the equilibrium one (5.6). The percentage of weight uptake by the solids is remarkably higher (~18%) in the smallest fraction (-38 μm) and centers around ~10% for the intermediate (38x150 μm) and top fractions (150x300 μm). Based on the latter statement, the reactivity of finer powders is again higher (as it was proofed for hematite) because of the higher external surface area of the particles compare to coarser ones to react with aqueous $CO_2$ and $SO_2$. Equilibrium results reported a value of 24% weight uptake, which is only slightly higher than the measured one for the finest powders.

ICP-AES analysis (Table 8-4) of segregated goethite fractions revealed the different observed reactivity was not due to a higher concentration of cations prone to be carbonated, i.e. iron, in the smallest fraction than in the other two ones.

Table 8-4. Major-element oxide concentrations (in wt.%) of goethite fractions as determined by ICP-AES.

| Particle size, µm | $Fe_3O_4$ | $Al_2O_3$ | MgO | MnO | $SO_3$ | $Na_2O$ | $K_2O$ | $SiO_2$ |
|---|---|---|---|---|---|---|---|---|
| **-38** | 90.68 | 0.20 | 0.22 | 0.07 | 0.31 | 0.05 | 0.01 | 1.94 |
| **38-150** | 97.71 | 0.10 | 0.03 | 0.06 | 0.29 | 0.05 | 0.01 | 2.10 |
| **150-300** | 95.40 | 0.03 | 0.03 | 0.06 | 0.19 | 0.05 | 0.01 | 3.81 |

### *8.2.1.2. Characterisation of solid products*

Geochemical modeling results predicted mainly siderite (4.1g) and some remaining goethite (0.9g) as the only solid phases at equilibrium under the same conditions of the experiments. Reacted solids were then studied by thermal analyses and compared with the parent material. TGA profiles for intermediate and top fractions show a lower weight loss than parent material in the temperature range where dehydroxilation of goethite occurs (Figure 8-6), between 250 and 400°C. This is indicative of goethite dissolution as a result of the reaction. This process happened to be slightly favored in the top fraction versus the intermediate one according to their weight loss of ~ 5.5 and 7% respectively. These results are not in agreement with values reported for percentage of weight uptake by the solids; the latter ones were ~ 10% for both fractions, indicating that solid phases that decompose above 900°C have to be responsible for that weight change.

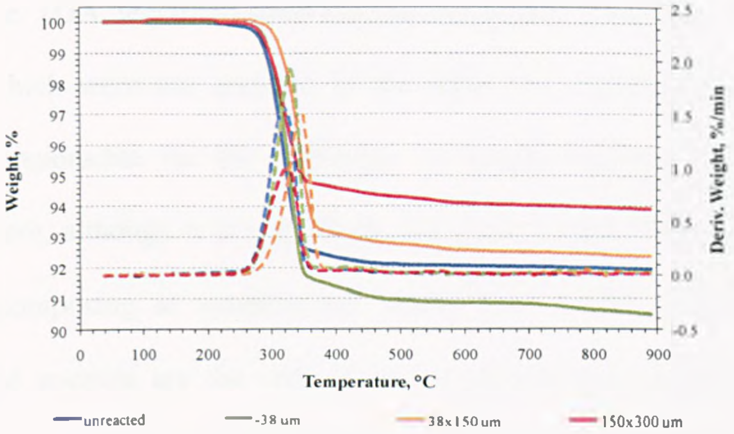

Figure 8-6. TGA curves of parent and reacted samples of goethite with different particle size. Dashed lines correspond to derivative weight curves.

The TGA profile for the finest fraction shows a small percentage of weight loss (~0.8%) around 400°C, which is the decomposition temperature of siderite (see section 7.1.1.2 in Chapter 7), so some iron carbonate precipitation could have happened in the experiment. A further weight loss is observed at ~ 800°C and it looks like it has not finished yet at 900°C. Sodium carbonate starts decomposing at ~ 800°C (see section 7.1.2.2.1 in Chapter 7) so this phase could be also present in the reacted material.

### *8.2.1.3. Summary*

General trends observed for the effect of particle size in the carbonation reaction of goethite are very similar to the ones observed for hematite. Dissolved iron remained ~ constant in the three experiments as well as brine pH; however, weight uptake was again much higher (~18%) in the finest fraction than in the intermediate and top ones (~10%). Bulk solid sample analyses, i.e. TGA, identified some siderite and sodium carbonate in the -38μm fraction, which were not detected in the other two fractions. These phases could be responsible for the difference in weight uptake (~8%) observed between them, although it is very likely that some residual brine and/or other phases decomposing at temperatures higher than 900°C are also present. Siderite and goethite are the only phases at equilibrium based on modeling results so, as expected, the extent of the reactions did not approach, in any of the experiments, the equilibrium conditions.

The top fraction (150x300 μm) was selected for the set of experiments evaluating the reaction time because it is more representative of a real-case scenario. However, the finest fraction (-38 μm) was used to assess the effect of gas concentration in the experiments in an aim to increase reaction kinetics and precipitation of siderite in a 24 h experiment. Problems encountered with the recovery process of the finest powders in experiments conducted with hematite were not encountered in experiments with goethite. Thereby, all the solids could be recovered from the reactor vessel and no material was left behind.

### 8.2.2. Effect of reaction time

Autoclave experiments numbered 4-6 in Table 8-3 were conducted to study the effect of reaction time on the goethite carbonation reaction. Reaction time ranged from 24 to 264 h as in the experiments with hematite so further comparison between the samples can be established. Experimental results are discussed below and compared with the equilibrium predicted case.

#### 8.2.2.1. *Analysis of fluid chemistry and solids weight uptake*

Iron concentration in solution did not change significantly as reaction time increased in the experiment (Figure 8-7), with a value ranging between 20 and 25 ppm, which differs from the predicted one of 0.02 ppm.

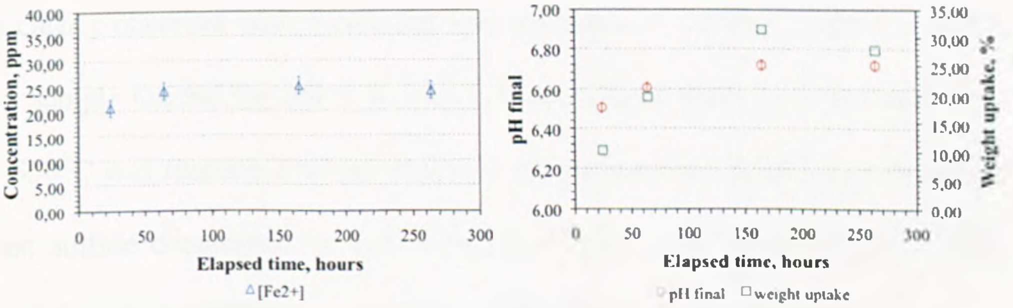

Figure 8-7. Dissolved iron (left) and measured final pH and solids weight uptake (%) (right) for goethite samples as a function of reaction time. Error bars size for weight uptake series is smaller than symbol size.

The weight uptake increased for increasing reaction times and reached a maximum of 31% after 165 h, which exceeds the equilibrium value (24%), followed by a slight decrease to 28% after 264 h (still higher than predicted value). This indicates dissolution of one and/or more compounds within that time interval. Brine pH did increase at longer reaction time intervals so goethite dissolution, which consumes $H^+$, might be occurring as time goes on and might be buffering the pH.

### *8.2.2.2. Characterisation of solid products*

#### *8.2.2.2.a. Thermogravimetric analysis*

Thermal analyses of reacted goethite samples were performed and compared with results for the unreacted material. TGA profiles are quite different depending on the duration of the experiment (Figure 8-8). The TGA profile for the 24 h experiment shows no difference with the one for the unreacted material except for a lower weight loss around 300°C, which indicates some of the starting goethite dissolved as a result of the experiment. A new weight loss is clearly observed with increasing reaction times at ~ 550°C, which is of 8% for sample reacted for 264 h. It seems obvious that a phase that decomposes at ~ 550°C was forming over the course of the experiment. Both iron sulfate and iron sulfide decompose in that temperature range (Siriwardane et al., 1999, Yani and Zhang, 2009), so any of them could have been precipitated.

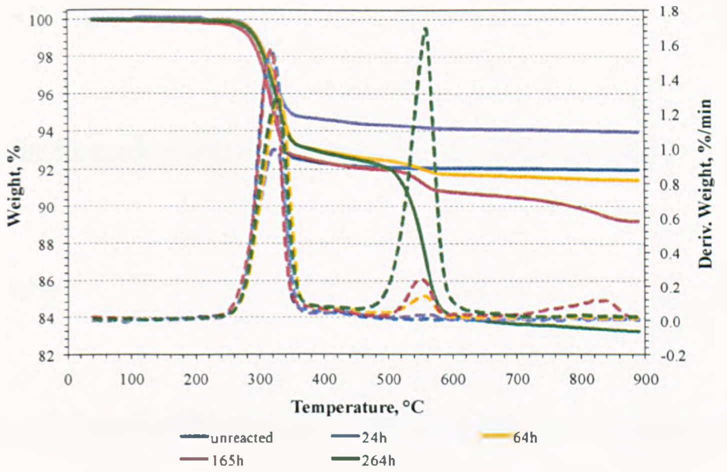

Figure 8-8. TGA curves of unreacted and reacted goethite samples collected at different reaction times. Dashed lines correspond to derivative weight curves.

A weight loss of ~1.5% was also observed at ca. 800°C for the sample collected after 165 h. This decomposition temperature agrees well with the one reported for sodium carbonate, based on TGA analysis of a standard sample (see section 7.1.2.2.1 in Chapter 7). This weight loss is not present in the sample reacted for 264 h so the observed decrease in weight uptake after 165 h might be related to dissolution of sodium carbonate.

It is important to identify which compound has been formed at ~550°C because its presence is quite significant at longer reaction intervals. Experimental investigations on pyrite synthesis (Roberts et al., 1969) from reaction of an iron oxyhydroxide (FeOOH) and a $H_2S$ aqueous solution at low temperature (25°C) have shown that the formation of pyrite in aqueous solution involves the formation of a disulphide ion, the production of which requires elemental sulfur. The latter one is formed in acid or neutral solution by oxidation of $H_2S$ by $Fe^{3+}$, according to the following reaction:

$S^{2-} + 2Fe^{3+} \rightarrow S + 2Fe^{2+}$ [8-4]

Then, the sulfur formed reacts with excess $S^{2-}$ to yield disulfide:

$H_2S + S \rightarrow H_2S_2$ [8-5]

The stability of the disulfide in aqueous medium is not pronounced but it rapidly reacts with $Fe^{2+}$ to yield pyrite.

Pyrite synthesis has been also reported from the action of $H_2S$ on a solution of iron sulfate (Allen et al., 1912). In reactions in closed vessels where the $H_2S$ cannot escape or be oxidized, pyrite formation takes place according to reaction 8.6 below:

$FeSO_4 + S + H_2S \rightarrow FeS_2 + H_2SO_4$ [8-6]

The above reaction was found to be slow at room temperature. At 200°C they obtained pyrite and marcasite ($FeS_2$ but in a different crystal system than pyrite) by reaction between a ferric salt and sodium thiosulfate. The thiosulfate reaction would probably happen via the formation of $S_2^{2-}$ ion as follows:

$2S_2O_3^{2-} + 2H_2O \rightarrow 2SO_4^{2-} + S + H_2S + 2H^+$ [8-7]

$H_2S \rightarrow 2H^+ + S^{2-}$ [8-8]

$S^{2-} + S \rightarrow S_2^{2-}$ [8-9]

$Fe^{2+} + S_2^{2-} \rightarrow FeS_2$ [8-10]

Later studies by Schoonen and Barnes (Schoonen and Barnes, 1991a, Schoonen and Barnes, 1991b) concluded that pyrite and marcasite form via an FeS precursor from solutions below 250 to 300°C. This precursor is amorphous FeS below 100°C and a crystalline, nearly stoichiometric monosulfide phase, above 100°C. The precursor is then replaced by progressively more sulfur-rich phases up to pyrite and marcasite. The rate of conversion above 100°C is higher when the solution contains an excess of thiosulfate, polythionates and/or polysulfides. They also concluded that marcasite is the predominant reaction product below pH 5, while pyrite dominates in neutral and alkaline solutions. Allen and co-workers (Allen et al., 1912) also reported that pyrite is the principal product if the solution is neutral or slightly acid.

Based on the above studies and the facts that: I) iron sulfate is very soluble (25.6 g/100 g $H_2O$ at 1atm and 20°C) (Lide, 1999) and II) a black precipitate (pyrite colour is black) was observed upon opening the reactor vessel, pyrite precipitation seems to be the process taking place over the course of the experiment.

Dissolved thiosulfate is likely to be present in the reactions, based on detection of dissolved thiosulfate in the long-term experiment discussed in section 8.1.1; hence, thiosulfate ions probably enhanced pyrite precipitation and, under the slightly acid pH measured in the experiments (ranging between 6.5 and 6.7) pyrite is the favored product instead of marcasite.

### 8.2.2.2.b. XPS analysis

Reacted solids were also analysed by XPS to determine any compositional change on the sample surface as a result of increasing reaction times. Sample reacted for 64 h was not analysed because differences observed in the TGA curves between samples reacted for 24 and 64 h were almost negligible. The atomic relative percentage difference for sodium, carbon, carbonate, chloride, sulfur and iron, with regards to the unreacted sample is depicted in Figure 8-9.

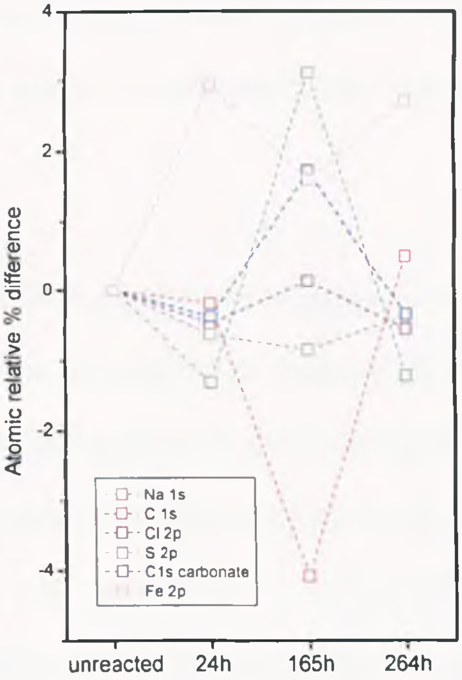

Figure 8-9. Atomic relative percentage difference for some elements on the surface of reaction products as a function of reaction time.

Same variation trends are shown for sodium, chloride and carbonate atoms, indicating those elements are linked somehow in the experiments: at 165 h, reaction time at which the weight uptake by the sample was observed to be the largest, sodium content increased significantly (~3%) compared to the rest of the atoms on the sample surface. Carbonate and chloride atoms also increased but not as much as sodium. Hence, sodium seems to be incorporated into structures containing carbonate and chloride atoms: sodium carbonate has probably precipitated after 165 h, which is in good agreement with results from TGA analysis, and residual brine could be also present due to the rinsing process of the sample.

Sulfur and iron content follow the same trend after 24 h, which would agree well with the observation from the TGA studies that pyrite precipitation occurs after that reaction time. However, because S atomic relative % differences are very small, pyrite is likely to be present in the bulk sample instead of the sample surface.

The trend of total carbon atoms relative percentage is opposite to the carbonate atoms after 24 h reaction, so the different contributions to the C1s XPS spectra are responsible for the different trends. XPS spectra for C1s and S2p regions are shown in Figure 8-10. The carbonate peak, only present in sample reacted for 165 h, appears at a BE of 289.4 eV. This value of BE is the same one as reported for a standard sodium carbonate sample, so the presence of sodium carbonate is then confirmed. The carbon peak at a BE of 292.3 eV is assumed to correspond to a carbon fluoride functionality, either $-CF_2$ or $-CF_3$ groups (Nakahara et al., 1994, Root, 2002), which is originally present as an impurity in the sample. This impurity is not present in reacted goethite samples as indicated by the absence of that peak in their C1s spectra.

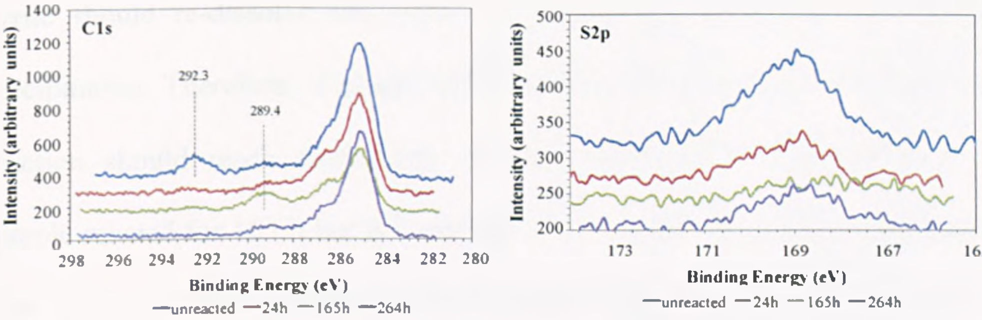

Figure 8-10. XPS C1s and S2p spectra of unreacted and reacted goethite samples collected at different reaction times.

The S2p spectra barely changed in reacted samples, verifying again that an iron-sulfur compound is not present on the surface of the solid.

### 8.2.2.3. *Summary*

Experimental tests with 0.4 % of $SO_2$ content evaluated the influence of reaction time on the carbonation reaction of goethite. Siderite precipitation was not observed after 264 h in the reaction products and pyrite precipitated instead as indicated by the thermal analysis studies. The more time elapsed, the more pyrite precipitated and percentage of weight uptake by the solids at 165 and 264 h (31 and 28% respectively) even exceeded the predicted one (24%). These results suggest that $SO_2$-derived dissolved bisulfide competed more effectively than dissolved $CO_2$ for the dissolved $Fe^{2+}$, resulting in precipitation of pyrite rather than siderite. It is important noting that surface techniques, i.e. XPS, did not reveal any pyrite precipitation on the goethite surface so bulk and surface compositional changes are different in this case. Precipitation of pyrite was also reported in previous studies with hematite (Palandri et al., 2005). Therein, nucleation of metastable pyrite occurred after ~ 17 h. Precipitated pyrite should re-dissolve and allow for further iron reduction and siderite precipitation. Therefore, if given sufficient time, the carbonate will form and reaction should reach equilibrium. Sodium carbonate is also observed in sample reacted for 165 h but it is not present later on in the 264 h experiment. Due to its soluble character, it is unlikely that sodium carbonate had precipitated during the experiment so it probably did either when quenching the reactor, or when rinsing the solids.

Dissolved iron concentration was higher than equilibrium one by three orders of magnitude, indicating goethite dissolution did occur but iron remained in solution instead of being trapped in a solid phase, i.e. siderite. Time constraints probably limit the nucleation and precipitation of iron carbonate.

Brine pH values were higher than predicted ones, which have been observed repeatedly in the different sets of experiments as a result of $CO_2$ evolving from the system upon the reactor depressurization process.

Comparison of these results with those reported from the long-term experiment conducted in a flexible-gold reaction cell (section 8.1) indicate that reaction variables play an important role for the carbonation reaction to take place. In the long-term experiment, siderite was verified after 24 days but reaction conditions were significantly different, i.e. higher temperature (150°C), higher pressure (300 bar) and higher $SO_2$ content (~12.9%) than in short-term experiments. Pyrite was not detected in the long-term experiment and dissolved $CO_2$ effectively formed siderite instead of being left in solution, as in the short-term experiments. A proof of this is the high dissolved iron concentration measured in the former ones (~20-25 ppm) versus the small concentration (< 2 ppm) measured in the long-term experiment. Even with a much lower solids concentration (10 g/L) in the short-term experiments than in the long-term one (67 g/L), and therefore an expected higher extent of the carbonation reaction, pyrite was favored over the iron carbonate. The short-term experiments are more representative of a real-case scenario, i.e., a fossil fuels combustion-derived flue gas stream, than the long-term one and reflect the behavior of the system near the injection well. Near the well, where a strong acidified zone is generated, pyrite will precipitate but further down the well, siderite precipitation would occur (as indicated by the long-term experiment). If the brine in the reservoir is high in Ca concentration, then formation of anhydrite ($CaSO_4$) is also likely to occur close to the well.

In a real-case scenario, there will be a porosity and permeability loss around the wellbore due to precipitation of pyrite as well as further down the well due to precipitation of siderite. Implications of precipitation of those secondary minerals for the geological storage of $CO_2$ are explained in detail in section 8.3.

### 8.2.3. Effect of gas composition

Experiments numbered 1, 7 and 8 in Table 8-3 evaluated the effect of varying the relative amount of $CO_2$ and $SO_2$ in the gas added to the system. Tested gas concentrations were the same as the ones used in experiments with hematite reported in section 7.1.3. of Chapter 7.

### *8.2.3.1. Analysis of fluid chemistry and solids weight uptake*

The predicted effect of increasing amounts of $SO_2$ in the gas added to the system in dissolved iron concentration and brine pH is the same as the one reported for experiments with hematite (section 7.1.3.1 of Chapter 7). Increasing $SO_2$ concentrations drive disproportionation reaction of $SO_2$ to the right yielding increasing amounts of sulfide and sulfate, so the brine gets more acidic. i.e. has a lower pH, and solid phases dissolution is enhanced. Thereby, a higher concentration of iron in solution is observed for higher $SO_2$ concentrations than for lower ones (Figure 8-11). Experimental trends agree well with predicted ones for dissolved iron and pH but measured values are still far from equilibrium (Figure 8-11 and Figure 8-12).

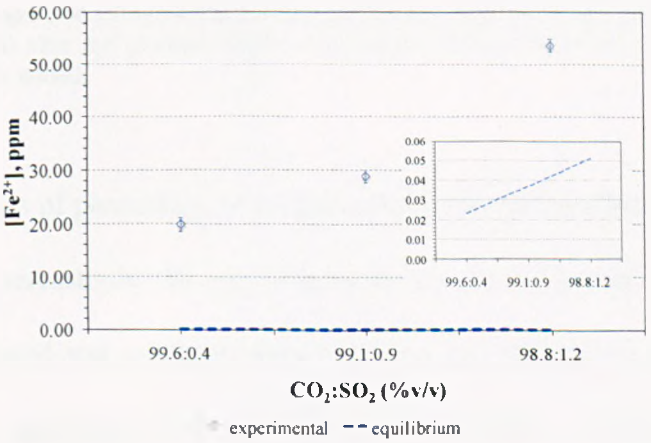

Figure 8-11. Comparison of experimental and predicted results for dissolved iron as a function of varying relative amounts of $CO_2$ and $SO_2$ in the gas added.

The predicted percentage of weight uptake by the solids does increase from 24 to 31% when the $SO_2$ content in the gas increases from 0.4 to 0.9%, but remains constant around 31% when the $SO_2$ concentration goes up to 1.2% (Figure 8-12). This plateau in the weight uptake curve is explained as follows. For a $CO_2$:$SO_2$ concentration of 99.1:0.9 (vol. %), 5 g of siderite and only 0.2 g of pyrite precipitated in the system, while for a $SO_2$ content of 1.2%, 4.8 and 0.4 g for siderite and pyrite respectively are present in the mineral assemblage. Hence, the amount of dissolved siderite was replaced by the amount of precipitated pyrite and the total mass weight of the solids in the system was the same, so the percentage of weight uptake will be the same as well.

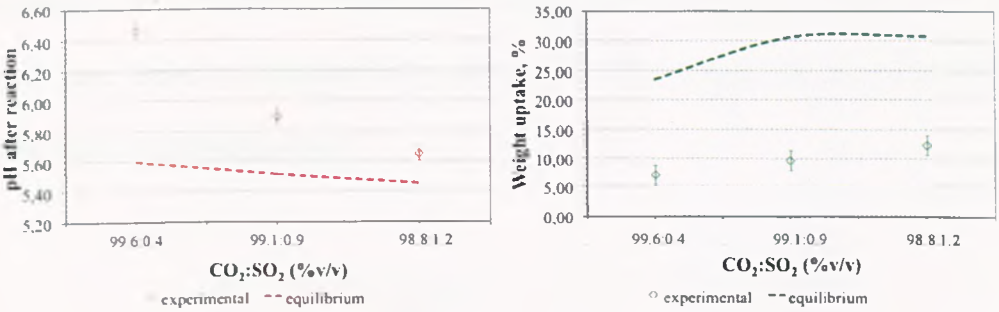

Figure 8-12. Comparison of experimental and predicted trends for brine pH (left) and solids weight uptake (%) after the reaction (right) as a function of varying relative amounts of $CO_2$ and $SO_2$ in the gas added.

Measured values of percentage of weight uptake remain constant (~18%) as the $SO_2$ content increases in the gas (Figure 8-12). As indicated by comparison between measured and predicted dissolved iron and pH values, the system did not reach the steady-state so the weight uptake trend is different from the predicted one.

#### 8.2.3.2. *Characterisation of reaction products*

##### 8.2.3.2.a. *Thermogravimetric analysis*

Thermal analysis showed some minor changes in the TGA curves of reacted goethite samples when compared between them and with the TGA curve for the unreacted material (Figure 8-13). Bulk composition of the sample did not seem to be modified to a significant extent after the experiments. A weight loss of ~0.8% is observed at ca. 400°C for the sample reacted with a $SO_2$ content of 0.4%. That temperature is the one observed for siderite decomposition so some iron carbonate might have precipitated in that sample. A minor weight loss is observed for the three reacted samples at the temperature where sodium carbonate starts to decompose (~ 800°C) so this compound could be also present in collected samples.

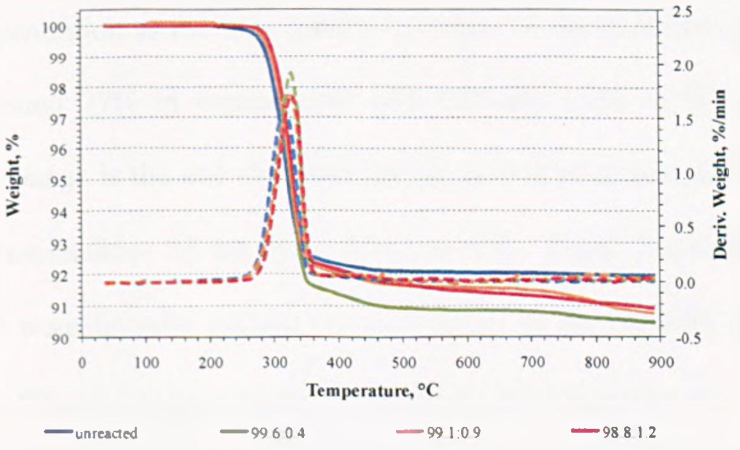

Figure 8-13. TGA curves of unreacted and reacted goethite samples with varying relative amounts of $CO_2$ and $SO_2$ in the gas added. Dashed lines correspond to derivative weight curves.

These results agree well with results from the weight uptake curve, since no major changes have occurred in the solid sample when the $SO_2$ content in the gas increased.

### *8.2.3.2.b. XPS analysis*

First, a detailed analysis of the C signal was conducted based on its high resolution scan and deconvolution of its profile was performed to study the contribution of the different peaks to the total curve (Figure 8-14). The solid black line represents experimental data and the total calculated fitting is shown in grey with circular markers. The deconvolution performed in the C1s spectra of sample reacted with 1.2% of $SO_2$ is shown as an example and the atomic concentration (%) of the different components for samples reacted with lower contents than 1.2% of $SO_2$ is also shown in Figure 8-14. In this case, the component with a BE that relates to carbonate carbon atoms increases its atomic concentration as the $SO_2$ content increases in the experiment, and gets constant around 27% in experiments with 0.9 and 1.2% of $SO_2$.The most significant change is the one observed for the carbon peak assigned to carbon fluoride functionalities of the type $-CF_2$ or $-CF_3$. These fluorinated-carbon compounds were initially present in the sample as an impurity and higher contents of $SO_2$ in the gas seemed to increase their presence on the sample surface. The BE of the carbonate peak appears at ~ 289.4 eV for all reacted samples, which corresponds to the BE of the carbon peak in sodium carbonate according to the bibliography (Moulder et al., 1995) and XPS analysis of a standard sample (see section 7.1.2.2.3 in Chapter 7). Thereby, sodium carbonate is present on the surface of the reacted samples, which is in agreement with observed changes in their TGA curves.

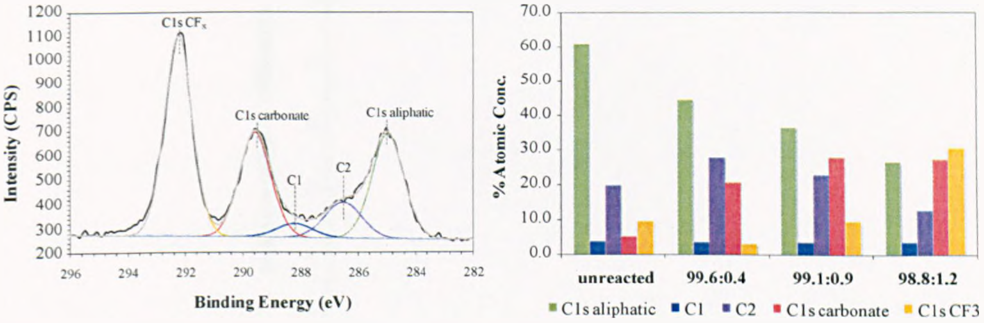

Figure 8-14. High resolution XPS in the C1s region for goethite sample reacted with a 1.2% $SO_2$ content (left) and atomic concentration (%) of components used to curve fit the spectra as a function of varying amounts of $CO_2$ and $SO_2$ in the gas added.

High resolution scans for the rest of the elements were also conducted and the atomic relative percentage difference with respect to the unreacted sample for those elements relevant for the discussion is depicted in Figure 8-15. Sodium and chloride variations follow the same trend so residual brine is likely to be deposited on the sample surface. The carbonate peak trend follows the one for the total carbon signal and although is similar to the sodium tendency, they do not match so well in the last two points. The sodium content barely changed from experiment with 0.9% of $SO_2$ to experiment with 1.2% of $SO_2$. However, a ~3% atomic increase was obtained for carbonate atoms. A small amount of other carbonate atoms could be then present in that sample, most likely those bound to iron in siderite because it is the main cation present in the experiment that is prone to be carbonated.

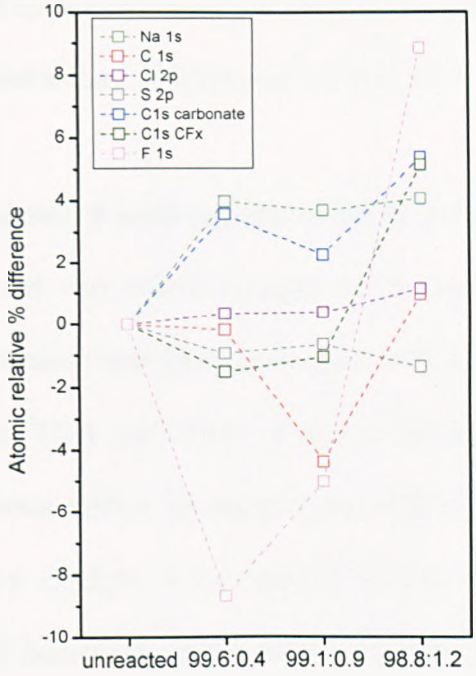

Figure 8-15. Atomic relative percentage difference for some elements on the surface of reaction products as a function of varying amounts of $CO_2$ and $SO_2$ in the gas added.

Observed variations in carbon atoms assigned to carbon-fluoride functionalities (C1s $CF_x$ line in Figure 8-15) are in close agreement with variations for fluoride atoms so this fact confirms the carbon-fluoride character of the bonds. The sulfur content did not change with increasing amounts of $SO_2$, so in this case, sulfur-containing compounds did not precipitate as a result of the reaction.

### *8.2.3.3. Summary*

Although changes in dissolved iron and brine pH as a function of varying amounts of $CO_2$ and $SO_2$ in the gas added are in good agreement with predicted ones by geochemical modeling, empirical values are still distant from the predicted ones at equilibrium because experiments were run for just 24h. The percentage of weight uptake by the solids remained constant at ~17% versus a 30% observed for experiments with 0.9 and 1.2% of $SO_2$.

Bulk and surface analyses of solid samples revealed compositional changes on the sample surface and very minor changes in the bulk composition of the samples. Sodium carbonate was identified as one of the reaction products by both techniques, i.e. TGA and XPS. It has probably precipitated in the quenching of the reactor and/or rinsing process of the solids because its high solubility makes very unlikely it was present during the experiment. Some siderite could be also present in sample with a 1.2% of $SO_2$ content according to surface compositional changes, but its presence is not clearly observed in the TGA curve; conversely, the TGA curve indicates some iron carbonate precipitation in the experiment with a gas concentration characteristic of a flue gas stream (99.6:0.4%), which is not present on the sample surface.

A significant finding was the higher amount of carbon-fluoride functionality-containing compounds on the solid samples surface at increasing amounts of $SO_2$ in the gas stream. Those compounds are impurities in the parent material and due to its natural character, could proceed from organic compounds present in the sample in very small quantities but still detectable by XPS.

A stronger and larger acidified zone will be generated in the vicinity of the injection well as a result of increasing amounts of $SO_2$ in the gas stream; consequently, reservoir porosity and permeability will be affected because of dissolution and precipitation of mineral phases and, ultimately, injectivity in the well could be reduced.

## 8.3. Implications for geological storage of $CO_2$

The experiments showed that the dissolution of goethite and the deposition of secondary minerals were encouraged by the addition of $CO_2$-$SO_2$ gas mixtures. The results confirmed that the alteration of goethite under $CO_2$-saturated-$SO_2$ gas streams and hydrothermal conditions has the potential to trap $CO_2$ in a mineral phase (siderite) (reaction 8-11). However, other secondary minerals, mainly pyrite, were also precipitated as a result of the reaction.

Precipitated minerals will reduce the porosity and permeability of the reservoir; the more extent of the carbonation reaction, the more porosity (and permeability) loss. Complete alteration of goethite to siderite would lead to a 41% increase of the mineral volume, based on the molar volumes of goethite (20.82 $cm^3/mol$) and siderite (29.38 $cm^3/mol$). If pyrite precipitates in the system (reaction [8-13]) instead of siderite, then the increase of mineral volume would be of 15%, almost three times less than the one for complete alteration to siderite. Should FeS (amorphous) precipitate (reaction [8-14]), then a 18% porosity increase would occur.

$$2FeOOH\ (goethite) + 2CO_2 + SO_2 \leftrightarrow 2FeCO_3 + H_2SO_4 \qquad [8\text{-}11]$$

$$8Fe^{3+} + HS^- + 4H_2O \leftrightarrow 8Fe^{2+} + SO_4^{2-} + 9H^+ \qquad [8\text{-}12]$$

$$4Fe^{2+} + SO_4^{2-} + 7HS^- + H^+ \leftrightarrow 4FeS_2 + 4H_2O \qquad [8\text{-}13]$$

$Fe^{2+} + HS^{-} \leftrightarrow FeS\ (amorphous) + H^{+}$ [8-14]

In the same example given for hematite, if the host reservoir had an average porosity of 20%, siderite precipitation would reduce the porosity of the reservoir in 5% while pyrite precipitation would only reduce it 2% and FeS (amorphous) 2.6%. However, in the former case FeS amorphous is always metastable with respect to pyrite and should re-dissolve in the aquifer to yield pyrite with the consequent increase in porosity (0.6%). Should pyrite re-dissolve as well, more S will become available for further reduction of $Fe^{3+}$ from goethite and further precipitation of siderite. The rapid formation of pyrite in natural sediments in anaerobic conditions can be explained by the combination of $Fe^{3+}$ and the $S_2^{2-}$ ion (Roberts et al., 1969). Hence, empirical observations do agree with field observations with regards to pyrite precipitation.

As for the hematite case, S-bearing minerals are likely to be precipitated in the vicinity of the injection well, where the zone is more acid than in the region further down the well. Associated problems of porosity (and permeability) loss will be also encountered, which could affect the injectivity in the well. Siderite will be stable in regions at longer distances from the wellbore, where the pH is more basic and carbonates precipitation is enhanced.

As for hematite particles, fine powders (< 38 μm) have a higher reactivity than coarser particles, which will lead to faster precipitation of secondary minerals. Porosity (and permeability) of the hosting reservoir will then be diminished and could potentially affect the injectivity at the injection site. On the positive side, the seal capacity of the caprock could be enhanced because secondary minerals could fill porosity and improve safety of the containment. On the other hand, slow reactivities may not adversely affect the injectivity in the well but problems derived from potential leakage of $CO_2$ into overlying formations could be encountered.

## 8.4. Comparison of hematite and goethite as potential reservoirs for $CO_2$ mineral trapping

A potential storage site for $CO_2$ sequestration needs to have three characteristics: i) a capacity high enough to allow storage of large volumes of $CO_2$, ii) a high injectivity to allow injection at desired rates and iii) a caprock seal to ensure $CO_2$ containment in the reservoir. The formation capacity depends on its porosity whereas a high injectivity depends on the permeability of the reservoir. Reactions among $SO_2$-bearing $CO_2$-dominated gas, brine and iron (hydr)oxides will lead to dissolution/precipitation processes that will affect the site characteristics mentioned above.

The possibility of siderite to precipitate in iron (hydr)oxide-containing systems is dependent on cation availability in formation water. A sufficient supply of cations needs to be available to precipitate with the bicarbonate in solution. Previous studies (Watson et al., 2004) have characterised late authigenic carbonate cements derived from magmatic incursions in sedimentary reservoirs, in an aim to identify which carbonates would occur as a result of geological sequestration of $CO_2$. In sedimentary basins with pH levels of about 5.5 within $CO_2$-rich accumulations, ferroan carbonates are the more stable carbonate mineralogy. Naturally-occurring siderite can be found as small concretions and disseminated precipitates in sedimentary basins; it can also be present as a cement (with a micritic or sparry texture), filling porosity and partially sealing fractures as well as reducing the overall permeability of the reservoir rock by closing pore throats. Also, it can occur as bands, nodules and individual crystals. Siderite is a typical carbonate in natural systems with very high $CO_2$ concentration fields. Ankerite ($Ca(Fe,Mg,Mn)(CO_3)_2$) and dolomite ($CaMg(CO_3)_2$) can also be found in moderately high $CO_2$ fields, following siderite precipitation (Watson et al., 2004). Thereby, siderite is a very promising option to trap $CO_2$ underground in a safe and stable form.

Hematite and goethite (as proxies for $Fe^{III}$ in sediments) reactivity in $CO_2$-$SO_2$-brine systems has been studied to elucidate which sample would be a better host repository for underground $CO_2$ storage and comparisons between both samples are established: long-term and short-term experiments are compared and some remarks and implications for geological storage of $CO_2$ are also highlighted.

Firstly, when comparing the long-term experiments for both samples (experiment described in section 8.1 and previous studies reported by Palandri and co-workers (Palandri et al., 2005)), siderite precipitation was observed at shorter reaction times (~576 h) in the experiment with goethite than in the one with hematite (~611 h). In the former one, two other metastable phases precipitated early (~17 h) in the experiment, pyrite and S, which did not precipitate in the experiment with goethite. Sodium carbonate and iron sulfate were identified on the surface of the reacted goethite sample but their presence was probably due to the quenching process rather than to the experiment. Quantitatively, 76 mg of $CO_2$ were sequestered in siderite per g of goethite versus 1.4 mg of $CO_2$ sequestered in siderite per g of hematite (as the best estimation). Then, in a long-term experiment with high $SO_2$ contents (11-13%), goethite reactivity was much higher than hematite one: not only siderite precipitated faster but also the amount of $CO_2$ trapped in mineral form was much higher in goethite than in hematite. Thereby, formations containing α-FeOOH (goethite) minerals, which for instance might occur as thin grain coatings with large surface area in red beds, will be a much better host repository for underground $CO_2$ sequestration than those containing $\alpha$-$Fe_2O_3$ (hematite).

Secondly, the whole set of short-term (ranging between 24 and 264 h) experiments conducted with both samples and a gas stream representative of a real-case scenario (section 7.1 in Chapter 7 for hematite and section 8.2 in this chapter for goethite) provides very valuable and novel information on mineralogy of the system under different reaction conditions. Alteration of goethite yielded pyrite as the main reaction product; in the reactions with the hematite sample, the kaolinite content of the sample seemed to be more altered than the iron oxide itself. Dawsonite precipitated with increasing reaction times in experiments with hematite and siderite could be only confirmed in the sample reacted for 264h. The main conclusion from the short-term experiments as far as reactivity is concerned, is that goethite was much more reactive than hematite, where its kaolinite content was responsible for most of the observed mineral alterations. Pyrite precipitated in experiments with goethite will eventually re-dissolve and released S that will reduce more $Fe^{3+}$ to $Fe^{2+}$, which will further precipitate as iron carbonate. Hence, siderite is the ultimate stable phase in hematite and goethite-containing systems, as it was proofed in the long-term experiments.

The highest reactivity of goethite is in good agreement with previous studies (dos Santos Afonso and Stumm, 1992) that concluded that goethite dissolution was faster than the hematite one. Goethite can be considered as an extended cross-linked polymer, which bears surface functional groups (-OH). The dissolution of iron oxides can be rationalised as the breaking of surface crystalline bonds, so the higher reactivity of goethite is related to the nature of its hydrogen bonds, which are easier to break than the metal-oxygen-metal bonds that characterise the hematite structure. The reductive dissolution of iron (III) oxides has been extensively reviewed (Zinder et al., 1986, Suter et al., 1991, dos Santos Afonso and Stumm, 1992) and reported to be a surface controlled reaction, where the dissolution rate is proportional to the surface complex of the reductant bound to the surface of the oxidant (dos Santos Afonso and Stumm, 1992).

It is also important to bear in mind that depending on the depth at which injection will take place, the presence of one mineral might prevail over the other. Hematite and goethite stability depends on conditions of temperature and pressure. In hydrothermal solutions neutral to weakly alkaline the decomposition temperature of goethite to hematite can be taken to be 150±20°C (Smith and Kidd, 1949). This means that in injections at higher depths than 6 km, provided that the geothermal gradient is the average 25°C/km, goethite will not be found in the host reservoir rock. However, such deep injections are highly unlikely in a full-scale operation due to the high drilling and operational costs involved. As for the pressure, the decomposition temperature of goethite is virtually insensitive to pressures, raising less than 5°C per 1000 atm, up to 2000 atm (Smith and Kidd, 1949).

Assuming a 100% pure hematite and goethite-containing reservoirs, their complete alteration to thermodynamically stable siderite will increase the mineral volume 95 and 41% respectively. The porosity loss because of that increase would be almost double in the hematite case (9%) than in the goethite one (5%). This porosity reduction would greatly affect the dynamics of the hydrothermal system, and if the porosity loss occurs in the pore throats, the system permeability will be reduced as well. In this regards, goethite would also be a much better host reservoir than hematite, since the porosity loss is almost half the value obtained in a hematite-containing reservoir. However, siderite precipitation, if pervasive enough, can occlude the remaining porosity of the caprock and enhance its seal capacity.

One downside of the operation with goethite would be the precipitation of S-bearing phases close to the injection well, which has not been observed to the same extent in reactions with hematite. However, the porosity loss (2%) might not pose a significant problem.

In some natural occurrences, siderite precipitation was observed after the reservoir rock had undergone extensive dissolution and $CO_2$-water-reaction (Watson et al., 2004). That is not the case in most of the experiments reported here due to time constraints. It is remarkable how natural siderite precipitates occur on grain boundaries, inhibiting the precipitation of other authigenic minerals, like kaolinite and quartz, derived from the same $CO_2$-induced diagenetic event.

Dissolution of carbonate cements is likely to occur when injecting the acid-gas mixture. Re-precipitation of those earlier carbonates will not obviously mineralogically store any of the injected $CO_2$. If net precipitation of secondary minerals, carbonates, S-bearing minerals or any other minerals like halite, is less than minerals dissolution, overall porosity and permeability in the reservoir is enhanced. This is especially important in the vicinity of the injection well, because injectivity is modified depending on the permeability variation. Minerals dissolution/precipitation reactions are time-dependant processes so injectivity will be a function of time as well.

In conclusion, goethite-containing reservoirs are a good option to geochemically trap $CO_2$-$SO_2$ gas mixtures, and they are more promising than hematite-containing reservoirs. The benefits of targeting goethite deposits would be twofold: not only the mineral trapping process is faster with goethite but also the expected consequences on hydrologic properties of the aquifer are not as limiting as for hematite-involving processes.

## 8.5. References

Allen, E. T., Crenshaw, J. L. & Jonhston, J. (1912) The mineral sulphides of iron. *American Journal of Science,* 33, 169-236.

dos Santos Afonso, M. & Stumm, W. (1992) Reductive dissolution of Iron (III) (hydr)oxides by hydrogen sulfide. *Langmuir,* 8, 1671-1675.

Greenberg, J. & Tomson, M. (1992) Precipitation and dissolution kinetics and equilibria of aqueous ferrous carbonate vs temperature. *Applied Geochemistry,* 7, 185-190.

Lide, D. R. (Ed.) (1999) *CRC Handbook of Chemistry and Physics.*

Moulder, J. F., Stickle, W. F., Sobol, P. E. & Bomben, K. D. (1995) *Handbook of X-ray Photoelectron Spectroscopy: a reference book of standard spectra for identification and interpretation of XPS data,* Physical Electronics.

Nakahara, M., Ozawa, K. & Sanada, Y. (1994) Change in the chemical structures of carbon black and active carbon caused by $CF_4$ plasma irradiation. *Journal of Materials Science,* 29, 1646-1651.

Palandri, J. L., Rosenbauer, R. J. & Kharaka, Y. K. (2005) Ferric iron in sediments as a novel $CO_2$ mineral trap:$CO_2$-$SO_2$ reaction with hematite. *Applied Geochemistry,* 20, 2038-2048.

Roberts, W. M. B., Walker, A. L. & Buchanan, A. S. (1969) The chemistry of pyrite formation in aqueous solution and its relation to the depositional environment. *Mineral. Deposita,* 4, 18-29.

Root, M. J. (2002) Carbon monofluorides derived from sponge and shot cokes. *Journal of Solid State Electrochemistry,* 6, 361-366.

Schoonen, M. A. A. & Barnes, H. L. (1991a) Mechanisms of pyrite and marcasite formation from solution: III. Hydrothermal processes. *Geochimica et Cosmochimica Acta,* 55, 3491-3504.

Schoonen, M. A. A. & Barnes, H. L. (1991b) Reactions forming pyrite and marcasite from solution: I. Nucleation of $FeS_2$ below 100°C. *Geochimica et Cosmochimica Acta,* 55, 1495-1504.

Siriwardane, R. V., Poston Jr., J. A., Fisher, E. P., Shen, M. & Miltz, A. L. (1999) Decomposition of the sulfates of copper, iron (II), iron (III), nickel, and zinc: XPS, SEM, DRIFTS, XRD and TGA study. *Applied Surface Science,* 152, 219-236.

Smith, F. G. & Kidd, D. J. (1949) Hematite-goethite relations in neutral and alkaline solutions under pressure. *American Mineralogist,* 34, 403-412.

Sun, W., Nesic, S. & Woollam, R. C. (2009) The effect of temperature and ionic strength on iron carbonate ($FeCO_3$) solubility limit. *Corrosion Science,* 51, 1273-1276.

Suter, D., Banwart, S. & Stumm, W. (1991) Dissolution of hydrous iron (III) oxides by reductive mechanisms. *Langmuir,* 7, 809-813.

Watson, M. N., Boreham, C. J. & Tingate, P. R. (2004) Carbon dioxide and carbonate elements in the Otway Basin: implications for geological storage of carbon dioxide. *The APPEA Journal,* 44(1), 703-720.

Yani, S. & Zhang, D. An experimental study into pyrite transformation during pyrolysis of Australian lignite samples. *Fuel* (2009), doi:10.1016/j.fuel.2009.07.025

Zinder, B., Furrer, G. & Stumm, W. (1986) The coordination chemistry of weathering: II. Dissolution of Fe(III) oxides. *Geochimica et Cosmochimica Acta,* 50, 1861-1869.

## CHAPTER 9

# CONCLUSIONS AND FUTURE WORK

# 9. Conclusions and future work

## 9.1. Conclusions

Herein, modelling and experimental results from novel hydrothermal experiments have been presented. Experiments emulate a $CO_2$ sequestration scenario by injecting $CO_2$-$SO_2$ gas streams into a NaCl-NaOH brine hosted in a iron oxide-containing aquifer. Iron-bearing minerals are reactive phases of the subsurface environment but this novel and promising concept has barely been explored before. Hence, this Thesis provides novel information on the mineralogical changes and fluid chemistry derived from the co-injection of $CO_2$-$SO_2$ gas mixtures and their geochemical sequestration in the hydrothermal systems mentioned above.

Firstly, a unique and state-of-the-art high pressure-high temperature system was developed to conduct the experimental work. The high and challenging complexity of dealing with gas mixtures and high pressures was successfully resolved and further assessed in a laboratory scale. Even more challenging was the operation with $SO_2$, which was one of the components of the gas stream; its corrosive nature as well as its low vapour pressure at ambient temperature, was the cause of several modifications and further optimization of the system. The final optimised system has been proven to be a versatile piece of equipment, capable of operating within a wide range of temperature (ambient-345°C), pressure (ambient-350 bar), stirring speed (0-1500 rpm) and gas concentration conditions. Its applicability for short-term (24 h) as well as long-term (days, weeks or longer) experiments along with its flexibility have been successfully demonstrated. Furthermore, the system could be adapted and used for many other applications and mixtures of gases different from the one it was originally built for.

In this work, geochemical modelling with CHILLER has been used to predict mineral dissolution behaviour and carbonate precipitation under equilibrium conditions. A wide range of reaction conditions were simulated that were further reproduced in laboratory experiments. Geochemical models are powerful tools to predict the final, i.e. equilibrium, stage in a geochemical system but they could be at fault so they need to be validated and refined through comparisons with laboratory experiments. Both, modelling and empirical tests, were conducted to understand hydrothermal reactions that closely match what would occur in CCS operations.

Experimental tests provided information on $CO_2$ mineral trapping in siderite and sensitivity of the reactive systems to different parameters: particle size of the solids, reaction time, gas composition, temperature, pressure, solids-to-liquid ratio and brine composition for experiments carried out with hematite. Conditions under which the experiments were conducted indicate that brine composition and its buffering effect play an important role on mineral dissolution/precipitation reactions. In $CO_2$-saturated systems, the acidity of $H_2CO_3$ along with the one of dissolved $H_2S$ and $H_2SO_4$ derived from the $SO_2$ disproportionation reaction accelerated and promoted the release of alkali metals, i.e. Al, and reduced $Fe^{2+}$ from the hematite sample into the solution; simultaneously, the deposition of secondary minerals (siderite, dawsonite and probably gibbsite, boehmite and S-bearing minerals) was promoted. Injection of $CO_2$-$SO_2$ gas mixtures in brines with initial low-pH values (< 7) could lead to extremely acid (pH < 1) final environments, which would promote minerals dissolution and enhancement of reservoir's porosity and permeability. However, injection in brines with initial high-pH values (> 12) lead to a completely different environment, where secondary minerals can precipitate like iron carbonate, which precipitation is the main target of this research work. The $SO_2$ content in the gas stream, i.e. gas composition, is strongly linked to the pH of the system and consequently, to the derived brine chemistry and altered mineralogy. The amount of siderite precipitate depends primarily on the $SO_2$ content of the gas stream: for typical $SO_2$-bearing $CO_2$-dominated gas streams derived from combustion of fossil fuels ($SO_2$ content ranges between 0.15 and 2% by volume), the highest amount of $SO_2$ would be desirable in order to get a maximum siderite precipitate and maximum amount of $CO_2$ trapped in mineral form. The more $SO_2$ present in the system, the more $Fe^{2+}$ can be reduced from the hematite sample, which will be further available for its precipitation in siderite. Experimental 24 h tests with increasing $SO_2$ contents in the gas stream indicated a more acidic environment, along with potential precipitation of S-bearing phases (pyrite, Fe-S amorphous and S native) when compared to experiments with lower $SO_2$ contents. Such experiments would be more representative of the initial situation in the reservoir area close to the well upon acid gas injection.

Total iron in red beds averages 1.7 to 3.5% and 2.35% to 2.9% for all kinds of sandstones (most of the iron is present as $Fe_2O_3$ versus FeO). Free (extractable) iron in the ferric oxide pigment averages about 0.67%; hence, these sediments contain ferric iron in quantities that can scrub all the $SO_2$ contained in a typical $CO_2$-$SO_2$ gas mixture derived from a waste gas stream; however, most $CO_2$ will remain in a supercritical or dissolved phase instead of being trapped as siderite. Should the $CO_2$:$SO_2$ ratio be higher than the one in the flue gas derived from fossil fuel-fired power plants, especially when considering gas fired power production, targeted sediments must contain additional divalent metals such as Ca or Mg, or additional sulphur-bearing gas must be added to the waste gas stream to effectively trap $CO_2$ in carbonate form. However, the latter option will not probably be allowed under current European Union Directive on the geological storage of $CO_2$ (2009/31/EC), where no wastes or other matter can be added for the purpose of disposal to $CO_2$ gas streams derived from $CO_2$ capture processes. Hence, the ideal repository for effectively trap a $CO_2$-$SO_2$ gas stream derived from fossil fuel-fired power plants would be a sandstone formation, where other cations prone to be carbonated, such as Ca or Mg, are present as well as Fe so $CO_2$ is not left unlocked in a free phase.

Although increasing reaction times obviously favoured the supersaturation and precipitation of secondary minerals, the former ones were also favoured under conditions of decreasing values of particle size of the solids, decreasing values of solids-to-liquid ratio and increasing reaction temperatures up to 100°C. Reaction pressure has a major effect on availability of dissolved $SO_2$ and $CO_2$ for further reaction with hematite and those cations in solution prone to be carbonated. However, the pressure effect on the formation of carbonates is not as important as reaction temperature.

In experiments with goethite the effect of the following reaction variables on the overall carbonation reaction was investigated: solids particle size, reaction time and gas composition. The rest of variables are expected to have a similar effect to the one reported in experiments with hematite. Reactivity of goethite was observed to be very different from hematite reactivity under the same reaction conditions. A comprehensive discussion on this is shown in Chapter 8, where goethite is justified to be a better host repository for $CO_2$ trapping in mineral form than hematite.

Rock-brine-gas reactions are important not only for carbonate formation as a trapping mechanism but also as for how they will affect mineralogy at injection site and cements. The effect of studied reactions on the hydrologic properties of the system, i.e. porosity and permeability, is also discussed in Chapters 7 and 8 as well as the relevance of each variable for the geological sequestration of $CO_2$.

Siderite precipitation has been observed in hydrothermal natural systems at pH of ~ 5.5; this pH would match well with the one expected from the geochemical process described in this work in distant zones from the injection well, which have also been reproduced in most of the experiments due to the buffering effect of the brine. In natural environments, siderite is usually precipitated within sediments during early diagenesis, where reducing conditions have developed through bacterial decomposition of organic matter. The iron for these minerals is $Fe^{2+}$ in the pore waters, mostly liberated by bacterial reduction of iron oxides/hydroxides on clays and organic matter in the sediment. However, other reductants, such as $H_2S$ and $SO_2$, could also be considered for the reduction of ferric iron contained in iron oxides/hydroxides, which is within the scope of this research work. Siderite is more common in non-marine sediments, although it does occur in many marine ironstones, mostly as a later diagenetic cement. If there is insufficient $Fe^{2+}$ relative to $Ca^{2+}$ and $Mg^{2+}$ in the pore waters, then ankerite, $CaMg_{0.5}Fe_{0.5}(CO_3)_2$ or ferroan calcite or ferroan dolomite may form in preference to siderite.

Siderite was verified as a reaction product in experiments with hematite and goethite reacted for 264 h and 576 h respectively. Experimental results obtained under the conditions studied might be moving towards equilibrium, at best, but most likely are far yet from the equilibrium case because of the shortness of the time available for doing the experiments. It is also important to note the difficulties on identifying the nature of precipitates; in some instances, thermal and XPS analysis failured to characterise those precipitates.

The geochemical code used in this study was not able to predict the trends on the effects of solids particle size and reaction time on the mineral carbonation reaction because it does not account for reaction kinetics. Overall, discrepancies between experimental and modelling results are considerable and, although the thermodynamic part of the calculations is built upon a solid framework, the modelling work could also be at fault or uncompleted: for instance, thermodynamic data for gibbsite is absent in the code and its precipitation is not considered. When considering the influence of aluminium (i.e. kaolinite) in the modelling work with hematite, the altered mineral assemblage is substantially different from simulation results considering a 100% pure hematite sample. Consequently, the importance of fully characterise the solid sample before any simulations are computed is vital for representative results. It is worth highlighting how geochemical modelling is only a tool to predict equilibrium in a chemical system. However, experimental work provides the real data to be input in the geochemical code in order to get a reliable tool that can be applied in a real-case scenario.

Overall, this study has provided an insight into the geochemical fixation of $CO_2$-$SO_2$ gas mixtures in brine-iron oxides hydrothermal systems. The modelling and experimental work presented here provides a starting point to move forward when studying underground storage of $CO_2$-$SO_2$ gas streams in chemical systems containing ferric iron. In this work $SO_2$, which may specifically be acceptable/allowed under future $CO_2$ capture regulations is the required reductant for the mineral trapping process to take place and could be co-injected with $CO_2$ instead of separated from the gas stream at great expense.

## 9.2. Suggestions for future work

Based on the results and conclusions from this research, there are several areas that are worthy of further studies and that could contribute significantly to augment fundamental research in the geological sequestration of $CO_2$ when other flue gas constituents are eliminated with it.

1. Equilibrium was not achieved in short-term (24h) experiments so fewer longer term experiments would be more useful.
2. To assess the influence of reaction variables, a suitable experimental design, that minimises the number of experiments to undertake, could

also be defined. The response surface methodology can be then applied as en empirical modelling-approach for determining the relationship between operating variables and response variables.

3. Employment of other analytical techniques such as TGA-MS (thermogravimetric analysis – mass spectrometry), SEM or XRD for long term experiments will, undoubtly, help in identifying and quantifying secondary minerals precipitated as a result of carbonation reactions.
4. Study of the sensitivity of the carbonation reaction with goethite to those variables that were not studied in this work, i.e. reaction temperature and pressure, solids-to-liquid ratio and brine composition. Additionally, stirring speed can also be included to assess the influence of diffusion processes in the system.
5. Experimental measurements of dissolved $CO_2$ as well as inorganic carbon content in solid samples could be conducted with a $CO_2$ coulometer in all experiments.
6. A detailed study of the kinetics of the reaction could be conducted. The reductive dissolution of hematite and goethite could be investigated under relevant conditions for geological $CO_2$ storage. The acquisition of reaction rates is an important work because those could greatly impact masses and forms of mineral trapping of $CO_2$.
7. Modelling simulations could be obtained with other geochemical codes that account for kinetics aspects and/or multiphase flow, which would greatly help in predicting the performance of carbon repositories.

8. Comparison amongst laboratory and simulation data with natural analogues is fundamental to understanding any potential mineral storage benefits of various geosequestration systems.
9. Reaction between $CO_2$-$SO_2$ gas mixtures-brine and other host repositories, like typical red bed sandstone formations and silicate minerals previously considered for mineral trapping studies (olivine, serpentine, basalt,...), could be conducted. The effect of $SO_2$ in precipitation of secondary minerals could then be evaluated. Moreover, a mineralogy characteristic of a current site where $CO_2$ is being injected could be targeted.
10. Experimental and modelling work of gas-rock-brine geochemical reactions containing other pH buffers, like bicarbonate, more analogous to most saline-aquifer sequestration targets, could be conducted.
11. Research studies of co-injection of $CO_2$ and other components ($NO_x$, $H_2S$, $CH_4$,...) present in a flue-gas stream into a wide variety of siliciclastic host rocks or carbonate rocks-hosted saline aquifers.

APPENDIX

# REACTIONS IN A HEMATITE-KAOLINITE-BRINE-$CO_2$-$SO_2$ SYSTEM

# Appendix. Reactions in a hematite-kaolinite-brine-$CO_2$-$SO_2$ system

Table A-1. Initial test file for CHILLER: $CO_2$-$SO_2$ reaction at 100°C and 250 bar with 10 g of rock ( 82.58% of hematite and 17.42% of kaolinite) in 400 mL of 1.0mNaCl, 0.5mNaOH brine using 165g (excess) $CO_2$. Parameters in the table are defined in CHILLER's manual (Reed and Spycher, 2006).

```
 < erpc>    < pH >    < pfluid >    < temp >    < tempc >    < volbox-1 >   < rhofresh >
 0.1 E-11    0.00      250.00        25.00        0.00          0.00           0.00

 < sinc >   < slim >   < totmix >
 0.0001      0.004

 < enth >   < senth >  < denth >    < totwat >   < solmin >      < rm>        < aqgrm >    < suprnt >
   0.00       0.00       0.00         90.00        0.00           0.00         1049.747     1.00E-20

  -----        c         ifra          ipun        nloop           iste           lims         looc
    0          3           0             2          400              0              1            0

  ient        itre       idea          ipsa         incr           incp           mins         neut
    0          0           0             1           0               0              1            0


  saq>      < name >    < mtot >     < mtry >    < gamma >     < comtot >
   1          H+          0.00       1.00E-07       1.00          0.00
   2          H2O         0.40       1.00E+00       1.00          0.00
   3          Cl-         0.40       0.99E+00       1.00          0.00
   4          SO4--     1.00E-05     1.00E-07       1.00          0.00
   5          HCO3-     1.00E-05     6.26E-06       1.00          0.00
   6          HS-       1.00E-16     2.68E-17       1.00          0.00
   7        SiO2(aq)    1.00E-16     0.10E-16       1.00          0.00
   8          Al+++     1.00 E-16    0.10E-18       1.00          0.00
  11          Fe++      1.00E-16     1.47E-17       1.00          0.00
  13          Na+         0.40       4.83E-02       1.00          0.00

 < min >             < mintry >

< nomox >   < wtpc >    < ppm >
  NaOH       100.0

< supnam >
 FCO2-3.5
 FCO2-3.0

< dontfr >
```

* The input file for CHILLER for the non-buffered case would be the same but with no titration with NaOH.

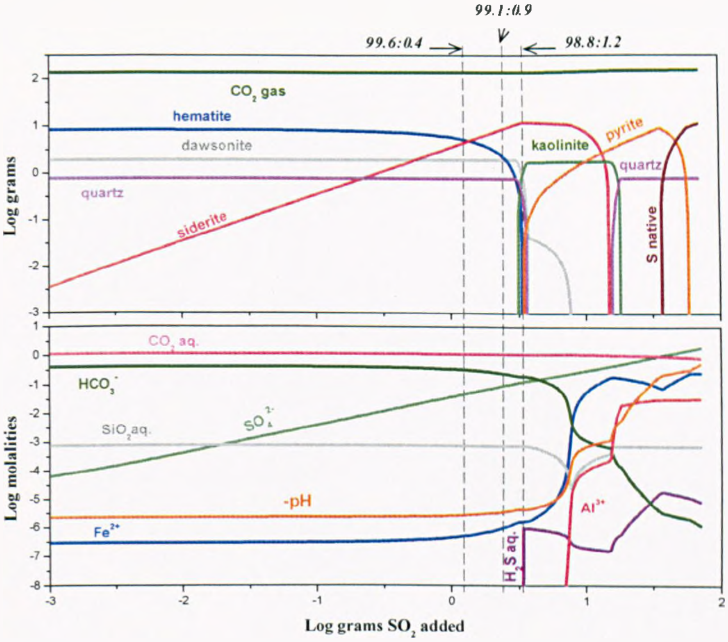

Figure A-1.Results from simulation at 100°C and 250 bar of the $CO_2$-$SO_2$ reaction with 10 g of rock (82.58% of hematite and 17.42% of kaolinite) in 400 mL of 1.0mNaCl, 0.5mNaOH brine using 165g (excess) $CO_2$: mineral/gas phase assemblage (top) and fluid composition (bottom).

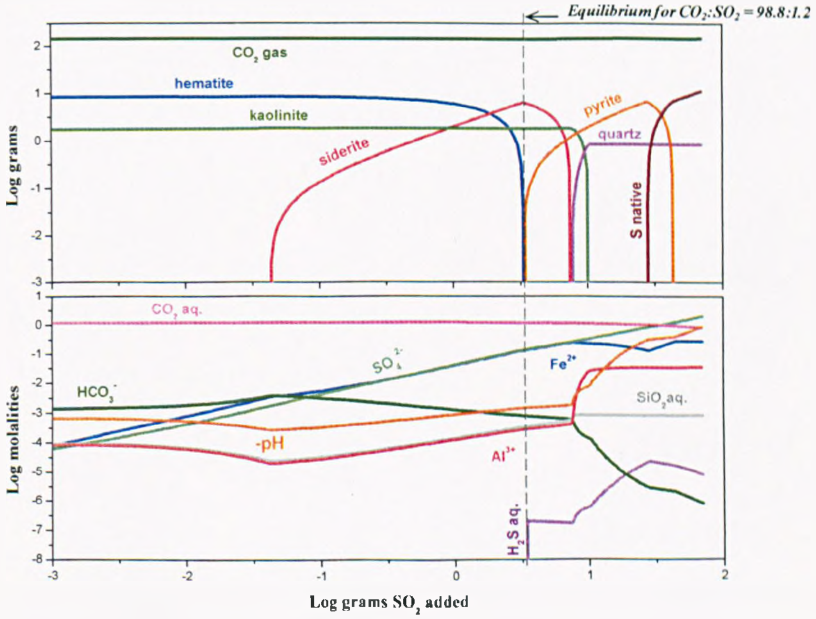

Figure A-2.Results from simulation at 100°C and 250 bar of the $CO_2$-$SO_2$ reaction with 10 g of rock (82.58% of hematite and 17.42% of kaolinite) in 400 mL of 1.0mNaCl brine using 165g (excess) $CO_2$: mineral/gas phase assemblage (top) and fluid composition (bottom).